COMPUTATIONAL STUDIES ON SELECTIVE AROMATIC C–F BOND ACTIVATION AT RHODIUM AND RUTHENIUM

Julien Panetier

Submitted for the degree of
Doctor of Philosophy

School of Engineering and Physical Sciences
Heriot-Watt University

January 2012

Abstract

Density functional theory (DFT) calculations have been carried out to study the selective C–F bond activation of fluoroaromatics at rhodium and ruthenium complexes.

The C–F activation reaction of C_6F_5H with $[Rh(SiR_3)(PMe_3)_3]$ (R_3 = Me_2Ph, Ph_3) to give $[Rh(4\text{-}C_6F_4H)(PMe_3)_3]$ and $FSiR_3$, has been studied computationally. Using a model system, $[Rh(SiMe_3)(PMe_3)_3]$, calculations show that the lowest energy process occurs via initial phosphine dissociation and subsequent C–F oxidative addition to give *trans*-$[Rh(4\text{-}C_6F_4H)(F)(SiMe_3)(PMe_3)_2]$, with computed free energies of activation ($\Delta G^{\ddagger}$) of +13.2 kcal/mol and +12.4 kcal/mol, respectively. Reductive elimination and phosphine association to give the final products $[Rh(4\text{-}C_6F_4H)(PMe_3)_3]$ and $FSiMe_3$ are found to be facile. In addition, calculations show that C–F activation at *trans*-$[Rh(SiMe_3)(PMe_3)_2]$ is more accessible kinetically and thermodynamically than C–H activation ($\Delta\Delta G^{\ddagger}$ = 2.9 kcal/mol, $\Delta\Delta G$ = 51.3 kcal/mol).

DFT calculations have been used to model the reaction of C_5NF_5 at the 2-position with $[Rh(X)(PEt_3)_3]$ (X = $Si(OEt)_3$, Bpin, where Bpin = pinacolate = $–OCMe_2CMe_2O–$). C–F activation at the computational models $[Rh(X)(PMe_3)_3]$ (X = $Si(OMe)_3$ and Bpin) shows that the lowest pathways proceed via novel silyl- and boryl-assisted C–F activation in which short Rh···N contacts are computed in the transition states. These occur via modest barriers ($\Delta G^{\ddagger}$ = +26.1 kcal/mol and +20.1 kcal/mol, respectively, relative to the two separated reactants) and also account for the experimental selectivity.

The hydrodefluorination (HDF) reaction of C_6F_5H at $[Ru(H)_2(CO)(NHC)(PR_3)_2]$ (NHC = SIMes, SIPr, IMes, IPr; R = Ph) to give 1,2,3,4-$C_6F_4H_2$, has been investigated. Calculations on small (NHC = IMe, R = H) and full systems (NHC = IMes, R = Ph) have allowed a novel class of reaction mechanism to be defined involving a nucleophilic attack of one hydride ligand at C_6F_5H. The most accessible pathway has a computed transition state energy of +20.1 kcal/mol in THF (PCM, approach). In addition, calculations reveal that the use of a more sterically encumbered full model system is essential to explain the unusual *ortho*-regioselectivity observed experimentally.

To my parents, Françoise and Michel

and my brother, Maxime

Acknowledgements

Firstly, I would like to thank my supervisor, Professor Stuart Macgregor, for his guidance, enthusiasm and encouragement throughout my PhD. I would like also to thank my collaborators Professors Michael Whittlesey and Thomas Braun for their experimental contributions which form the basis for most of the work reported in this thesis. I am also grateful to Professor Odile Eisenstein and Doctors Christophe Raynaud and Eric Clot for their welcome during my internship in Montpellier.

I would also like to thank the previous and current members of the "Computational Inorganic Chemistry Group" for their help and the great atmosphere they created in the laboratory. Particularly, Abu, Andrés, Dave, Jenni, Jonas and Stefan for their friendship and their support during my Masters and PhD degrees.

I owe special thanks to Amalia for her love, advice and support during these last years. "*Muchas gracias por todo y siempre estarás en mi corazón*".

I would also like to thanks my parents, Françoise and Michel, and my brother Maxime for being always present for me. I am also grateful for the support I received from all my friends, especially Bapt, Charis, Dom, Gauthier, Gerard, Jean-Jo, Loic, Lucia, Nico, Patricia, Santi, Stephen, Vins and Zincou.

ACADEMIC REGISTRY
Research Thesis Submission

Name*:*	Julien Panetier		
School/PGI:	School of Engineering and Physical Sciences - Chemistry		
Version: *(i.e. First, Resubmission, Final)*	Final	Degree Sought (Award **and** Subject area)	PhD

Declaration

In accordance with the appropriate regulations I hereby submit my thesis and I declare that:

1) the thesis embodies the results of my own work and has been composed by myself
2) where appropriate, I have made acknowledgement of the work of others and have made reference to work carried out in collaboration with other persons
3) the thesis is the correct version of the thesis for submission and is the same version as any electronic versions submitted*.
4) my thesis for the award referred to, deposited in the Heriot-Watt University Library, should be made available for loan or photocopying and be available via the Institutional Repository, subject to such conditions as the Librarian may require
5) I understand that as a student of the University I am required to abide by the Regulations of the University and to conform to its discipline.

* *Please note that it is the responsibility of the candidate to ensure that the correct version of the thesis is submitted.*

Signature of Candidate*:*	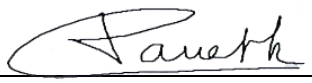	Date:	17/04/2012

Submission

Submitted By *(name in capitals):*	
Signature of Individual Submitting:	
Date Submitted:	

For Completion in the Student Service Centre (SSC)

Received in the SSC by *(name in capitals):*			
Method of Submission *(Handed in to SSC; posted through internal/external mail):*			
*E-thesis Submitted (**mandatory for final theses)***			
Signature:		Date:	

Please note this form should bound into the submitted thesis.

Updated February 2008, November 2008, February 2009, January 2011

Table of Contents

List of Publications

1. M. Teltewskoi, J. A. Panetier, S. A. Macgregor, T. Braun, "A Highly Reactive Rhodium(I) Boryl Complex as a Useful Tool for C–H Bond Activation and Catalytic C–F Bond Borylation", *Angew. Chem. Int. Ed.*, 2010, **49**, 3947.

2. J. A. Panetier, S. A. Macgregor, M. K. Whittlesey, "Catalytic Hydrodefluorination of Pentafluorobenzene by [Ru(NHC)(PPh_3)$_2$(CO)H_2]: A Nucleophilic Attack by a Metal-Bound Hydride Ligand Explains an Unusual *Ortho*-Regioselectivity", *Angew. Chem. Int. Ed.*, 2011, **50**, 2783.

3. V. I. Bakhmutov, F. Bozoglian, K. Gómez, G. González, V. V. Grushin, S. A. Macgregor, E. Martin, F. M. Miloserdov, M. A. Novikov, J. A. Panetier, L. V. Romashov, "CF_3–Ph Reductive Elimination from [(Xantphos)Pd(CF_3)(Ph)]", *Organometallics*, 2012, **31**, 1315.

4. L. J. L. Haller, S. A. Macgregor, J. A. Panetier, "Computational Studies on the Reactivity of Transition Metal Complexes Featuring N-Heterocyclic Carbene Ligands" In *N-Heterocyclic Carbenes: From Laboratory Curiosities to Efficient Synthetic Tools*, Ed S. Díez-González, RSC Catalysis Series No. 6, 2011, 42.

5. A. G. Algarra, S. A. Macgregor and J. A. Panetier, "Mechanistic Studies of C–X Bond Activation at Transition Metal Centres" In *Comprehensive Inorganic Chemistry II*, Ed S. Álvarez, *Accepted*.

Chapter 1: Literature Introduction

This chapter deals with intermolecular C–F bond activation of fluoroaromatics at transition metal (TM) complexes. The discussion begins with a background to fluorine chemistry before reviewing experimental and computational studies. This chapter is based mainly on three topics, that are related to the studies in this thesis: 1) oxidative addition; 2) ligand-assisted C–F activation; and 3) hydrodefluorination reactions.

1.1 Background and Applications

The isolation of elemental fluorine was first reported in 1886 by Moissan,[1] however, the practical use of fluorinated organic compounds started in the 1920s.[2] One of the earliest examples (1927) is known as the Balz-Schiemann reaction which consists of introducing fluorine into specific positions of aromatic compounds.[3] In the 1930s, fluorinated organic compounds were used in industry with the introduction of chlorofluorocarbons (CFCs) as refrigerants in cooling and air conditioning equipment, fire extinguishing chemicals and aerosol propellants.[4] In 1938, Plunkett synthesised the first fluoropolymer, poly(tetrafluoroethylene), known as PTFE or Teflon.[5] In the 1940s, Simons and co-workers developed the electrochemical fluorination (ECF), process used in the production of a variety of perfluorinated organic compounds.[6] Industrial organofluorine chemistry was further developed with the Manhattan Project and the construction of the first nuclear weapon.[7] At that time, fabrication of highly resistant materials (e.g. PTFE), lubricants and coolants was needed in order to handle the extremely aggressive uranium hexafluoride (UF_6).

In the 1950s, fluorinated organic compounds started to be used as potential drugs, mostly because of the properties of F (similar size to H, but much higher electronegativity), its propensity to hydrogen-bonding and the increased lipophilicity and physiochemical effects of fluorinated groups.[4] In 1974, the industrial development of fluorinated compounds took a step back, however, after the prediction of the ozone-depleting effect of CFCs[8] and the subsequent observation of the ozone hole over the Antarctic in 1980. In 1987, the Montreal Protocol initiated the phase-out of most CFCs. Since then, CFCs were mainly substituted by other fluorine-containing chemicals such as hydrofluorocarbons (HFCs) and fluorinated ethers. Nowadays, fluorinated organic compounds are widely used in the electronics, agrochemical and pharmaceutical

industries. In 2006, Thayer noted that "approximately 40 % of all agrochemicals and 20 % of all pharmaceuticals on the current market are organic molecules containing at least one fluorine atom".[9] In 2008, three of the top 10 drugs were fluorinated organic compounds: Lipitor, Seretide and Risperdal (see Figure 1.1).[10]

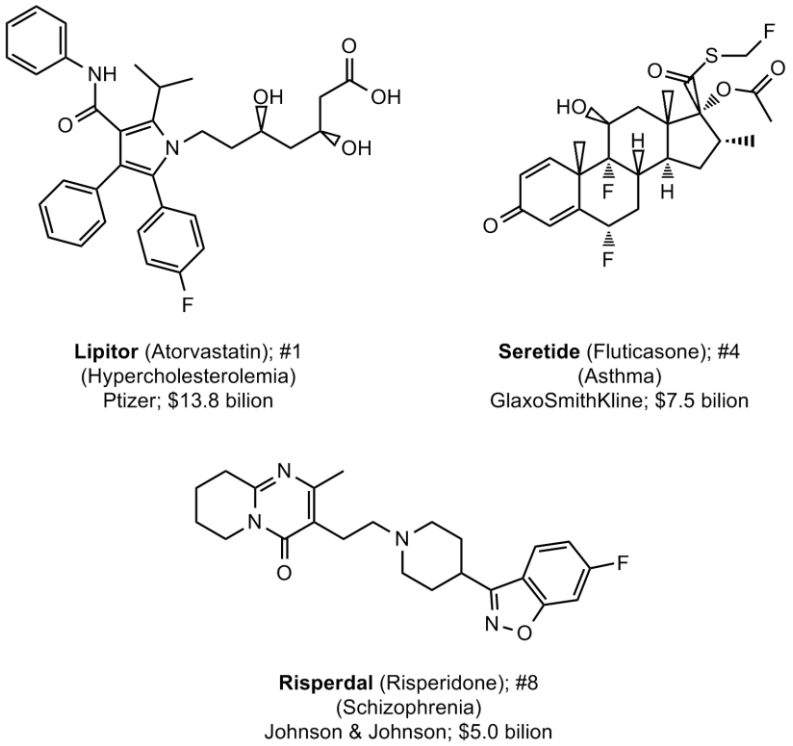

Figure 1.1: Three of the top 10 drugs in 2008 containing at least one fluorine atom.[10]

The synthesis of fluoroaromatics represents a significant challenge of modern synthetic chemistry. The most common synthetic methods are reductive aromatization, the fluoroformate process, the Halex process or the Balz-Schiemann reaction.[2-3] This last reaction is actually one of the major industrial processes in the synthesis of monofluorinated arenes (see Figure 1.2).[3] This consists of the fluorination of an arene diazonium tetrafluoroborate intermediate by heating up to 120 °C to yield the monofluorinated arene product. The reproducibility of the reaction yield is, however, quite poor and the arene diazonium tetrafluoroborate is potentially toxic, explosive and corrosive. Another variant of the Balz-Schiemann reaction has been reported by Yoneda and Fukuhara where, in this case, the arene diazonium tetrafluoroborate is not isolated but generated *in situ*, in the presence of 70 % HF-pyridine with $NaNO_2$ at 0 °C.[11] The resulting diazonium salt is then heated up to 160 °C. Despite the generation of large quantities of unwanted waste products such as $NaBF_4$, NaCl and HCl, this reaction is still performed on a large scale because of the lack of alternative methods.

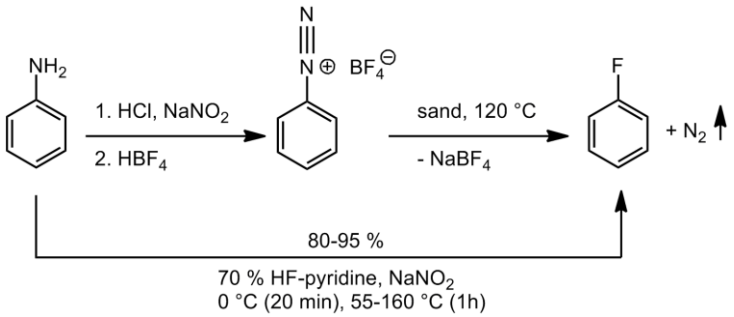

Figure 1.2: Balz-Schiemann reaction and its new variant.[3,11]

Other environmental and cost efficient methods, however, have been and are being developed through the use of transition metal catalysis. This approach is similar in that they consist of selective fluorination into the aromatic compound. One example is the copper-catalysed oxidative fluorination developed at Dupont (see Figure 1.3).[12] This is a "greener" alternative of the Balz-Schiemann reaction as the undesired chemical waste products, copper and HF, react at 400 °C in the presence of oxygen to regenerate the CuF_2 reactant and H_2O.

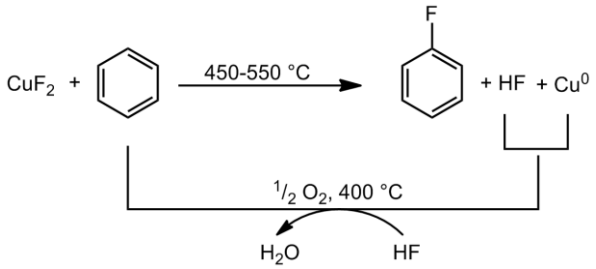

Figure 1.3: Oxidative fluorination of benzene by CuF_2.[12]

In contrast, transition metal complexes can also be employed to prepare fluorinated organic compounds by selective defluorination, rather than by selective fluorination.[13] The benefit of this approach is that it results in the synthesis of desired fluorinated organic compounds under mild conditions that are hard to access by conventional reactions. The use of fluoroaromatics in catalysis has therefore received much attention and several examples of catalytic cross-coupling[13d,13e,14] and hydrodefluorination[15] processes have emerged. Cross-coupling reactions are based on the activation of C–F bonds of fluorinated organic compounds and the subsequent formation of new C–C bonds, while hydrodefluorination (HDF) reactions consist of the substitution of fluorine by hydrogen (see Figure 1.4).

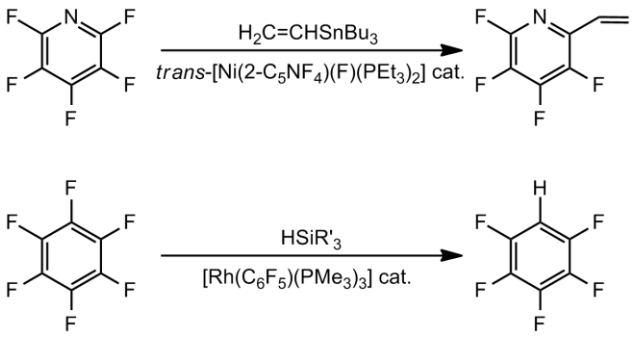

Figure 1.4: Examples of catalytic cross-coupling[13d,14b] (top) and hydrodefluorination[15a] (bottom, where R′ = Ph, OEt) reactions.

The major challenge of these reactions is in the activation of the C–F bond. Indeed this bond is known to be one of the strongest single bonds to a heteroatom that carbon can form and results from the electrostatic interactions between the polarised $C^{\delta+}$ and $F^{\delta-}$ atoms (e.g. C_6F_5–F bond energies = +116 kcal/mol).[13k,16] Several examples of stoichiometric intermolecular C–F bond activation are known and have been classified in four fundamentals patterns by Braun and Perutz: 1) oxidative addition; 2) M–C bond formation with E–F elimination, where E = H, Si; 3) hydrodefluorination with M–F bond formation, and 4) nucleophilic attack.[13j,13k]

The following sections will mainly review reaction mechanisms of selective aromatic C–F activation in the presence of other bonds.

1.2 Survey of Experimental Studies of Intermolecular Aromatic C–F Bond Activation at Transition Metal Complexes

1.2.1 Oxidative Addition at Group 10 Metals

C–F oxidative addition of fluoroaromatics is mainly observed for complexes of group 10 metals and rarely otherwise. The use of nickel complexes to afford C–F activation is by far the most common. The first example in which C–F activation results in the formation of an oxidative product was studied experimentally by Fahey and Mahan.[17] They reported the C–F activation of C_6F_6 at $[Ni(COD)_2]$ (**1**, COD = 1,5-cyclooctadiene) in the presence of PEt_3 to give *trans*-$[Ni(C_6F_5)(F)(PEt_3)_2]$ (**2**, see Figure 1.5). In 1997, Yamamoto and Abla studied the C–F activation of C_6F_6 at $[Ni(Et)_2(bpy)]$ (bpy = 2,2′-bypyridine) and reported the first example of *cis*-biarylnickel (II) complex $[Ni(C_6F_5)_2(bpy)]$.[18] The same year, Perutz and co-workers fully characterised **2**, formed upon C–F activation of C_6F_6 at **1**/PEt_3, by X-ray crystallography and nuclear magnetic resonance (NMR) spectroscopy, and improved the yield of the reaction.[19] The same group studied several examples of C–F activation of fluoroaromatics at Ni(0).[13d,19-20] In one case, C–F bond activation of C_6F_5H at $[Ni(PEt_3)_4]$ gives a mixture of the three nickel fluoride isomers along with phosphoranes and the hydrodefluorination product 1,2,4,5-$C_6F_4H_2$. Moreover, partial fluoropyridine substrates undergo selective C–F activation over C–H activation (see **3** and **4** in Figure 1.5).[19,21] In 1999, C–F activation of 2,4,6-trifluoropyrimidine in hexane in the presence of PEt_3 at **1** was observed to give **5**.[22]

Mechanistic studies have permitted the isolation of key intermediates and allowed greater understanding of the reaction mechanism. Pörschke *et al.*, for example, reported the initial formation of an η^2-arene intermediate $[Ni(\eta^2\text{-}C_6F_6)(^tBu_2PCH_2CH_2P^tBu_2)]$ for the C–F activation of C_6F_6 at $[\{Ni(^tBu_2PCH_2CH_2P^tBu_2\}_2(\mu\text{-}\eta^2\text{-}\eta^2\text{-}C_6H_6)]$ prior to formation of $[Ni(C_6F_5)(F)(^tBu_2PCH_2CH_2P^tBu_2)]$.[23] A similar observation has been reported for the C–F activation of $C_{10}F_8$ at **1**/PEt_3 to give *trans*-$[Ni(2\text{-}C_{10}F_7)(F)(PEt_3)_2]$ (**7**) after initial formation of **6** (see Figure 1.6).[24]

More recently, Johnson *et al.* studied the C–F activation of C_6F_5X (X = F, H) at $[Ni(\eta^2\text{-}C_{14}H_{10})(PEt_3)_2]$ (**8**).[25] With C_6F_5H C–F activation occurs at the 2-position to give *trans*-$[Ni(2\text{-}C_6F_4H)(F)(PEt_3)_2]$ with 97 % selectivity. Moreover, the same group showed that

1,2,4,5-$C_6F_4H_2$ and 1,2,3,5-$C_6F_4H_2$ undergo C–H activation which then converts to the thermodynamic C–F products (see **9** and **10** in Figure 1.6).[26]

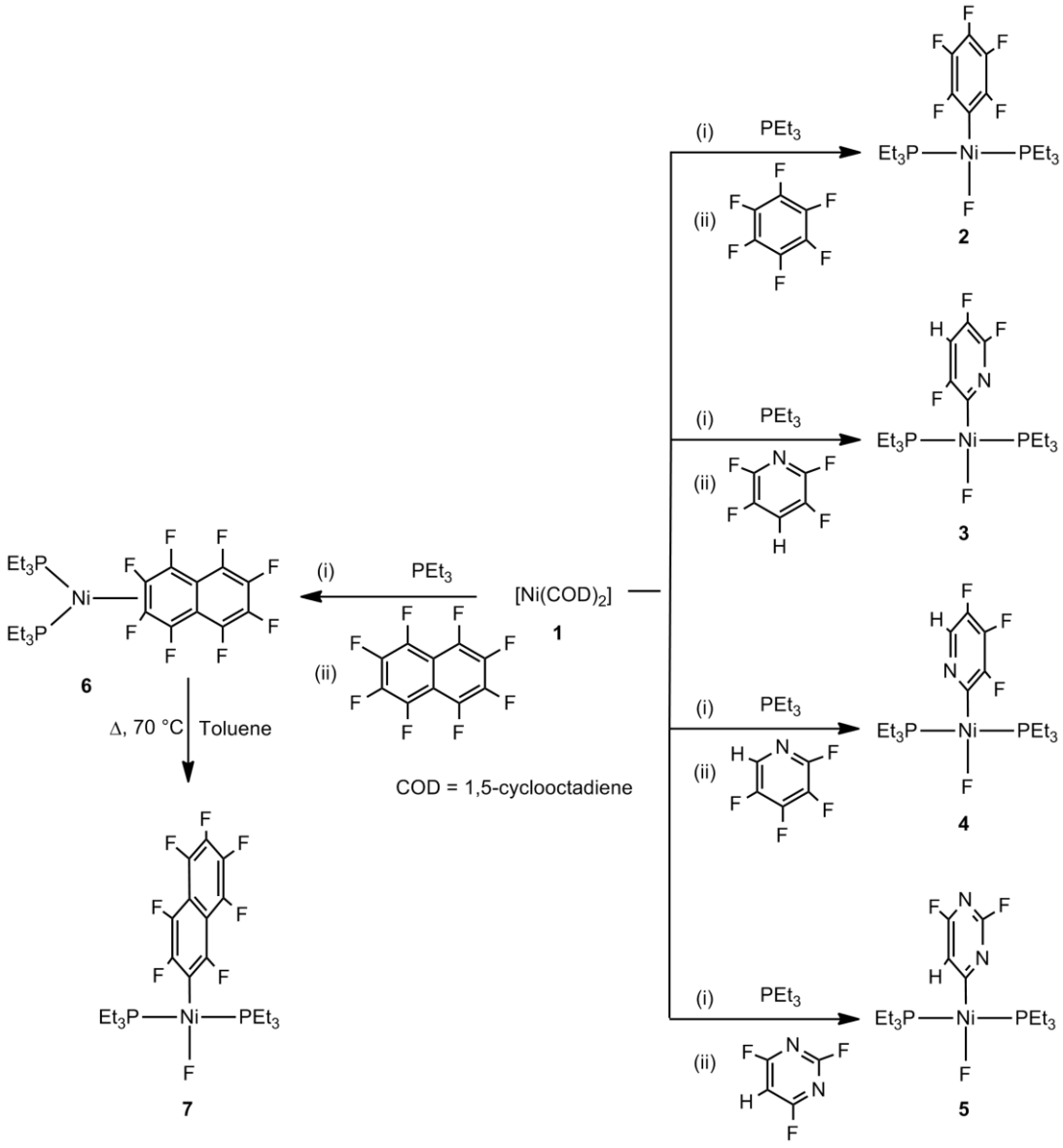

Figure 1.5: Landscape of C–F activation of fluoroaromatics at 1/PEt_3.[13d,17,19-22,24]

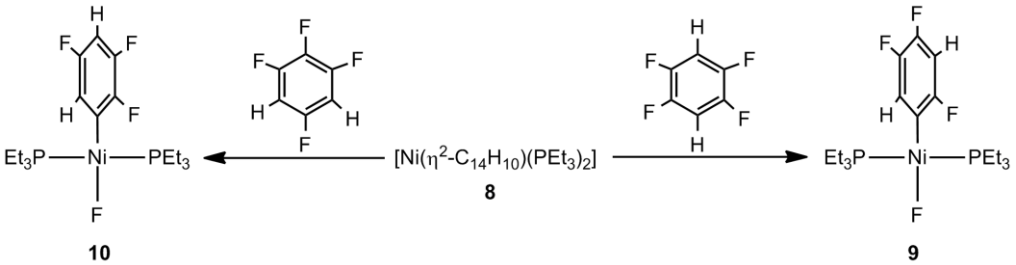

Figure 1.6: C-F activation of 1,2,4,5-$C_6F_4H_2$ and 1,2,3,5-$C_6F_4H_2$ at 8.[26]

In contrast to the previous examples, Johnson and co-workers have shown that by using a different type of phosphine ligand, activation of 1,2,4,5-$C_6F_4H_2$ at [Ni(η^2-$C_{14}H_{10}$)(P^iPr_3)$_2$] (**11**) resulted only in the C–H activation product [Ni(4-C_6F_4H)(H)(P^iPr_3)$_2$] (**12**).[27] In addition, even after hours heating at 100 °C, no C–F activation products are observed suggesting that **12** is the kinetic and thermodynamic product. This contrasts with the general idea that C–H activation is kinetically more favourable while C–F activation is thermodynamically more accessible.

Braun and co-workers also showed that the outcome of the reaction between [Ni(COD)$_2$] (**1**) and 5-chloro-2,4,6-trifluoropyrimidine depends on the phosphine ligand used.[14d,28] When the reaction is performed in the presence of PCy_3, P^iPr_3 or PPh_3 C–F activation took place to give **13**, **14** and **15**, respectively, while the C–Cl product is observed with PEt_3 (**16**, see Figure 1.7)

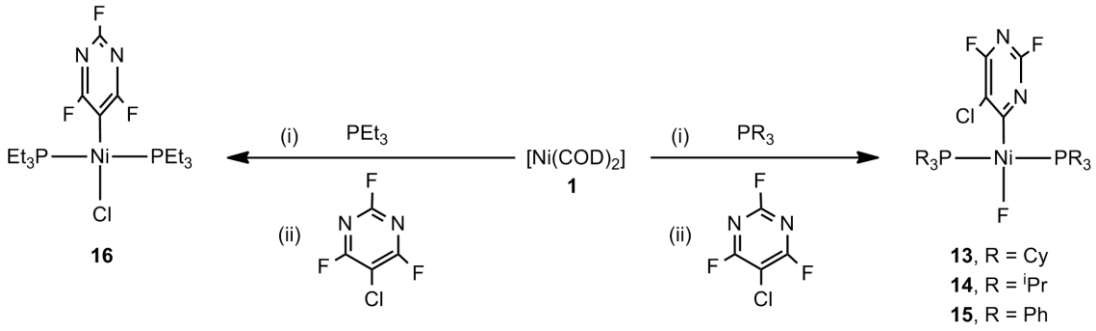

Figure 1.7: Selective C–F activation and C–Cl activation of 5-chloro-2,4,6-trifluoropyrimidine at 1.[14d,28]

On the other hand, substitution of excess of phosphine ligand by a nonaromatic imine has been showed to perform selective C–F activation over C–H activation of C_6F_5H and isomers of $C_6F_4H_2$ at **1** (see Figure 1.8).[29]

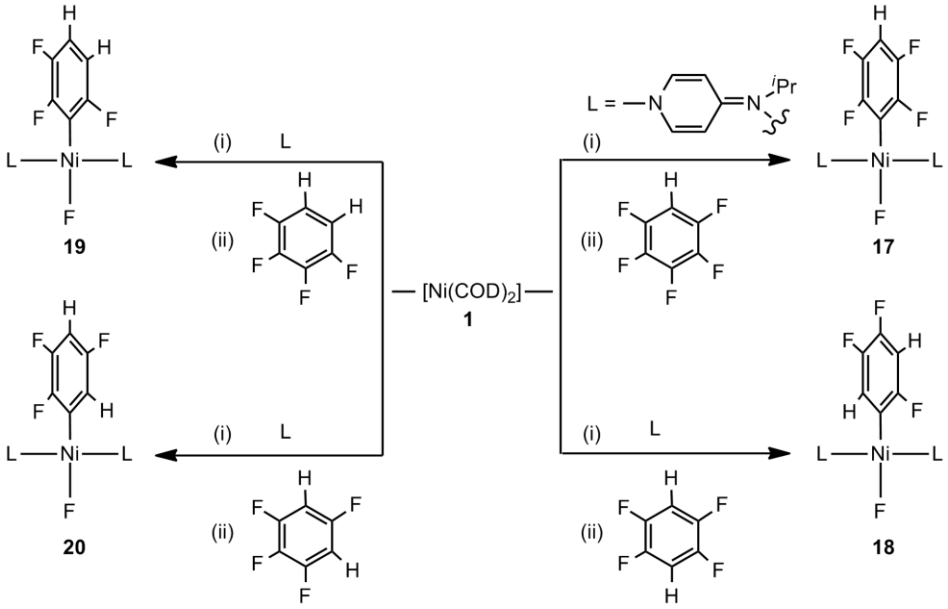

Figure 1.8: Selective C–F activation over C–H activation of C_6F_5H and $C_6F_4H_2$ at 1 in the presence of a nonaromatic imine.[29]

Since the isolation and characterisation of the first stable N-heterocyclic carbene (NHC) by Arduengo *et al.*[30] in 1991, the use of these species as ligands for catalysis has emerged.[31] Radius and co-workers reported a series of papers in which nickel(0)-NHC complexes, $[Ni_2(^iPr_2Im)_4(COD)]$ (**21**) and $[Ni(^iPr_2Im)_2(\eta^2\text{-}C_2H_4)]$ (**22**, $^iPr_2Im$ = 1,3-bis(*iso*propyl)imidazol-2-ylidene), are used to afford C–F activation of fluoroaromatics.[32] For instance, **22** performs C–F activation of C_5NF_5 at the 4-position while the reaction occurs at the 2-position at **1** in the presence of PEt_3 (see Figure 1.9).[19]

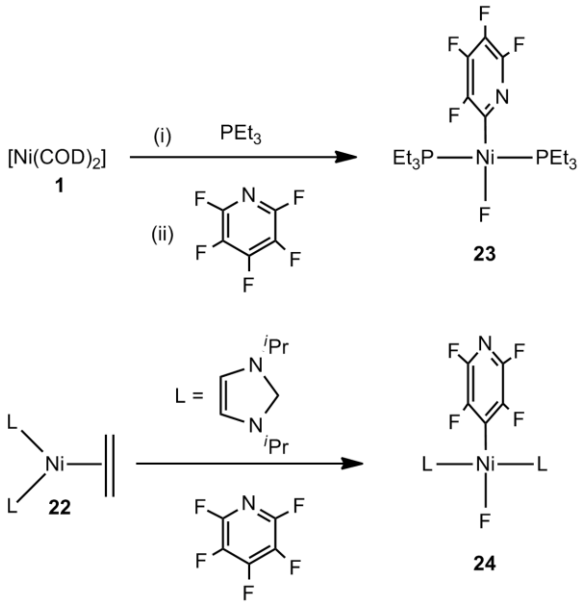

Figure 1.9: C–F activation of C_5NF_5 at Ni(0).[19,32d]

Some examples are also known for selective C–F activation of fluoroaromatics at Pd metal centres. Perutz and co-workers, for instance, reported the C–F activation of C_5NF_5 at the 4-position with $[Pd(PR_3)_2]$ (R = Cy, ^{i}Pr) in toluene at 100 °C to give *trans*-$[Pd(4\text{-}C_5NF_4)(F)(PR_3)_2]$ (see Figure 1.10).[33] In the same study, the authors showed that formation of *trans*-$[Pd(4\text{-}C_5NF_4)(F)(PR_3)_2]$ can be obtained in better yield by using a chelating palladium complex, $[Pd(Me_2)(tmeda)]$ (tmeda = tetramethylethylenediamine) as starting point in the presence of C_5NF_5 and PR_3 (R = Cy, ^{i}Pr). In contrast, $[Pd(PR_3)_2]$ does not undergo C–F activation with 2,3,5,6-C_5NF_4H even at 100 °C. One year later, Grushin *et al.* reported the C–F activation of C_6F_6 at $[Pd(PR_3)_2]$ (R = Cy, ^{i}Pr) in THF at 70 °C and observed the formation of *trans*-$[Pd(C_6F_5)(F)(PR_3)_2]$.[34]

C–F activation at platinum metal centres has also been studied. The first example of oxidative addition was reported by Hofmann and Unfried, involving the C–F activation of C_6F_6 at room temperature at {Pt(dtbpm)} to give $[Pt(C_6F_5)(F)(dtbpm)]$ (dtbpm = bis(di-*t*-butylphosphino)methane).[35] In 2000, Perutz and co-workers also showed that *trans*-$[Pt(H_2)(PCy_3)_2]$ undergoes C–F activation of C_6F_6 to give a mixture of *trans*-$[Pt(H)(C_6F_5)(PCy_3)_2]$ and *trans*-$[Pt(H)(FHF)(PCy_3)_2]$ in a 13:1 ratio.[36] Later on, the same group studied the reaction of C_5NF_5 at $[Pt(PR_3)_2]$ (R = Cy, ^{i}Pr) in THF at room temperature.[33] Unexpectedly, C–F activation occurs at the 4-position to form *trans*-$[Pt(4\text{-}C_5NF_4)(R)(PR_3)(PR_2F)]$ in which F is displaced onto a phosphine ligand and one alkyl substituent transfers onto the metal centre (see Figure 1.10).

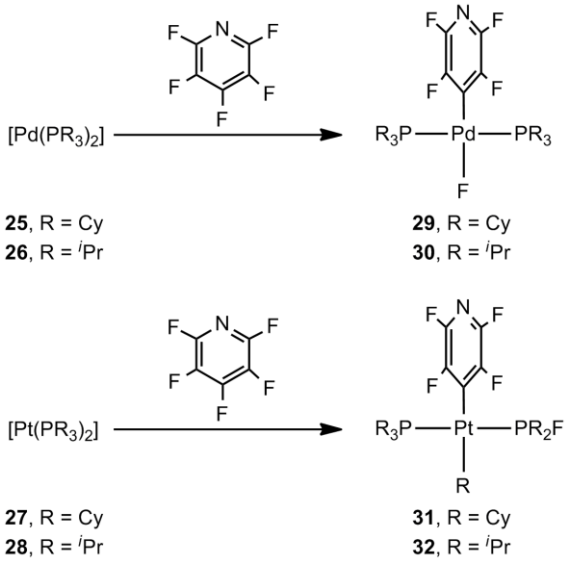

Figure 1.10: C–F activation of C_5NF_5 at $[Pd(PR_3)_2]$ (top) and C–F and P–C activation of C_5NF_5 at $[Pt(PR_3)_2]$ (bottom).[33]

Grushin and co-workers observed similar results for the reaction of C_6F_6 at $[Pt(PCy_3)_2]$ in THF at 70 °C which undergoes C–F and P–C activation to form *trans*-$[Pt(C_6F_5)(Cy)(PCy_3)(PCy_2F)]$.[34] More recently, Perutz *et al.* reported the C–F activation of 2,3,5-trifluoro-4-(trifluoromethyl)pyridine at $[Pt(PR_3)_2]$ (R = Cy, ^{i}Pr, Cyp = cyclopentyl) to give *cis*-$[Pt(F)\{2\text{-}C_5NF_2H(CF_3)\}(PR_3)_2]$ which then converts to *trans*-$[Pt(F)\{2\text{-}C_5NF_2H(CF_3)\}(PR_3)_2]$ either thermally or photochemically (see Figure 1.11).[37]

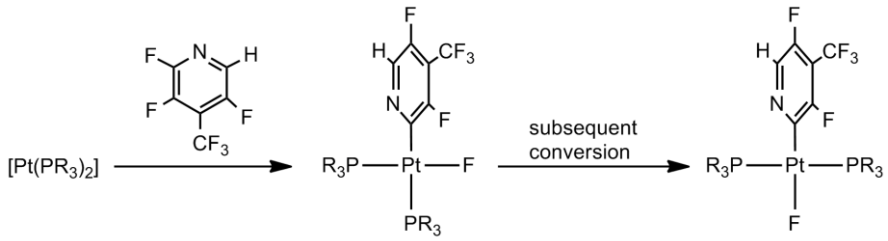

Figure 1.11: C–F activation of 2,3,5-trifluoro-4-(trifluoromethyl)pyridine at $[Pt(PR_3)_2]$.[37]

C–F activation of fluoroaromatics at group 10 metal centres has shown to be selective over activation of other bonds. The choice of the ligand and the metal is crucial for the outcome of the reaction. For example, C–F activation of C_5NF_5 at $\{Ni(PR_3)_2\}$ occurs mostly at the 2-position in contrast to $[M(PR_3)_2]$ (M = Pd, Pt) which proceeds at the 4-position.

1.2.2 Hydrodefluorination (HDF) Reactions

Hydrodefluorination reactions are another class of intermolecular C–F activation that results in the substitution of fluorine by hydrogen. In the following section, key experimental papers are reviewed by the transition metal groups involved.

(i) At Group 4 Metals

The first example of HDF at group 4 transition metal centres was reported by Kiplinger and Richmond.[38] In this study, the authors showed that $C_{10}F_8$ can react at $[Zr(\eta^5\text{-}C_5H_5)_2(Cl)_2]$ (**37**) in THF with Mg as terminal reductant to give 1,3,4,5,6,7,8-$C_{10}F_7H$ (**38**, see Figure 1.12). To explain the C–F activation, an oxidative addition mechanism at the low-valent zirconocene fragment $\{Zr(\eta^5\text{-}C_5H_5)_2\}$ was proposed.

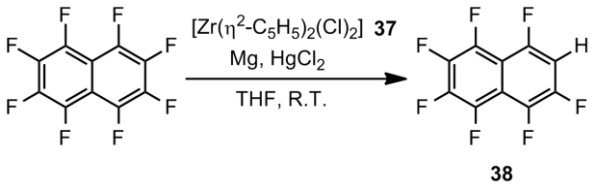

Figure 1.12: HDF of octafluoronaphthalene at $[Zr(\eta^2\text{-}C_5H_5)_2(Cl)_2]$ to give 38.[38]

The same group also reported the HDF and aromatization of cyclic perfluorocarbons at room temperature by using reduced titanocene and zirconocene complexes (see Figure 1.13).[39]

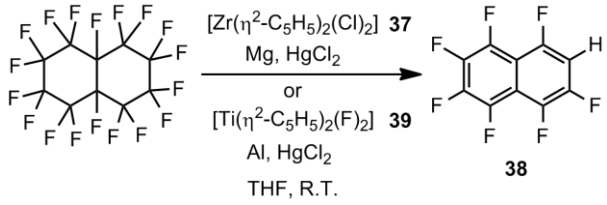

Figure 1.13: HDF and aromatization of perfluorodecalin at titanocene and zirconocene complexes to give 38.[39]

Since the first example of HDF reported by Kiplinger and Richmond at zirconocene complexes, Jones *et al.* employed the related species, $[Zr(\eta^5\text{-}C_5H_5)_2(H)_2]_2$ (**40**), $[Zr(\eta^5\text{-}C_5Me_5)_2(H)_2]$ (**41**) and $[Zr(\eta^5\text{-}C_5H_5)_3(H)]$ (**42**) to perform HDF of other fluoroaromatics.[13f,40] With **41**, C_6F_6 reacts at 85 °C in cyclohexane-d_{12} to give a mixture of $[Zr(\eta^5\text{-}C_5Me_5)_2(F)(H)]$ (**43**), $[Zr(\eta^5\text{-}C_5Me_5)_2(C_6F_5)(H)]$ (**44**), and C_6F_5H in a 2:1:1 ratio (see Figure 1.14).[40a,40b]

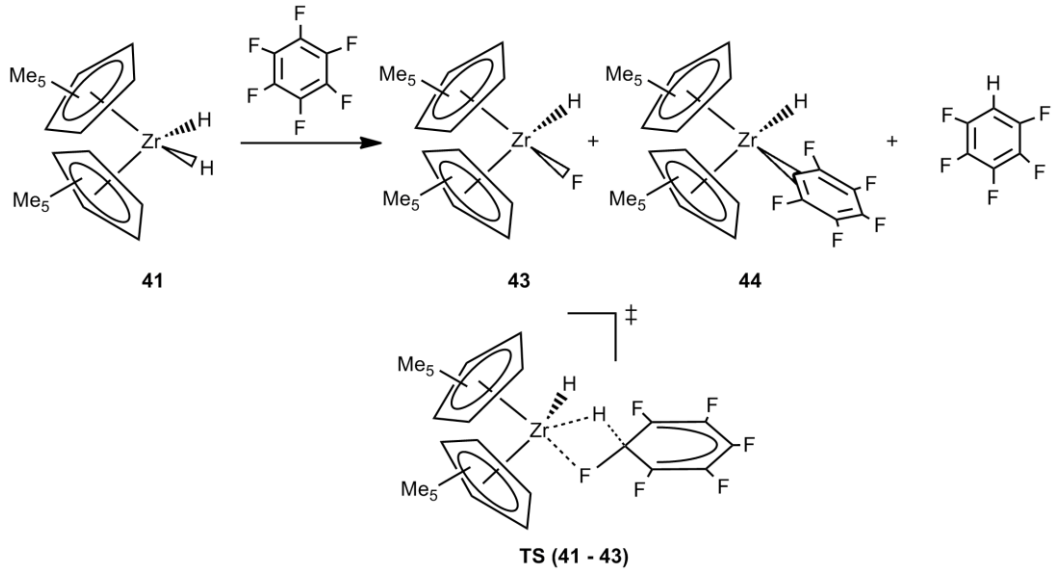

Figure 1.14: HDF reaction of C_6F_6 at $[Zr(\eta^5\text{-}C_5Me_5)_2(H)_2]$ and the postulated σ-bond metathesis transition state TS (41 – 43).[13f,40a,40b]

To explain the formation of **43**, a σ-bond metathesis transition state, **TS (41 – 43)**, has been postulated as shown in Figure 1.14. In addition, **44** is thought to be formed by 1) initial migration of hydride to η^5-C_5Me_5; 2) attack of the Zr(II) on the arene ring to eliminate HF; and 3) reaction of HF with [Zr(η^5-C_5Me_5)$_2$(H)$_2$] to give **43** and H_2.[13f,40b] In contrast, the reaction under similar conditions with C_6F_5H at **41** resulted in C–H activation rather than C–F activation.[40b] However, a mixture of hydrodefluorinated products, 1,2,3,4- and 1,2,4,5-$C_6F_4H_2$ in a 1.3:1 ratio, was also obtained.

HDF of fluorobenzene and 1-fluoronaphthalene has also been reported in the Jones group.[13f,40c] C_6FH_5 reacts at **41** under 1.3 atm of H_2 in cyclohexane-d_{12} at 85 °C and results in a mixture of **43**, [Zr(η^5-C_5Me_5)$_2$(C_6H_5)(H)] (**45**), and C_6H_6 in a 1:0.75:1 ratio. Formation of C_6H_6 and **43** is postulated to go through a similar transition state to **TS (41 – 43)**, while **45** is formed by *ortho*-C–H activation of C_6FH_5 and subsequent *β*-fluoride elimination to give a benzyne ligand which then inserts into the Zr–H. However, the main disadvantage of this reaction is that it is very slow, requiring up to 40 days. 1-fluoronaphtalene reacts faster than C_6FH_5 to give naphthalene and **43** at 85 °C, but it takes 4 days.[13f,40c]

Therefore, development of new catalysts is needed for faster and better conversion. One way to quantify the efficiency of a catalytic HDF reaction is to use the turnover number (TON), defined by:[15f]

$$\text{TON} = \frac{\text{number of fluoroaromatic product(s)} \times \text{number of HDF steps}}{\text{moles of catalyst}} \quad (5.1)$$

In 2007, Rosenthal and co-workers reported the catalytic HDF of C_5NF_5 at [*rac*-(ebthi)(Zr(H)(*μ*-H)]$_2$, (**46**, ebthi = 1,2,-ethylene-1,1′-bis(η^5-tetrahydroindenyl), and [Zr(η^5-C_5Me_5)$_2$(H)$_2$(*μ*-H)]$_2$ (**47**) in the presence of ^{i}Bu$_2$AlH to give 2,3,5,6-C_5NF_4H and ^{i}Bu$_2$AlF.[41] The best TON was obtained with 0.5 % of **46** at room temperature for 24 hours with a TON = 67, however, the conversion was relatively low (44 %). A better conversion (90 %) was seen with 10 % of **46** but the TON decreased considerably (TON = 7).

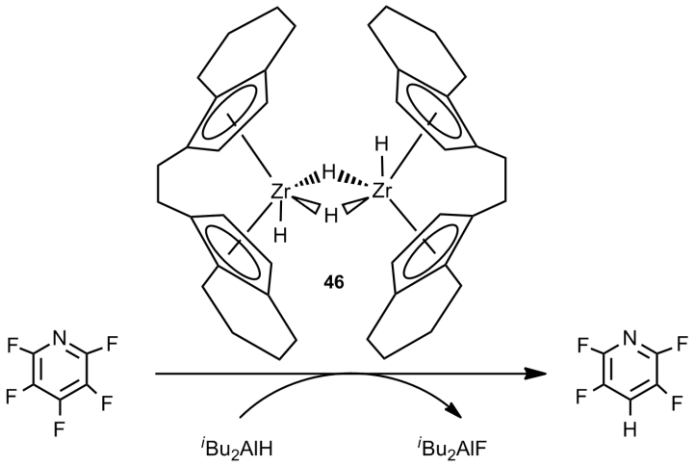

Figure 1.15: HDF reaction of C_5NF_5 at 46 to give 2,3,5,6-C_6NF_4H.[41]

Lanthanides have also been used for HDF reactions. Andersen, Eisenstein and co-workers, for instance, reported a joint experimental and computational study on the HDF of C_6F_6 at [Ce(Cp')$_2$H] [Cp' = 1,3,4-(Me_3C)$_3$(C_5H_2)] to form [Ce(Cp')$_2$F], H_2 and 1,2,4,5-$C_6F_4H_2$. [Ce(Cp')$_2$F] and 1,2,4,5-$C_6F_4H_2$ are formed after decomposition of [Ce(Cp')$_2$(C_6F_5)].[42] DFT calculations on the mechanism of this reaction have been performed and the results are discussed in Section 1.3.3.

(ii) At Group 8 Metals

Group 8 transition metals have also been employed to perform HDF of fluoroaromatics. In 2005, Holland et *al*. reported the HDF of C_6F_6, C_6F_5H and C_5NF_5 using β-diketiminate complexes of iron(II) in the presence of silanes as the reductant.[15c] In addition, the HDF of C_6F_5H occurred at the 4-position in the presence of $HSiEt_3$ to give 1,2,4,5-$C_6F_4H_2$ with a TON of 0.2 after 4 days at 45 °C (see Figure 1.16). With C_5NF_5, formation of 2,3,5,6-C_5NF_4H is observed with a TON of 3.6 under the same conditions.

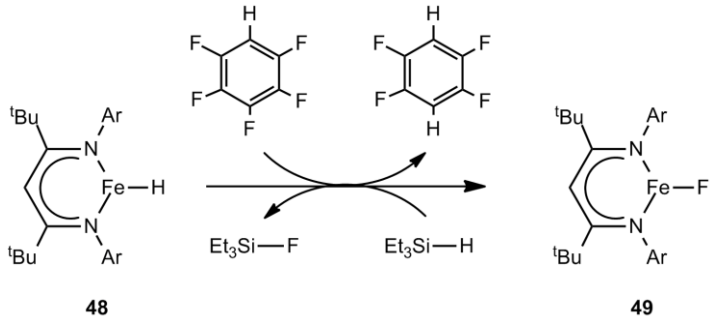

Figure 1.16: HDF reaction of C_6F_5H using β-diketiminate complexes of iron(II).[15c]

This last result contrasts with that of Whittlesey and co-workers who reported HDF of C_6F_6, C_6F_5H and C_5NF_5 catalysed by $[Ru(H)_2(CO)(NHC)(PPh_3)_2]$ (**50**, NHC = SIMes, SIPr, IMes, IPr) in the presence of $HSiEt_3$ in THF at 70 °C (see Figure 1.17).[15f] With C_6F_5H and C_5NF_5 C–F activation occurs at the 2-position to yield 1,2,3,4-$C_6F_4H_2$ and 2,3,4,5-C_5NF_4H, respectively. HDF of C_6F_5H gave a TON up to 7.4 after 19.45 hours while with C_5NF_5 the TON is 13.6 under similar conditions. However, the TON for C_6F_5H could go up to 200 with 0.21 % of catalyst in neat fluoroaromatic, but still required 400 hours reaction time. DFT calculations have been performed to elucidate this unusual *ortho*-regioselectivity for HDF of C_6F_5H and the results are presented in Chapter 5 of this thesis.

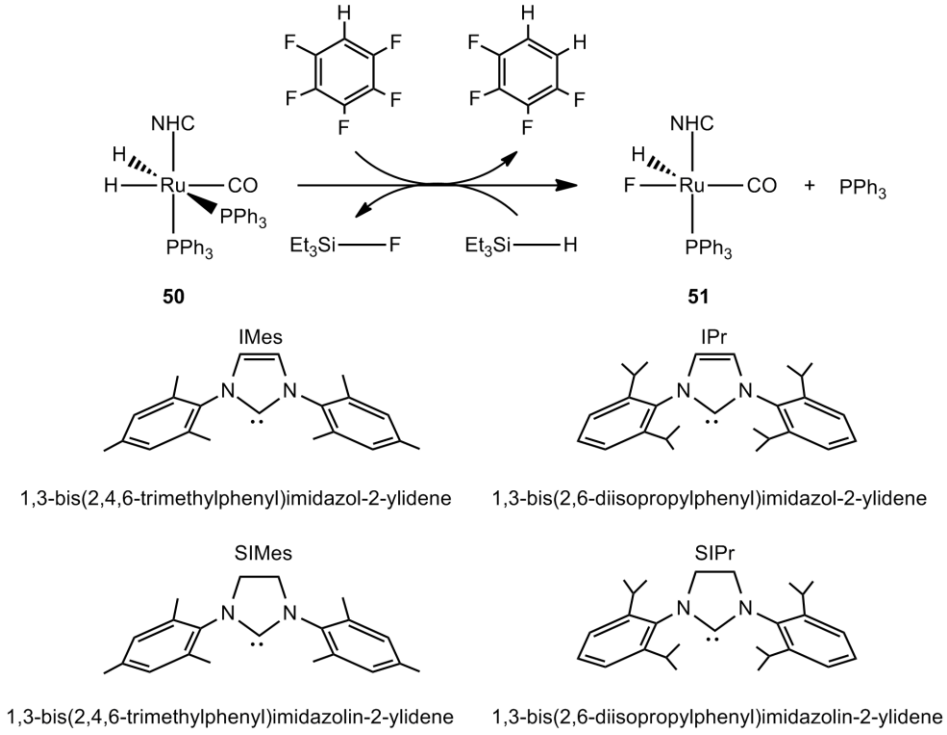

Figure 1.17: HDF reaction of C_6F_5H catalysed by $[Ru(H_2)(CO)(NHC)(PPh_3)_2]$.[15f]

(iii) At Group 9 Metals

The first example of catalytic HDF of C_6F_6 and C_6F_5H at group 9 metal centres was reported by Milstein and Aizenberg in 1994, using $[Rh(SiR_3)(PMe_3)_3]$ (R_3 = Me_2Ph, Ph_3) in the presence of $HSiR'_3$ (R′ = Ph, OEt) to give C_6F_5H and 1,2,4,5-$C_6F_4H_2$, respectively (see Figure 1.18).[15a] The initial step for the reaction between C_6F_6 and $[Rh(SiR_3)(PMe_3)_3]$, corresponds to C–F activation to give $[Rh(C_6F_5)(PMe_3)_3]$ (**54**) and $FSiR_3$. In the presence of $HSi(OEt)_3$, complex **56** was isolated and characterised by ^{31}P,

^{1}H and ^{19}F NMR data and confirmed by an X–ray crystallographic study. From **56** subsequent C–H reductive elimination yields C_6F_5H and regenerates the original rhodium-silyl complex. In addition, Milstein and Aizenberg showed that C_6F_5H reacts at **54** in the presence of $HSi(OEt)_3$ to give exclusively 1,2,4,5-$C_6F_4H_2$ with a TON of 33 after 48 hours at 94 °C. This *para* selectivity is similar to the one observed by Holland and co-workers, however, differs from that seen by Whittlesey *et al.*[15c,15f] Perutz and co-workers also studied the reaction of 2,3,5,6-C_5NF_4H at $[Rh(SiPh_3)(PMe_3)_3]$ and obtained a mixture of C–F and C–H activation products, $[Rh(2\text{-}C_5NF_3H)(PMe_3)_3]$ and $[Rh(4\text{-}C_5NF_4)(PMe_3)_3]$, respectively, in a 1.3:1 ratio, along with $FSiPh_3$ and $HSiPh_3$.[43] Interestingly, C–F activation occurred at the 2-position and the product can further react with $HSiPh_3$ to give 2,3,5-$C_5NF_3H_2$ and an unidentified rhodium complex.

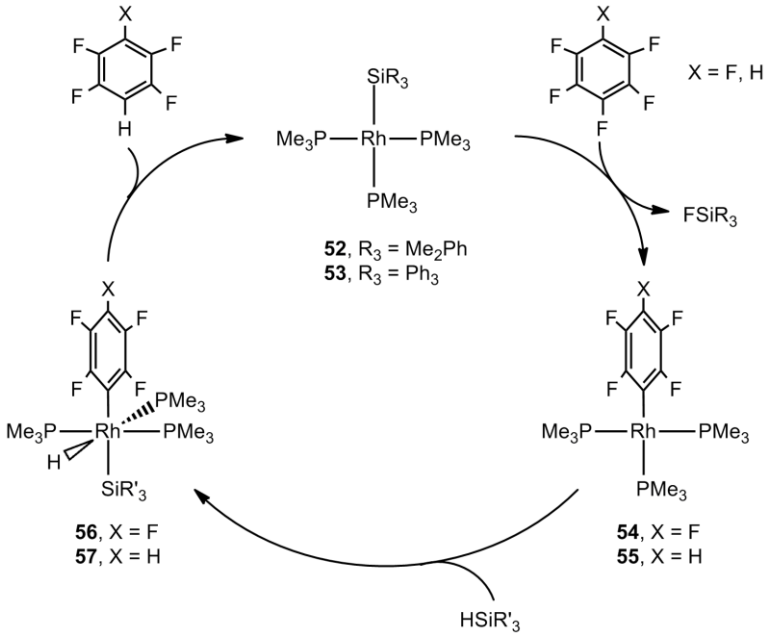

Figure 1.18: Catalytic HDF of C_6F_5X at $[Rh(SiR_3)(PMe_3)_3]$.[15a]

In 1995, Milstein and Aizenberg showed that H_2 can be used as reductant instead of $HSiR'_3$ to perform HDF of C_6F_6 and C_6F_5H in the presence of a base (e.g. NEt_3) at $[Rh(C_6F_5)(PMe_3)_3]$ (**54**) and $[Rh(H)(PMe_3)_4]$ (**58**).[15b] Species **54** is found to be more reactive than **58** with a TON up to 56 after 20 hours at 95-100 °C, corresponding to the conversion of C_6F_5H to 1,2,4,5-$C_6F_4H_2$ in the presence of NEt_3 and K_2CO_3. In relation to that, Braun *et al.* studied the C–F activation of C_5NF_5 in the presence of NEt_3 at $[Rh(H)(PEt_3)_3]$ to give $[Rh(4\text{-}C_5NF_4)(PEt_3)_3]$ (**59**).[14c] Later on, the same group showed that **59** could performed catalytic HDF of C_5NF_5 with H_2 in the presence of

NEt_3/Cs_2CO_3 to give 2,3,5,6-C_5NF_4H. After 2 days at atmospheric pressure and room temperature TONs up to 12 were obtained.

Grushin and Young also used a rhodium hydride complex, $[Rh(Cl)_2(H)(PCy_3)_2]$, to perform the HDF of 1-fluoronaphthalene in the presence of H_2 and aqueous alkali at 95 °C.[44] The same year, Angelici and co-workers reported the HDF of C_6FH_5 and 1,2-$C_6F_2H_4$ under 4 atm of H_2 at 70 °C in the presence of NaOAc by using rhodium pyridylphosphine and bipyridyl complexes tethered to heterogeneous Pd-SiO_2.[45]

(iv) At Group 10 Metals

A few examples of HDF at group 10 metal centres have also been reported. Fort and co-workers, for instance, studied the HDF of monofluoroaromatics by using Ni(0)/NHC complexes in the presence of chloride and Na^{i}OPr or other β-hydrogen-containing alkoxides.[46]

Braun and co-workers showed that *trans*-$[Pd(4\text{-}C_5NF_4)(F)(P^iPr_3)_2]$ (**60**) could react with $HSiPh_3$ for 2 hours at 70 °C in THF to give 2,3,5,6-C_5NF_4H in 52 % yield.[47] More recently, a catalytic HDF reaction has been developed in which *trans*-$[Pd(4\text{-}C_5NF_4)(F)(PR_3)_2]$ (R = ^{i}Pr, Cy) reacts with C_5NF_5 and HBpin for 3 days at 60 °C in THF to yield 2,3,5,6-C_5NF_4H and $[Pd(PR_3)_2]$ (see Figure 1.19).[48]

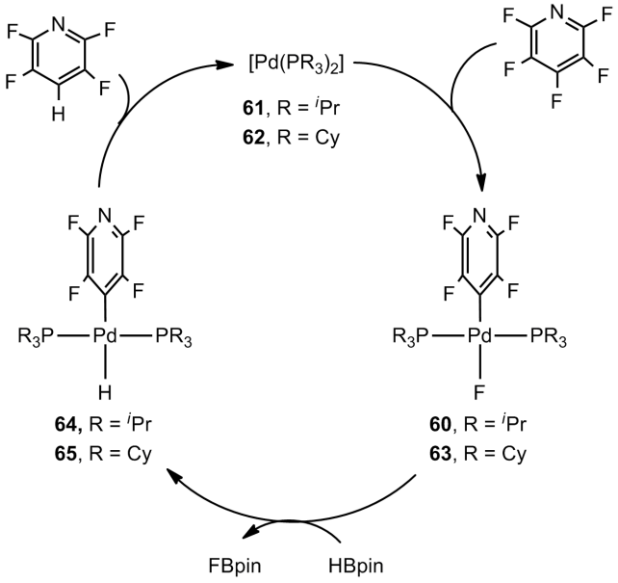

Figure 1.19: Catalytic HDF of C_6NF_5 at $[Pd(PR_3)_2]$ to give 2,3,5,6-C_5NF_4H.[48]

However, the yields of the reaction for formation of 2,3,5,6-C_5NF_4H are lower than the previous study,[47] being 44 % (TON = 4 for R = ^{i}Pr) and 30 % (TON = 3, for R = Cy).

1.2.3 Other Mechanisms

Other types of C–F activation are thought to occur experimentally, such as electron transfer and nucleophilic attack processes. Therefore, the following section will review some key examples of these two types of intermolecular C–F activation.

In 1992, Hintermann *et al.* reported the C–F activation of 4-XC_6F_4CN (X = F, H, CN) at *trans*-$[Pt(H)_2(PCy_3)_2]$ (**66**) to yield *trans*-$[Pt(H)(4\text{-}XC_6F_3CN)(PCy_3)_2]$ (**67**) and HF.[49] The authors proposed an electron transfer mechanism, in which one electron is transferred from **66** to the substrate to generate 4-$XC_6F_3CN^{\bullet -}$ followed by the attack of F^- on H to give the products. In addition to **66**, *trans*-$[Pt(H)(F)(PCy_3)_2]$ and *trans*-$[Pt(H)(FHF)(PCy_3)_2]$ were also observed. Several years later, Perutz and co-workers observed similar behaviour for the C–F activation of fluoroaromatics at *cis*-$[Ru(H)_2(dmpe)_2]$ (dmpe = 1,2-bis(dimethylphosphino)ethane) which results in the formation of *trans*-$[Ru(C_6F_5)(H)(dmpe)_2]$ and HF.[50] In addition, the authors obtained *trans*-$[Ru(C_6F_5)(FHF)(dmpe)_2]$, as a side product. To explain the selective C–F activation at the 4-position of partial fluorinated substrates (C_6F_5H, 1,2,3,4-$C_6F_4H_2$ and 1,2,3-$C_6F_3H_3$), the authors also postulated an electron transfer pathway.

Intermolecular C–F activation via nucleophilic attack has also been observed experimentally. The first example of such process was reported by King and Bisnette in 1964. In this paper, the authors studied the nucleophilic substitution of C_6F_6 by the anion $[Fe(\eta^5\text{-}C_5H_5)(CO)_2]^-$ in THF to form $[Fe(\eta^5\text{-}C_5H_5)(C_6F_5)(CO)_2]$ and fluoride ion.[51] Jones and co-workers proposed a nucleophilic attack pathway for the reaction of fluoroaromatics (Ar^F-F) in pyridine or 1:1 pyridine/benzene at $[Rh(\eta^5\text{-}C_5Me_5)(H)_2(PMe_3)]$ (**68**) to give the C–F cleavage products $[Rh(\eta^5\text{-}C_5Me_5)(Ar^F)(H)(PMe_3)]$ and HF.[52] Interestingly, the authors showed that the reaction is autocatalysed by fluoride ion which deprotonates **68** to give **69**, suitable to perform C–F cleavage.

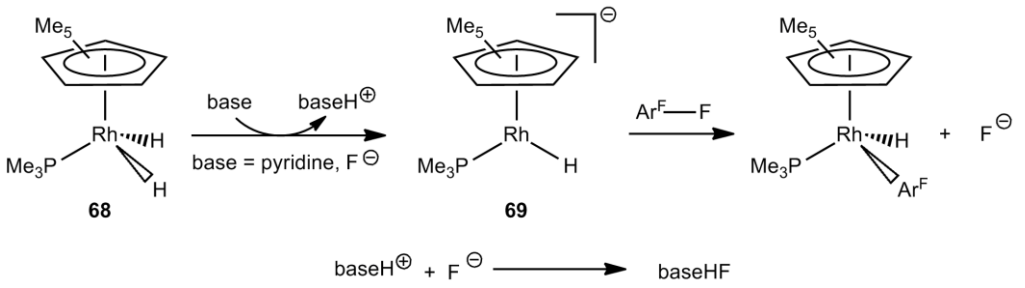

Figure 1.20: C–F activation of fluoroaromatics at 68 to give [Rh(η^5-C_5Me_5)(Ar^F)(H)(PMe_3)] and HF.[52]

In 1991, Milstein and co-workers reported the C–F activation of C_6F_6 at [Ir(Me)(PEt_3)$_3$] (**70**, see Figure 1.21).[53] Upon heating the solution at 60 °C, C–F cleavage occurs but a fluorophosphine complex, *trans*-[Ir(C_6F_5)(PEt_3)$_2$(PEt_2F)] (**71**) was observed along with the elimination of ethane and methane. Although the authors postulated an electron transfer pathway, more recent DFT calculations discarded both this and an oxidative addition process. In reality, C–F activation proceeds via a nucleophilic attack in which the displaced F^- is trapped by the adjacent phosphine ligand to give a metallophosphorane intermediate. This so-called phosphine-assisted C–F activation will be discussed in Section 1.32.[54]

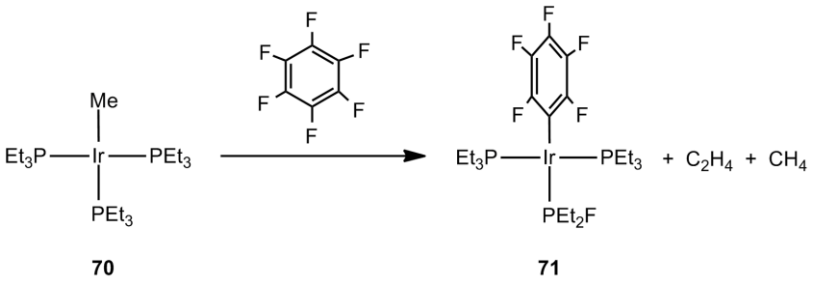

Figure 1.21: C–F activation of C_6F_6 at [Ir(Me)(PEt_3)$_3$].[53]

1.3 Survey of Computational Studies of Intermolecular Aromatic C–F Bond Activation at Transition Metal Complexes

The last 20 years have seen the rapid growth of computational methods such as density functional theory (DFT) as a practical tool to study reaction mechanisms.[55] Figure 1.22, which represents the number of publications containing the keyword "density functional theory" in chemistry and in all different fields, has been obtained by using the Web of Knowledge Database. This graph clearly shows by itself how DFT has emerged since 1990.

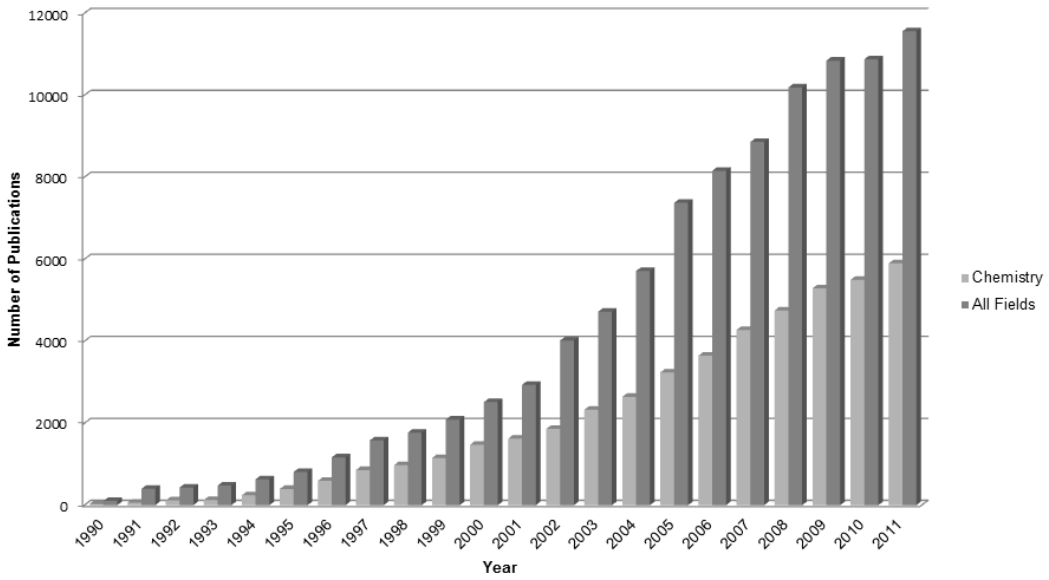

Figure 1.22: Number of publications containing the keyword "density functional theory" during the last 21 years.

Nowadays, DFT is the main computational technique employed to understand the reactivity of transition metal (TM) complexes. The availability of more powerful computing hardware gives the possibility of modelling experimental problems and allows the location of reactive species along a potential energy surface (PES). However, challenges remain.[56]

One of the earliest examples involving the reaction mechanism of intermolecular C–F activation at TM systems has been reported in 1997 by Su and Chu who studied the C–F activation of CH_3F at *trans*-$[M(X)(PH_3)_2]$ (M = Rh, Ir; X = CH_3, H, Cl). Since then the field has diversified and several computational studies of intermolecular C–F activation of fluoroaromatics have been reported.

The following section will review key examples in this field and will also stress the point that a dialogue between experimentalists and theoreticians is essential. Indeed, most of the studies covered involve collaborations.

In the first section, oxidative addition from a computational perspective will be introduced before a discussion of the first reported examples of ligand-assisted C–F activation. Finally, studies of other mechanisms such as hydrodefluorination and nucleophilic attack processes will be covered.

1.3.1 Oxidative Addition

The first example in this area was reported in 1998 by Eisenstein, Caulton and Perutz on the oxidative addition of 1,4-$C_6F_2H_4$ at osmium and rhodium complexes.[57] This work, which is also one of the earliest studies on intermolecular aromatic C–F activation in the presence of other bonds, highlights the thermodynamic preference for C–F activation over C–H activation. B3LYP calculations show that [Os(4-C_6FH_4)(F)(CO)(PH_3)$_2$], obtained after C–F activation, is 16.2 kcal/mol more stable than its C–H activated isomer, [Os(2-$C_6F_2H_3$)(H)(CO)(PH_3)$_2$]. Further calculations confirm that C–F activation is more accessible thermodynamically, with [Rh(η^5-C_5Me_5)(4-C_6FH_4)(F)(PH_3)] being 2.7 kcal/mol more stable than [Rh(η^5-C_5Me_5)(2-$C_6F_2H_3$)(H)(CO)(PH_3)$_2$]. However, C–H activation is observed experimentally which implies that this process must be kinetic in origin. This is confirmed by calculations in which the transition state for C–F activation is +23.9 kcal/mol above that of C–H activation.

In 2004, McGrady and Perutz studied computationally the oxidative addition of C_6X_6 (X = F, H) at [M($H_2PCH_2CH_2PH_2$)] fragments (M = Ni, Pt; see Figure 1.23).[58] C–F activation at [Ni($H_2PCH_2CH_2PH_2$)] proceeds from an η^2-C_6F_6 adduct (**73**, E = -25.0 kcal/mol), in which a 3-centred transition state **TS (73 – 74)** (E = -2.5 kcal/mol) is computed to give [Ni(C_6F_5)(F)($H_2PCH_2CH_2PH_2$)] (**74**, E = -44.7 kcal/mol). Similar features are seen for M = Pt in which C–F activation occurs from **78** (E = -16.4 kcal/mol) via **TS (78 – 79)** (E = +12.9 kcal/mol) to give [Pt(C_6F_5)(F)($H_2PCH_2CH_2PH_2$)] (**79**, E = -40.6 kcal/mol).

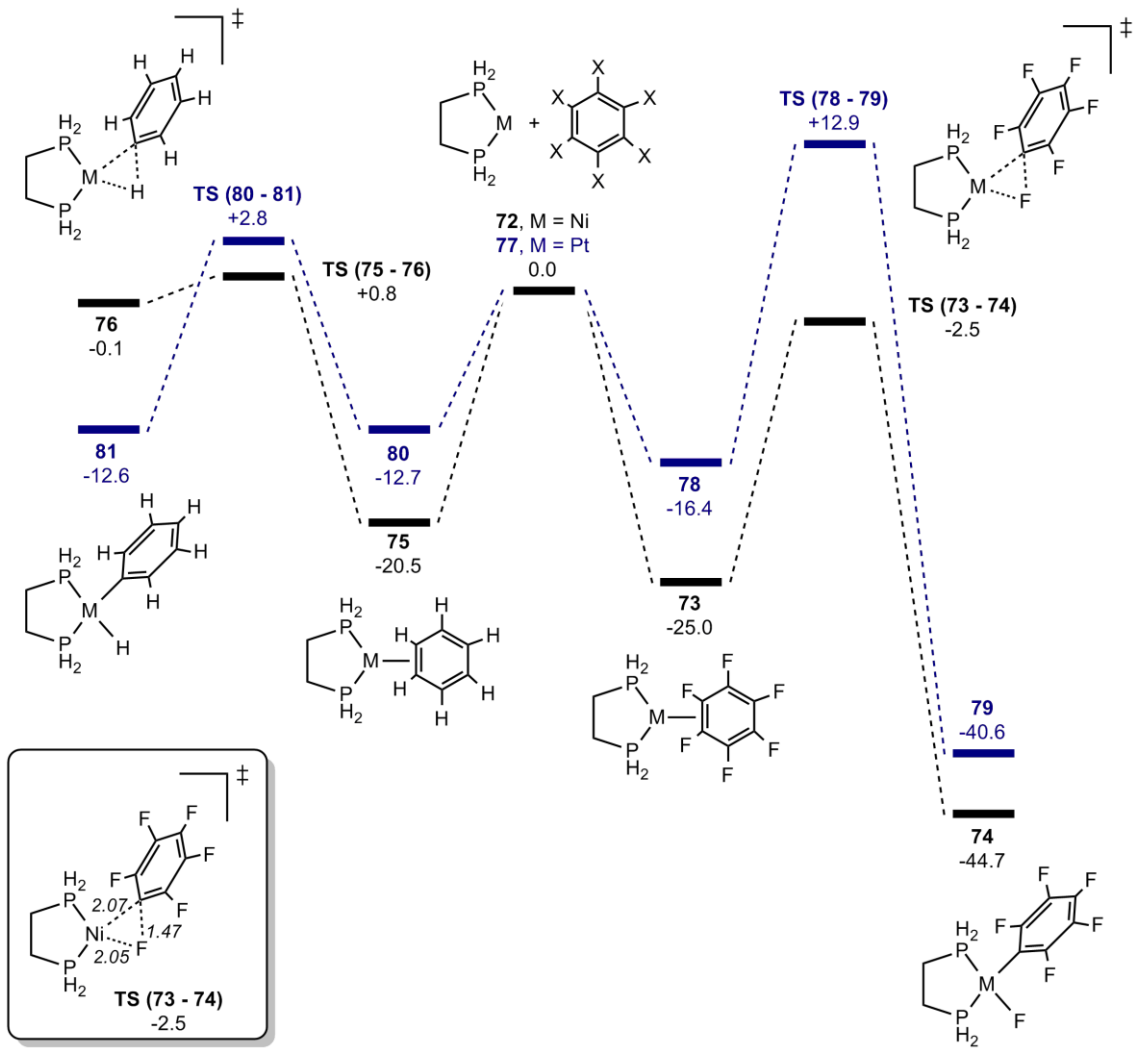

Figure 1.23: Comparison of computed reaction profiles (B3LYP, kcal/mol) for the C–X bond activation of C_6X_6 at [M($H_2PCH_2CH_2PH_2$)] with M = Ni (in black) and Pt (in blue), where X = H (left) and X = F (right).[58] Computed selected distances are in Å.

C–H activation of C_6H_6 has also been computed at [M($H_2PCH_2CH_2PH_2$)] complexes. Both Ni and Pt showed formation of an η^2-C_6H_6 adduct, **75** and **80**, respectively, prior to C–H activation. The C–H cleavage step is found to be more accessible kinetically for Pt at **80** compared to Ni ($\Delta E^{\ddagger}_{Pt}$ = +15.5 kcal/mol, $\Delta E^{\ddagger}_{Ni}$ = +21.3 kcal/mol). In addition, the reaction at Pt is also more favourable thermodynamically than at Ni (ΔE_{Ni} = +20.4 kcal/mol, ΔE_{Pt} = +0.1 kcal/mol).

These differences in energies for C–F and C–H activation were explained by the nature of the M–F and M–H interactions for the two metal centres. For Pt, the greater radial extent of the 5d orbitals tends to strengthen the M–H interaction and therefore favours the C–H activation. In addition, the same feature destabilises the Pt–F interaction due to greater Pt(dπ)-F(pπ) repulsion. Overall, [Ni($H_2PCH_2CH_2PH_2$)] is predicted to have

enhanced selectivity for C–F activation, even in the presence of C–H bonds. With [Pt($H_2PCH_2CH_2PH_2$)] both C–F and C–H activation are feasible and C–F activation is thermodynamically preferred. As with other oxidative additions at Group 10 [ML_2] species[59] a bent geometry imposed by a chelate ligand enhances reactivity. Indeed, calculations at [Ni(PH_3)$_2$] show a 10 kcal/mol destabilisation of both the η^2-C_6F_6 adduct and the final oxidative addition product.

Since the work of McGrady and Perutz, several examples of computational studies on selective aromatic C–F activation at nickel complexes have emerged.[32c,60] In 2008, Radius and co-workers reported a joint experimental and computational study on the selective C–F activation of a range of fluoroaromatics at [Ni_2(^{i}Pr_2Im)$_4$(COD)] (**21**) and [Ni(^{i}Pr_2Im)$_2$(η^2-C_2H_4)] (**22**, ^{i}Pr_2Im = 1,3-bis(*iso*propyl)imidazol-2-ylidene).[32d] In all cases, C–F activation occurs after formation of an η^2-adduct, as previously described by McGrady and Perutz. Therefore all energy barriers are relative to the lowest η^2-species. C–F activation of C_6F_6 at {Ni(^{i}Pr_2Im)$_2$} occurs via a three-centred transition state with a computed energy of +24.3 kcal/mol (see Table 1.1). With $C_{10}F_8$, C–F activation at the 2-position is more accessible kinetically and thermodynamically than at the 1-position ($\Delta\Delta H^{\ddagger}$ = 1.8 kcal/mol, $\Delta\Delta H$ = -7.8 kcal/mol) with a computed barrier of 25.5 kcal/mol. C–F activation of $C_6F_5CF_3$ at {Ni(^{i}Pr_2Im)$_2$} has also been computed. Calculations show that activation of $C_6F_5CF_3$ at the 4-position is kinetically and thermodynamically preferred.

Table 1.1: Computed energies (kcal/mol) for C–F activation of fluoroaromatics at {Ni(^{i}Pr_2Im)$_2$} relative to the most stable η^2-adduct.[32d]

Ar^F-F	TS	*trans*-[Ni(F)(Ar^F)(^{i}Pr_2Im)$_2$]	Selectivity
C_6F_6	+24.3	-31.3	–
$C_{10}F_8$	+27.3	-18.9	1-position
	+25.5	-26.8	2-position
$C_6F_5CF_3$	+24.6	+8.0[a]	2-position
	+26.2	+0.5[a]	3-position
	+21.7	0.0[a]	4-position

[a] **Only relative energies were reported for these species.**

Selective C–F activation over C–H activation is also seen for the activation of 1,2,4-$C_6F_3H_3$ and 1,2,3-$C_6F_3H_3$. With 1,2,4-$C_6F_3H_3$, C–F activation occurs at the 2-position

with a transition state located at 24.3 kcal/mol above the η^2-adduct. Activations at the 1- and 4-positions are 3.1 kcal/mol and 5.7 kcal/mol higher in energy, respectively. Finally, with 1,2,3-$C_6F_3H_3$ the calculations indicate a kinetic preference for reaction at the 2-position ($\Delta H^{\ddagger}$ = 20.8 kcal/mol) although in this case this is not borne out experimentally where activation at the 1-position dominates. DFT calculations have also been employed to aid the spectroscopic characterisation of intermediates in the C–F activation process, including mononuclear [$Ni(PEt_3)_2(\eta^2$-$C_6F_{6-n}H_n)$] and dinuclear [$Ni(PEt_3)_2]_2(\mu$-η^2:η^2-$C_6F_{6-n}H_n$) species (n = 0-2).[25,26b]

Other examples of selective C–F activation in the presence of C–H bonds have also been studied computationally. In 2007, Harman *et al.* reported the reaction of [$TpW(NO)(PMe_3)(\eta^2$-$C_6H_6)$] (**82**, Tp = trispyrazolylborate) with C_6FH_5 to give [$TpW(C_6H_5)(F)(NO)(PMe_3)$] (**83**, see Figure 1.24).[61] In contrast to the above studies, C_6FH_5 reacts through a κ^1-F (or a κ^1-H) intermediate. LSDA calculations showed that both C–F activation and *ortho*-C–H activation are facile but the reversibility of the C–H activation ($\Delta E^{\ddagger}$ = +12.5 kcal/mol for the reverse reductive coupling) added to the irreversible C–F activation (ΔE = -52.0 kcal/mol) account for formation of **83**. It should be, however, noted that an η^2-adduct of C_6FH_5 has been located on the PES but it is found not to be on the pathway for either C–H or C–F bond cleavage.

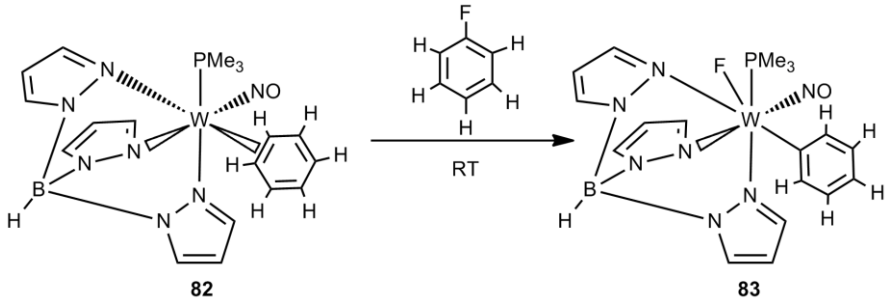

Figure 1.24: C–F activation of C_6FH_5 with 82.[61]

In 2002, Rzepa and co-workers also studied the C–F activation of monofluoroarenes and showed that the reaction is promoted by the choice of ring substituents.[62] Oxidative addition of C_6FH_5 at [$Pd(PH_3)_2$] has a computed barrier of 41.2 kcal/mol, however, this barrier is reduced by 5.7 kcal/mol for 4-$C_6FH_4NO_2$ and by 13.1 kcal/mol for 2-$C_6FH_4NO_2$. In addition, these effects appear to be additive as with 2,4-$C_6FH_3(NO_2)_2$ the activation barrier is reduced by 19.4 kcal/mol to +21.8 kcal/mol. The large effect of the

2-NO_2 group is linked to a short Pd···O contact in the transition state. Indeed, COSMO (H_2O) calculations showed formation of a stable Meisenheimer-type structure **84** (E = -7.4 kcal/mol, see Figure 1.25) in which the subsequent loss of F^- is facile.

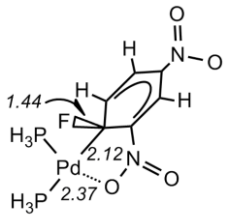

84

Figure 1.25: Computed stable Meisenheimer intermediate by using a COSMO solvation model in H_2O. Selected key distances are in Å.

Bahmanyar and co-workers reported similar results for the reaction of 2-fluoro-5-nitrobenzoate with [$Pd(PH_3)_2$] in which an even stronger Pd···O interaction of 2.13 Å is computed in the transition state.[63]

1.3.2 Ligand-Assisted C–F Activation

More recently, a new type of mechanism for intermolecular aromatic C–F activation has emerged. In 2008, Macgregor and co-workers reported the first examples of ligand-assisted C–F activation, involving a "phosphine-assisted C–F bond activation".[37,54] This reaction pathway consists of a nucleophilic attack of an electron-rich metal-phosphine complex, [$ML_n(PR_3)$] (**85**), at electron deficient polyfluorinated aromatics to form a new M-Ar^F bond (see Figure 1.26).

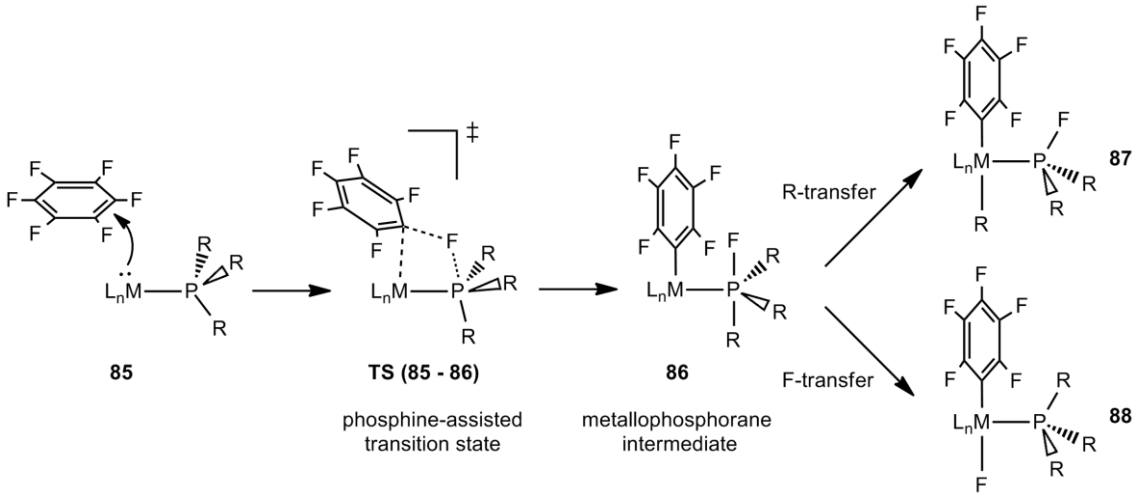

Figure 1.26: Phosphine-assisted C-F bond activation and formation of a metallophosphorane intermediate.[64]

However, the displaced F^- is trapped by a phosphine ligand such that the C–F bond adds over the M–PR_3 bond to give a metallophosphorane intermediate, $[L_nM(Ar^F)(PR_3F)]$, **86**.[64] This process, which involves a 4-centred transition state **TS (85 – 86)**, contrasts with the 3-centered structures associated with concerted oxidative addition. From **86** subsequent transfer of an R group to the metal centre then generates a metal-alkyl complex, **87**, with a fluorophosphine co-ligand. Alternatively, F can transfer to generate a metal-fluoride, **88**, similar to a conventional oxidative addition product. Interestingly, species **87** and **88** are both oxidized products; however, the mechanism does not correspond to oxidative addition.

Phosphine-assisted C–F activation was first characterised for the reactions of C_6F_6 at $[Ir(Me)(PEt_3)_3]$[54] and of C_5F_5N at $[Pt(PR_3)_2]$[37] which, in both cases, leads to fluorophosphine ligands being observed experimentally[33,53] (see Figures 1.10 and 1.21). BP86 calculations on the C–F activation of C_6F_6 at the model system *trans*-$[Ir(Me)(PH_3)_2(PH_2Et)]$ (**89**) showed that the reaction proceeds from an encounter complex (**90**) with a computed free energy of +5.1 kcal/mol in which the C_6F_6 ring lies approximately parallel to the Ir coordination plane at a distance of about 3.5 Å (see Figure 1.27).

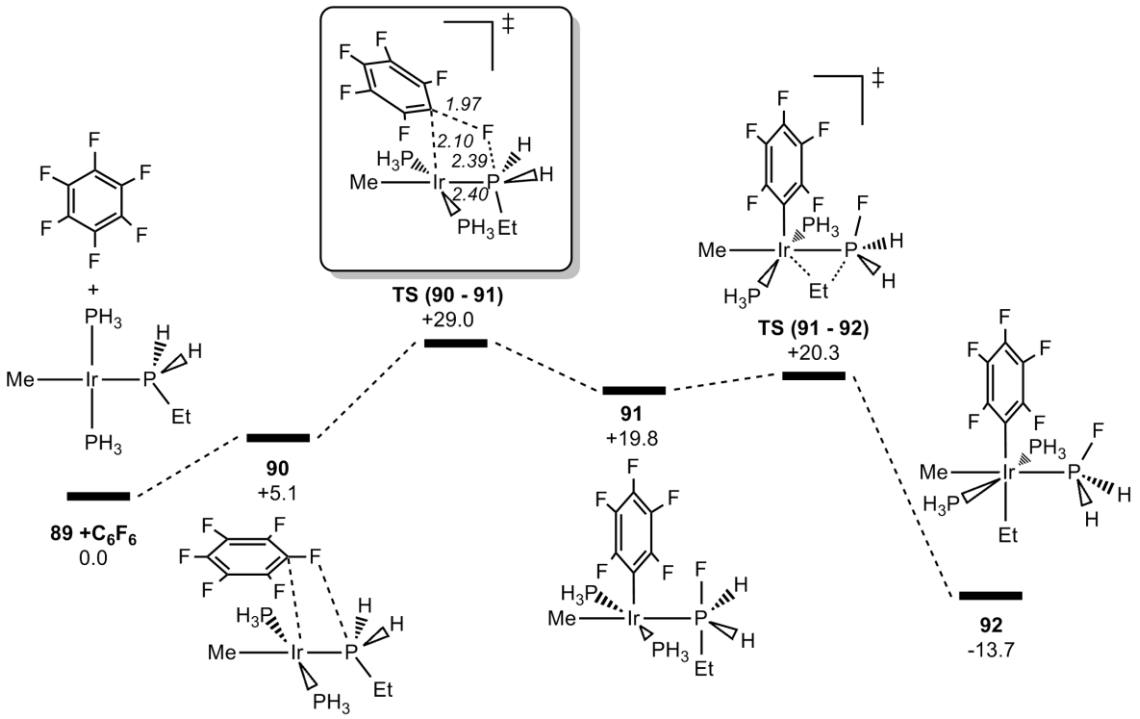

Figure 1.27: Computed reaction profile for phosphine-assisted C-F activation of C_6F_6 at *trans*-$[Ir(Me)(PH_3)_2(PH_2Et)]$ to give the metallophosphorane intermediate 91 followed by axial Et group transfer to Ir to form 92.[54] Computed free energies are in kcal/mol and selected distances are in Å.

Subsequent nucleophilic attack from **90** leads to the 4-centred transition state, **TS (90 – 91)** (G = +29.0 kcal/mol), with a short Ir–C contact (2.10 Å) and significant lengthening of the C–F bond (1.97 Å). **TS (90 – 91)** links to a metallophosphorane intermediate, *trans*-[Ir(C_6F_5)(Me)(PH_3)$_2$(PH_2EtF)] (**91**) with a computed energy of +19.8 kcal/mol from which the axial Et group transfers to Ir to form *trans*-[Ir(C_6F_5)(C_2H_5)(Me)(PH_3)$_2$(PH_2F)] (**92**, G = -13.7 kcal/mol). From **92**, subsequent *β*–H elimination and CH_4 reductive elimination give the final model product *trans*-[Ir(C_6F_5)(PH_3)$_2$(PH_2F)] (**93**, G = -27.7 kcal/mol). In addition, the authors showed that phosphine-assisted C–F activation is promoted by more electron-rich metal centres and that the barrier to C–F activation is lowered by 4-5 kcal/mol for each *ortho*-F present in the substrate.

At the same time, BP86 calculations were performed for the C–F activation of C_5NF_5 at [Pt(PR_3)$_2$] (R = ^{i}Pr, Cy) to give *trans*-[Pt(4-C_5NF_4)(R)(PR_3)(PR_2F)].[33] A computational model, [Pt(PH_3)(PH_2Me)] (**94**), was used leading to *trans*-[Pt(4-C_5NF_4)(Me)(PH_3)(PH_2F)] (**97**). Calculations have also characterised alternative routes to both *trans*- and *cis*-[Pt(4-C_5NF_4)(F)(PH_3)(PH_2Me)], **98** and **99**, respectively, as shown in Figure 1.28. Complexes **98** and **99** are more favourable thermodynamically than **97**, indicating that formation of the last of these must be kinetic in origin. Calculations showed that **97** can be formed directly from [Pt(PH_3)(PH_2Me)] via a phosphine-assisted transition state, **TS (94 – 97)** (E = +20.8 kcal/mol). In this case, the P–Pt–P angle is almost linear and the {PH_2MeF}$^-$ phosphoranide moiety is cis to a vacant coordination site to which the Me group can transfer from P to Pt to give **97**. This final product is therefore formed via a one step process and involves concerted C–F and P–C activation.

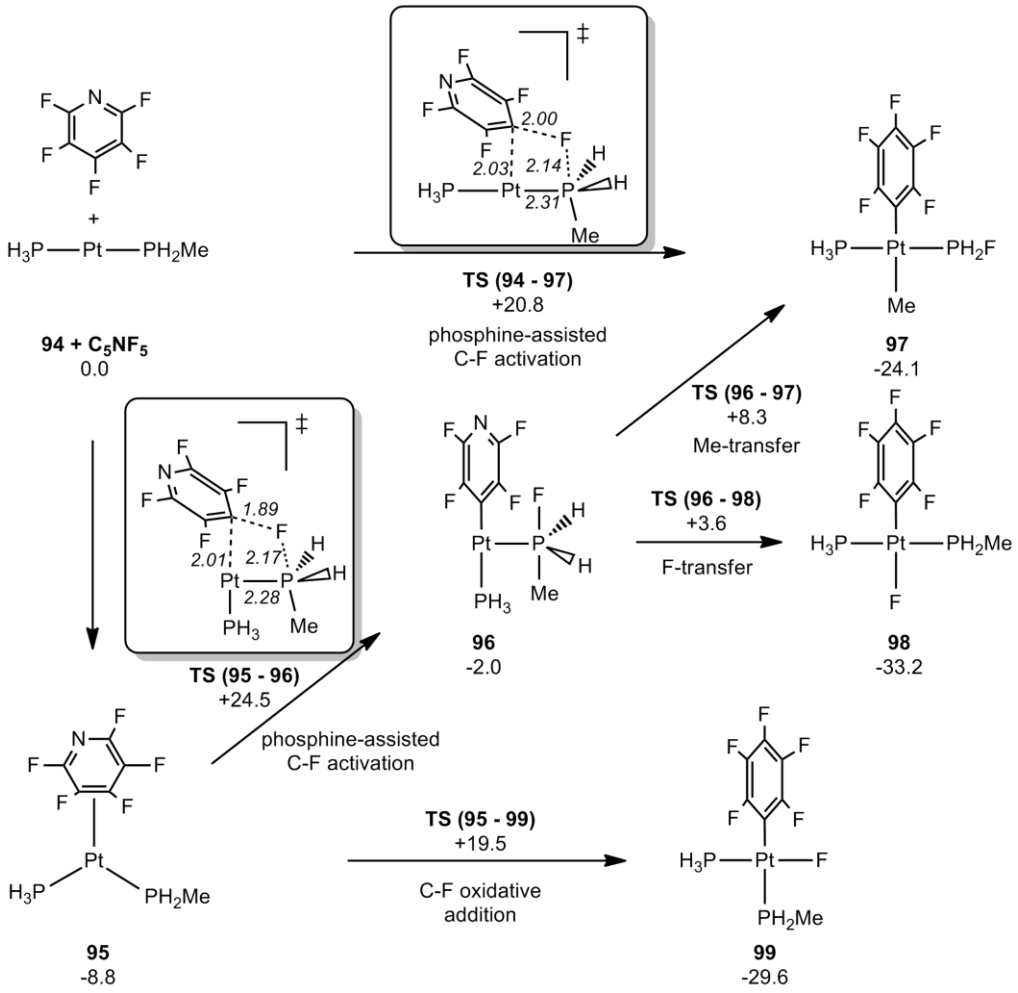

Figure 1.28: Mechanistic landscape for C-F bond activation of C_5NF_5 at [Pt(PH_3)(PH_2Me)].[37] Computed energies are in kcal/mol and selected distances are in Å.

Alternatively, initial formation of an η^2-adduct is postulated (**95**, E = -8.8 kcal/mol) followed by phosphine-assisted C–F activation through **TS (95 – 96)** (E = +24.5 kcal/mol) in which the P–Pt–P angle is now bent. In this case, a metallophosphorane intermediate is located (**96**, E = -2.0 kcal/mol) in which Me- or F-transfer can occur to give **97** or **98** respectively. Formation of the latter occurs through **TS (96 – 98)** (E = +3.6 kcal/mol) and is found to be more accessible than formation of **97** via **TS (96 – 97)** (E = +8.3 kcal/mol). Finally, a conventional 3-centred transition state for oxidative addition have also been located, **TS (95 – 99)**, with a computed energy of 19.5 kcal/mol. This transition state is therefore close in energy to **TS (94 – 97)** (E = +20.8 kcal/mol), suggesting that oxidative addition should be competitive with phosphine-assisted C–F activation. No oxidative addition product analogous to **99** was seen experimentally, however. More recently, C–F activation of C_6F_6 at [Pt(PR_3)$_2$] has been studied computationally and similar features have been observed.[65]

In 2010, a phosphine-assisted oxidative addition pathway has been computed for the reaction of C_5NF_5 at $[Ni(PMe_3)]_2$ (**100**) to give *trans*-$[Ni(2\text{-}C_5NF_4)(F)(PMe_3)_2]$ (**103**).[60] This C–F activation at the 2-position contrasts with the previous example in which the reaction occurs at the 4-position.[33] BP86 calculations showed initial formation an η^2-arene intermediate $[Ni(\eta^2\text{-}C_5NF_5)(PMe_3)_2]$ (**101**, E = -23.6 kcal/mol) from which C–F activation occurs via a phosphine-assisted transition state, **TS (101 – 102)** (E = -7.2 kcal/mol), to form a metallophosphorane intermediate (**102**, E = -15.6 kcal/mol, see Figure 1.29).

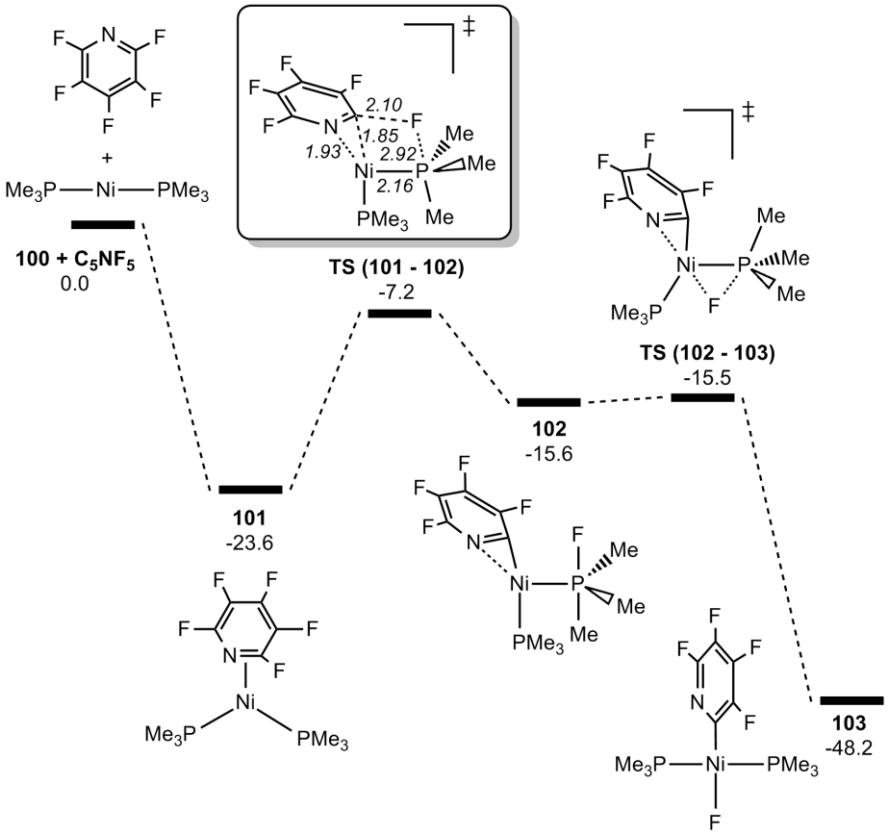

Figure 1.29: Computed reaction profile for C–F activation of C_5NF_5 at 100.[60] Computed energies are in kcal/mol and selected distances are in Å.

The final product *trans*-$[Ni(2\text{-}C_5NF_4)(F)(PMe_3)_2]$ (**103**, E = -48.2 kcal/mol) is formed from **102** via **TS (102 – 103)** (E = -15.5 kcal/mol) in which F is transferred onto Ni. The key feature in this process is the short computed Ni···N contact (1.93 Å) in which the N lone-pair stabilises the transition state **TS (101 – 102)**. This interaction is strong enough to alter the regioselectivity in favour of the 2-position. It should be, however, noted that for the C–F activation of C_5NF_5 at $[Pt(PH_3)(PH_2Me)]$ a similar interaction was computed but in this case this was not strong enough to affect the outcome of the reaction which proceeds via C–F activation at the 4-position.

Another type of ligand-assisted C–F activation has been reported by Nakamura and co-workers in which the combination of mixed *P,O*-chelating ligands and the presence of Lewis acidic Mg^{2+} centres promotes C–F activation of C_6FH_5 at Ni (see Figure 1.30).[66] The C_6FH_5 moiety can bind the Mg^{2+} centre such that it introduces a stabilising Mg···F interaction in the η^2-adduct **105**. C–F cleavage is postulated to occur via **TS (105 -106)** to give Ni-phenyl species **106** located at -40.8 kcal/mol. Attempts to optimise the η^2-adduct **105** showed spontaneous formation of **106** suggesting that the process is barrierless.

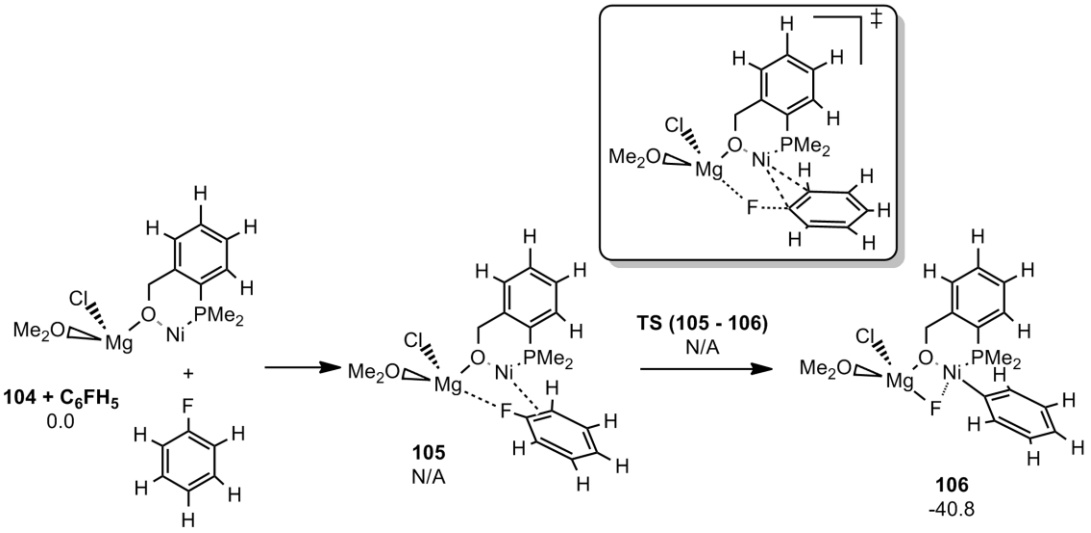

Figure 1.30: Spontaneous C–F activation of C–F activation of C_6FH_5 at Ni. Free energies are in kcal/mol.[66]

1.3.3 Other Mechanisms

As discussed in the experimental section, other types of intermolecular aromatic C–F activation have been put forward. The following section will review examples of HDF and nucleophilic attack processes.

(i) Hydrodefluorination Reactions

Eisenstein and Andersen reported a joint computational and experimental study on the HDF of C_6F_6 at $[Ce(Cp')_2(H)]$ [Cp' = 1,3,4-$(Me_3C)_3(C_5H_2)$].[42] Using a $[La(\eta^5\text{-}C_5H_5)_2(H)]$ model, initial calculations ruled out processes based either a σ-bond metathesis transition state (see Figure 1.31) or initial hydride transfer onto the arene ring.

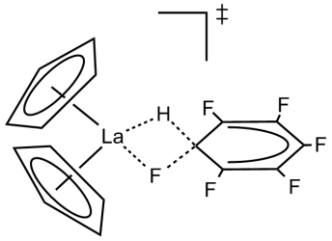

Figure 1.31: σ-bond metathesis transition state for HDF of C_6F_6 at [La(η^5-C_5H_5)$_2$(H)].[42]

However, a mechanism involving initial formation of a σ-adduct (**108**, G = -8.2 kcal/mol) has been computed in which one F substituent on the ring interacts with the La metal centre (see Figure 1.32).

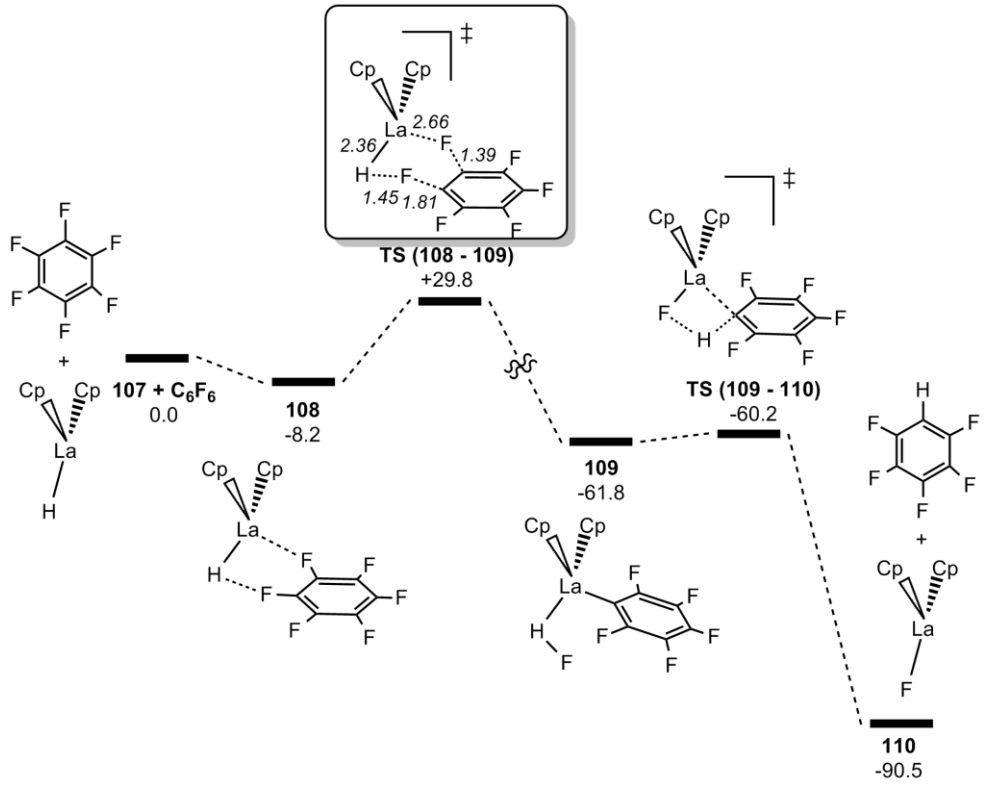

Figure 1.32: Computed free energy reaction profile for HDF of C_6F_6 at [La(η^5-C_5H_5)$_2$(H)].[42] Computed free energies are in kcal/mol and selected distances are in Å.

This acts as a 'hook' and brings an *ortho*-C–F bond close to the hydride ligand. C–F activation from **108** proceeds via **TS (108 – 109)** (G = +29.8 kcal/mol) in which F transfers onto hydride to generate [La(η^5-C_5H_5)$_2$(C_6F_5)(HF)] (**109**, G = -61.8 kcal/mol). The final products C_6F_5H and [La(η^5-C_5H_5)$_2$(F)] (**110**, G = -90.5 kcal/mol) are obtained via **TS (109 – 110)** (G = -60.2 kcal/mol) corresponding to a proton transfer. In addition, the authors showed that this C–F activation process involves a significant redistribution

of charge with the negatively hydride becoming protonic and the originally positively charged *ortho*-carbon becoming carbanionic.

(ii) Nucleophilic Attack by a Ligand

Another type of intermolecular C–F activation of fluoroaromatics was reported by Lledós and co-workers, involving a nucleophilic attack by a bridging-S ligand in $[Pt_2(\mu\text{-}S)_2(R_2P(CH_2)_3PR_2)_2]$ (**111**, R = Ph; **114**, R = H).[67] Experimentally, the reaction between **111** and C_6F_6 gives $[Pt(o\text{-}S_2C_6F_4)(R_2P(CH_2)_3PR_2)]$ (**112**) and $[Pt_3(\mu_3\text{-}S)_2(R_2P(CH_2)_3PR_2)_3][F]_2$ (**113)**. DFT calculations (B3LYP, Toluene) with R = H showed that the bridging S ligand in $[Pt_2(\mu\text{-}S)_2(H_2P(CH_2)_3PH_2)_2]$ can attack the C_6F_6 ring in a conventional S_NAr process via **TS (114 – 115)** (E = +31.5 kcal/mol, see Figure 1.33) to give **115** (E = +0.5 kcal/mol).

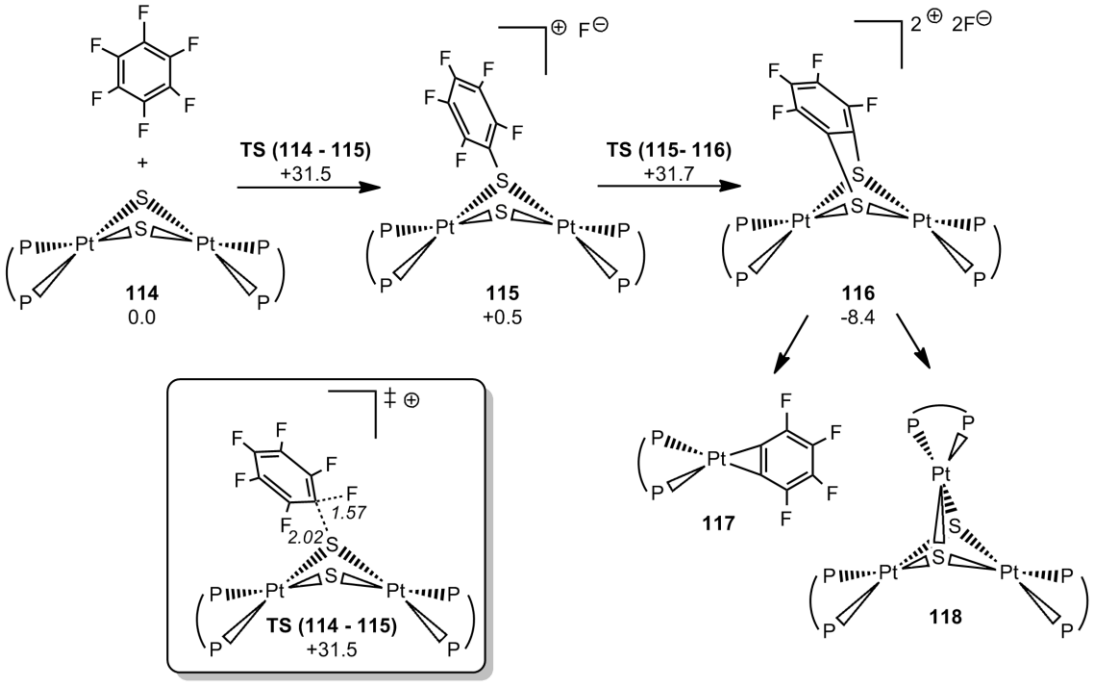

Figure 1.33: Computed mechanism for the reaction of $[Pt_2(\mu\text{-}S)_2(H_2P(CH_2)_3PH_2)_2]$ with C_6F_6.[67] Computed energies are in kcal/mol and selected distances are in Å.

After rearrangement of **115**, a second S_NAr step can occur at the 2-position of the SC_6F_5 ligand with a computed transition state energy of +31.7 kcal/mol, corresponding to **TS (115 – 116)** to give **116** (E = -8.4 kcal/mol) as an initial product. This species can then react to finally yield **117** and **118**; however, these steps were not studied computationally. The high barriers for this double S_NAr process are consistent with the

slow reaction seen experimentally which occurs in toluene for 5 days. In contrast, reaction with C_5F_5N is rapid at room temperature, but results only in the first S_NAr step. Calculations in this case show a much reduced barrier for initial attack of the μ-S ligand at the 4-position of the ring with a computed transition state energy of +20.5 kcal/mol, however, the second attack has a higher barrier of +34.1 kcal/mol.

1.4 Thesis Overview

The aim of the work presented in this thesis is to investigate the selective aromatic C–F activation. The main technique employed is density functional theory (DFT) and the computational details used are given in Chapter 2. In addition, a more detailed description of DFT is provided in Chapter 6.

Chapter 3 focuses on the C–F activation of C_6F_5H at $[Rh(SiR_3)(PMe_3)_3]$ (R_3 = Me_2Ph, Ph_3), the first step of the catalytic HDF reaction reported by Milstein and Aizenberg.[15a] This chapter provides an explanation for the selective C–F activation, observed experimentally, in the presence of C–H bonds. In addition, a novel type of ligand-assisted C–F activation, involving the silyl ligand, is also described.

Chapter 4 presents a study of the C–F activation of C_5NF_5 at the 2- and 4- positions at $[Rh(X)(PEt_3)_3]$ (X = $Si(OEt)_3$, Bpin, where Bpin = pinacolate = $–OCMe_2CMe_2O–$).[68] This chapter shows that C–F activation of C_5NF_5 at the 2-position occurs via a silyl-and boryl-assisted processes and therefore explains the experimental observations.

Chapter 5 details the investigation of possible reaction mechanism for the HDF reaction of C_6F_5H at $[Ru(H)_2(CO)(NHC)(PPh_3)_2]$ (NHC = SIMes, SIPr, IMes, IPr) reported by Whittlesey and co-workers.[15f] Several pathways are considered to explain the formation of 1,2,3,4-$C_6F_4H_2$ seen experimentally, and the lowest process occurs via a novel nucleophilic attack of one hydride ligand at the fluoroarene moiety.

Chapter 2: Computational Details

This chapter deals with the practical aspects of the calculations that have been used in this thesis. A more comprehensive discussion of the methodologies involved can be found in Chapter 6.

(i) Method and Functionals

Density functional theory (DFT) calculations were performed with the Gaussian03[69] and Gaussian09[70] software packages. The BP86 functional, including the gradient corrected exchange functional of Becke[71] and correlation functional of Perdew[72], was used. BP86 belongs to the generalized gradient approximation (GGA) functionals. Other functionals (e.g. hybrid-GGA, meta-GGA) have also been tested. In this case, it has been found that the outcome of the reaction in Chapter 3 was similar to the one computed with BP86 (see Chapter 6). In addition, BP86 does not compute a percentage of exact exchange, known to increase the computational expensive of the calculations.

(ii) Pseudo-Potentials and Basis sets

The Stuttgart/Dresden (SDD) pseudo-potentials and the associated basis sets were employed to describe Ru, Rh, P and Si.[73] P and Si were augmented by a set of d-orbital polarisation functions[74] (ζ = 0.387 and 0.284, respectively), while 6-31G** basis sets were employed for all other atoms.[75] The use of different basis sets has also been tested, including triple-zeta polarised (6-311G**), diffuse double-zeta polarised (6-31++G**) and diffuse triple-zeta polarised (6-311++G**) basis sets.[76] Calculations showed that the use of more extended basis sets does not significantly affect the final results, therefore 6-31G** basis sets were employed in this thesis.

(iii) Optimisation Procedure

Reactants and intermediates were optimised without symmetry constraints by using the default SCF convergence criterion (10^{-8} au) and the keyword "opt". In this case, the optimisation procedure was run until a stationary point on the potential energy surface (PES) was found. From these geometries, frequency calculations were performed to confirm the location of minima (no imaginary frequency).

In order to locate a transition state, a stationary point thought to be connected to it is optimised. This intermediate can be obtained from an X-ray crystallographic structure (e.g. reactant) or built from chemical intuition. Once the structure is optimised a scan can be performed by varying one or several parameters (e.g. bond lengths, bond angles). The purpose of this step is to locate a maximum on the potential energy surface (PES) corresponding to a transition state. Before optimising this stationary point, a frequency calculation was performed in order to confirm the presence of the desired imaginary frequency. Identification of the proper imaginary frequency leads to the optimisation of the structure (without any constraint) and its characterisation by a frequency calculation. In some cases, the use of "opt=calcall" option (force constants are computed at every point) was required for example when the transition state was on a flat part of the PES. After location of the transition state, intrinsic reaction coordinate (IRC) calculations were used in order to connect the stationary point to the adjacent intermediates, in the reverse and forward directions, on the PES.

(iv) Conformation Searching

The majority of the stationary points in this thesis were subjected to extensive conformational searching following the recently published protocol developed in our group.[77] For each initial structure a molecular dynamics (MD) simulation was performed using the Tinker program and the MM3 force field. During the simulation, the metal-ligand bonds were fixed, due to a lack of parameters, in order to allow the movement of the substituents on the ligands. MD simulations were run for 1 nanosecond in an NVT ensemble, with coordinates being collected every picosecond to generate 1000 structures. The trajectories were propagated using the modified Beeman integration algorithm and a Berendsen thermostat was used to keep the temperature around 1000 K. This relatively high temperature was used in order to ensure that the conformational space was fully explored. The 1000 structures were then optimised with the MM3 force field with the same metal-ligand bond constraints as above. Up to 100 energetically reasonable structures were then selected for optimisation at the DFT level using the "opt=loose" option and SCF convergence of 10^{-6} au. Typically, the lowest 10 energy structures were then optimised as previously described without the "opt=loose" option.

As an example, the [Rh{$SiOMe_3$}(PMe_3)$_3$] complex in Chapter 4 was subjected to this conformational searching procedure. After optimisation of the 1000 structures at the molecular mechanics level, 39 different structures were collected. In this case, all the structures were optimised at the DFT (BP86) level using the "loose" option and the SCF convergence of 10^{-6} au. After optimisation, the difference in energies between the two extreme structures was 1.7 kcal/mol. The lowest 10 energy structures were then optimised and, in this case, the difference in energy between the less and most stable structure was around 0.5 kcal/mol. The most stable conformation is reported in this thesis.

(v) Energies

All reported energies in this thesis include a correction for zero-point energies at 0 K and free energies are at 298.15 K and 1 atm, unless otherwise stated. These energies have been obtained from the frequency calculations. In addition, the effect of solvation has been investigated using the polarisable continuum model (PCM, radii=UFF). This effect was found to be minimal in Chapters 3 and 4 but important in Chapter 5. Therefore, computed energies in THF have been reported in that case.

(vi) Physical Chemistry Background

The following sections include more detail on the background physical chemistry in order to understand the thermodynamic quantities such as enthalpy, entropy and Gibbs free energy which comes out of the Gaussian package software.

For all systems, the allowed energy states of molecules are quantified and can be found by solving the Schrödinger equation for a particle in a box defined by:[78]

$$-\frac{\hbar^2}{2m}\frac{d^2\psi(x)}{dx^2} + V(x)\psi(x) = \varepsilon\psi(x) \qquad (2.1)$$

where $\hbar$ is the reduced Planck constant, m the mass of the particle, x the position of the particle while $V(x)$, $\psi(x)$ and ε are the potential energy, the wave function and the allowed energy of the particle, respectively. When the Schrödinger equation is solved, each wave function, $\psi(x)$, has an associated energy ε_n, where n is the quantum number.

Also, the number of wave functions that have the same energy, ε_n, corresponds to the degeneracy of that level, g_n.

Molecules do not have only electronic energy ($\varepsilon_{elec} = -D_e$) but also kinetic translational energy. In the case of a particle of mass m in a one dimensional interval $0 \leq x \leq a$, the allowed translational energy is given by:

$$\varepsilon_{trans} = \frac{n^2 h^2}{8ma^2} \quad n = 1,2,\ldots \tag{2.2}$$

However, for a particle in a three-dimensional volume such as a rectangular parallelepiped of sides a, b, and c, the allowed energies in Equation 2.2 becomes:

$$\varepsilon_{trans} = \frac{h^2}{8ma^2}\left(\frac{n_x^2}{a^2} + \frac{n_y^2}{b^2} + \frac{n_z^2}{c^2}\right) \quad \begin{matrix} n_x = 1,2,\ldots \\ n_y = 1,2,\ldots \\ n_z = 1,2,\ldots \end{matrix} \tag{2.3}$$

In addition to translational energy, molecules have vibrational and rotational motions. The vibrational motion of a diatomic molecule can be modelled by a harmonic oscillator. In a one-dimensional harmonic oscillator, the energy is restricted to the quantized values:

$$\varepsilon_{vib} = \frac{h}{2\pi}\left(\frac{k}{\mu}\right)^{1/2}\left(\upsilon + \frac{1}{2}\right)$$

$$\varepsilon_{vib} = h\nu\left(\upsilon + \frac{1}{2}\right) \quad \upsilon = 0,1,2,\ldots \tag{2.4}$$

with ν being the vibrational frequency read as:

$$\nu = \frac{1}{2\pi}\left(\frac{k}{\mu}\right)^{1/2}. \tag{2.5}$$

k is the *force constant* of the string associated with the bond and μ the *reduced mass* of the molecule given by:

$$\mu = \frac{m_1 m_2}{m_1 + m_2}. \tag{2.6}$$

One important feature of Equation 2.4 is that for $\upsilon = 0$, the energy of the ground state is not zero. This therefore corresponds to the lowest energy level called the *zero-point energy* of the harmonic oscillator.

In the case of polyatomic molecules, the vibrational motion decomposes into $3N - 5$ (linear) or $3N - 6$ (non-linear) normal modes in which each acts as independent harmonic oscillator:

$$\varepsilon_{vib} = \sum_{j=1}^{n_{vib}} h\nu_j \left(\upsilon_j + \frac{1}{2}\right) \quad \upsilon_j = 0,1,2,\ldots \tag{2.7}$$

Also molecules rotate. The simplest model to describe these rotational motions is the *rigid rotator model*. In this case the distance between two atoms, R_e, of masses m_1 and m_2, is fixed. Therefore the kinetic energy of the rigid rotator is:

$$K = \frac{1}{2} I\omega^2 \tag{2.8}$$

where ω is the angular velocity and I the *moment of inertia* defined by:

$$I = \mu R_e^2. \tag{2.9}$$

In addition, when the Schrödinger equation is solved for a rigid rotator then the allowed energies is expressed as:

$$\varepsilon_{rot} = \frac{\hbar^2}{2I} J(J+1) \quad J = 0,1,2,\ldots \tag{2.10}$$

and each energy level has a degeneracy, g_{rot}, equal to:

$$g_{rot} = 2J + 1 \qquad J = 0,1,2,\ldots \tag{2.11}$$

In summary, the energy of a molecule in the rigid rotator harmonic approximation is defined by:

$$\varepsilon_{total} = \varepsilon_{trans} + \varepsilon_{vib} + \varepsilon_{rot} + \varepsilon_{elec} \tag{2.12}$$

(vii) Thermodynamic Quantities

Thermodynamic quantities such as enthalpy, entropy and Gibbs free energy are obtained from translational, vibrational, rotational and electronic energies. The starting point in each case is the *canonical* partition function $Q(N, V, \beta)$ given by:

$$Q(N, V, \beta) = \sum_j e^{-\beta E_j(N,V)} \tag{2.13}$$

in which E_j are the energies of the eigenvalues of the Schrödinger's equation for a system of interest and β is the inverse of the temperature read as:

$$\beta = \frac{1}{k_B T} \tag{2.14}$$

where k_B is the Boltzmann constant and T the temperature in kelvin.

Equation 2.13 can be however rewritten in terms of T to give:

$$Q(N, V, T) = \sum_j e^{-E_j(N,V)/k_B T}. \tag{2.15}$$

This last partition function can be further reduced to molecular partition functions $q(V, T)$ by dividing by $N!$:

$$Q(N, V, T) = \frac{[q(V, T)]^N}{N!}. \tag{2.16}$$

Finally the partition function of a molecular ideal gas can be deduced from Equation 2.16 to give:

$$Q(N,V,T) = \frac{[q_{trans}q_{rot}q_{vib}q_{elec}]^N}{N!}. \tag{2.17}$$

In Equation 2.17, q_{trans} is defined by:

$$q_{trans}(V,T) = \left(\frac{2\pi M k_B T}{h^2}\right)^{3/2} V \tag{2.18}$$

where M is the total mass of the molecule and h is Planck's constant.

In addition, the volume V for a specific system can be calculated for an ideal gas:

$$PV = NRT. \tag{2.19}$$

Knowing that $N = n/N_A$ and $k_B N_A = R$ it follows that $V = k_B T/P$ and this can be substituted in Equation 2.18 to obtain:

$$q_{trans}(V,T) = \left(\frac{2\pi M k_B T}{h^2}\right)^{3/2} \frac{k_B T}{P}. \tag{2.20}$$

The electronic partition function can be written as a sum over levels read as:

$$q_{elec}(T) = \sum_{i}^{levels} g_{ei} e^{-\varepsilon_{ei}/k_B T} \tag{2.21}$$

where g_{ei} is the degeneracy of the energy level and ε_{ei} is the energy of the *i*th electronic level.

However as described previously the energy of the ground electronic state is $\varepsilon_{e1} = -D_e$ therefore the partition function in Equation 2.21 can be rewritten as:

$$q_{elec}(T) = g_{e1} e^{D_e/k_B T} + g_{e2} e^{-\varepsilon_{ei}/k_B T} + \cdots \tag{2.22}$$

At this stage, it should be mentioned that in the Gaussian software package the first electronic excitation energy is considered to be much greater than $k_B T$. Therefore, the first and higher excited states are not taken into account at any temperature and the electronic partition function is simplified to:

$$q_{elec}(T) = g_{e1} e^{D_e / k_B T} \tag{2.23}$$

The rotational partition function is defined by:

$$q_{rot}(T) = \frac{\pi^{1/2}}{\sigma} \left(\frac{T^3}{\Theta_{rot,A} + \Theta_{rot,B} + \Theta_{rot,C}} \right)^{1/2} \tag{2.24}$$

where σ is the symmetry number of the molecule and $\Theta_{rot,j}$ the characteristic rotational temperature given by:

$$\Theta_{rot,j} = \frac{\hbar}{2 I_j k_B} \qquad j = A, B, C. \tag{2.25}$$

Finally, the vibrational partition function is equal to:

$$q_{vib}(T) = \prod_{j=1}^{n_{vib}} \frac{e^{-\Theta_{vib,j}/2T}}{1 - e^{-\Theta_{vib,j}/T}} \tag{2.26}$$

with $\Theta_{vib,j}$ being a characteristic vibrational temperature read as:

$$\Theta_{vib,j} = \frac{h v_j}{k_B}. \tag{2.27}$$

All these partition functions are important as they are needed to calculate the entropy contribution S given by:

$$S = N k_B \ln q + k_B \ln N! + N k_B T \left[\frac{\partial \ln q}{\partial T} \right]_V \tag{2.28}$$

In addition, to the entropy contribution, the different partition functions can be used to determine the internal thermal energy, E:

$$E = Nk_BT^2\left[\frac{\partial \ln q}{\partial T}\right]_V \tag{2.29}$$

and from the internal energy, the heat capacity, C_V:

$$C_V = \left(\frac{\partial E}{\partial T}\right)_{N,V}. \tag{2.30}$$

In the Gaussian software package, the zero-point energy, ε_{ZPE}, is calculated using only the non-imaginary frequencies. In addition to that, the correction to the internal thermal energy, E_{tot}, is obtained by:

$$E_{tot} = E_{trans} + E_{rot} + E_{vib} + E_{elec}. \tag{2.31}$$

Once E_{tot} is known, the thermal correction to enthalpy can be deduced by:

$$H_{corr} = E_{tot} + k_BT \tag{2.32}$$

and with Equations 2.28 and 2.32, the thermal correction to Gibbs free energy is obtained:

$$G_{corr} = H_{corr} - TS_{tot} \tag{2.33}$$

where S_{tot} is given by:

$$S_{tot} = S_{trans} + S_{rot} + S_{vib} + S_{elec}. \tag{2.34}$$

It should also be mentioned that all previous energies include the zero-point energy.

Finally in the output file of the software, the following energies can be found:

$$Sum\ of\ eletronic\ and\ zero\text{-}point\ energies = \varepsilon_0 + \varepsilon_{ZPE}$$
$$Sum\ of\ eletronic\ and\ thermal\ energies = \varepsilon_0 + E_{tot}$$
$$Sum\ of\ eletronic\ and\ thermal\ enthalpies = \varepsilon_0 + H_{corr}$$
$$Sum\ of\ eletronic\ and\ thermal\ free\ energies = \varepsilon_0 + G_{corr}$$

where ε_0 is the total electronic energy.

In addition, if the Gibbs free energy of activation, $\Delta G^{\ddagger}$, is known therefore the rate constant of a specific reaction can be calculated by using the Eyring equation:

$$k(T) = \kappa \frac{k_B T}{h} e^{\frac{-\Delta G^{\ddagger}}{RT}}. \qquad (2.35)$$

where κ is the proportional constant. Equation 2.35 is widely used in transition state theory (TST) which assumes a special type of chemical equilibrium between reactants and activated transition state complexes.

Chapter 3: Mechanistic Study of C–F Bond Activation of Pentafluorobenzene at $[Rh(SiR_3)(PMe_3)_3]$

3.1 Introduction

This chapter describes computational studies aimed at modelling the C–F bond activation of pentafluorobenzene with $[Rh(SiR_3)(PMe_3)_3]$ (R_3 = Me_2Ph, Ph_3), the first step of the catalytic hydrodefluorination reaction reported by Milstein and Aizenberg.[15a] Experimentally, the stoichiometric reaction between $[Rh(SiMe_2Ph)(PMe_3)_3]$ and C_6F_5H occurs at 110 °C to yield quantitatively $[Rh(4\text{-}C_6F_4H)(PMe_3)_3]$ and $FSiMe_2Ph$ (Figure 3.1) while the same catalyst reacts with C_6F_6 at room temperature. Also, Milstein and co-workers showed that $[Rh(SiMe_2Ph)(PMe_3)_3]$ is non-rigid at room temperature on the NMR time scale, giving rise to broad signals in $^{31}P\{^1H\}$ NMR spectrum.[79] This last feature is important as the fluxionality for 4-coordinate monovalent d^8 complexes is quite rare. This indicates that the high trans-influence of silyl ligands may facilitate phosphine dissociation resulting in intermolecular exchange of the phosphine ligands in the 16-electron complexes.

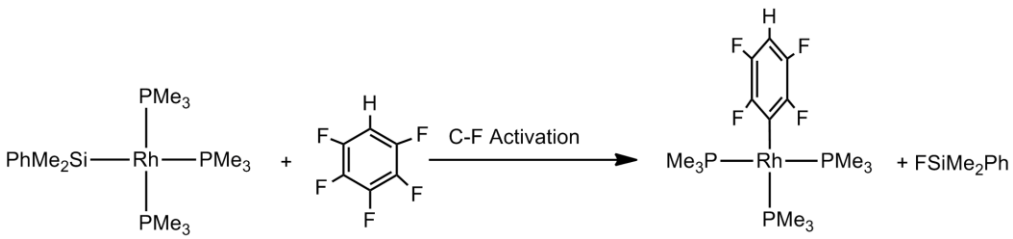

Figure 3.1: C–F bond activation of C_6F_5H by $[Rh(SiMe_2Ph)(PMe_3)_3]$ to form $[Rh(4\text{-}C_6F_4H)(PMe_3)_3]$ and $FSiMe_2Ph$.[15a]

To explain the selectivity of C–F bond activation, Milstein and Aizenberg proposed two possible mechanisms. The first one is the C–F oxidative addition of C_6F_5H followed by Si–F reductive elimination. This mechanism was not favoured by the authors as, at that time, oxidative addition of partially fluorinated arenes resulted mostly in C–H rather than C–F bond activation. In addition, Milstein and Aizenberg proposed an electron transfer mechanism for the C–F cleavage step in which an electron can be transferred from the rhodium silyl complex to the substrate to generate $C_6F_5H^{\bullet-}$ and $[Rh(SiR_3)(PMe_3)_3]^{\bullet+}$, followed by the attack of F^- on silicon to yield $[Rh(4\text{-}C_6F_4H)(PMe_3)_3]$ and $FSiR_3$. This type of mechanism had been postulated by Milstein

and co-workers[53] and subsequently by several other groups.[49-50,52] In one case, Jones and Edelbach reported the C–F bond activation of fluoroaromatic species by [Rh(η^5-C_5Me_5)$(H)_2$(PMe_3)] in pyridine or 1:1 pyridine/benzene.[52] To assess the possibility of an electron transfer reaction, a series of electrochemical measurements on the oxidation of [Rh(η^5-C_5Me_5)$(H)_2$(PMe_3)] and the reduction potential of the polyfluoroaromatics were performed. These experiments showed that the electron transfer of the overall process is uphill by more than 2 V which would require a minimum barrier of 45.0 kcal/mol.

Electron transfer therefore seems unlikely, although this pathway has been modelled and the results will be presented here. In addition, to assess the C–F activation of C_6F_5H with [Rh(SiR_3)$(PMe_3)_3$] (**1$_{SiMe3}$**), two other mechanisms have been computed (Figure 3.2). Pathway 1, is the formal C–F oxidative addition of C_6F_5H, to yield a 18-electron rhodium(III) silyl complex (e.g. ***fac*-3**) followed by Si–F reductive elimination. Pathway 2 is a silyl-assisted C–F bond activation similar to the phosphine-assisted mechanism described in Chapter 1. In this case, C–F activation involves fluorine transfer directly onto silicon with simultaneous Rh–C_{aryl} bond formation.

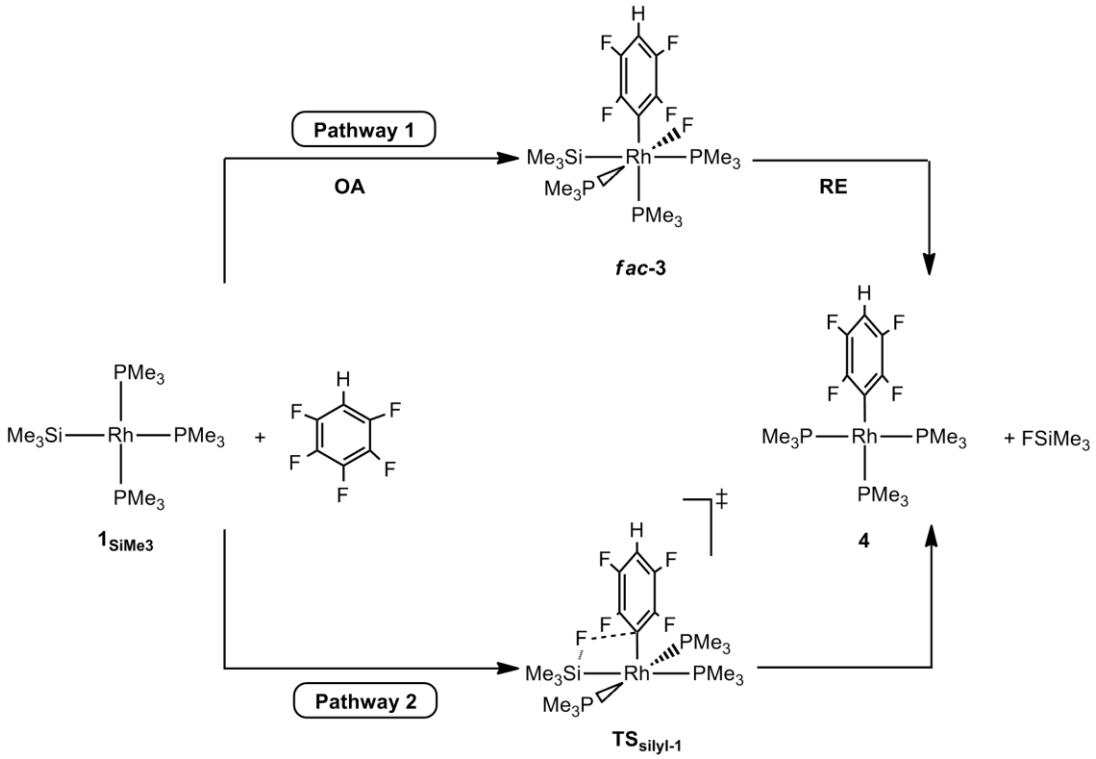

Figure 3.2: Possible reaction mechanisms for C–F activation of C_6F_5H at 1_{SiMe3}.

3.1.1 Comparison between Experimental and Calculated Structures

This study started by computing three distinct rhodium(I) silyl complexes, $[Rh(SiMe_3)(PMe_3)_3]$ (**1**$_{\mathbf{SiMe3}}$), $[Rh(SiMe_2Ph)(PMe_3)_3]$ (**1**$_{\mathbf{SiMe2Ph}}$) and $[Rh(SiPh_3)(PMe_3)_3]$ (**1**$_{\mathbf{SiPh3}}$), to compare the calculated bond lengths and bond angles with the reported experimental data (see Table 3.1 and Figure 3.3).[79-80]

Table 3.1: Experimental (Exp.) and calculated (Calc.) bond lengths (Å) and bond angles (degrees) in $[Rh(SiR_3)(PMe_3)_3]$ (R_3 = Me_3, Me_2Ph, Ph_3).[79-80]

	1$_{\mathbf{SiMe3}}$	**1**$_{\mathbf{SiMe2Ph}}$		**1**$_{\mathbf{SiPh3}}$	
	Calc.	Calc.	Exp.[79]	Calc.	Exp.[80]
Rh–Si	2.402	2.408	2.3804 (10)	2.387	2.317 (1)
Rh–P1	2.363	2.377	2.3094 (9)	2.376	2.332 (1)
Rh–P2	2 283	2.314	2.2708 (6)	2.322	2.266 (1)
Rh–P3	2.305	2.314	2.2708 (6)	2.308	2.271 (1)
Si–Rh–P1	144.86	154.59	156.43 (3)	147.15	143.24 (3)
P2–Rh–P3	140.28	154.94	159.98 (3)	148.51	148.21 (3)

The first optimised structure was **1**$_{\mathbf{SiMe3}}$ which showed a distorted square-planar geometry in which the Si–Rh–P1 and P2–Rh–P3 angles are respectively 144.9° and 140.3°. The high *trans*-influence of the silyl ligand is also seen with an elongation of 0.07 Å of the Rh–P1 bond trans to $SiMe_3$, compared to the Rh–P2 and Rh–P3 distances cis to $SiMe_3$. These features are as well observed in the **1**$_{\mathbf{SiMe2Ph}}$ complex, studied experimentally by Milstein and Aizenberg.[79] In their crystallographic structure, the Si–Rh–P1 and P2–Rh–P3 angles of respectively 156.4° and 160.0°, are in good agreement with the computed bond angles in **1**$_{\mathbf{SiMe2Ph}}$ (Si–Rh–P1 = 154.6°; P2–Rh–P3 = 154.9°). Also, an elongation of the Rh–P1 bond by 0.04 Å was observed experimentally compared to the Rh–P2 and Rh–P3 distances, close to the computed value (0.06 Å). The major discrepancy between the experimental and computational structures is the Rh–P1 bond length which the calculations overestimate by 0.07 Å. In addition, the structure of **1**$_{\mathbf{SiPh3}}$ was studied experimentally by Thorn and Harlow.[80] The experimental and computed structures show a greater distortion compared to **1**$_{\mathbf{SiMe3}}$ and **1**$_{\mathbf{SiMe2Ph}}$ due to the presence of bulkier phenyl substituents. Also, the major difference in **1**$_{\mathbf{SiPh3}}$ between the two structures is seen in the Rh–Si bond length which is 0.07 Å shorter (*cf.* 2.32 Å experimental, 2.39 Å calculated).

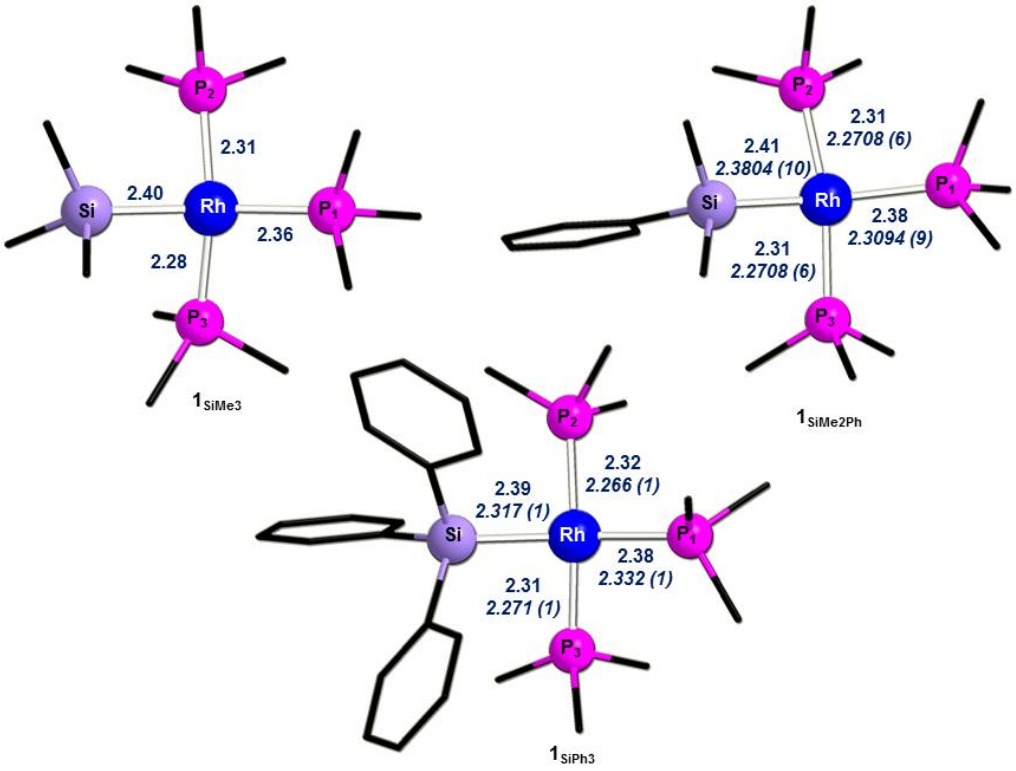

Figure 3.3: Computed geometries (with selected key distances in Å) in $\mathbf{1}_{SiMe3}$, $\mathbf{1}_{SiMe2Ph}$ and $\mathbf{1}_{SiPh3}$. Experimental bond lengths for $\mathbf{1}_{SiMe2Ph}$ and $\mathbf{1}_{SiPh3}$ are shown in italics.[79-80] Hydrogen atoms are omitted for clarity.

Overall, the computed bonds lengths and bond angles are in reasonable agreement with the reported experimental data. Therefore, the computational model $[Rh(SiMe_3)(PMe_3)_3]$ (**$\mathbf{1}_{SiMe3}$**) has been used to study the experimental reaction between $[Rh(SiMe_2Ph)(PMe_3)_3]$ (**$\mathbf{1}_{SiMe2Ph}$**) and C_6F_5H.

3.1.2 Electron Transfer Pathway

In a first step, an electron transfer pathway from **$\mathbf{1}_{SiMe3}$** to C_6F_5H to form the separated radicals, $[Rh(SiMe_3)(PMe_3)_3]^{\bullet+}$ and $C_6F_5H^{\bullet-}$, has been computed. Calculations show that this process is kinetically unfavoured with a change in energy of +120.2 kcal/mol in the gas phase. This decreases to +79.2 kcal/mol when hexafluorobenzene solvent is taken into account via a PCM approach. Therefore, this mechanism has been ruled out.

3.2 Pathway 1: C–F Oxidative Addition and Subsequent Si–F Reductive Elimination

3.2.1 C–F Oxidative Addition

Along Pathway 1, in addition to the *fac*-isomer (***fac*-3**), illustrated in Figure 3.2, two further isomers can be formed, namely ***mer*-3**, with 4-C_6F_4H trans to $SiMe_3$, and ***mer*-3′** with 4-C_6F_4H cis to $SiMe_3$ (see Figure 3.4). In ***mer*-3**, F is cis to $SiMe_3$ and can access reductive elimination directly, whereas in ***mer*-3′** F is trans $SiMe_3$ and so a prior isomerisation step will be required.

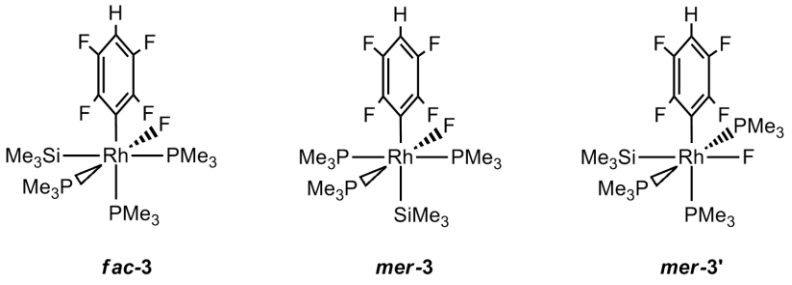

Figure 3.4: Three possible isomers formed upon C–F activation of C_6F_5H to $\mathbf{1_{SiMe3}}$.

In this chapter, all selected key distances are in Å while all energies are in kcal/mol, relative to the two separated reactants, $\mathbf{1_{SiMe3}}$ and C_6F_5H, denoted by **2**. Also, figures show free energies in italics and non-participating hydrogen atoms are omitted for clarity. The stationary points involved for the C–F oxidative addition of C_6F_5H at $\mathbf{1_{SiMe3}}$ are shown in Figure 3.5.

The highest energy pathway corresponds to the formation of ***mer*-3** (H = -26.3 kcal/mol) via **TS (2 – *mer*-3)** (H = +34.6 kcal/mol) in which the key C1···F1 bond distance is stretched to 1.58 Å. Short Rh···C1 and Rh···F1 contacts are also computed (Rh···C1 = 2.45 Å, Rh···F1 = 2.58 Å) and the Rh–Si bond increases to 2.53 Å (*cf.* 2.40 Å in $\mathbf{1_{SiMe3}}$), due to the approach of the 4-C_6F_4H moiety trans to the $SiMe_3$ ligand. Surprisingly, **TS (2 – *mer*-3)** shows a contact between P2 and F1 with a distance of 2.83 Å. Related to this is the orientation of the C_6F_5H moiety, which is distorted away from the expected coplanar arrangement for a concerted oxidative addition. This distortion can be quantified, for an oxidative addition or reductive elimination process by α, the angle between the L_{eq}–M–L_{eq} and X–M–Y planes. In the current example, X corresponds to

the ipso carbon of 4-C_6F_4H, C1, while Y represents F1 (see Figure 3.6). L_{eq} are the ligands trans to these, here Si and P1. In this case, α = 20.5° and showed that the transition state is twisted away from normal oxidative addition probably due to the interaction with P2.

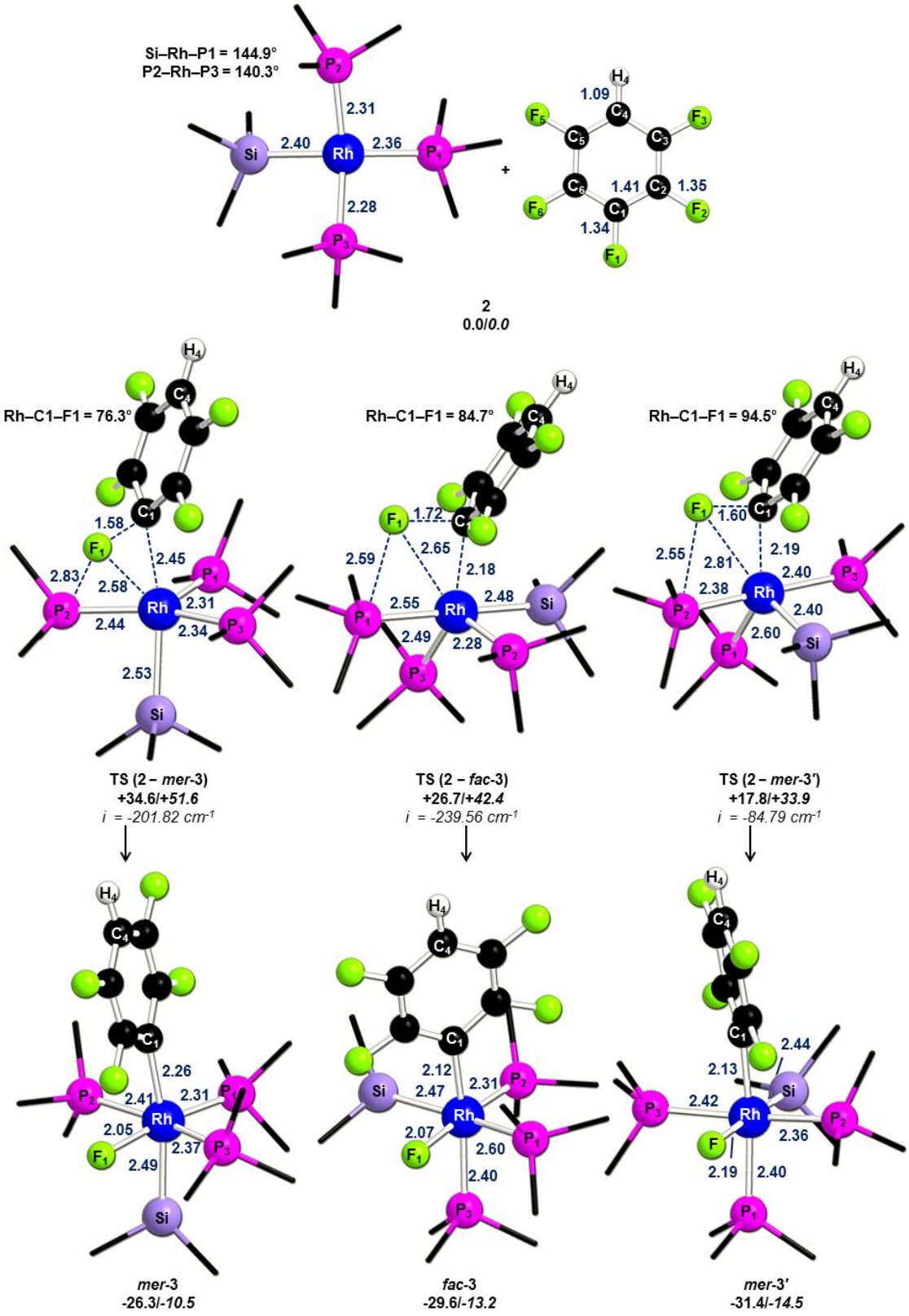

Figure 3.5: Computed geometries and energies to give *mer*-3, *fac*-3 and *mer*-3′.

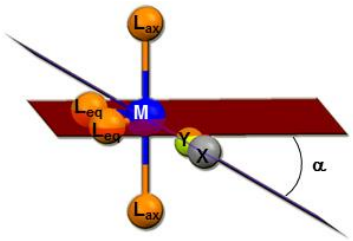

Figure 3.6: Schematic representation of α, angle between the L_{eq}–M–L_{eq} and X–M–Y planes.

The next most accessible pathway proceeds via **TS (2 – *fac*-3)** (H = +26.7 kcal/mol) to form ***fac*-3** (H = -29.6 kcal/mol). Significant elongation of the breaking C1···F1 bond to 1.72 Å is also computed while the Rh···C1 and Rh···F1 interactions shorten to 2.18 Å and 2.65 Å, respectively. The Rh···F1 contact is slightly longer than the distance between P1 and F1 (P1···F1 = 2.59 Å), suggesting that P1 is more involved in the C–F cleavage step. Moreover the C1···F1 vector is more twisted relative to the P2–Rh–P3 plane (α = 54.3°) and thus again differs from the usual 3-centred concerted oxidative addition. A similar transition state has been reported for the C–F activation of C_6F_6 at [Ir(Me)(PEt_3)$_3$] (see Figure 3.7).[54]

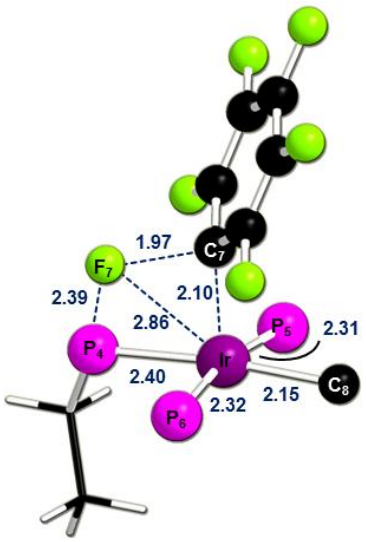

Figure 3.7: Computed transition state for the phosphine-assisted C–F activation of C_6F_6 at [Ir(Me)(PH_3)$_2$(PH_2Et)].[54]

In this study, C–F activation of C_6F_6 at [Ir(Me)(PH_3)$_2$(PH_2Et)] occurs via a phosphine-assisted mechanism and in this case α is 58.1° (relative to the P5–Ir–P6 plane), close to the one in **TS (2 – *fac*-3)**. However, to quantify this ligand-assisted process, the authors used the P4–Ir–C7–F7 angle which is therefore more suitable than using α, as the phosphine ligand is involved. For the iridium transition state, the P4–Ir–C7–F7 angle is

equal to +34.5° while in **TS (2 – *fac*-3)** the P1–Rh–C1–F1 angle is -32.3°. These similarities suggest that **TS (2 – *fac*-3)** differs from the traditional concerted oxidative addition in that a degree of phosphine-assistance is computed, in which Rh, C1, F1 and P1, all participate. Further characterisation of **TS (2 – *fac*-3)**, via IRC calculations, confirmed that fluorine moves toward P1 and weakly interacts with the phosphine ligand, suggesting an anionic phosphoranide $\{PFMe_3\}^-$ moiety, before transferring to the rhodium metal centre to yield ***fac*-3** (H = -29.6 kcal/mol). Despite many attempts no metallophosphorane intermediates have been located.

Finally, the lowest C–F oxidative addition process occurs via **TS (2 – *mer*-3′)** and has a computed barrier of only +17.8 kcal/mol. In the transition state, the C1···F1 bond increases to 1.60 Å while the Rh···F1 distance remains rather long (2.81 Å). As seen in **TS (2 – *fac*-3)**, a short P2···F1 contact (2.55 Å) is also computed, suggesting that the phosphine ligand is more than a simple spectator and participates in the C–F activation. Indeed, this P2···F1 interaction is again shorter than the Rh···F1 distance and in this case α is 72.2° while the P2–Rh–C1–F1 angle is -20.7°. IRC calculations from **TS (2 – *mer*-3′)** confirmed that fluorine weakly interacts with P2, before being transferred to Rh to form ***mer*-3′** (H = -31.4 kcal/mol).

The reaction profiles along Pathway 1 for the C–F activation to yield ***mer*-3**, ***fac*-3** and ***mer*-3′** are shown in Figure 3.8. The stability of the three different isomers follows the trend: ***mer*-3** (H = -26.3 kcal/mol) < ***fac*-3** (H = -29.6 kcal/mol) < ***mer*-3′** (H = -31.4 kcal/mol). In ***mer*-3′**, F is trans to $SiMe_3$ and therefore has the best arrangement of ligands, having the strongest electron donor ligand ($SiMe_3$) trans to the weakest donor (F). In addition, in ***mer*-3** the Rh–Si bond trans to 4-C_6F_4H is slightly more elongated than in ***fac*-3**, in which 4-C_6F_4H is trans to PMe_3, suggesting that 4-C_6F_4H has a higher *trans*-influence than PMe_3. Therefore, ***mer*-3** is the least stable species because the high *trans*-influence ligand $SiMe_3$ is trans to 4-C_6F_4H. From these observations, a final trend for the *trans*-influence of the different ligands can be drawn: $SiMe_3$ > 4-C_6F_4H > PMe_3 > F.

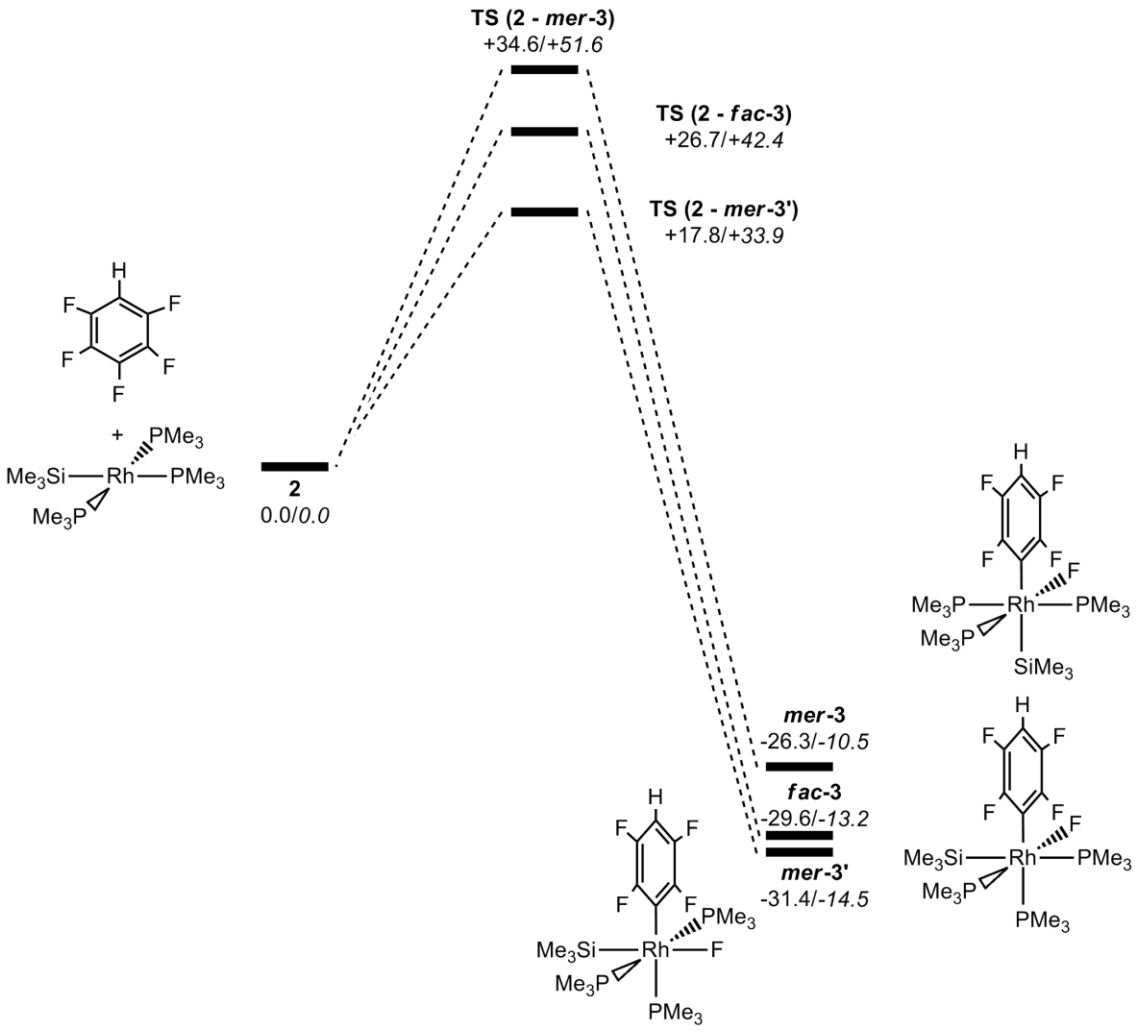

Figure 3.8: Formation of *mer*-3, *fac*-3 and *mer*-3′ via C–F activation, along Pathway 1.

The above comparisons for the three different isomers in terms of energies and geometries can rationalise the difference in stability of the three different transition states: **TS (2 – *mer*-3)** (H = +34.6 kcal/mol) **< TS (2 – *fac*-3)** (H = +26.7 kcal/mol) < **TS (2 – *mer*-3′)** (H = +17.8 kcal/mol). **TS (2 – *mer*-3′)** is the most stable transition state as $SiMe_3$ is trans to vacant site while in **TS (2 – *fac*-3)** and **TS (2 – *mer*-3)** silyl is trans to PMe_3 and 4-C_6F_4H, respectively. In addition, **TS (2 – *fac*-3)** is more accessible than **TS (2 – *mer*-3)** because in the former $SiMe_3$ is trans to PMe_3 while in the latter silyl is trans to 4-C_6F_4H. The difference in energy between **TS (2 – *mer*-3′)** and **TS (2 – *fac*-3)** can be explained by the position of the phosphine ligand interacting with F1 as both transition states occurs with a degree of phosphine-assistance. In the latter, P1 which interacts with F1 is trans to $SiMe_3$ while in the former, P2 is trans to a weaker σ-donor ligand (PMe_3). This suggests that PMe_3 in **TS (2 – *mer*-3′)** is relatively more electron deficient and thus stronger stabilises F1, making the process more accessible.

As mentioned above, **TS (2 – *mer*-3′)** and **TS (2 – *fac*-3)** show a degree of phosphine-assistance and therefore differ from the traditional concerted oxidative addition process. During the C–F cleavage step, no metallophosphorane intermediates have been located and the final products are oxidative species. In comparison, Perutz et *al*. reported the C–F activation of C_5NF_5 at $[Ni(PMe_3)_2]$ which occurs via a phosphine-assisted mechanism.[60] In this study, a metallophosphorane intermediate is located before F being transferred to Ni to give *trans*-$[Ni(C_5NF_4)(F)(PMe_3)_2]$. Therefore, the final species is an oxidative product; however the mechanism is not oxidative addition. This process has been described as "phosphine-assisted oxidative addition" and is similar to **TS (2 – *mer*-3′)** and **TS (2 – *fac*-3)** where a degree of phosphine-assistance is computed and the final products are Rh(III) species. The difference is the lack of a metallophosphorane intermediate.

*3.2.2 Si–F Reductive Elimination from **mer-3**, **fac-3** and **mer-3′***

The final product $[Rh(4\text{-}C_6F_4H)(PMe_3)_3]$ (**4**) is observed experimentally after elimination of $FSiMe_3$.[15a] Therefore a Si–F reductive elimination step has to be considered from ***mer*-3**, ***fac*-3** and ***mer*-3′**. For ***mer*-3** and ***fac*-3** this process can happen directly and the computed structures and relative energies involved in this process are shown in Figure 3.9.

The lower pathway for reductive elimination occurs from ***mer*-3** and through the 3-centred transition state **TS (*mer*-3 – 4)** (H = -20.1 kcal/mol). In the transition state, the C1–Rh–P1 angle widens to 115.3° (*cf.* 97.9° in ***mer*-3**) and an elongation of the breaking Rh···Si and Rh···F1 bonds, to 2.65 Å and 2.28 Å, respectively, is computed. The Si···F1 contact decreases significantly to 1.87 Å and α which is, in this case, the angle between the Si–Rh–P1 and C1–Rh–F1 angles is 8.9°, consistent with the 3-centred nature of the process. This is in strong contrast with the previous C–F oxidative transition states. The final product **4** is obtained after release of $FSiMe_3$ and has a computed energy of -59.4 kcal/mol (G = -59.0 kcal/mol).

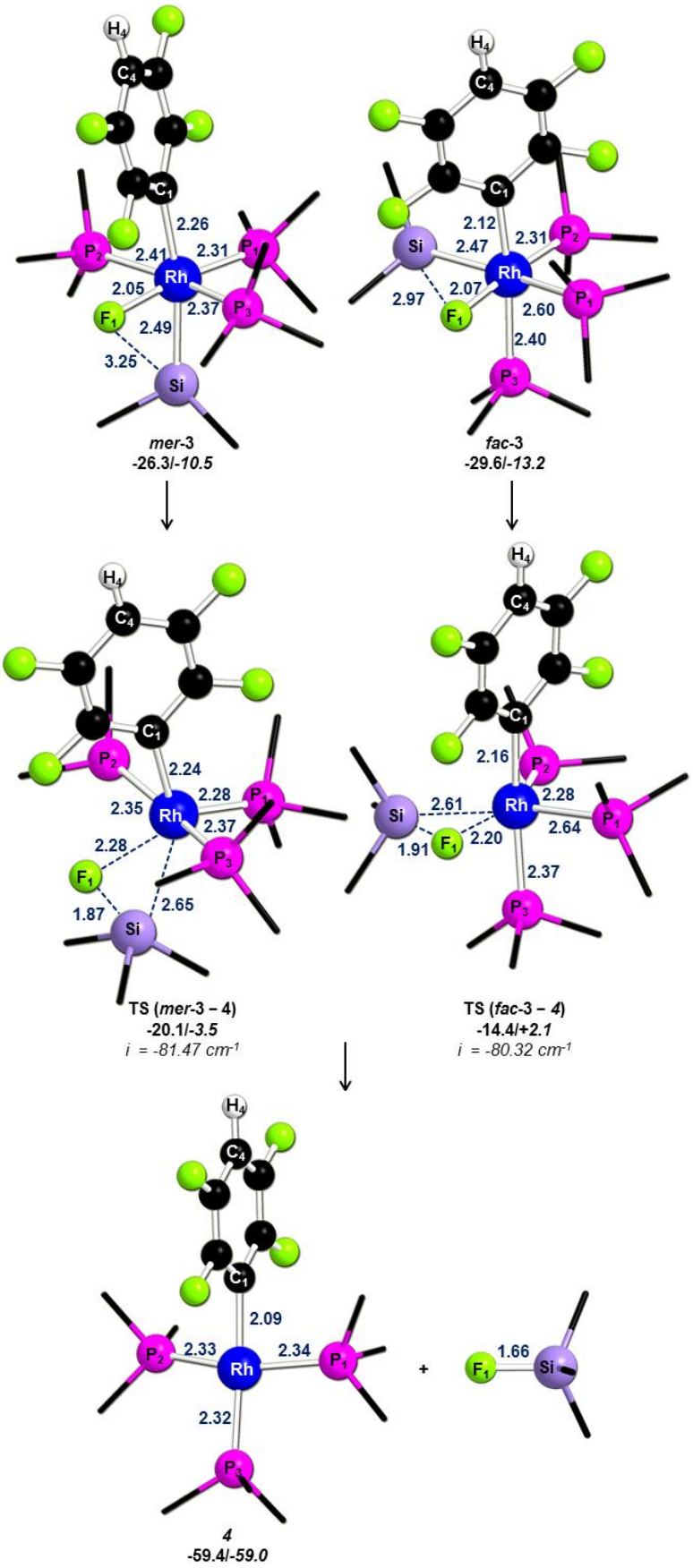

Figure 3.9: Computed geometries and energies for Si–F reductive elimination from *mer*-3 and *fac*-3.

The second reductive elimination pathway proceeds from ***fac*-3** via the 3-centred transition state **TS (*fac*-3 – 4)** (H = -14.4 kcal/mol). In **TS (*fac*-3 – 4)**, the Rh···F1 and Rh···Si distances lengthen to 2.20 Å and 2.61 Å, respectively, while a short Si···F1 interaction is computed (1.91 Å), all consistent with the Si–F reductive elimination process. As seen in **TS (*mer*-3 – 4)**, the process is almost coplanar, with α equal to 5.4°.

The reaction profiles for Si–F reductive elimination from ***mer*-3** and ***fac*-3** are shown in Figure 3.10. **TS (*mer*-3 – 4)** is more stable than **TS (*fac*-3 – 4)** by 5.7 kcal/mol. This difference in energy can be understood by looking at the Rh–Si bond. In ***mer*-3**, the Rh–Si bond (2.49 Å) is slightly weaker than in ***fac*-3** (2.47 Å), as in the former $SiMe_3$ is trans to 4-C_6F_4H, which facilitates the process. Finally, computed free energies further favour formation **4** compared to the other stationary points, as two species are formed from one molecule.

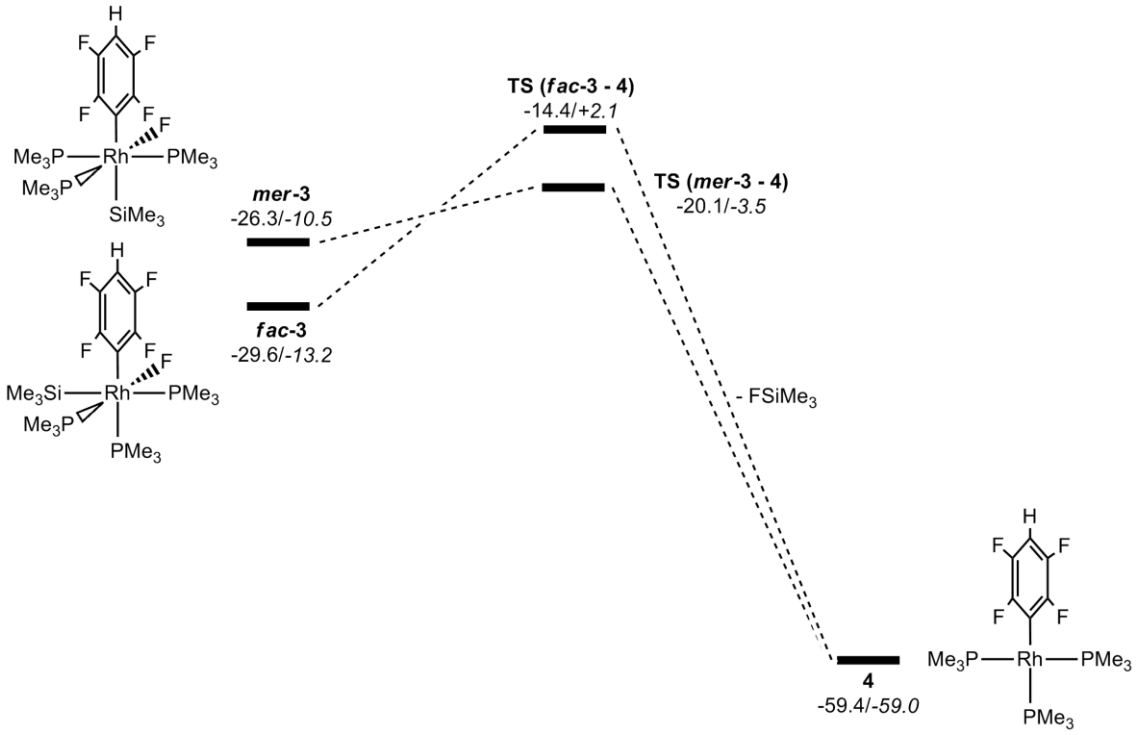

Figure 3.10: Formation of [Rh(4-C_6F_4H)(PMe_3)$_3$], 4, and $FSiMe_3$ via Si–F reductive elimination from *mer*-3 and *fac*-3.

The formation of $FSiMe_3$ from ***mer*-3′** has also been computed and two different approaches have been considered (Figure 3.11). One way to isomerise ***mer*-3′** is to dissociate PMe_3 either trans to trimethylphosphine (***cis*-5**) or trans to 4-C_6F_4H (***trans*-5**).

From these two putative rhodium(III) silyl complexes an isomerisation process can occur where F moves cis to $SiMe_3$ to give respectively ***cis*-5′** and ***trans*-5′**. From these two species, the dissociated phosphine could bind the metal centre to form respectively ***fac*-3** and ***mer*-3″**. Si–F reductive elimination from ***fac*-3** has already been discussed and proceeds through a transition state at -14.4 kcal/mol (G = +2.1 kcal/mol).

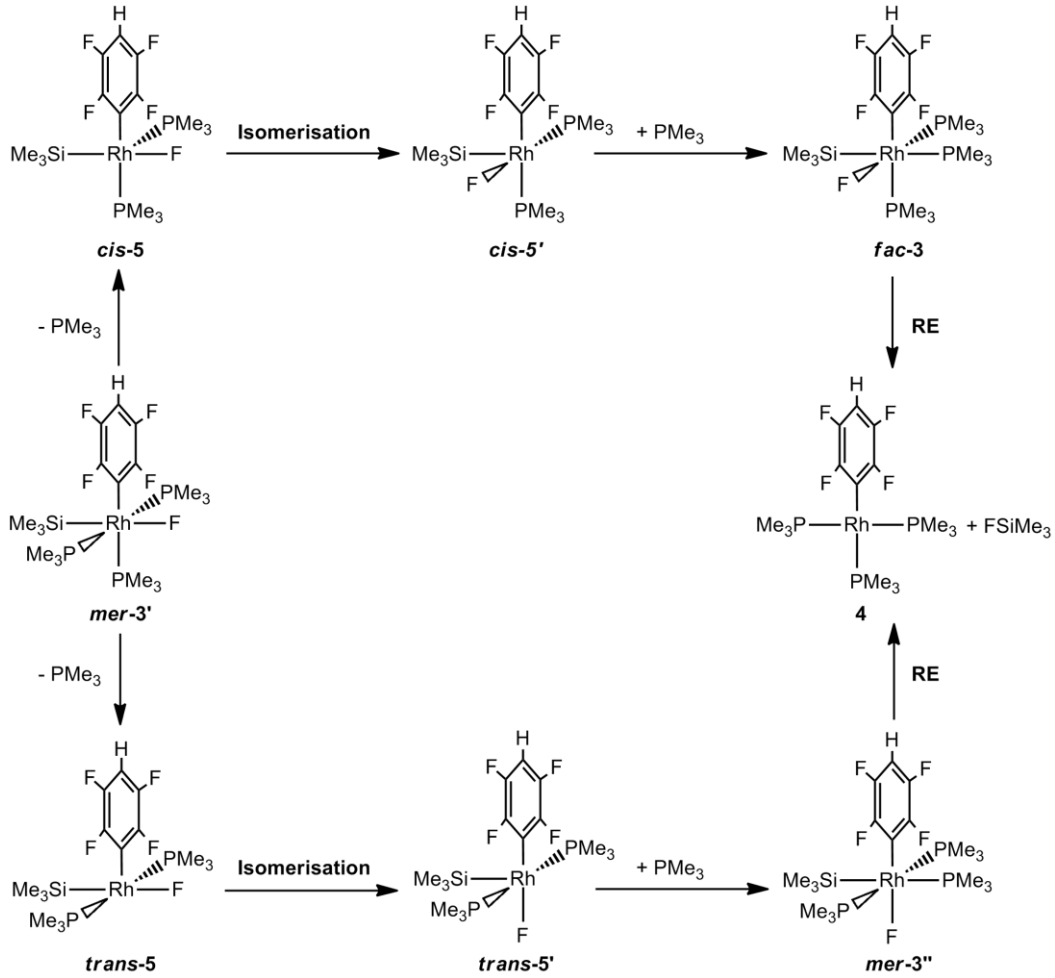

Figure 3.11: Possible pathways for the isomerisation of *mer*-3′ to afford Si–F reductive elimination.

In contrast to the sequence in Figure 3.11, attempts to optimise ***cis*-5** and ***trans*-5** resulted in isomerisation with F moving cis to $SiMe_3$ to give ***cis*-5′** and ***trans*-5′**, respectively, while $SiMe_3$ ends up trans to the vacant site. This isomerisation process again reflects the high *trans*-influence of $SiMe_3$. After further calculations two transition states have been located, for direct formation of ***cis*-5′** and ***trans*-5′** from ***mer*-3′**, where the phosphine dissociates at the same time as the isomerisation occurs. The computed geometries and relative energies of the stationary points are shown in Figure 3.12.

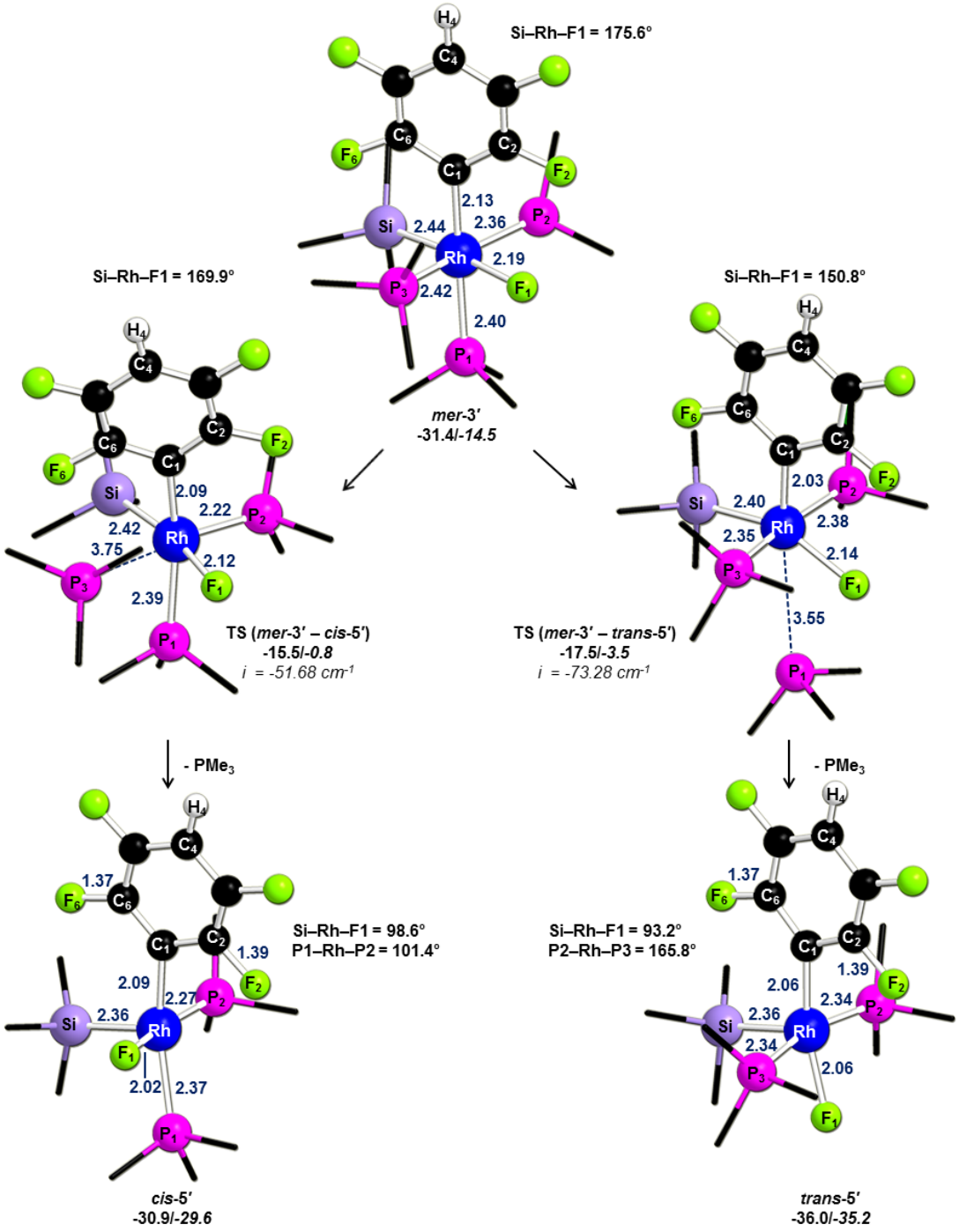

Figure 3.12: Computed geometries and energies for the phosphine loss/isomerisation to give *cis*-5′ and *trans*-5′.

The higher transition state yields ***cis*-5′** via **TS (*mer*-3′ – *cis*-5′)** (H = -15.5 kcal/mol). In the transition state, the Rh···P3 distance lengthens to 3.75 Å as phosphine is dissociated and the Si–Rh–F1 angle decreases to 169.9° (*cf.* 175.6° ***mer*-3′**). The second transition **TS (*mer*-3′ – *trans*-5′)** (H = -17.5 kcal/mol), gives ***trans*-5′** in which the breaking Rh···P1 bond lengthens to 3.55 Å while the Si–Rh–F1 angle bends back to 150.8° (*cf.* 175.6° ***mer*-3′**).

Species ***cis*-5′** and ***trans*-5′** both have square pyramidal geometries and a distorted 4-C_6F_4H ligand. ***Cis*-5′** exhibits Rh–C1–C2 and Rh–C1–C6 angles of 110.2° and 134.9°, respectively, while the same angles are 112.5° and 134.4°, respectively, in ***trans*-5′**. These distortions are driven by some interactions between the metal centre and the C2–F2 bond. In ***cis*-5′**, the Rh···C2 and Rh···F2 contacts are 2.89 Å and 2.88 Å, respectively, and the C2–F2 bond elongates to 1.39 Å. In addition, ***trans*-5′** shows similar features (Rh···C2 = 2.90 Å, Rh···F2 = 2.93 Å, C2–F2 = 1.39 Å). It should also be mentioned that experimentally these 5-coordinate complexes are known to have a fluxional behaviour as the energy barrier between trigonal bipyramid and square pyramidal is often quite low.

Overall, **TS (*mer*-3′ – *trans*-5′)** is 2.0 kcal/mol more stable than **TS (*mer*-3′ – *cis*-5′)**. This small difference in energy may come from the higher *trans*-influence of 4-C_6F_4H compared to PMe_3 which promotes Rh···P1 dissociation in ***mer*-3′**. The stabilisation of ***trans*-5′** by 5.1 kcal/mol compared to ***cis*-5′** is explained by having 4-C_6F_4H trans to F while in the later 4-C_6F_4H is trans to PMe_3. In addition, the phosphine loss/isomerisation step to form ***trans*-5′** from ***mer*-3′** is exothermic by 4.6 kcal/mol (ΔG = -20.7 kcal/mol). This stabilisation of ***trans*-5′** again confirms the high *trans*-influence of $SiMe_3$ which prefers to be trans to a vacant site.

At this point, PMe_3 addition to ***cis*-5′** and ***trans*-5′** gives ***fac*-3** and ***mer*-3″**, respectively (see Figure 3.11). It should be, however, mentioned that Si–F reductive elimination from both 5-coordinates species is also possible and will be considered in Section 3.5.3. Species ***mer*-3″** is found to be slightly less stable than ***fac*-3** by 1.4 kcal/mol and has an unusual distorted octahedral geometry in which the Si–Rh–P1 and Si–Rh–F angles are 141.6° and 62.6°, respectively (Figure 3.13). These distortions appear to be driven by a weak Si···F1 interaction of 2.41 Å, as this contact is generally much longer in the other isomers (***mer*-3**, Si···F1 = 3.25 Å; ***fac*-3**, Si···F1 = 2.91 Å).

Si–F reductive elimination from ***mer*-3″** occurs through the 3-centred transition state **TS (*mer*-3″ – 4)** (H = -27.0 kcal/mol). This transition state has C1 symmetry, however a second negative eigenvalue has been found after the frequency calculations. This exhibits an imaginary frequency of -6.83 cm^{-1} corresponding to the rotation of the fluoroaryl ligand and could not be removed, despite many attempts, using very tight

optimisations. This discrepancy, however, should not significantly affect the energy of the transition state. In **TS (*mer*-3″ – 4)**, the C1–Rh–Si angle widens to 129.8° (*cf.* 115.8° in ***mer*-3″**). The Si···F1 distance shortens to 1.80 Å and the Si···F1 vector is coplanar with the C1–Rh–P1 plane (α = 0.0°), as expected for a reductive elimination process. In addition, both Rh···Si and Rh···F1 distances lengthen to respectively 2.95 Å and 2.24 Å whereas the Rh–P1 bond remains rather long (2.63 Å), trans to the vacant site.

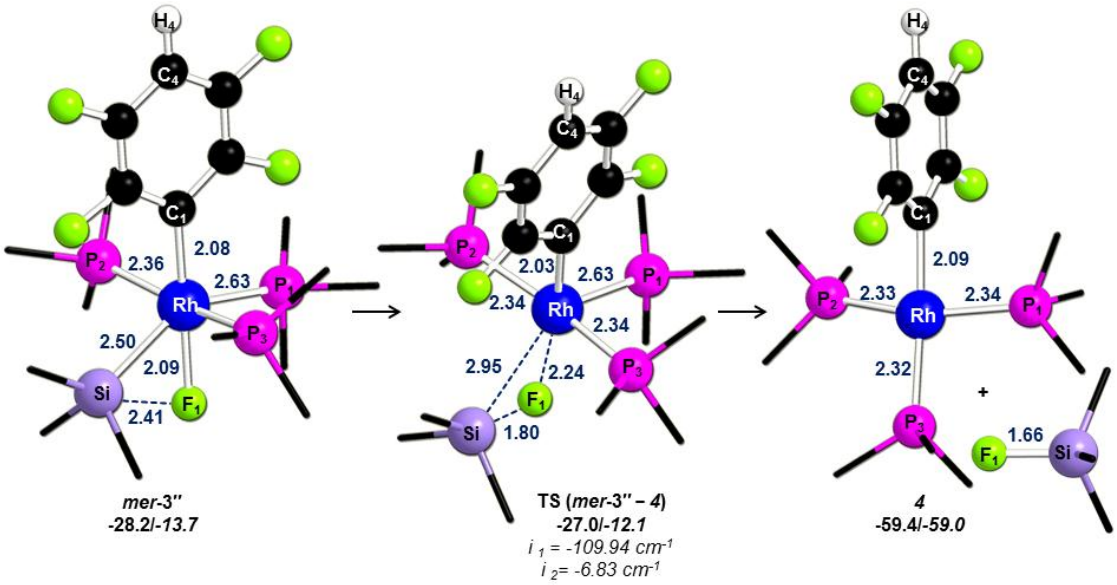

Figure 3.13: Computed geometries and energies for Si–F reductive elimination from *mer*-3″.

The reaction profiles for the Si–F reductive elimination from ***mer*-3′** are shown in Figure 3.14. The most accessible process is through the transition state **TS (*mer*-3′ – *trans*-5′)** with a computed enthalpy of -17.5 kcal/mol where PMe_3 dissociates trans to 4-C_6F_4H and F moves cis to $SiMe_3$. From ***trans*-5′**, PMe_3 can bind trans to $SiMe_3$ to form ***mer*-3″**. Reductive elimination from ***mer*-3″** is then facile, with a barrier of 1.2 kcal/mol (H = -27.0 kcal/mol) to form **4** and $FSiMe_3$. Along this pathway the rate-limiting process is the phosphine loss/isomerisation step (H = -17.5 kcal/mol) to yield ***trans*-5′**.

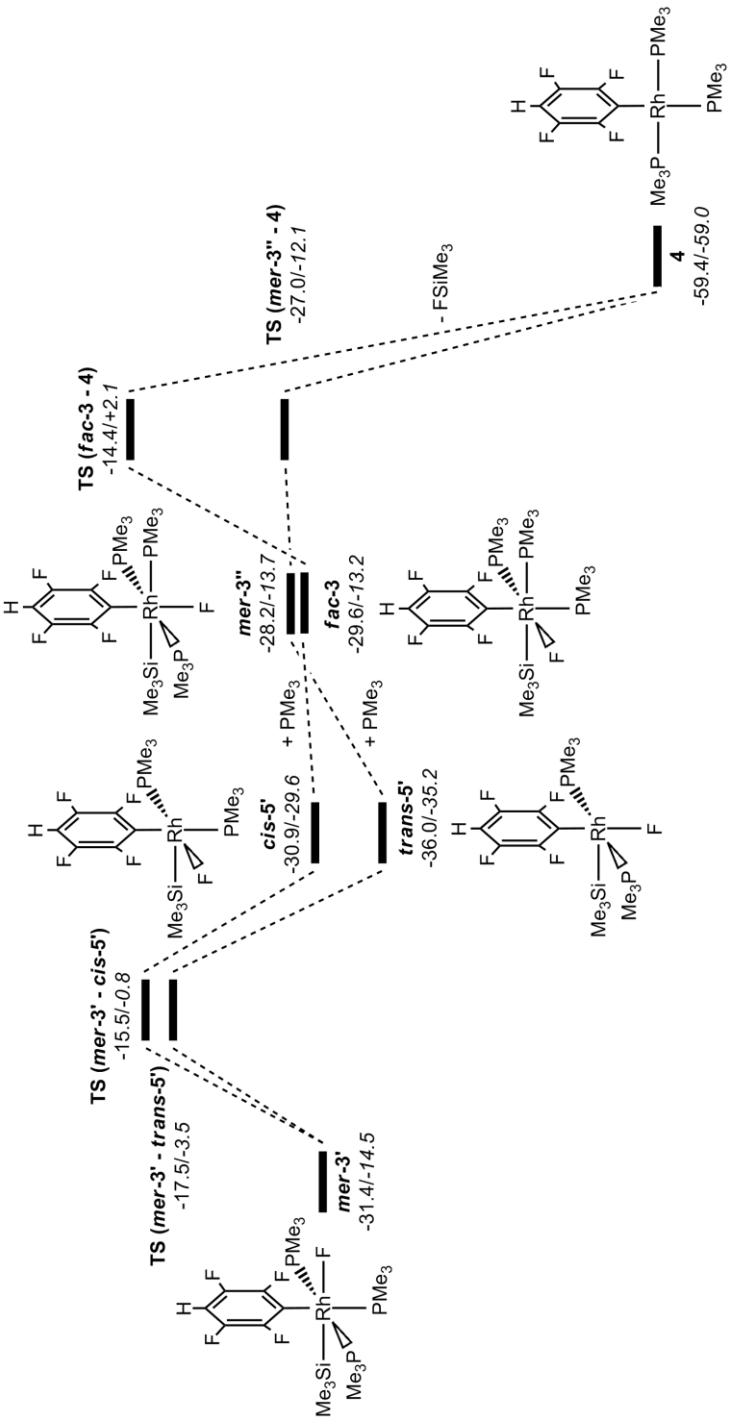

Figure 3.14: Formation of [Rh(4-C_6F_4H)(PMe_3)$_3$], 4, and $FSiMe_3$ via Si–F reductive elimination from *mer*-3′.

Reaction profiles comparing the formation of **4** and $FSiMe_3$ from ***mer*-3**, ***fac*-3** and ***mer*-3′** are given in Figure 3.15. The highest energy process goes via **TS (*fac*-3 – 4)** and has a computed enthalpy of -14.4 kcal/mol. The next most accessible pathway is from ***mer*-3′** via **TS (*mer*-3′ – *trans*-5′)** (H = -17.5 kcal/mol) while the easiest process is from ***mer*-3** through **TS (*mer*-3 – 4)** (H = -20.1 kcal/mol). The computed free energies show that the phosphine loss/isomerisation step from ***mer*-3′** and the direct reductive

elimination from ***mer*-3** become competitive (G = -3.5 kcal/mol) as the entropy favours the dissociation of the phosphine ligand in the former.

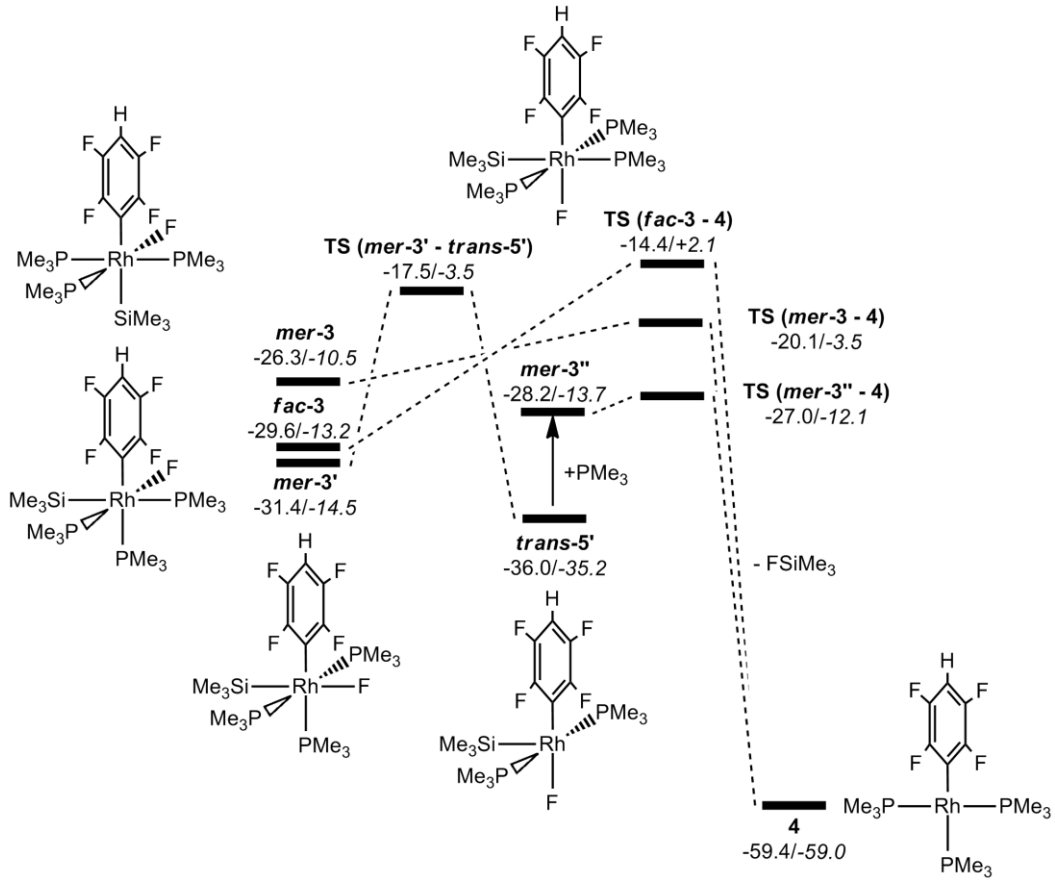

Figure 3.15: Formation of [Rh(4-C_6F_4H)(PMe_3)$_3$], 4, and $FSiMe_3$ via Si–F reductive elimination from *mer*-3, *fac*-3 and *mer*-3′.

3.2.3 Summary of Pathway 1

The key stationary points for Pathway 1 are shown in Figure 3.16. The lowest lying process involves formation of ***mer*-3′** with a barrier of +17.8 kcal/mol. Once ***mer*-3′** is formed, isomerisation to ***mer*-3″** is required followed by Si–F reductive elimination. It should be noted that C–F activation is always the rate-limiting transition state and gives the three possible isomers, ***mer*-3**, ***fac*-3** and ***mer*-3′**. From these species, formation of **4** and $FSiMe_3$ is then facile. The computed free energies increase the energies of the stationary points, which involve associative processes, by around 16.0 kcal/mol. Species ***trans*-5′** and **4** are stabilised as they involve dissociation of one ligand. Finally, calculations showed that the C–F activation of C_6F_5H to form ***mer*-3′** occurs with a certain degree of phosphine-assistance and therefore differs from the traditional 3-

centred concerted oxidative addition. Overall the process is highly exothermic by 59.4 kcal/mol (G = -59.0 kcal/mol).

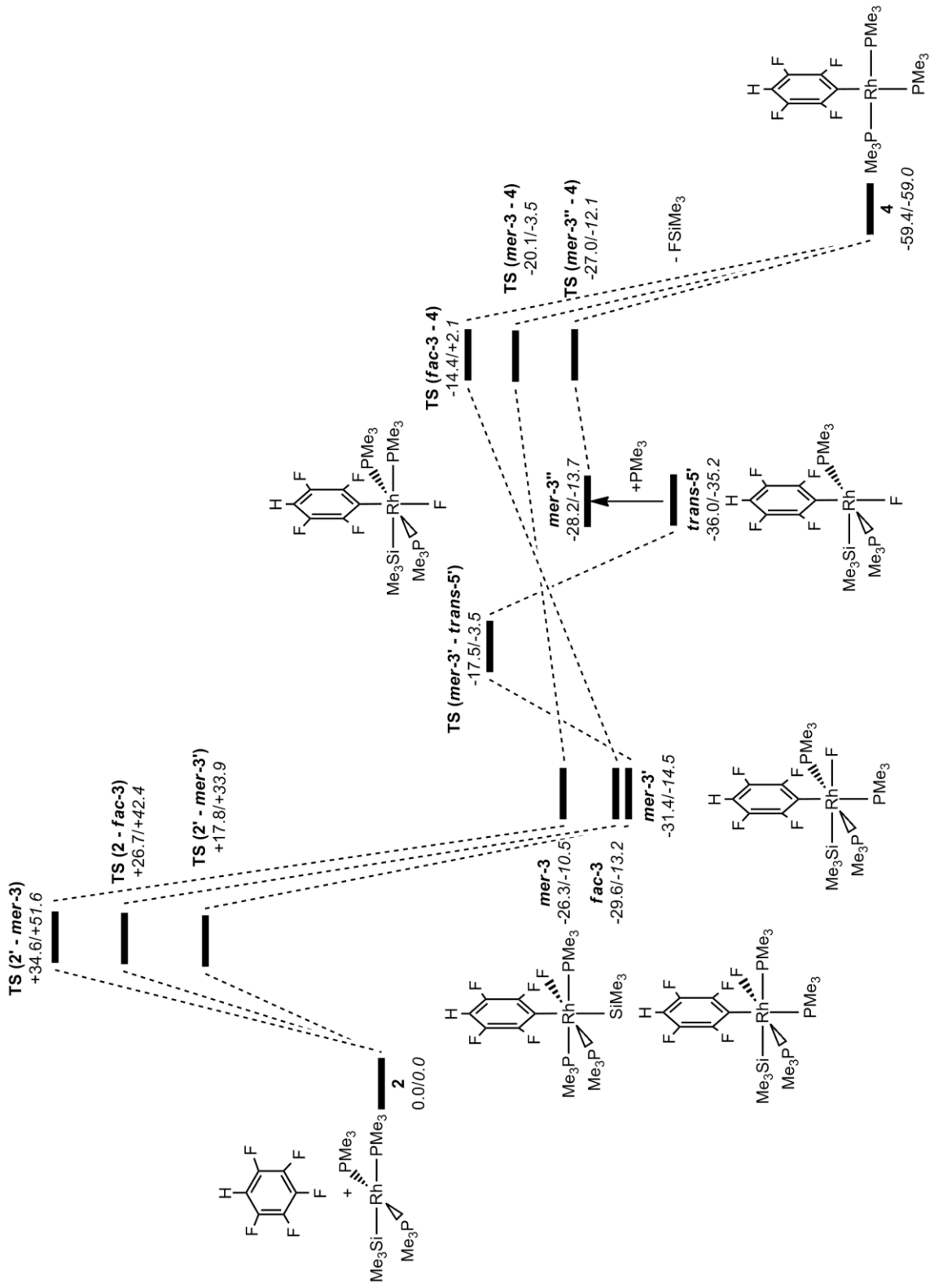

Figure 3.16: Formation of [Rh(4-C_6F_4H)(PMe_3)$_3$], 4, and $FSiMe_3$ via C–F activation of C_6F_5H at $\mathbf{1}_{SiMe_3}$.

3.3 Pathway 2: Silyl-Assisted C–F Bond Activation

This mechanism occurs with fluorine being transferred directly onto silicon with simultaneous Rh–C_{Aryl} bond formation to yield **4** and $FSiMe_3$ (Figure 3.2). Several transition states and stationary points have been computed for Pathway 2 but only the lowest energy mechanism for C–F activation will be discussed in detail. The first step is the formation of the η^2-arene intermediate **6** which has a trigonal bipyramidal geometry in which the $SiMe_3$ ligand is in an equatorial position. In addition, the C1=C2 bond distance increases to 1.48 Å, consistent with the Dewar-Chatt-Duncanson model where the C1=C2 bond is weakened by the π-back donation from the metal centre to the π* antibonding orbital of the C_6F_5H moiety. A transition state, **TS (2 – 6)** (H = +16.1 kcal/mol) for formation of **6** has been computed by lengthening the Si–Rh–P1 angle (in this case, Si–Rh–P1 = 132.9°).

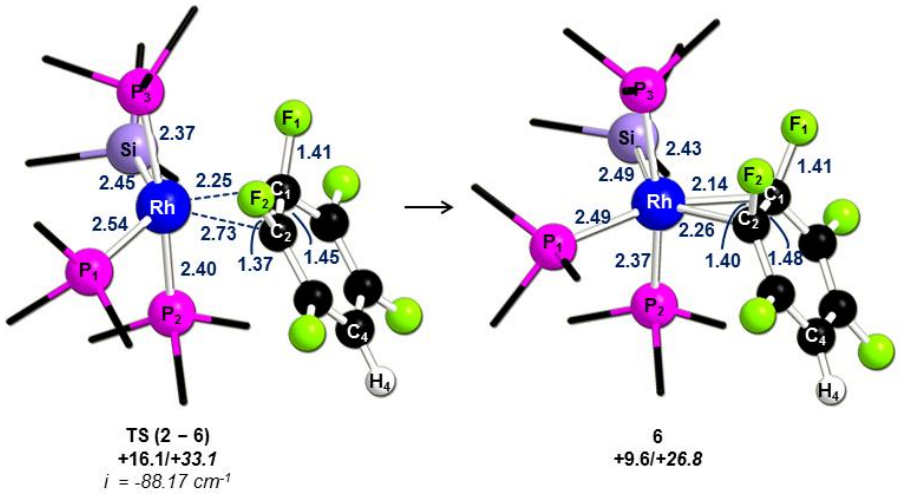

Figure 3.17: Computed geometries and energies for formation of 6.

From **6**, a transition state has been located for C–F activation, **TS (6 – 4)** (H = +20.1 kcal/mol, see Figure 3.18), in which the C1···F1 is stretched to 1.72 Å. Moreover, the Si···F1 contact actually lengthens by 0.24 Å to 4.04 Å, implying little or no degree of silyl-assistance. Instead, it is the P3···F1 interaction that shortens, by 0.61 Å to 2.61 Å, suggesting that the phosphine ligand again participates in the C–F activation similar to **TS (2 – *fac*-3)** and **TS (2 – *mer*-3′)** (see Figure 3.19, for a comparison of all three). In addition this P3···F1 interaction is shorter than the Rh···F1 contact (3.01 Å) and α is 64.3°. In this case, a better way to quantify this process is by using the torsion angles. In **TS (6 – 4)**, the P3–Rh–C1–F1 is -21.1°, very similar to the P2–Rh–C1–F1 angle

(-20.7°) in **TS (2 – *mer*-3′)** and relatively close to the P2–Rh–C1–F1 angle (-32.3°) in **TS (2 – *fac*-3)**.

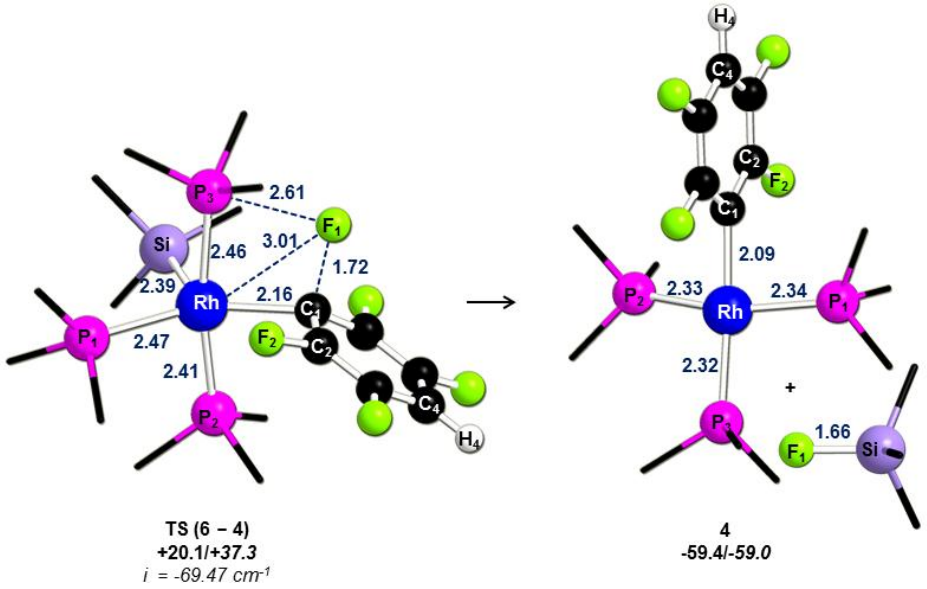

Figure 3.18: Computed geometries and energies for C–F activation to give 4 and $FSiMe_3$.

These three transition states exhibit similar geometries, suggesting that **TS (6 – 4)** also proceeds via a degree of phosphine-assistance. However, unlike **TS (2 – *fac*-3)** and **TS (2 – *mer*-3′)**, instead of having F transferred on the metal centre, IRC calculations show that F moves toward silicon to afford directly the fluorosilane elimination. These different outcomes can be understood by looking at the interactions between the metal centre and the 4-C_6F_4H moiety (see Figure 3.20).

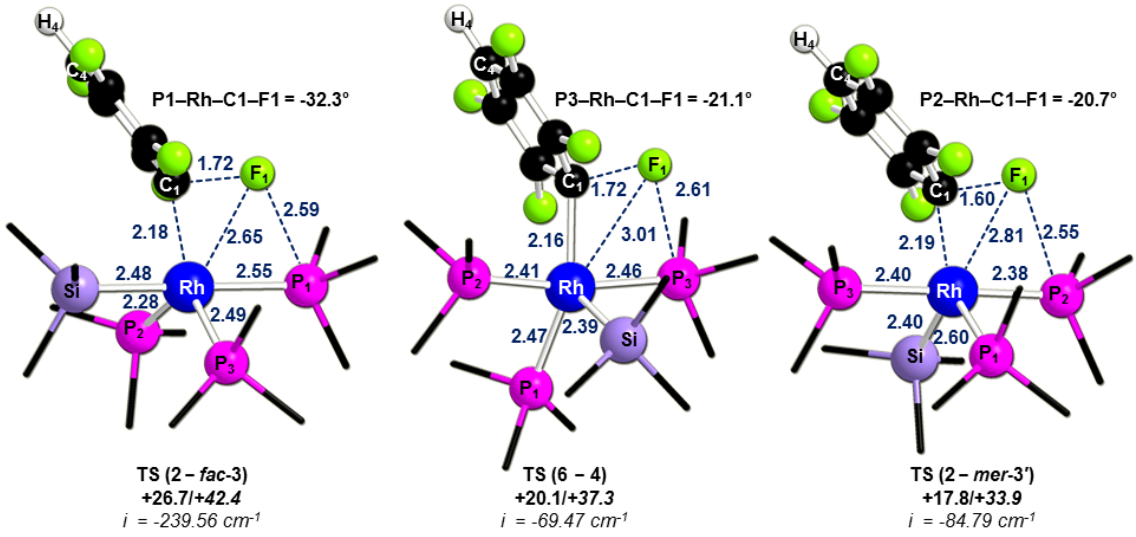

Figure 3.19: Computed geometries and energies for C–F activation via TS (2 – fac-3), TS (6 – 4) and TS (2 – mer-3′), respectively.

In all these cases, evidence is seen for interaction with the C2–F2 bond. However, these are weak in **TS (2 – *fac*-3)** and **TS (2 – *mer*-3′)** and so easily displaced, allowing F to move onto the metal centre. In contrast, a much stronger interaction is seen in **TS (6 – 4)** with short Rh···C2 and Rh···F2 contacts of 2.79 Å and 2.74 Å, respectively, while the C2–F2 distance lengthens to 1.41 Å. These block the vacant site at the metal and F therefore cannot be transferred onto Rh to form a 6-coordinate species. Instead F is moved onto silicon to yield **4** and $FSiMe_3$ directly.

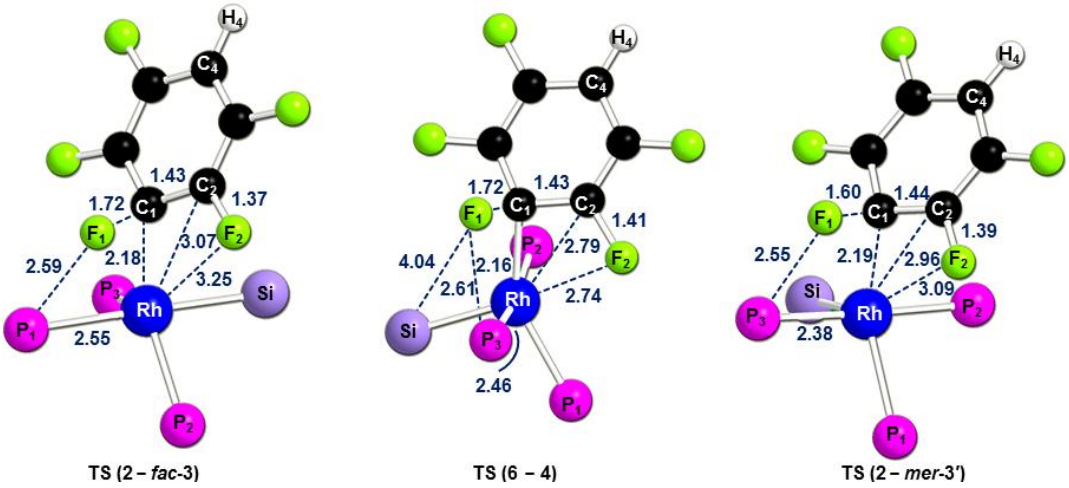

Figure 3.20: Computed geometries showing the interactions of the 4-C_6F_4H moiety with the rhodium metal centre in TS (2 – *fac*-3), TS (6 – 4) and TS (2′ – *mer*-3′).

3.3.1 Summary of Pathway 2

The lowest reaction profile along Pathway 2 is shown in Figure 3.21. Computed enthalpies show that the rate-limiting transition state is associated with **TS (6 – 4)** (H = +20.1 kcal/mol). The computed free energy of this transition state is +37.3 kcal/mol.

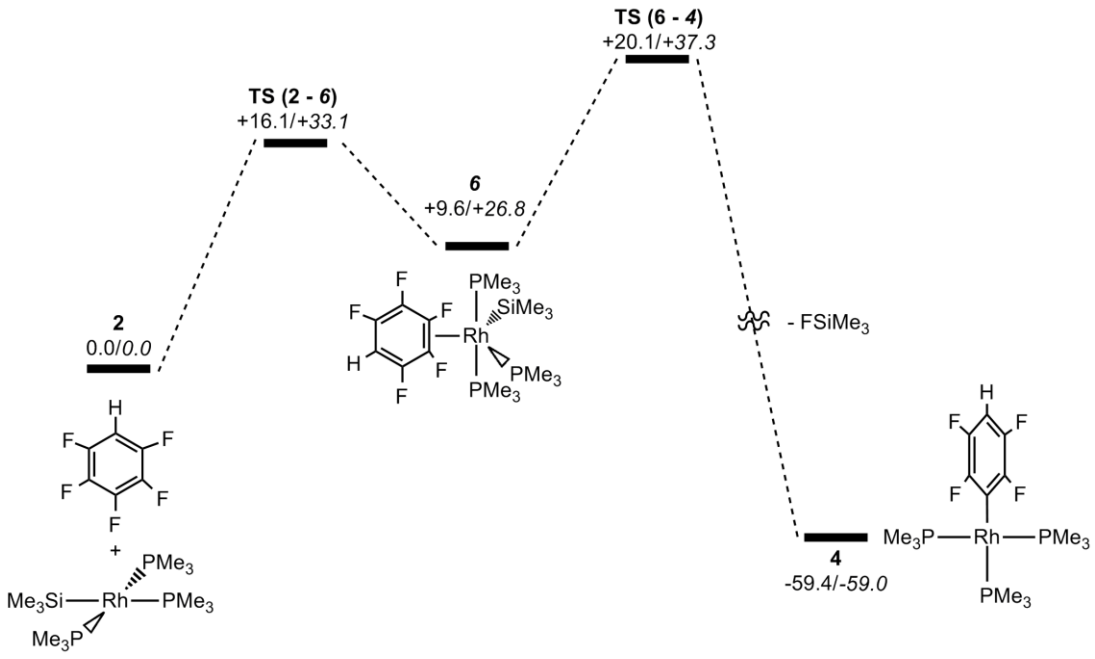

Figure 3.21: Reaction profile along Pathway 2 to form 4 and $FSiMe_3$.

As **TS (6 – 4)** differs from the anticipated 4-centred transition state, attempts were made to characterise a silyl-assisted mechanism and two other transition states have been computed as shown in Figure 3.22. Both are higher in energy than **TS (6 – 4)** and show different binding modes of the C_6F_5H ring. The lower transition state is $\mathbf{TS_{silyl\text{-}1}}$ (H = +26.0 kcal/mol) in which the breaking C1···F1 bond is rather long (1.81 Å) and the Si–Rh–C1–F1 angle equal to +10.6, consistent with the silyl-assisted nature of the process. Also, the Si···F1 distance of 2.13 Å shows that fluorine is moving toward silicon, consistent with a lengthening of the Rh···Si distance to 2.50 Å. IRC calculations confirm the formation of the Si–F1 bond. However, instead of $FSiMe_3$ formation, one methyl group from $SiMe_3$ is transferred onto the rhodium metal centre and PMe_3 trans to $SiMe_3$ dissociated.

An even higher energy process has been computed via $\mathbf{TS_{silyl\text{-}2}}$ (H = +31.7 kcal/mol). In the transition state, the P2–Rh–P3 bends back to 106.2° due to the η^2-binding mode of C_6F_5H (Rh–C1 = 2.01 Å, Rh–C2 = 2.10 Å). The key C1···F1 distance lengthens to 1.63 Å and the Si–Rh–C1–F1 angle equal to +15.5. In addition, the silyl ligand is completely dissociated from the rhodium metal centre (Rh···Si = 3.37 Å) and the Si···F1 distance is rather short (2.02 Å). IRC calculations showed that fluorine is transferred onto silicon to release $FSiMe_3$ and leads to a shallow intermediate in which the C2 is bound to Rh (Rh–C2 = 2.15 Å).

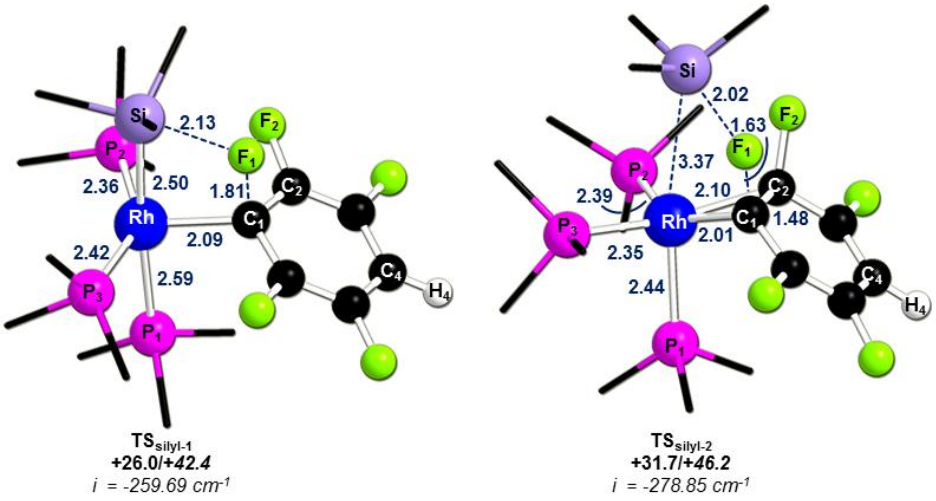

Figure 3.22: Computed transition states and energies for silyl-assisted C–F activation via a 4-centred transition state. Both derived from an isomer of 6 where in this case the $SiMe_3$ ligand is in an axial position.

3.3.2 Comparison of Pathway 1 and Pathway 2

The reaction profiles for the lowest energy processes along Pathway 1 and Pathway 2 are shown in Figure 3.23. The rate-limiting transition state along Pathway 1 is the C–F activation via **TS (2 – *mer*-3′)** (H = +17.8 kcal/mol). This step is lower than the silyl-assisted pathway via **TS (6 – 4)** by 2.3 kcal/mol. The computed free energies increase this difference to 3.4 kcal/mol in favour of **TS (2 – *mer*-3′)**. This suggests that C–F activation at the 4-coordinate rhodium(I) silyl complex $\mathbf{1_{SiMe3}}$ will involve the C–F activation with a degree of phosphine-assistance to give the exothermic intermediate ***mer*-3′** (H = -31.4 kcal/mol).

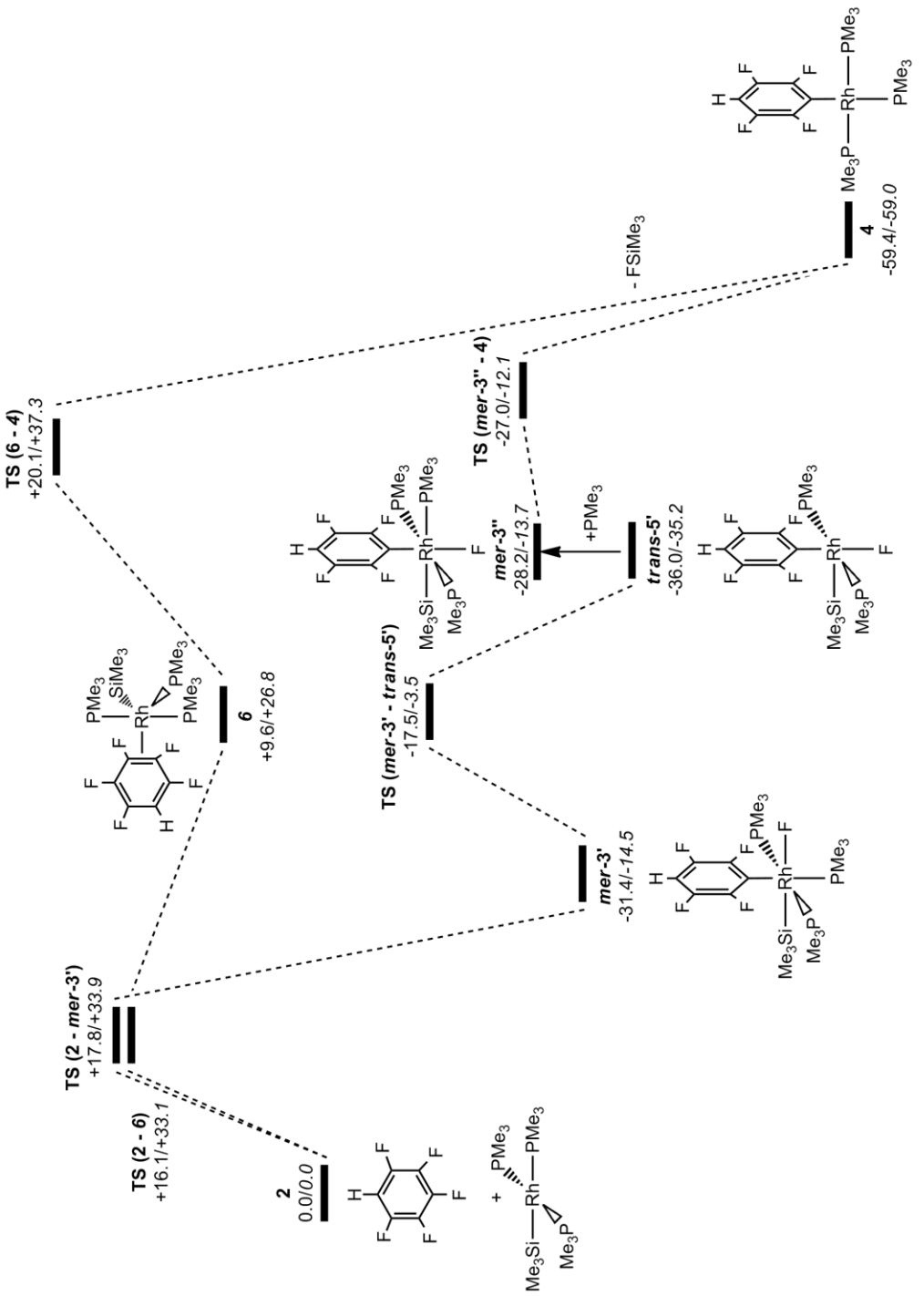

Figure 3.23: Formation of [Rh(4-C_6F_4H)(PMe_3)$_3$], 4, and $FSiMe_3$ along Pathways 1 and 2.

3.4 C–H Oxidative Addition and $HSiMe_3$ Formation via Reductive Elimination

*3.4.1 C–H Oxidative Addition to form **fac-8***

Experimentally, the reaction of C_6F_5H with $\mathbf{1_{SiMe3}}$ yields only C–F activation, however, C–H activation as a potential side reaction has also been considered.[15a] Calculations have been performed on the oxidative addition of C_6F_5H to form the three distinct isomers ***mer*-8**, ***mer*-8′** and ***fac*-8**. Reaction via the last of these was found to be the most accessible and so will be discussed here. The computed geometries and energies of the stationary points involved in this process are shown in Figure 3.24.

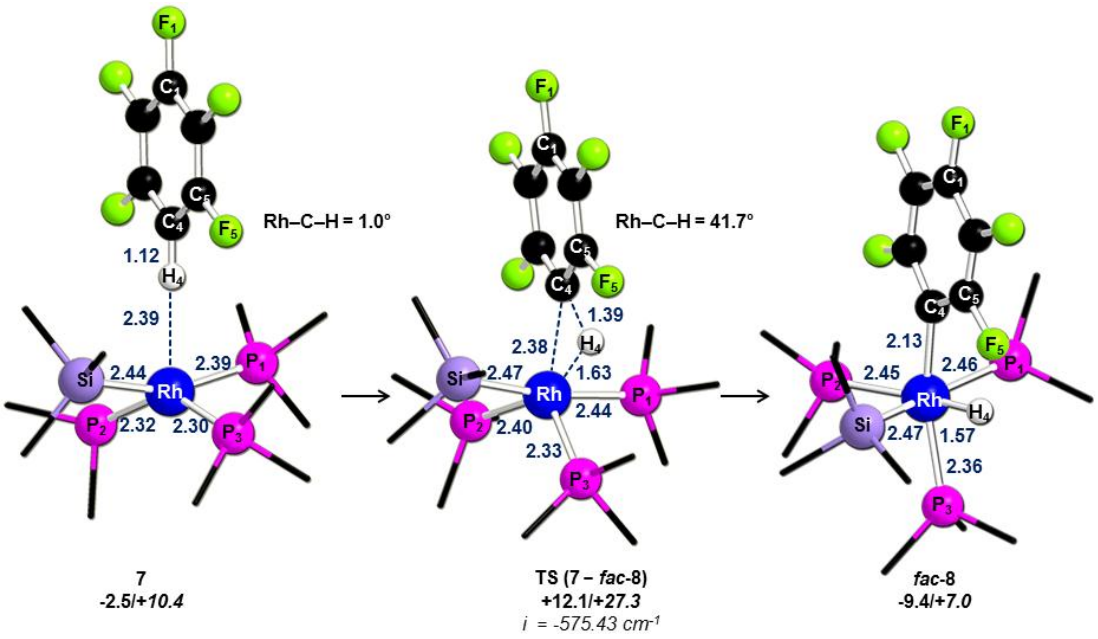

Figure 3.24: Computed geometries and energies for formation of *fac*-8.

Initially the approach of C_6F_5H toward the metal centre forms a loosely bound adduct **7** (H = -2.5 kcal/mol, G = +10.4 kcal/mol). Compound **7** exhibits an elongation of the C–H bond to 1.12 Å due to a weak Rh···H contact (2.39 Å). Formation of ***fac*-8** occurs via **TS (7 – 8)** in which the breaking C4···H4 bond lengthens to 1.39 Å and Rh···H4 interaction shortens to 1.63 Å. In addition, **TS (7 – 8)** has a late geometry in terms of the Rh···H4 contact with a distance of 1.63 Å (*cf.* 1.57 Å in ***fac*-8**). Also α is equal to +19.7° and confirms a near-coplanar arrangement in the transition state; however, the P2–Rh–C4–C5 dihedral angle of +151.4° is quite unusual. This suggests that C–H oxidative addition is not conventional and so natural atomic charges were computed in order to understand the nature of this process (see Figure 3.25).

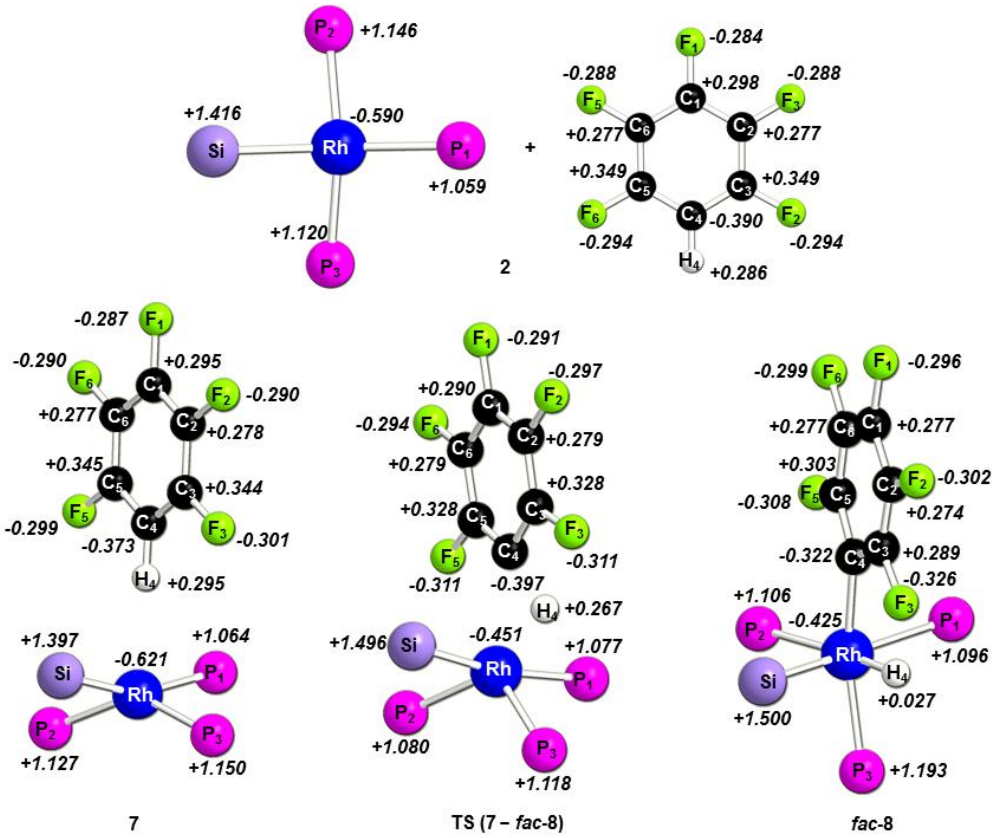

Figure 3.25: Selected computed natural atomic charges for the C–H activation to yield *fac*-8.

The computed natural atomic charges show that C4 becomes slightly less negative in **7** (-0.373 *cf.* -0.390 in free C_6F_5H) and H4 more positive (+0.295 *cf.* +0.286 in free C_6F_5H) while the C_6F_5H moiety becomes slightly more negative (total charge = -0.006 *cf.* +0.002 in free C_6F_5H). In addition, the rhodium metal bears a large negative charge (-0.621 *cf.* -0.590 in $\mathbf{1_{Me3}}$) and is more basic in the adduct **7**. In the transition state **TS (7 – 8)**, some charge redistribution from the metal centre to the C_6F_5H moiety is also computed. The Rh metal centre is less negative (-0.451 *cf.* -0.621 in **7**) as the C_6F_5H moiety becomes more negative (total charge = -0.130 *cf.* -0.06 in **7**). In addition, C4 (-0.397 *cf.* -0.373 in **7**) and H4 (+0.267 *cf.* +0.295 in **7**) become less positively charged. These features suggest that this C–H activation proceeds via an acid-base reaction where the rhodium complex deprotonates C_6F_5H.

*3.4.2 Si–H Reductive Elimination from **fac-8***

Computed geometries and energies for the Si–H reductive elimination from ***fac*-8** are shown in Figure 3.26. This process occurs through the transition state **TS (*fac*-8 – 9)** with an activation barrier of +15.0 kcal/mol (H = +5.6 kcal/mol). In the transition state,

the P1–Rh–P2 angle widens to 121.0° (*cf.* +101.7° in ***fac*-8**) and the process is almost coplanar (α = 14.6°). Also, the Rh···Si contact increases to 2.99 Å as the bond breaks while the Si···H shortens by 1.04 Å to 1.63 Å. **TS (*fac*-8 – 9)** links to the final product **9** and $HSiMe_3$. Overall, the process is slightly exothermic by -8.2 kcal/mol (ΔG = -7.7 kcal/mol).

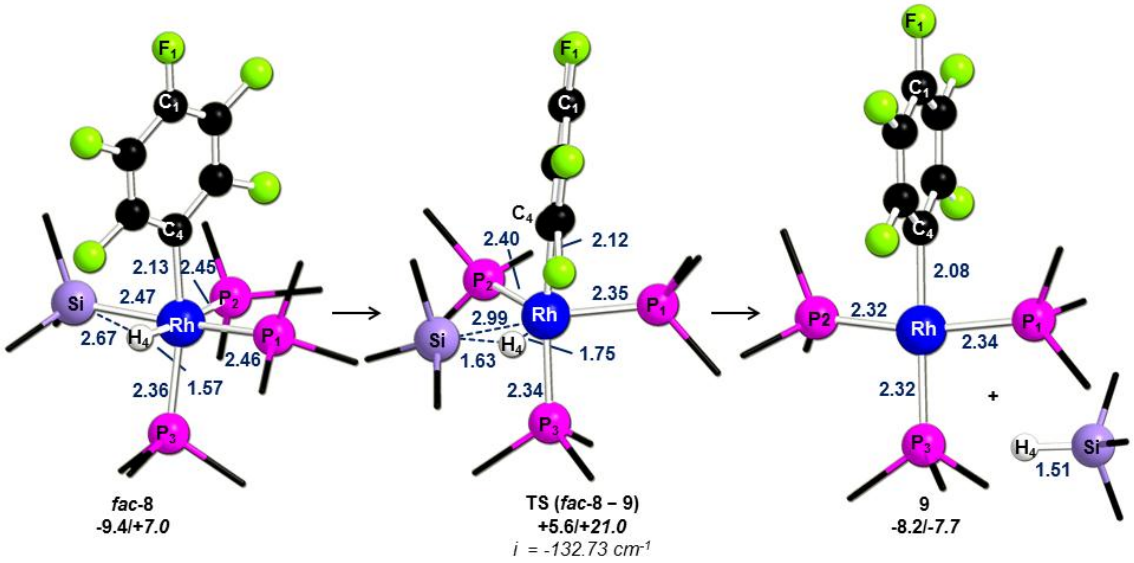

Figure 3.26: Computed geometries and energies for Si–H reductive elimination from *fac*-8.

Finally, the complete reaction profiles for C–F and C–H bond activation are compared in Figure 3.27. In both cases, the rate-limiting transition states for C–F and C–H activation correspond to the oxidative addition steps. C–H activation is kinetically preferred ($\Delta\Delta H^{\ddagger}$ = 5.7 kcal/mol, $\Delta\Delta G^{\ddagger}$ = 6.6 kcal/mol) however, C–F activation is thermodynamically more favourable (ΔΔH = 51.2 kcal/mol, ΔΔG = 51.3 kcal/mol). Experimentally, only C–F activation is observed, and so this implies that C–H activation may occur, but is reversible. An alternative interpretation is that C–F activation proceeds via a different pathway that is kinetically more favourable. It was therefore decided to study the C–F activation at $\mathbf{1_{SiMe3}}$ after an initial phosphine dissociation.

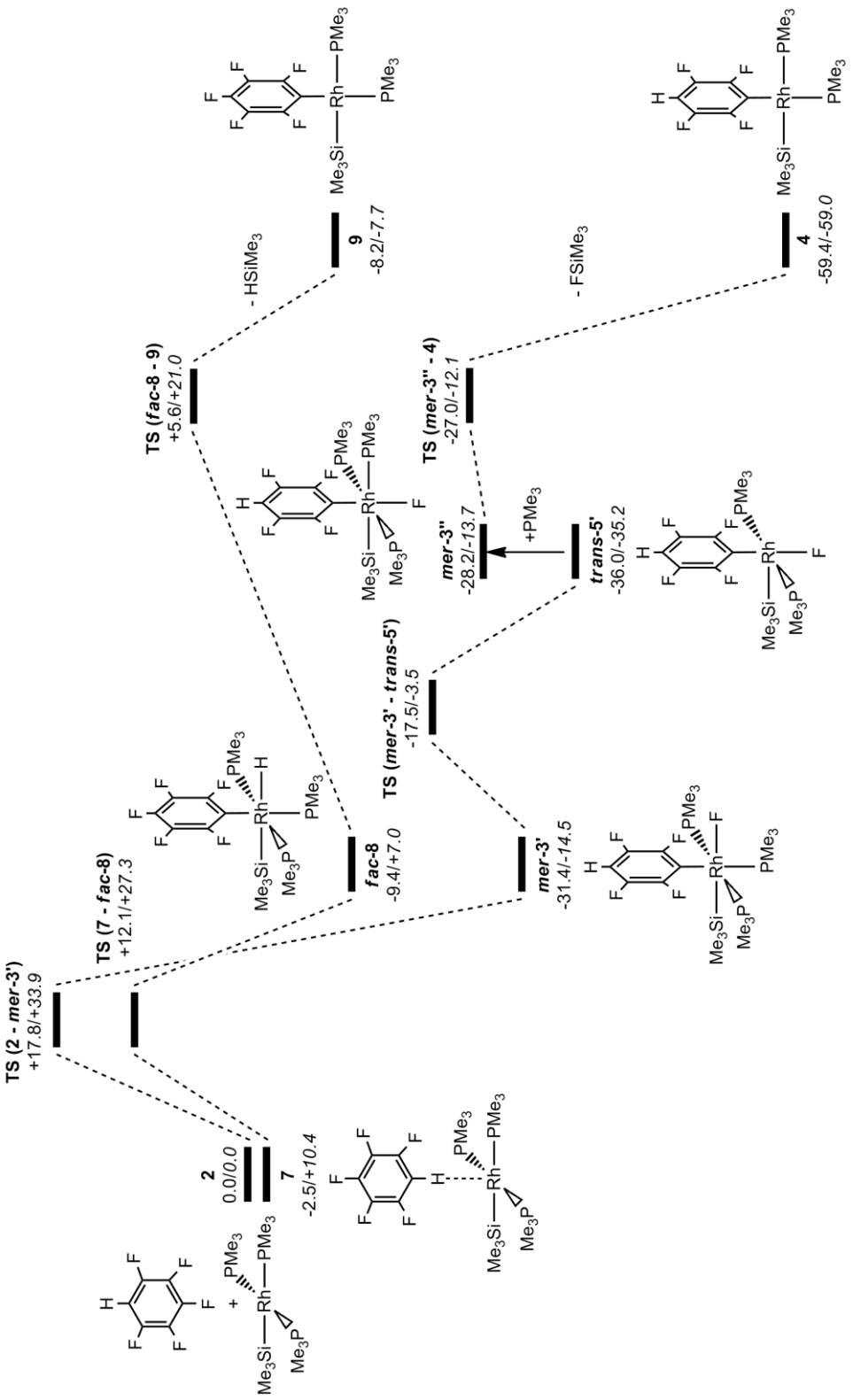

Figure 3.27: Complete reaction profiles for C–F and C–H bond activation.

3.5 Phosphine Substitution Followed by C–F activation of C_6F_5H at *trans*-[Rh(SiMe$_3$)(PMe$_3$)$_2$] (*trans*-**1**$_{SiMe3}$)

3.5.1 Phosphine Dissociation

As discussed previously, species **1**$_{SiMe3}$ showed an elongation of the Rh–P1 bond trans to $SiMe_3$ by 0.06 Å compared to the Rh–P2 and Rh–P3 distances. This elongation facilitates phosphine dissociation and a transition state for this step has been located as shown in Figure 3.28. As expected, **TS (1 – *trans*-1)**$_{SiMe3}$ shows an increase of the Rh···P1 distance to 3.97 Å and the Rh–Si bond shortens to 2.31 Å, as a vacant site is created trans to $SiMe_3$. The activation barrier for this step is +17.0 kcal/mol but computing the free energy decreases this barrier to +13.2 kcal/mol. The enthalpy of 3-coordinate *trans*-[Rh(SiMe$_3$)(PMe$_3$)$_2$] (***trans*-1**$_{SiMe3}$) is found to be +16.6 kcal/mol higher than the separated reactant but the free energy is only +2.3 kcal/mol. Phosphine dissociation cis to $SiMe_3$ was also computed and it was found that the 3-coordinate ***cis*-1**$_{SiMe3}$ has a computed enthalpy of +21.8 kcal/mol (G = +7.7 kcal/mol).

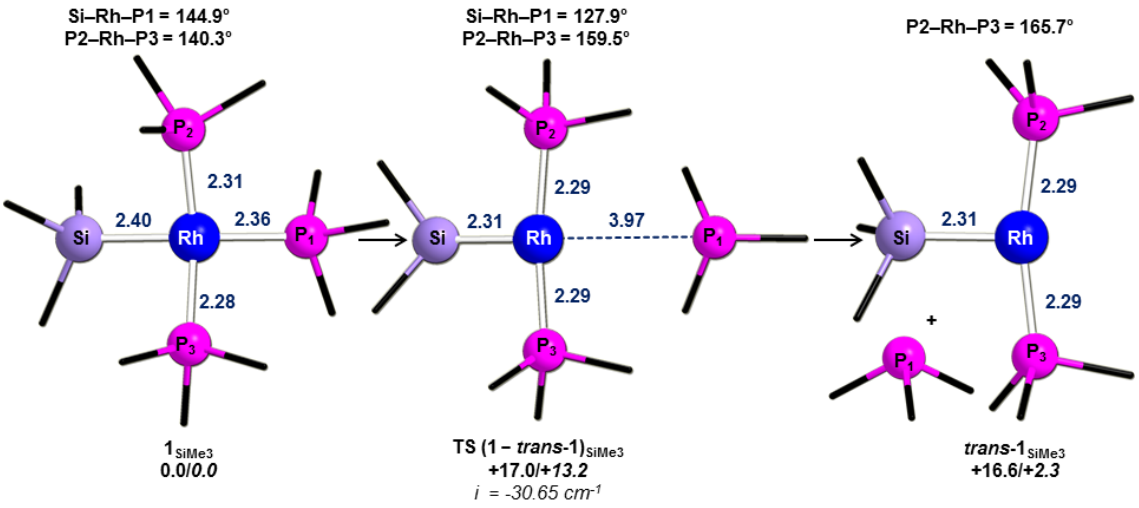

Figure 3.28: Computed geometries and energies for phosphine dissociation to form *trans*-1$_{SiMe3}$.

After formation of ***trans*-1**$_{SiMe3}$, two pathways, analogous to Pathways 1 and 2, have been considered (see Figure 3.29). Pathway 3, is the C–F oxidative addition of C_6F_5H at ***trans*-1**$_{SiMe3}$, to yield a 16-electron rhodium(III) silyl complex (e.g. ***trans*-5′**) followed by Si–F reductive elimination. Pathway 4 is a silyl-assisted C–F bond activation at ***trans*-1**$_{SiMe3}$ where the Rh-C_{aryl} bond is formed with the direct transfer of fluorine onto silicon.

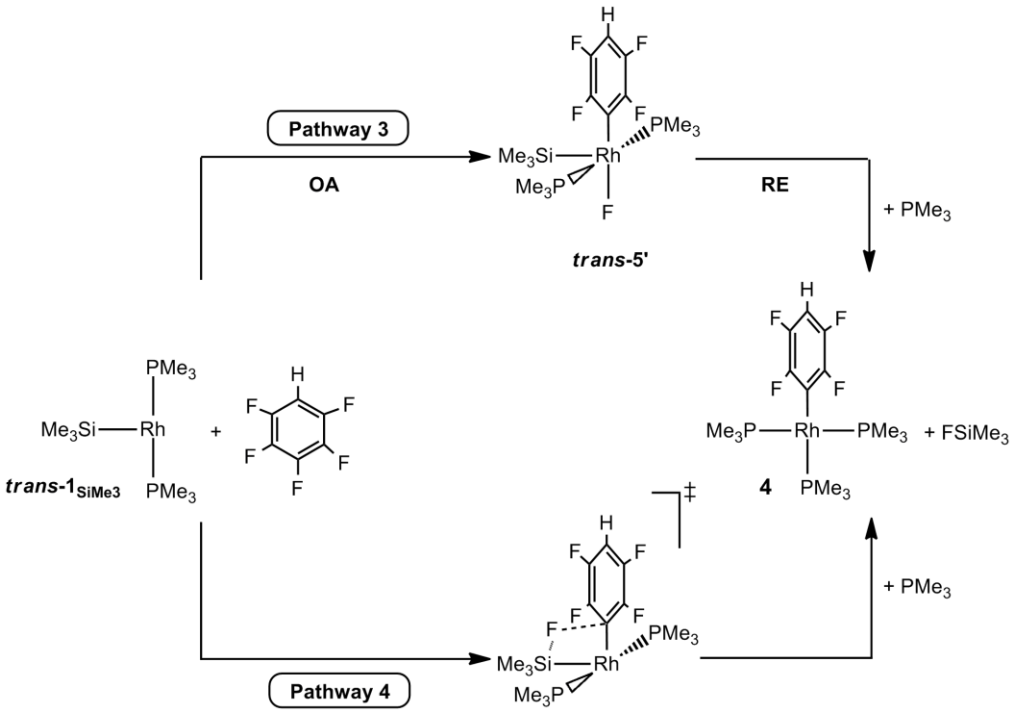

Figure 3.29: Possible reaction mechanisms for C–F activation of C_6F_5H at *trans*-$\mathbf{1_{SiMe3}}$.

3.5.2 Pathway 3: C–F Oxidative Addition of C_6F_5H at ***trans-1$_{SiMe3}$***

The first step along Pathway 3 is the approach of C_6F_5H toward the metal centre and this was found to form either an η^2-intermediate (**6b′**) or a η^1-complex (**6d′**), as shown in Figure 3.30. The higher energy process goes through **TS (6a′ – 6b′)** (H = +12.9 kcal/mol) in which the C_6F_5H ring lies roughly parallel to the metal coordination plane and the P2–Rh–P3 angle slightly bends back to 147.6° (*cf.* 154.1° in **6a′**). In the transition state, the Rh···C2 contact decreases to 3.00 Å and the Rh···C1 interaction shortens to 3.33 Å.

The lower energy pathway occurs via **TS (6c′ – 6d′)** (H = +10.8 kcal/mol) to form **6d′** where the P2–Rh–P3 angle is barely perturbed (149.3° *cf.* 152.1° in **6c′**). In **TS (6c′ – 6d′)**, the Rh···C1 distance decreases to 2.94 Å while the Rh···C2 contact remains rather long at 3.44 Å.

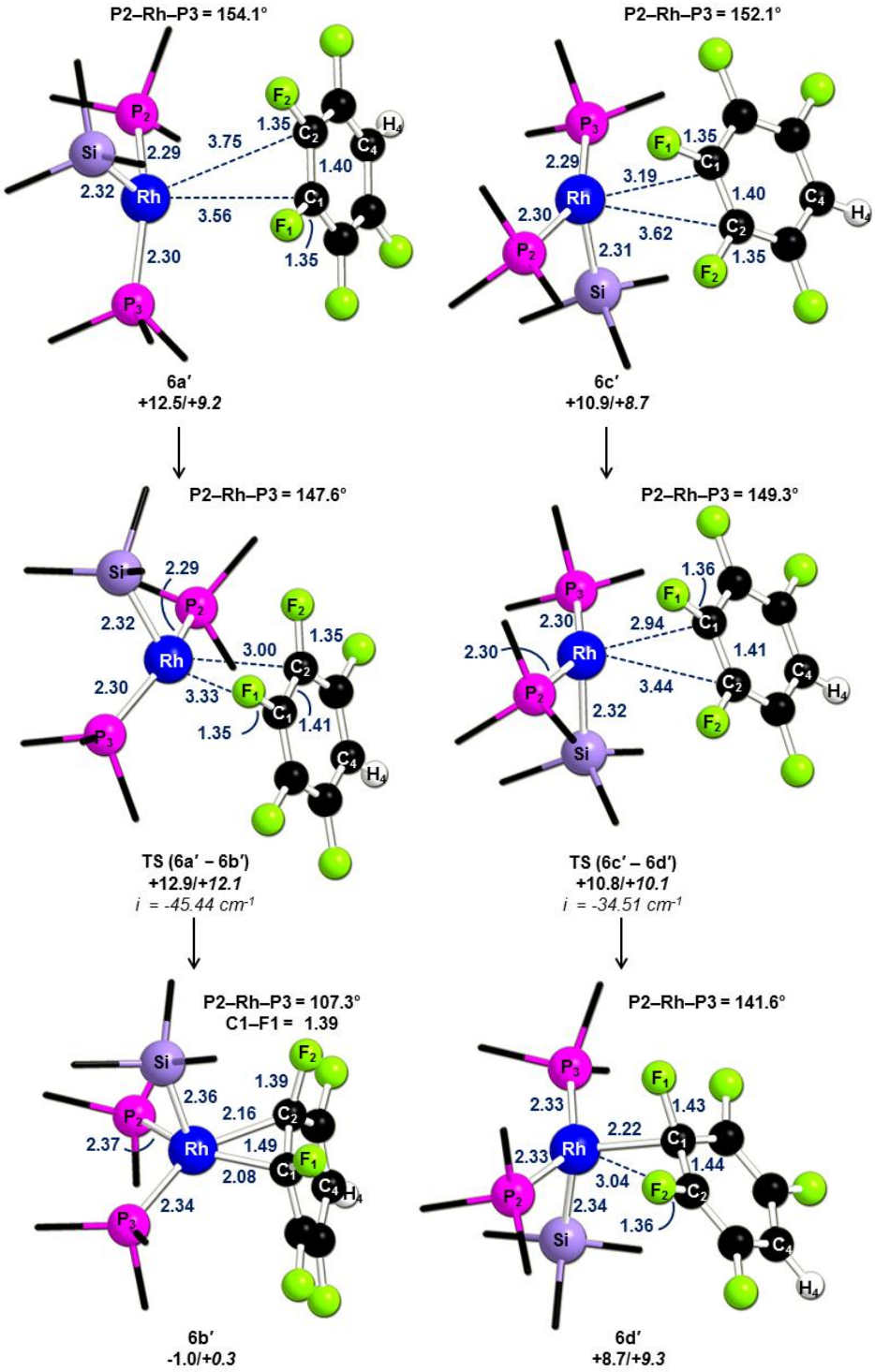

Figure 3.30: Computed geometries and energies for formation of 6b′ and 6d′.

Species **6b′** (H = -1.0 kcal/mol) adopts an unexpected trigonal bipyramid geometry with a vacant axial site trans to $SiMe_3$. The unusual structure of **6b′** is due to the π-back donation of the Rh metal centre to the C_6F_5H ring as shown in Figure 3.31. The high *trans*-influence of $SiMe_3$ can also be important in stabilising this intermediate. A similar intermediate to **6b′** has been reported by Grushin, Macgregor and co-workers where

$[M(CF_3)(PR_3)_3]$ (M = Rh, Ir; R = H, Ph) adopted a trigonal bipyramid geometry with a vacant axial site trans to CF_3.[81]

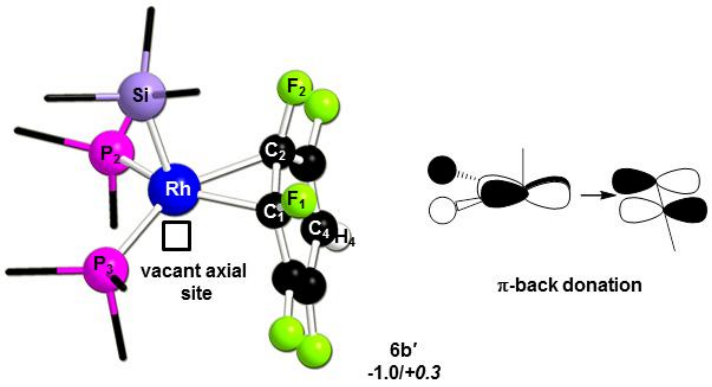

Figure 3.31: π-back donation from the Rh metal centre to C_6F_5H.

In the second species **6d′** (H = +8.7 kcal/mol), the P2–Rh–P3 angle narrows to 141.6° and the fluoroaromatic ring is bound in an η^1-fashion (Rh–C1 = 2.22 Å). An interaction between Rh and F1 is also computed (Rh···F1 = 2.58 Å), as well as an elongation of the key C1–F1 bond to 1.43 Å.

After formation of **6b′** and **6d′**, C–F oxidative addition occurs to give either ***cis*-5′** or ***trans*-5′**, as shown in Figure 3.32. From **6b′** the rhodium metal centre migrates away from the aromatic π system along the C1–F1 bond, leading to the C–F oxidative addition transition state **TS (6b′ – *cis*-5′)** (H = +19.5 kcal/mol). In addition, the key C1···F1 bond distance lengthens to 1.52 Å. **TS (6b′ – *cis*-5′)** links to ***cis*-5′** (H = -30.9 kcal/mol).

The lower lying C–F oxidative addition step along Pathway 3 proceeds via **TS (6d′ – *trans*-5′)** (H = +10.9 kcal/mol) in which the C1···F1 bond increases to 1.69 Å and the Rh···F1 distance shortens to 2.34 Å. **TS (6d′ – *trans*-5′)** links, after an isomerisation process to ***trans*-5′** (H = -36.0 kcal/mol) in which F is trans to 4-C_6F_4H and $SiMe_3$ trans to a vacant site.

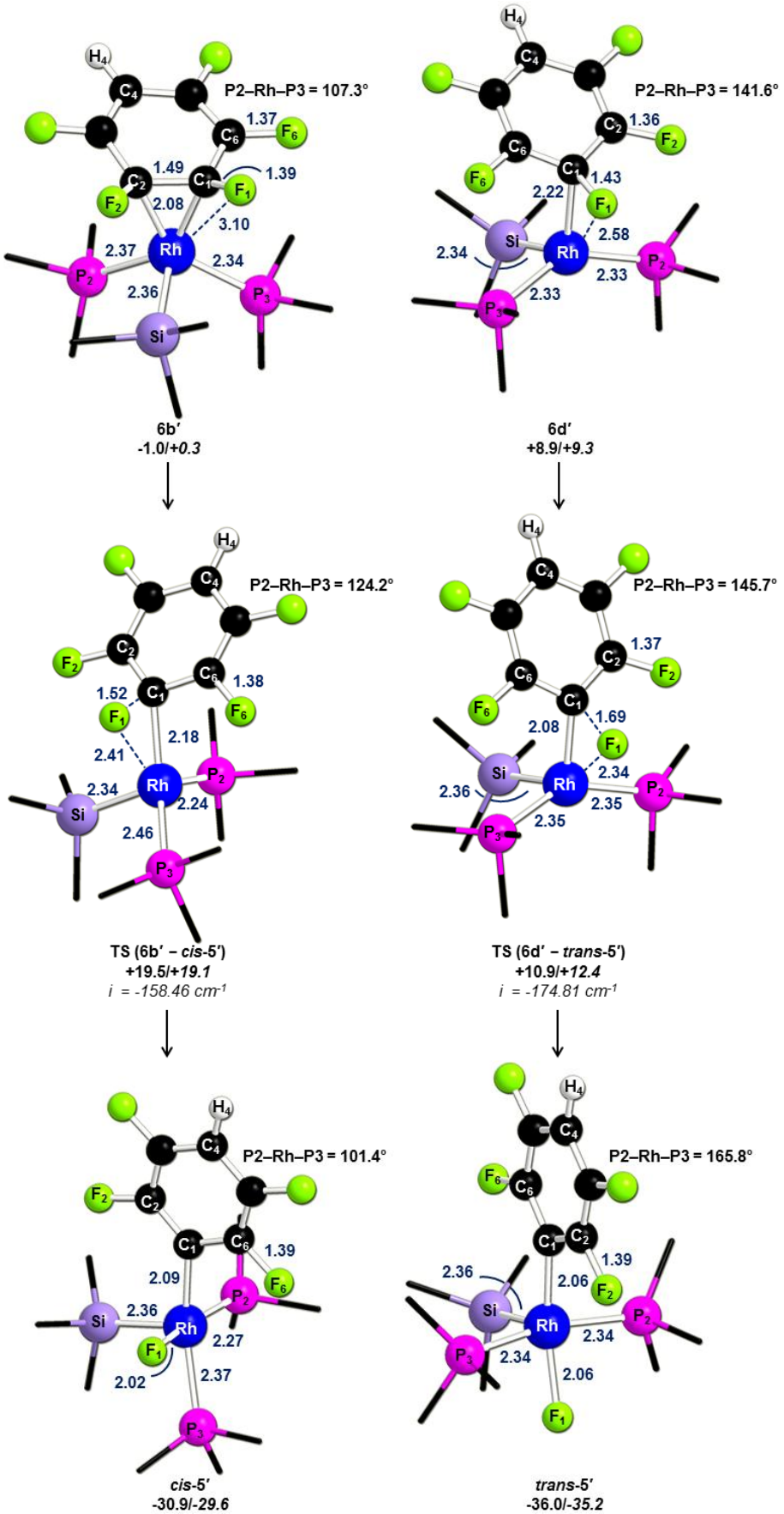

Figure 3.32: Computed geometries and energies for C–F oxidative addition to form *cis*-5′ and *trans*-5′.

3.5.3 Pathway 3: Si–F Reductive Elimination

After formation of the two isomers ***cis*-5′** and ***trans*-5′**, Si–F reductive elimination is required to give, after phosphine association, [Rh(4-C_6F_4H)(PMe_3)$_3$], **4**, and $FSiMe_3$. The computed geometries and energies for this process from ***cis*-5′** and ***trans*-5′** are shown in Figure 3.33.

The less accessible reductive elimination pathway proceeds from ***cis*-5′** via **TS (*cis*-5′ – *cis*-5″)** and is associated with a computed energy of -25.7 kcal/mol. In the transition state, the Si–Rh–P2 angle increases to 114.1° (*cf.* 93.1° in ***cis*-5′)** and the Si···F1 contact significantly decreases to 2.19 Å. In contrast, both the Rh···Si and Rh···F1 bonds are almost unchanged.

Reductive elimination at 5-coordinate ***trans*-5′** occurs via **TS (*trans*-5′ – *trans*-5″)** (H = -28.4 kcal/mol). In the transition state, as seen in **TS (*cis*-5′ – *cis*-5″)**, the Si–Rh–C1 angle widens to 118.6° (*cf.* 101.7° in ***trans*-5′**) and the major changes is the shortening of the Si···F distance to 2.20 Å.

Species ***cis*-5″** and ***trans*-5″** retain an interaction with the fluorosilane group (Rh–F1 = 2.35 Å in ***cis*-5″**, Rh–F1 = 2.39 Å in ***trans*-5″**). This is due to some electron transfer from one lone pair from F to Rh. The final product **4** can be formed by displacing $FSiMe_3$ by the dissociated phosphine ligand. A transition state has been located, **TS (*trans*-5″ – 4)**, for the lowest energy profile from ***trans*-5″** with a computed energy of -36.4 and a barrier of 1.3 kcal/mol (see Figure 3.34). Computed free energies increases the energy of **TS (*trans*-5″ – 4)** to -28.4 kcal/mol and the barrier to 10.6 kcal/mol, however, the process remains facile.

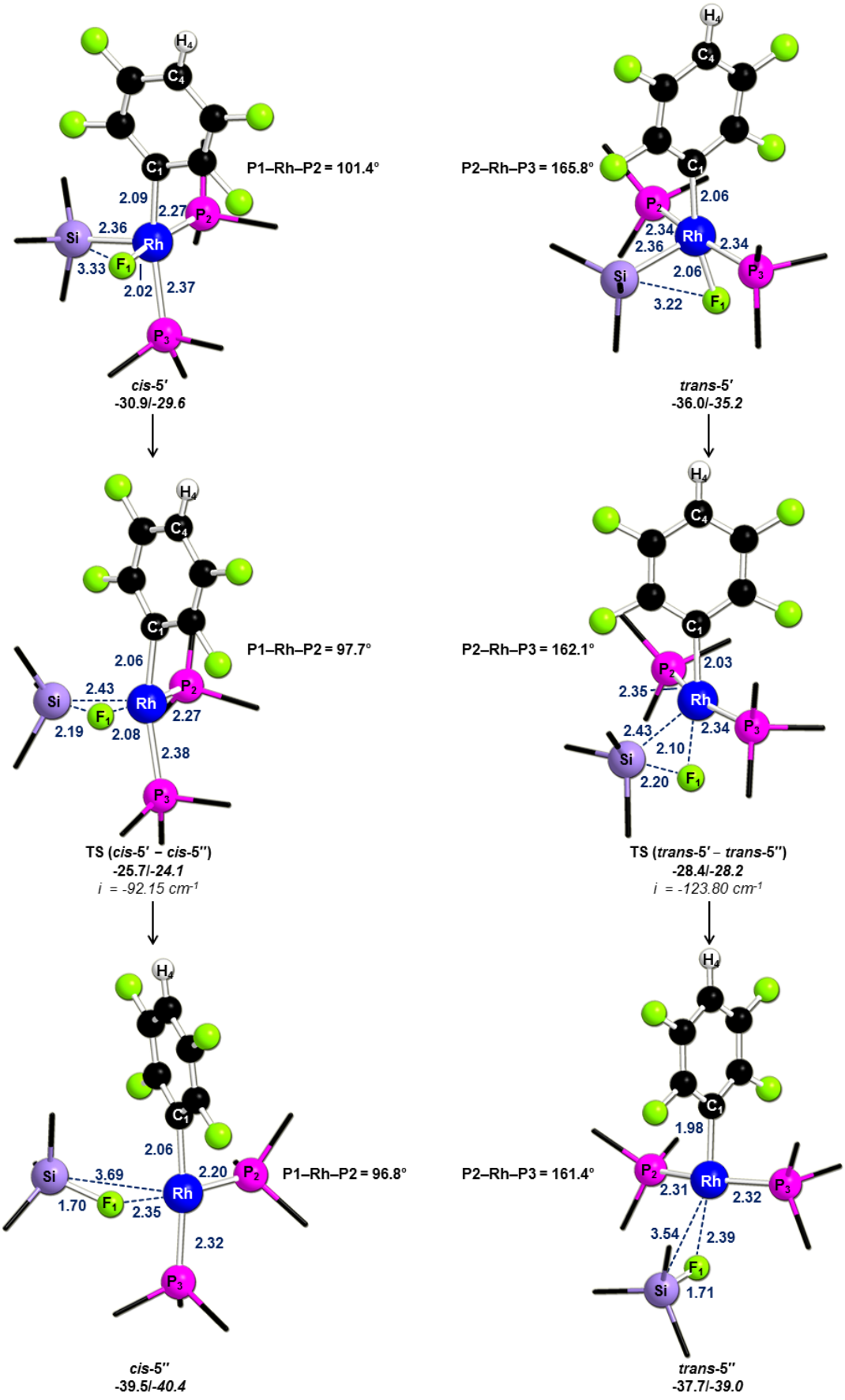

Figure 3.33 Computed geometries and energies for Si–F reductive elimination from *cis*-5′ and *trans*-5′.

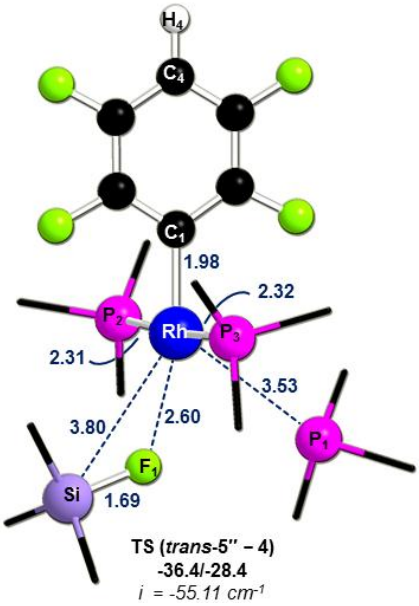

Figure 3.34: Computed transition state and energies for formation of 4 and FSiMe3 from *trans*-5″.

In **TS (*trans*-5″ – 4)**, the Rh···F1 distance increases to 2.60 Å and Si–F1 bond is almost formed (1.69 Å *cf.* 1.66 in free $FSiMe_3$). The PMe_3 ligand approaches the metal centre (Rh···P1 = 3.53 Å) to give **4** and $FSiMe_3$.

The reaction profile for the lowest energy process along Pathway 3 is shown in Figure 3.35. The first step is the phosphine dissociation with a computed barrier of +17.0 kcal/mol. From ***trans*-1′$_{Me3}$**, formation of the η^1-species **6d′** occurs via **TS (6c′ – 6d′)** (H = +10.8 kcal/mol). Once **6d′** is formed, C–F activation process occurs through the 3-centred transition state **TS (6d′ – *trans*-5′)** (H = +10.9 kcal/mol) to form ***trans*-5′**. Si–F reductive elimination proceeds directly from this species and is found to be facile (**TS (*trans*-5′ – *trans*-5″)**, H = -28.4 kcal/mol). The rate limiting-transition state along Pathway 3 is the phosphine dissociation, however, computed free energies show that phosphine dissociation and C–F oxidative addition are competitive with computed free energies of respectively +13.2 kcal/mol and +12.4 kcal/mol.

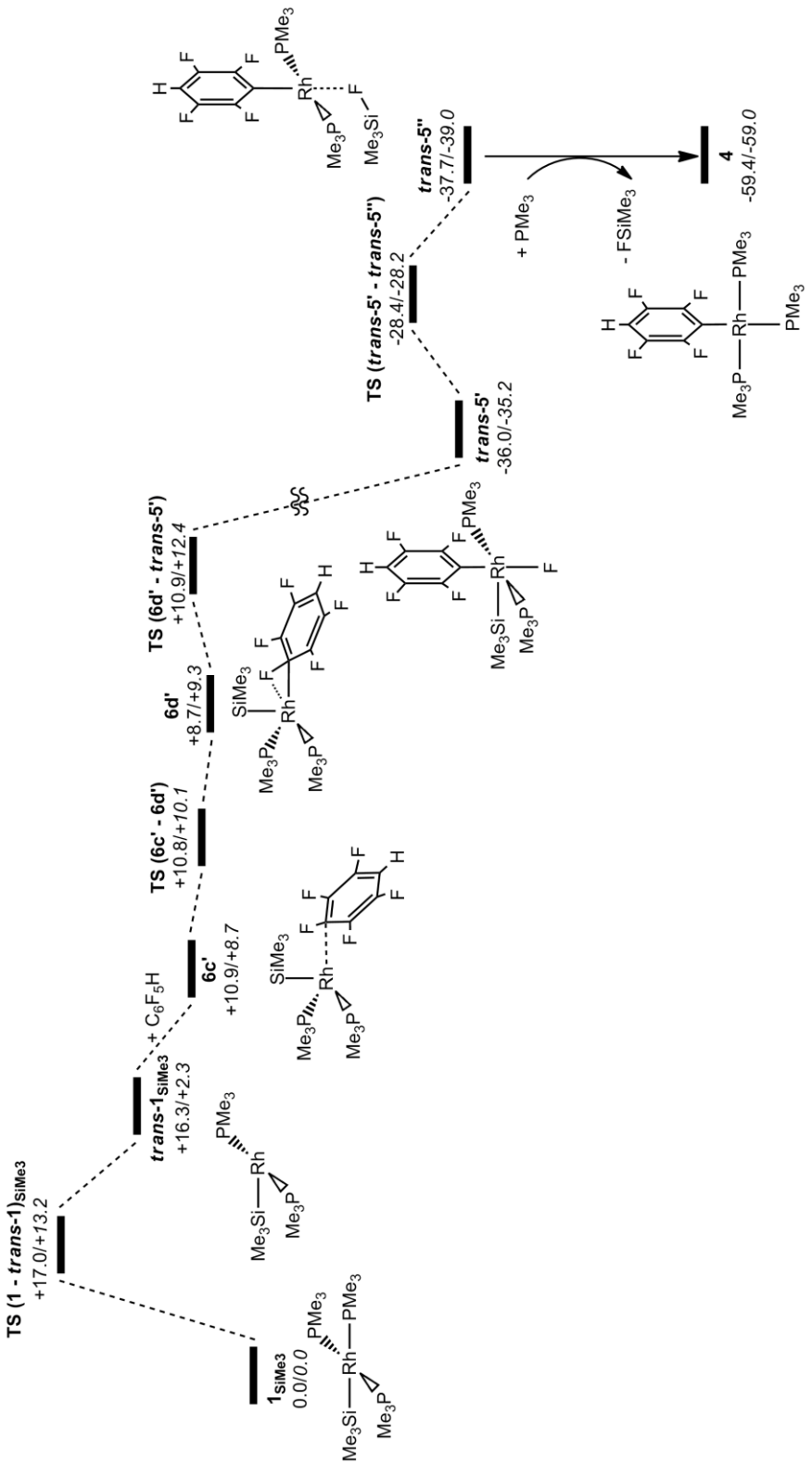

Figure 3.35: Formation of [Rh(4-C_6F_5)(PMe_3)$_3$], 4, and $FSiMe_3$ via C–F activation at $\mathbf{1_{SiMe3}}$.

3.5.4 Pathway 4: Silyl-Assisted C–F activation at ***trans-1***$_{SiMe3}$

Pathway 4 starts with the formation of **6b′**, previously described in Section 3.5.2, and two distinct transition states have been located for the silyl-assisted process (Figure 3.36).

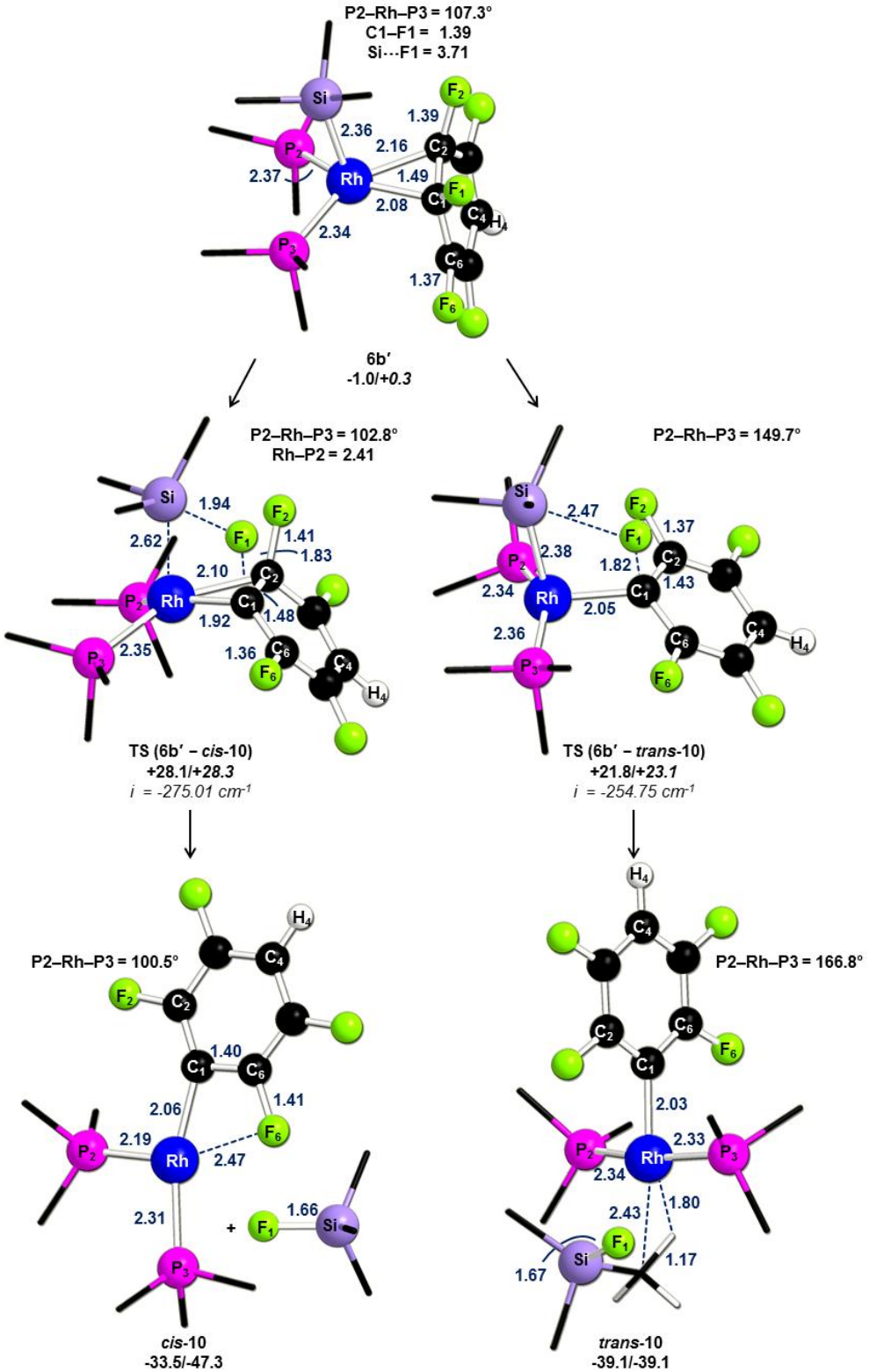

Figure 3.36: Computed geometries and energies for silyl-assisted C–F activation from 6b′.

The first transition state **TS (6b′ – *cis*-10)** is the higher energy process with a computed transition state at +28.1 kcal/mol (G = +28.3 kcal/mol). In **TS (6b′ – *cis*-10)**, the aromatic π system remains bound to the metal centre with computed short Rh–C1 and Rh–C2 distances of 2.10 Å and 1.92 Å, respectively. The breaking C1···F1 distance lengthens to 1.83 Å and the Si–Rh–C1–F1 angle is +3.5° while the Si···F1 interaction decreases to 1.94 Å, consistent with a 4-centred transition state.

From **6b′**, a second transition state has been located **TS (6b′ – *trans*-10)** (H = +21.8 kcal/mol) in which the rhodium metal centre migrates away from the aromatic π system along C1–F1 leading to the widening of the P2–Rh–P3 angle to 149.7°. In the transition state, the C1···F1 distance increases to 1.82 Å and the Si···F1 distance decreases to 2.47 Å (Si–Rh–C1–F1 = +19.2). **TS (6b′ – *trans*-10)** has an early geometry compared to **TS (6b′ – *cis*-10)** in terms of the Rh–Si and Si···F1 distances, being 2.38 Å and 2.47 Å, respectively (**TS (6b′ – *cis*-10)**, Rh···Si = 2.62 Å, Si···F1 = 1.94 Å). This last feature may explain the stabilisation of the former.

The transition state **TS (6b′ – *cis*-10)** leads to the formation of ***cis*-10** in which the fluorosilane group is fully dissociated, however, a relatively strong interaction between the rhodium metal centre and one *ortho* fluorine of the aryl ligand is computed (Rh···F6 = 2.47 Å). This contact explains the distortion of the P3–Rh–C1 angle to 161.4° and the elongation of the C6–F6 bond to 1.41 Å (Rh···C6 = 2.69 Å).

A related feature can be seen for ***trans*-10** where one methyl group from $SiMe_3$ is interacting with the metal centre. The C–H bond lengthens to 1.17 Å while the Rh···C and Rh···H distances are 2.43 Å and 1.80 Å, respectively. The fluorosilane group can be fully dissociated by the incoming phosphine ligand to give **4** and $FSiMe_3$. This step is computed to be facile and involves a transition state similar to that in Figure 3.34.

The reaction profile for the lowest energy process along Pathway 4 is shown in Figure 3.37. The rate limiting-transition state is the silyl-assisted C–F activation through **TS (6b′ – *trans*-10)** with a computed enthalpy of 21.8 kcal/mol (G = +23.4 kcal/mol). In addition, this transition state is found to be higher than C–F oxidative addition along pathway 3 through **TS (6d′ – *trans*-5′)** (H = +10.9 kcal/mol, G = +12.4 kcal/mol) to

form ***trans*-5′**, and so this indicates that C–F activation at ***trans*-$\mathbf{1_{SiMe3}}$** would goes via an oxidative addition pathway rather than a silyl-assisted mechanism.

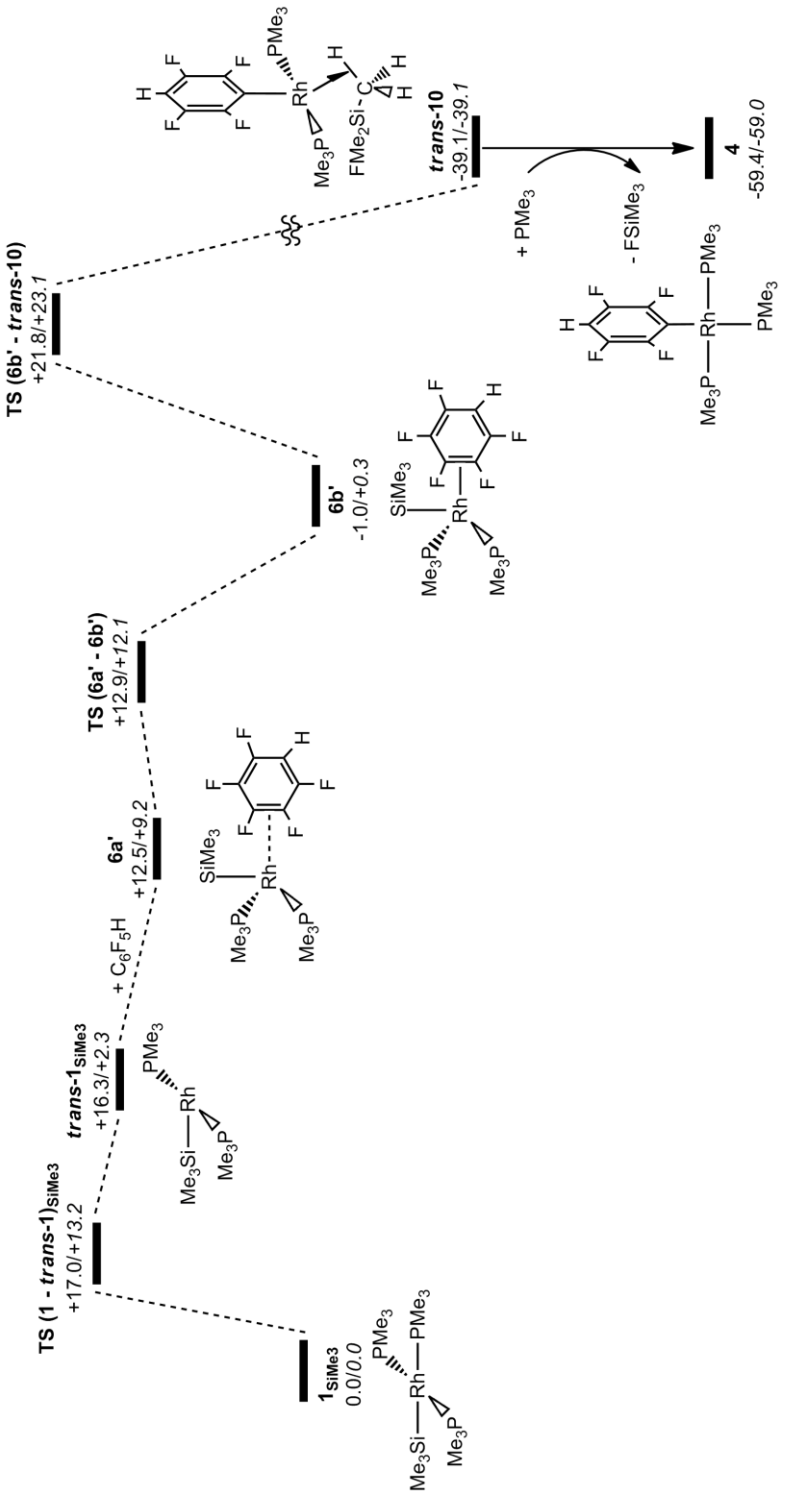

Figure 3.37: Reaction profile for C–F activation at $\mathbf{1_{SiMe3}}$ along Pathway 4.

3.6 C–H Oxidative Addition at *trans*-$\mathbf{1_{SiMe3}}$ and $HSiMe_3$ Formation via Reductive Elimination

3.6.1 C–H Oxidative Addition at ***trans-1$_{SiMe3}$*** *to form* ***cis-12***

The C–H activation of C_6F_5H at ***trans*-1$_{SiMe3}$** has also been considered to form either ***cis*-12** or ***trans*-12**. Reaction via the former was found to be more accessible and so will be discussed here. The computed geometries and energies of the stationary points involved in this process are shown in Figures 3.38 and 3.39.

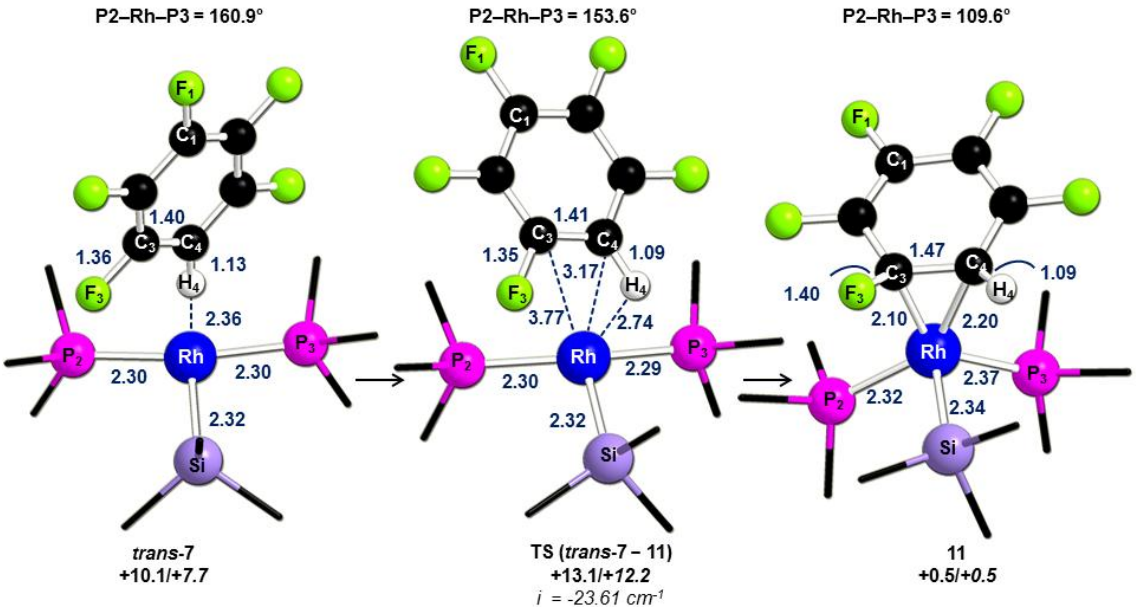

Figure 3.38: Computed geometries and energies for formation 11.

C–H activation proceeds via initial formation of a η^2-coordinated arene complex **11**, as shown in Figure 3.38. The approach of C_6F_5H results in adduct ***trans*-7** (H = +10.1 kcal/mol) in which the C4–H4 bond elongates to 1.13 Å (*cf.* 1.09 Å in free C_6F_5H) due to a weak Rh···H4 contact (2.36 Å). From ***trans*-7**, a transition state has been located, **TS (*trans*-7 – 11)** (H = +13.1 kcal/mol), in which the P2–Rh–P3 angles decreases to 153.6° to bind C_6F_5H in a η^2-fashion via π-back donation and the C3=C4 bond lengthens to 1.41 Å. **TS (*trans*-7 – 11)** links to species **11** in which the C3=C4 bond increases to 1.47 Å and the C3–F3 distance lengthens to 1.40 Å. It should be noted that **11** is slightly higher in energy than **6b′** (H = -1.0 kcal/mol, G = +0.3 kcal/mol) in which the fluoroarene coordinates to the metal complex via a CF=CF bond.[13j]

After formation of the η^2-complex **11**, C–H occurs via **TS (11 – *cis*-12)** to form ***cis*-12** as shown in Figure 3.39. In the transition state, the breaking C4···H4 bond elongates to 1.30 Å while the Rh···H4 contact decreases to 1.73 Å. The intermediate ***cis*-12** is calculated to be slightly exothermic relative to the η^2-adduct (ΔH = -2.1 kcal/mol, ΔG = -1.2 kcal/mol).

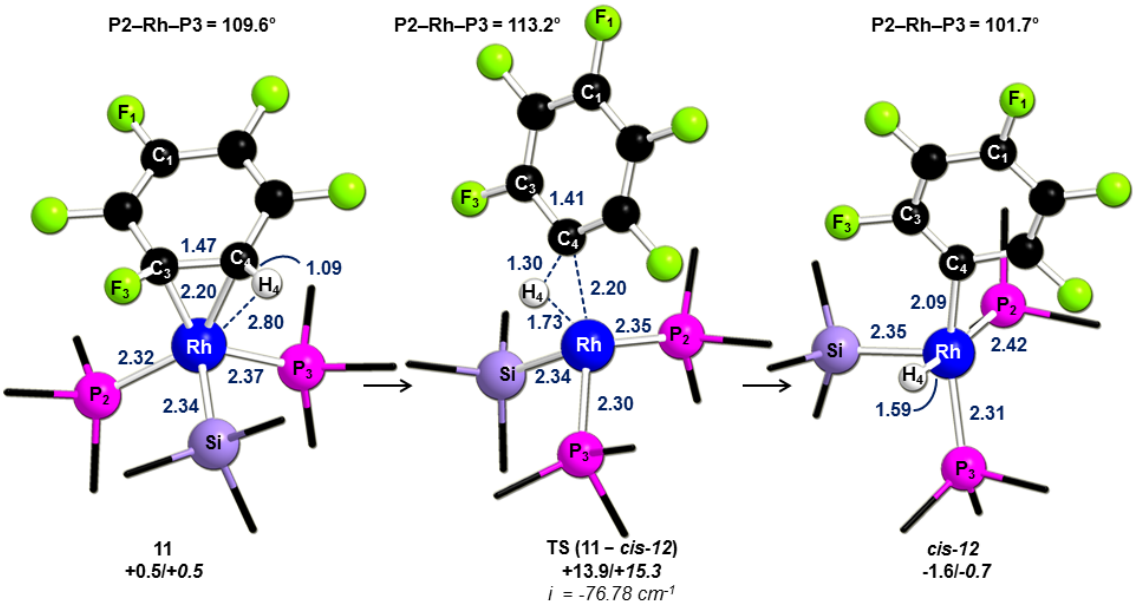

Figure 3.39: Computed geometries and energies for C–H oxidative addition to give *cis*-12.

*3.6.2 Reductive Elimination from **cis-12***

The Si–H reductive elimination from ***cis*-12** has also been considered in the present study. However, despite many attempts no transition state at the 5-coordinate ***cis*-12** has been located. Moreover, by computing the 14-electron complex *cis*-[Rh(C_6F_5)(PMe_3)$_2$] and $HSiMe_3$, calculations have showed that these species are +22.7 kcal/mol higher in energy than ***cis*-12** (ΔG = +7.4 kcal/mol). Therefore, this represents a lower limit to the barrier of this process.

Finally, the reaction profiles for C–F activation (in black) and C–H activation (in blue) at $\mathbf{1}_{\mathbf{SiMe3}}$ via initial phosphine dissociation are compared in Figure 3.40. Computed enthalpies show that the rate-limiting transition states correspond to the phosphine dissociation step ($\Delta H^{\ddagger}$ = +17.0 kcal/mol). However, calculations show that C–F activation is kinetically and thermodynamically more favourable than C–H activation ($\Delta\Delta H^{\ddagger}$ = 3.0 kcal/mol, $\Delta\Delta H$ = 51.2 kcal/mol). It should be also mentioned that the

lower limit computed for Si–H reductive elimination has an energy of +21.1 kcal/mol and is therefore higher than the C–H oxidative addition step (H = +13.9 kcal/mol). However, in reality some other species (PMe_3, solvent molecule) could come in and stabilise the unsaturated ***cis*-12** species. Therefore, the Si–H reductive elimination can be considered to be more accessible kinetically than the C–H oxidative addition step.

With computed free energies, phosphine dissociation becomes competitive with the C–F activation oxidative addition with transition state energies located at +13.2 kcal/mol and +12.4 kcal/mol. Moreover, these two processes are both lower than C–H activation with a computed energy of +15.3 kcal/mol. Overall, C–F activation is computed to be more accessible kinetically and thermodynamically than C–H activation ($\Delta\Delta G^{\ddagger}$ = 2.9 kcal/mol, $\Delta\Delta G$ = 51.3 kcal/mol).

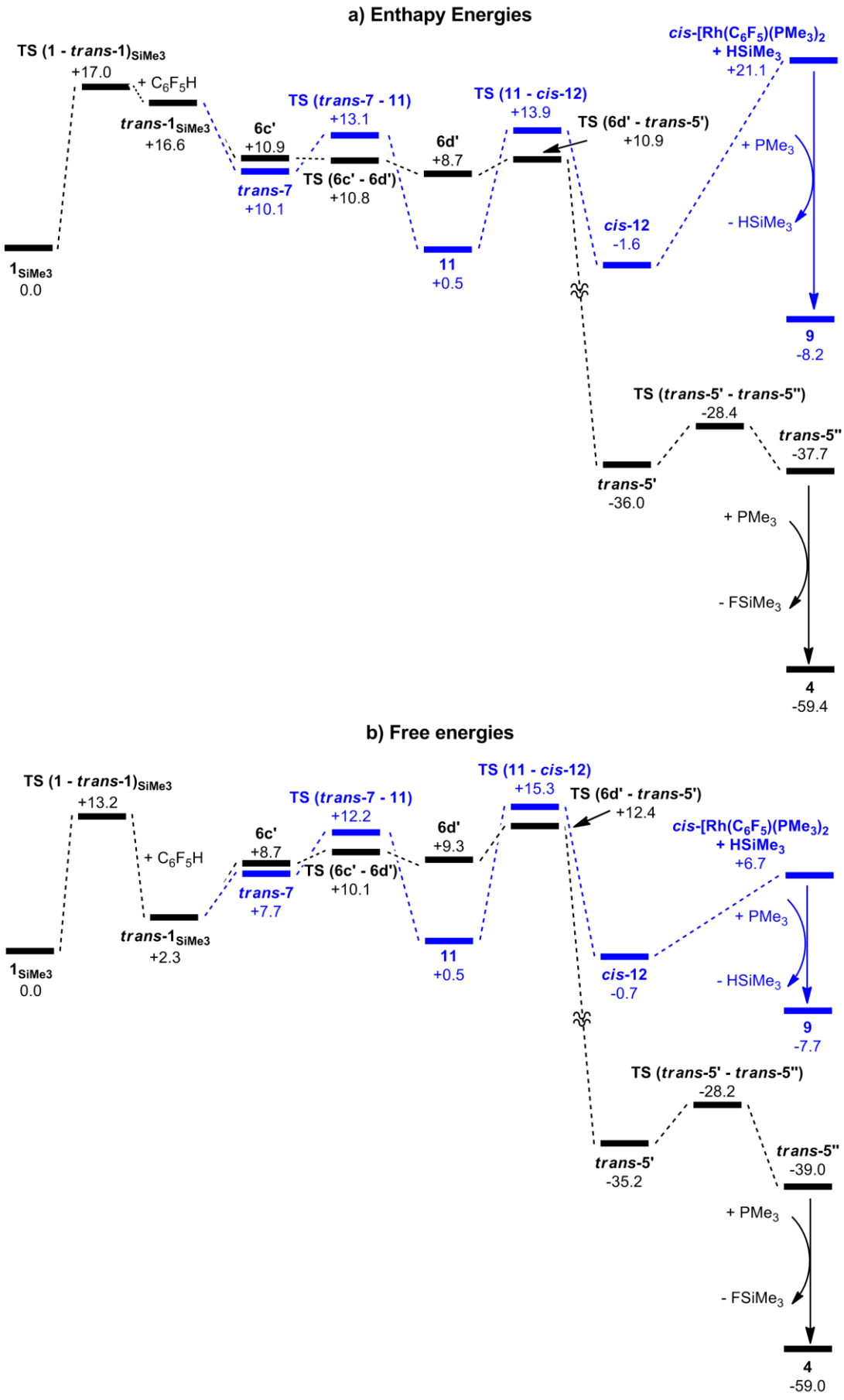

Figure 3.40: Reaction profiles for C–F activation (in black) and C–H activation (in blue) at $\mathbf{1_{SiMe3}}$. The energies for the reaction profiles are a) enthalpy energies and b) free energies

3.7 Summary for C–F and C–H Activation of C_6F_5H at $\mathbf{1_{SiMe3}}$

The key stationary points for C–F activation and C–H activation of C_6F_5H at $\mathbf{1_{SiMe3}}$ are schematised in Figure 3.41. Computed enthalpies show that the rate-limiting transition states for the reaction of C_6F_5H at $\mathbf{1_{SiMe3}}$, without initial phosphine dissociation, are always the C–F and C–H oxidative addition steps. Direct C–H activation at $\mathbf{1_{SiMe3}}$ is preferred over C–F activation with a transition state located at +12.1 kcal/mol ($\Delta\Delta H^{\ddagger}$ = 5.7 kcal/mol). However, C–F activation is much more favourable thermodynamically ($\Delta\Delta H$ = 51.2 kcal/mol). In contrast, after initial phosphine dissociation, C–F activation becomes more accessible kinetically than C–H activation at ***trans*-$\mathbf{1_{SiMe3}}$** with a transition state located at +10.9 kcal/mol. Direct C–H activation at $\mathbf{1_{SiMe3}}$ and C–F activation at ***trans*-$\mathbf{1_{SiMe3}}$** are competitive ($\Delta\Delta H^{\ddagger}$ = 1.2 kcal/mol in favour of C–H activation), however initial phosphine dissociation prior to C–F activation required a barrier of +17.0 kcal/mol and therefore C–H activation is preferred (H = +12.1 kcal/mol).

Computed free energies confirm that direct C–H activation at $\mathbf{1_{SiMe3}}$ (G = +27.3 kcal/mol) is more accessible kinetically than C–F activation (G = +33.9 kcal/mol) while the latter is more favourable thermodynamically ($\Delta\Delta G$ = 51.3 kcal/mol). Reaction of C_6F_5H at ***trans*-$\mathbf{1_{SiMe3}}$** shows that C–H oxidative addition and C–F activation have computed energies located at +15.3 kcal/mol and +12.4 kcal/mol, respectively. This implies that the latter is again kinetically more accessible. In addition, computed free energies now favour the loss of PMe_3 with a computed transition state of +13.2 kcal/mol. In this case, phosphine dissociation and C–F activation at ***trans*-$\mathbf{1_{SiMe3}}$** are competitive. Moreover, this pathway now becomes lower in energy that direct C–H activation at $\mathbf{1_{SiMe3}}$ and thus account for the selectivity of C–F activation observed experimentally.

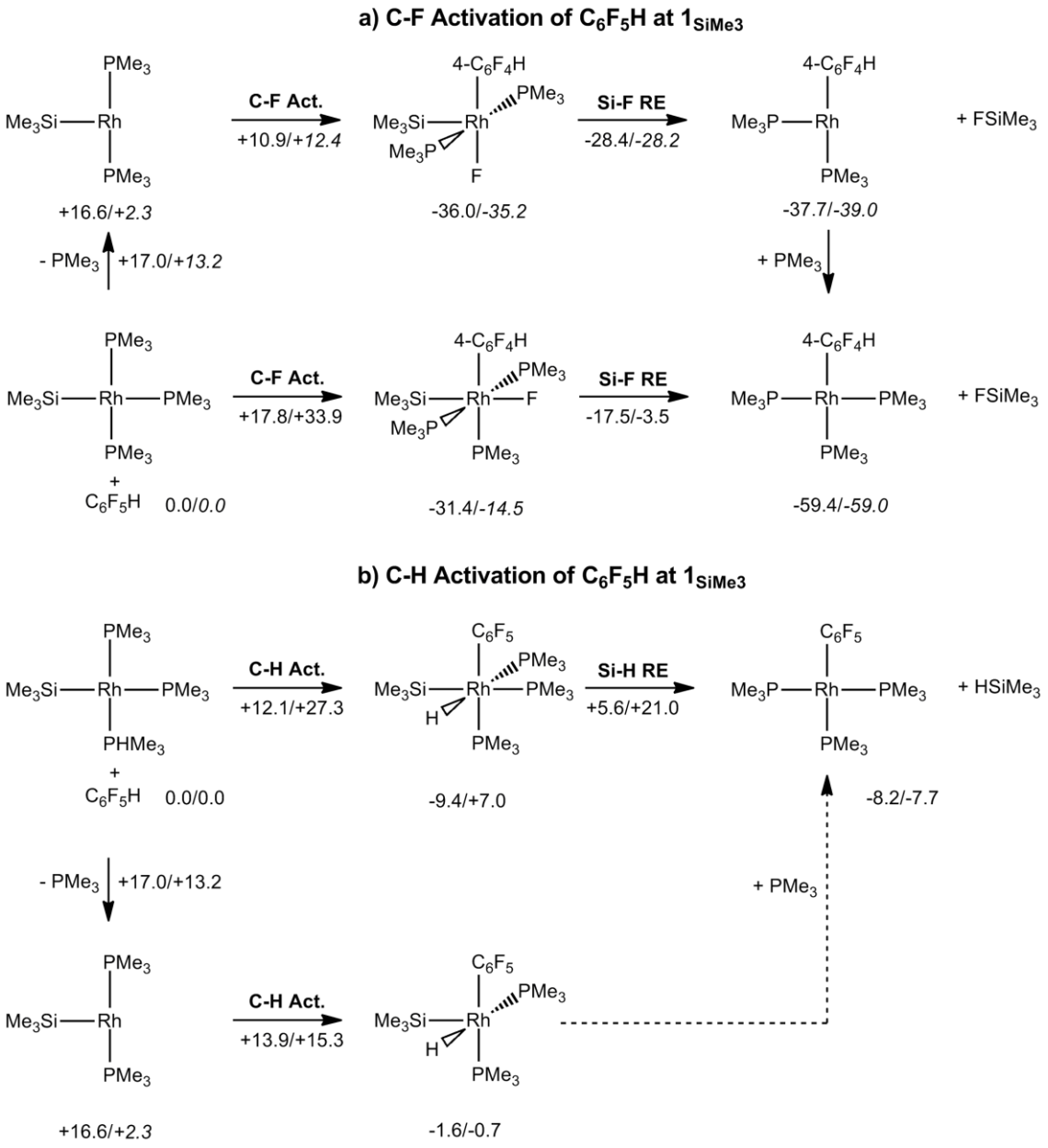

Figure 3.41: Computed enthalpies (plain) and free energies (italics) for C–F activation and C–H activation of C_6F_5H at 1_{SiMe3}.

3.8 Conclusions

Density functional theory calculations have been used to model the reaction between [Rh(SiR_3)(PMe_3)$_3$] and C_6F_5H. The most accessible process involves 1) phosphine substitution to form a η^1-arene species; 2) C–F activation of C_6F_5H; 3) Si–F reductive elimination; and 4) $FSiMe_3$ displacement by the incoming dissociated phosphine. This mechanism is consistent with the selectivity observed experimentally where only the C–F cleavage product is formed. Moreover, computed free energies show that C–F activation is more accessible kinetically and thermodynamically than C–H activation. It should also be mentioned that phosphine dissociation ($\Delta G^{\ddagger}$ = +13.2 kcal/mol) is competitive with C–F oxidative addition ($\Delta G^{\ddagger}$ = +12.4 kcal/mol). This last result contrasts with what is observed experimentally with C_6F_6 which occurs at room temperature while C–F activation of C_6F_5H proceeds at 110 °C. Indeed, if dissociation of PMe_3 is the rate-limiting transition state no difference should be seen experimentally between the two substrates. However, ligand dissociation is difficult to estimate computationally as the entropy contribution is not properly described and this affects the energy barrier. In addition, dissociation of PMe_3 is found to be functional dependent as shown in Chapter 6 (see Tables 6.2 and 6.3). One way to know if experimentally this pathway occurs will be to perform the reaction in excess of PMe_3 and to see if there is any effect on the rate of C–F activation of C_6F_6 and C_6F_5H. If the reaction is shut down this implies that dissociation of PMe_3 is important. Also, as mentioned previously the broad signals in the $^{31}P\{^1H\}$ NMR spectrum may provide an evidence for dissociation of PMe_3 prior to C–F activation.

In addition, a transition state via a ligand-assisted C–F activation has been computed for direct elimination of $FSiMe_3$, involving the transfer of F onto one PMe_3 ligand before to bind silicon to form [Rh(4-C_6F_4H)(PMe_3)$_3$] after fluorosilane elimination. In this case, an initial trigonal bipyramidal precursor η^2-intermediate is formed. This last feature will be relevant for the discussion in Chapter 4.

Chapter 4: C–F Bond Activation at the 2- and 4-positions of Pentafluoropyridine at $[Rh(X)(PEt_3)_3]$ ($X = Si(OEt)_3$, Bpin)

4.1 Introduction

The aim of this chapter is to study the C–F bond activation of C_5NF_5 at the 2- and 4-positions (i.e., the C–F bond *ortho* and *para* to the pyridyl nitrogen) at $[Rh(X)(PEt_3)_3]$ ($X = Si(OEt)_3$, Bpin, where pin = pinacolate = $–OCMe_2CMe_2O–$). Experimentally, treatment of $[Rh\{Si(OEt)_3\}(PEt_3)_3]$ at room temperature with one equivalent of C_5NF_5 in toluene yields $[Rh(2\text{-}C_5NF_4)(PEt_3)_3]$ and $[Rh(4\text{-}C_5NF_4)(PEt_3)_3]$ in a 9:1 ratio, while $[Rh(Bpin)(PEt_3)_3]$ yields exclusively $[Rh(2\text{-}C_5NF_4)(PEt_3)_3]$ under the same conditions (see Figure 4.1).[68] In addition, $[Rh(Bpin)(PEt_3)_3]$ was characterized in solution and the $^{31}P\{^1H\}$ NMR spectrum at room temperature revealed only one broad signal. This indicates a dynamic behaviour which involves the exchange of the phosphine ligand. When the reaction between $[Rh\{Si(OEt)_3\}(PEt_3)_3]$ and C_5NF_5 is conducted at -20 °C, only the selectivity at the 2-position is observed. In addition, both of these systems afford C–F activation without formation of fluorophosphoranes (e.g. F_2PEt_3) which are usually obtained between free phosphine and C_5NF_5. This indicates that phosphine dissociation does not occur and therefore the C–F activation of C_5NF_5 proceeds directly at the 4-coordinate $[Rh(X)(PEt_3)_3]$. This is in contrast with Chapter 3 where C–F activation of C_6F_5H happened after initial phosphine dissociation. In this case, only C–F activation at $[Rh(X)(PEt_3)_3]$ will be discussed in this chapter.

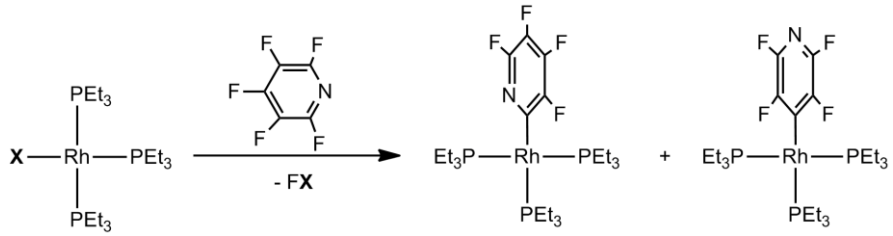

X = Si(OEt)$_3$	25°C	9	:	1
	-20 °C	1	:	0
X = Bpin	25 °C	1	:	0

Figure 4.1: C–F bond activation of C_5NF_5 at $[Rh(X)(PEt_3)_3]$ ($X = Si(OEt)_3$ or Bpin).

These two rhodium(I) complexes show an unusual selectivity as C–F bond activation of C_5NF_5 most frequently involves reaction at the 4-position and such selectivity can be

associated with initial nucleophilic attack. Activation at the 2-position is less common, although it has been suggested that it might occur via a phosphine-assisted C–F activation process.[60]

In order to assess the C–F activation of C_5NF_5 at the 2- and 4-positions, two computational models, [Rh{Si(OMe)$_3$}(PMe$_3$)$_3$], **1$_{Si(OMe)3}$**, and [Rh(Bpin)(PMe$_3$)$_3$], **1$_{Bpin}$**, have been used to model the reaction between [Rh(X)(PEt$_3$)$_3$] and C_5NF_5. In principle, C–F activation may occur via an oxidative addition process (Pathway 1) in which three isomers can be formed or via a ligand-assisted mechanism (Pathway 2), as shown in Figure 4.2.

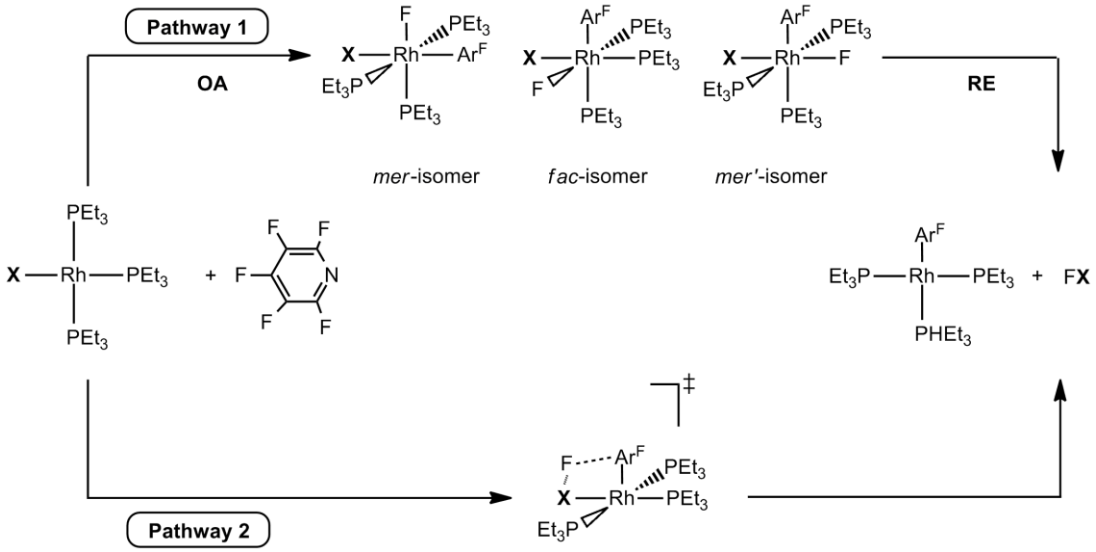

Figure 4.2: Possible reaction mechanisms for C–F activation at the 2- and 4-positions of C_5NF_5 at [Rh(X)(PEt$_3$)$_3$] (X = Si(OEt)$_3$ or Bpin) to yield [Rh(Ar^F)(PEt$_3$)]$_3$ (Ar^F = 2-C_5NF_4 or 4-C_5NF_4).

4.2 Computational Studies on the Reactions of [Rh{Si(OMe)$_3$}(PMe$_3$)$_3$] with C_5NF_5

4.2.1 Pathway 1: C–F Oxidative Addition of C_5NF_5 at the 2-Position

In this chapter, all selected key distances are in Å while all energies are in kcal/mol, relative to the two separated reactants, $\mathbf{1_{Si(OMe)3}}$ and C_5NF_5, denoted by **13**. Also figures shown free energies in italics and hydrogen atoms are omitted for clarity. The stationary points involved in the C–F activation of C_5NF_5 at the 2-position to form ***mer*-15**, ***fac*-15** and ***mer*-15′** are shown in Figure 4.3.

The first isomer is ***mer*-15** (H = -24.4 kcal/mol) which is formed via **TS (13 – *mer*-15)** (H = +23.9 kcal/mol), being the highest process for C–F activation at the 2-position. In the transition state, the key C2···F2 bond lengthens to 1.58 Å and the C2···F2 vector is slightly twisted relative to the Si–Rh–P1 plane (α = 30.0°). Weak Rh···C2 (2.31 Å) and Rh···F2 (2.48 Å) interactions are also computed while the Rh···N1 distance is 3.13 Å, which suggests that the nitrogen atom is not directly involved in the process. However, as seen in Chapter 3, F2 weakly interacts with P2 with a computed distance of 2.83 Å, although this remains rather long compared to the Rh···F2 contact (2.48 Å).

The second most accessible C–F activation process occurs with the formation of ***fac*-15** (H = -25.3 kcal/mol) via **TS (13 – *fac*-15)** (H = +20.4 kcal/mol). An elongation of the C2···F2 distance to 1.65 Å is computed and the C2···F2 vector is found to be coplanar to the P2–Rh–P3 plane (α = 7.2°), consistent with a concerted oxidative addition process. This feature differs from the previous transition state, **TS (2 – *fac*-3)** in Chapter 3, in which the fluorine atom interacted with one phosphine ligand (P1···F1 = 2.59 Å) before being transferred onto the rhodium metal centre. Instead of having a weak P1··· F2 contact in **TS (13 – *fac*-15)**, a Si··· F2 interaction is computed (2.88 Å). In addition, the Rh···N1 interaction remains rather long (2.94 Å).

An alternative transition state with a weak degree of phosphine-assistance has also been located for formation of ***fac*-15** but found to be higher in energy (**TS′ (13 – *fac*-15)**, H = +22.5 kcal/mol, see Figure 4.4).

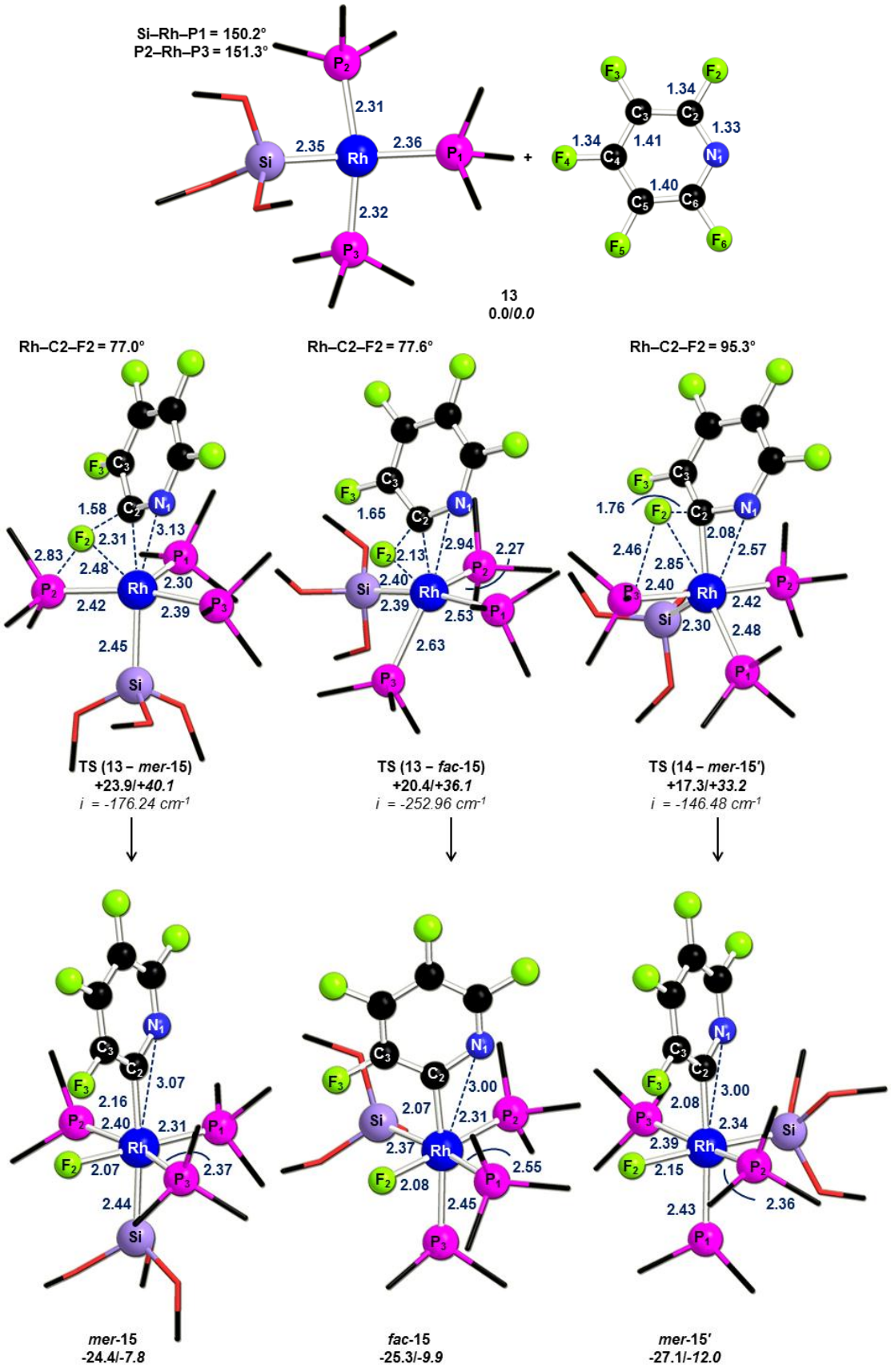

Figure 4.3: Computed geometries and energies for C–F oxidative addition at the 2-position of C_5NF_5.

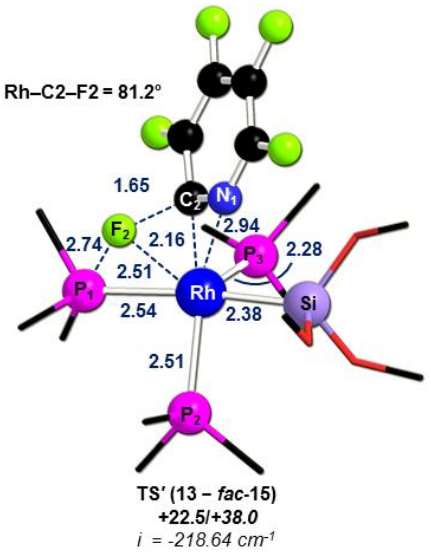

Figure 4.4: Computed transition state and energies for TS′ (13 – *fac*-15).

TS′ (13 – *fac*-15) has been obtained from the extensive conformation searching as described in Chapter 2. In the computed transition state **TS′ (13 – *fac*-15)**, the C2···F2 vector is more twisted relative to the P2–Rh–P3 plane (α = 40.2°) than in **TS (13 – *fac*-15)** (α = 7.2°), however the P1–Rh–C2–F2 angle is -43.8°. In addition, the P1···F2 interaction is computed to be 2.74 Å and remains long compared to the Rh···F2 distance (2.51 Å). These features show that the C–F activation through **TS′ (13 – *fac*-15)** has a weak degree of phosphine-assistance.

Finally, the lowest C–F oxidative addition pathway corresponds to the formation of ***mer*-15′** (H = -27.1 kcal/mol) via **TS (14 – *mer*-15′)** and has a computed barrier of +17.3 kcal/mol. Significant elongation of the breaking C2···F2 bond to 1.76 Å is computed while the Rh–C2 bond is formed (2.08 Å). **TS (14 – *mer*-15′)** shows similar features to **TS (2 – *mer*-3′)** in that the P3···F2 interaction (2.46 Å) is shorter than the Rh···F2 contact (2.85 Å). Also, the C2···F2 vector is twisted relative to the Si–Rh–P1 plane (α = 71.5°) and the P3–Rh–C2–F2 angle is +23.3°. This suggests that **TS (14 – *mer*-15′)** clearly has a stronger degree of phosphine-assistance than **TS (13 – *fac*-15)**. In addition, a Rh···N1 interaction of 2.57 Å is also computed.

In contrast with **TS (13 – *mer*-15)** and **TS (13 – *fac*-15)** that link in the reverse direction to **13**, **TS (14 – *mer*-15′)** leads to a η^2-arene intermediate **14** (H = +0.4 kcal/mol, see Figure 4.5).

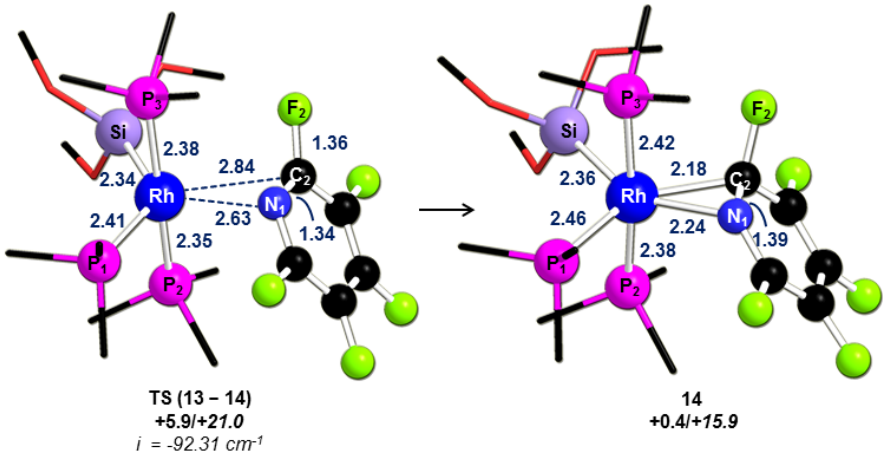

Figure 4.5: Computed geometries and energies for formation of the η^2-arene intermediate 14.

The η^2-arene intermediate **14** exhibits a trigonal bipyramidal geometry with the $Si(OMe_3)_3$ ligand in an equatorial position. Complex **14** shows an elongation of the C2=N1 bond to 1.39 Å, consistent with the Dewar-Chatt-Duncanson model. A transition state, **TS (13 – 14)** (H = +5.9 kcal/mol) for formation of this intermediate, has been located by increasing the Si–Rh–P1angle (in this case, Si–Rh–P1 = 128.5° *cf.* 109.3° in **14**).

The reaction profiles for the C–F oxidative addition of C_5NF_5 at the 2-position are shown in Figure 4.6. The stability of the three distinct isomers follows the trend: ***mer*-15** (H = -24.4 kcal/mol) < ***fac*-15** (H = -25.3 kcal/mol) < ***mer*-15′** (H = -27.1 kcal/mol). The *mer′*-isomer, in this case ***mer*-15′,** has again the best arrangement of ligands, having the strongest electron donor ligand $Si(OMe)_3$ trans to the weakest donor (F). However, the difference in energy between ***mer*-15** and ***mer*-15′** is only 2.7 kcal/mol, while in Chapter 3 the difference in energy between ***mer*-3** and ***mer*-3′** was higher (ΔH = 5.1 kcal/mol). This last point, can be explained by a weaker *trans*-influence of $Si(OMe_3)_3$ compared to $SiMe_3$. For instance, in ***fac*-15** the Rh–P1 bond trans to $Si(OMe_3)_3$ is 2.55 Å while in ***fac*-3** the same bond was 2.60 Å, trans to $SiMe_3$. In addition, 2-C_5NF_4 has a higher *trans*-influence than PMe_3. Indeed, in ***fac*-15**, the Rh–Si bond trans to PMe_3 is 2.37 Å while in ***mer*-15** this bond is elongated to 2.44 Å, trans to 2-C_5NF_4. Therefore, ***mer*-15** is the least stable isomer as both 2-C_5NF_4 and $Si(OMe_3)_3$ are trans to each other. A final trend for the trans-influence of the different ligand can be drawn: $Si(OMe_3)_3$ > 2-C_5NF_4 > PMe_3 > F, similar to what has been observed in Chapter 3.

The stability of the three different transition states is the following: **TS (13 – *mer*-15)** (H = +23.9 kcal/mol) < **TS (13 – *fac*-15)** (H = +20.4 kcal/mol) < **TS (14 – *mer*-15′)** (H = +17.3 kcal/mol). **TS (14 – *mer*-15′)** is the lowest lying transition state as $Si(OMe_3)_3$ is computed to be trans to the vacant site while in **TS (13 – *fac*-15)** and **TS (14 – *mer*-15′)**, the silyl ligand is trans to PMe_3 and 2-C_5NF_4, respectively. Comparing **TS (14 – *mer*-15′)** and **TS (2 – *mer*-3′)** shows that both transition states have similar energies with transition states located at +17.3 kcal/mol and +17.8 kcal/mol, respectively. This implies that the weak Rh···N1 contact of 2.57 Å computed in **TS (14 – *mer*-15′)** does not contribute in the stabilisation of the transition state. In contrast, formation of *mer*- and *fac*-isomers is more accessible kinetically at $\mathbf{1_{Si(OMe)3}}$ than at $\mathbf{1_{SiMe3}}$ and may again reflect the weaker *trans*-influence of $Si(OMe_3)_3$. **TS (13 – *mer*-15)**, for instance, is 10.7 kcal/mol lower than **TS (2 – *mer*-3)** ($\Delta\Delta G^{\ddagger}$ = 11.5 kcal/mol) and **TS (13 – *fac*-15)** is more favourable than **TS (2 – *fac*-3)** by 6.3 kcal/mol ($\Delta\Delta G^{\ddagger}$ = 6.3 kcal/mol). Computed free energies increase all the energies of the stationary points by around 16.0 kcal/mol, as in Chapter 3, as the associative processes involved are equivalent.

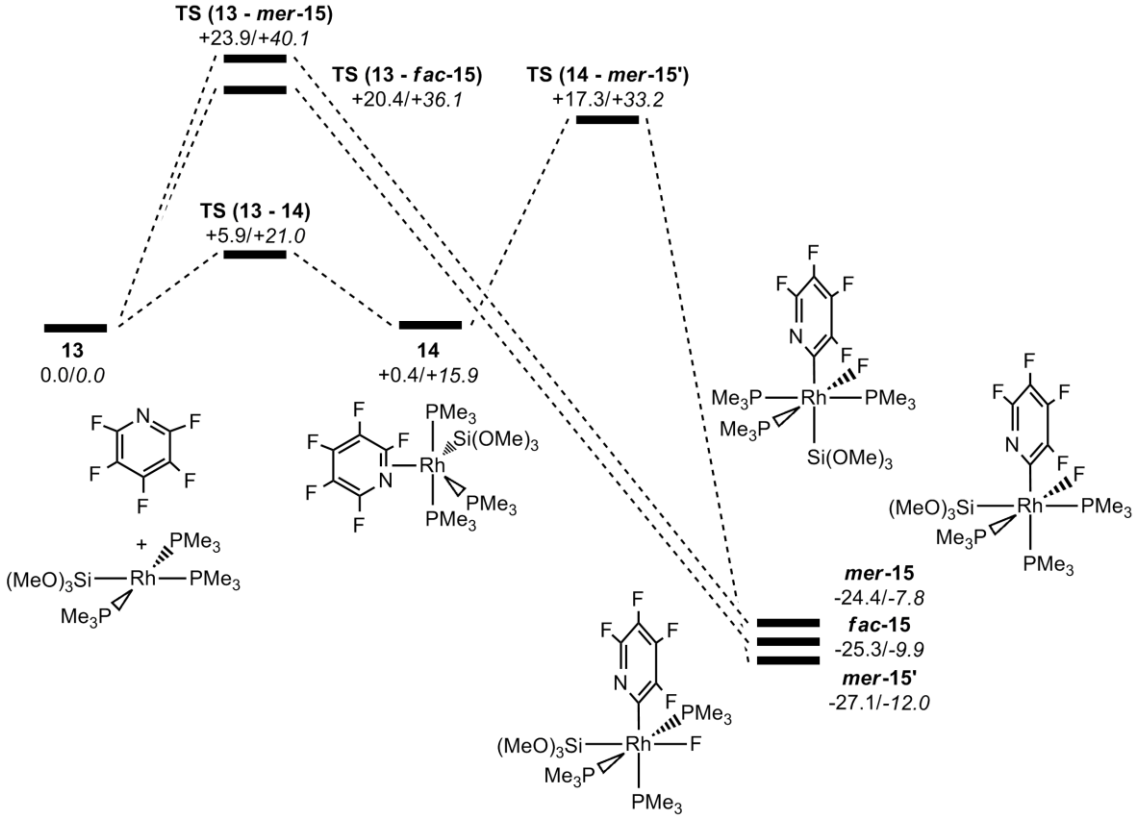

Figure 4.6: Formation of *mer*-15, *fac*-15 and *mer*-15′ via C–F oxidative addition at the 2-position.

4.2.2 Pathway 1: Phosphine Loss/Isomerisation and Subsequent Si–F Reductive Elimination from ***mer-15′***

As described in Chapter 3, the C–F oxidative addition step is the overall rate-limiting process, along Pathway 1. In this chapter, calculations have been performed on the Si–F reductive elimination from the three isomers and confirmed this argument. Therefore, Si–F reductive elimination step will only be discussed for the lowest lying C–F activation transition state which is derived from ***mer*-15′**.

Species ***mer*-15′** requires a phosphine loss/isomerisation step prior to Si–F reductive elimination. This process can occur via phosphine dissociation, either trans to 2-C_5NF_4 or trans to PMe_3 to give, after spontaneous isomerisation of F cis to $Si(OMe)_3$, ***trans*-17′** and ***cis*-17′**, respectively. Overall, as seen for the phosphine loss/isomerisation of ***mer*-3′** in Chapter 3, reaction via the former was found to be more favourable and so will be discussed here (see Figure 4.7).

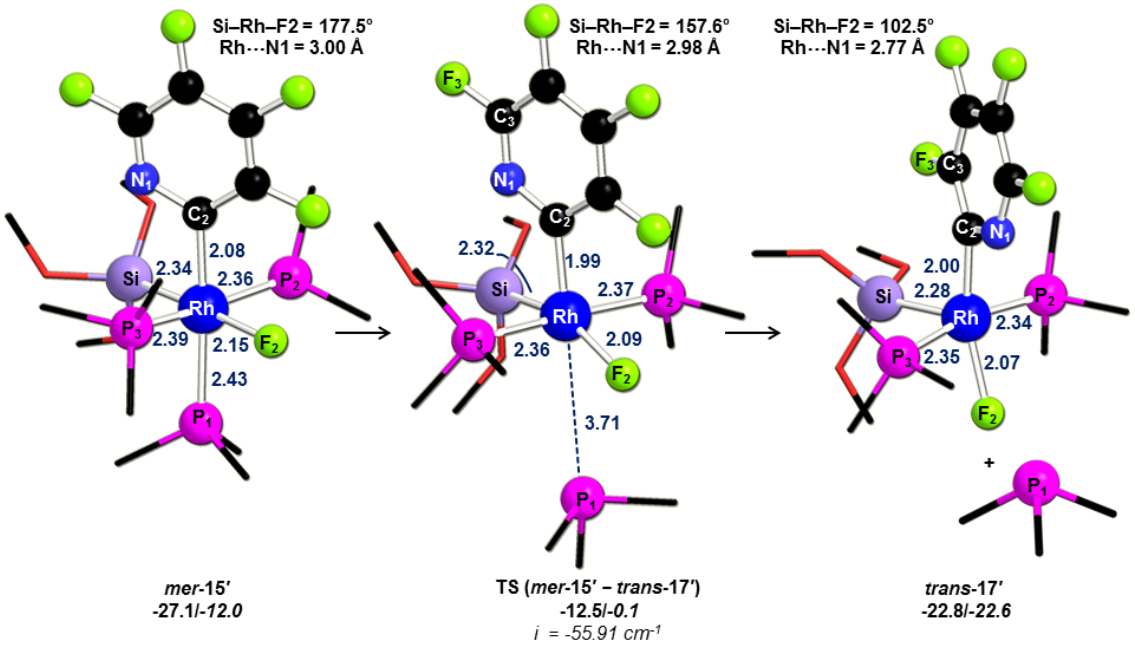

Figure 4.7: Computed geometries and energies for the phosphine loss/isomerisation step to give *trans*-17′.

From ***mer*-15′**, a transition state has been located, **TS (*mer*-15′ – *trans*-17′)** (H = -12.5 kcal/mol), to give ***trans*-17′** (H = -22.8 kcal/mol). The computed transition state shows that the Rh···P1 distance increases to 3.71 Å as the phosphine dissociates and at the same time, the Si–Rh–F2 angle bends back to 157.6°, as F2 begins to move cis to $Si(OMe)_3$. ***Trans*-17′** has a square planar geometry and a distorted 2-C_5NF_4 ligand

(Rh–C2–N1 = 109.2°, Rh–C2–C3 = 133.1°) and may come from the weak Rh···N1 interaction (2.77 Å). Interestingly, ***trans*-17′** is slightly less stable than ***mer*-15′** by 4.3 kcal/mol while in the previous chapter ***trans*-5′** (H = -36.0 kcal/mol) was downhill compared to ***mer*-3′** (H = -31.4 kcal/mol). This reflects again the weaker *trans*-influence of $Si(OMe)_3$ compared to $SiMe_3$. However, computed free energies show that ***trans*-17′** is lower in energy than ***mer*-15′** by 10.6 kcal/mol, as it involves a dissociative process.

Si–F reductive elimination from ***trans*-17′** proceeds via **TS (*trans*-17′ – *trans*-17″)** (H = -15.7 kcal/mol) with the shortening of the Si···F2 distance by 1.01 Å to 2.38 Å (see Figure 4.8). **TS (*trans*-17′ – *trans*-17″)** links to ***trans*-17″** (H = -18.7 kcal/mol) in which the $FSi(OMe)_3$ group is loosely bound to the rhodium metal centre. The highly exothermic product $[Rh(2\text{-}C_5NF_4)(PMe_3)_3]$ (**16**, H = -32.6 kcal/mol, see Figure 4.9) is then formed by displacing the $FSi(OMe)_3$ group by the dissociated phosphine. This process is expected to be facile (*cf.* Figure 3.34 in Chapter 3).

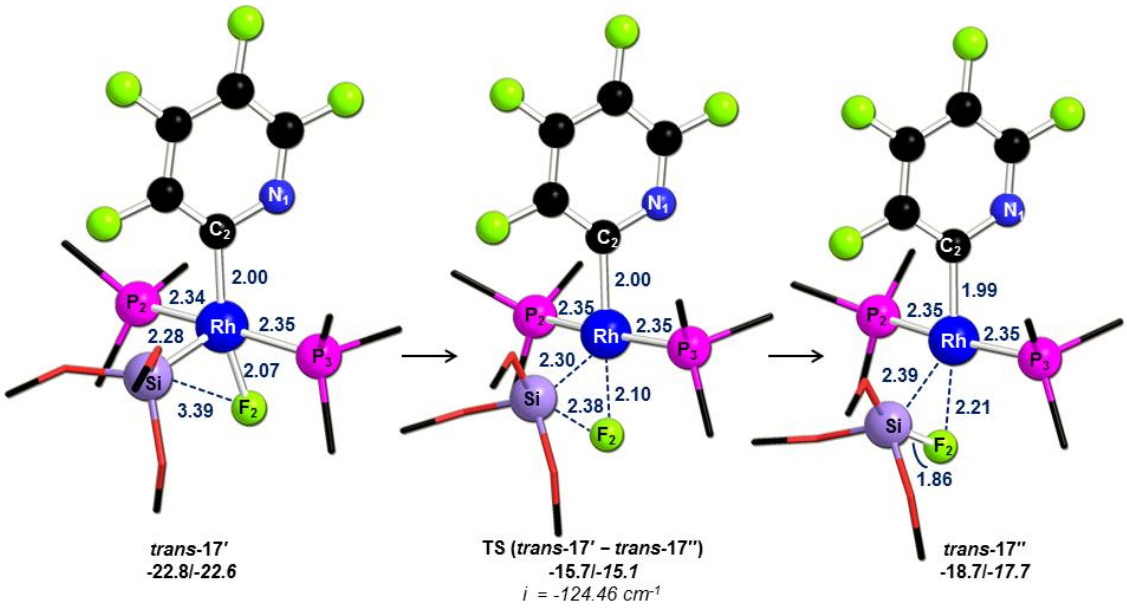

Figure 4.8: Computed geometries and energies for Si–F reductive elimination to give *trans*-17″.

In addition, from ***trans*-17′** PMe_3 can bind trans to $Si(OMe)_3$ to give ***mer*-15″** (H = -24.4 kcal/mol) which shows an unusual distorted octahedral geometry (see Figure 4.9). This distortion was already observed in ***mer*-3″** although there it was less pronounced. ***Mer*-15″** has a similar Si–Rh–P1 angle (141.5° *cf.* 141.6° in ***mer*-3″**), however, the Si–Rh–F2 angle is more distorted (49.7° *cf.* Si–Rh–F1 = 62.6° in ***mer*-3″**). This difference

in the Si–Rh–F2/F1 angles can be explained by the stronger Si···F2 contact in ***mer*-15″** (1.95 Å) compared to ***mer*-3″** (Si···F1 = 2.41 Å).

From ***mer*-15″**, a transition state for Si–F reductive elimination has been found, **TS (*mer*-15″ – 16)** (H = -16.9 kcal/mol) by increasing the P1–Rh–C2 angle to 137.2°. This step is also characterised by a significant elongation of the Rh···F2 distance to 2.53 Å while the Rh···Si contact increases by only 0.07 Å to 2.50 Å. In contrast, **TS (*mer*-3″ – 4)** showed that both Rh···Si and Rh···F1 distances were elongated by 0.45 Å to 2.95 Å and by 0.15 Å to 2.24 Å, respectively. This difference again reflects the greater Lewis acidic character of $SiOMe_3$ where the Si···F2 bond is almost formed in ***mer*-15″**. Also, in **TS (*mer*-15″ – 16)**, the Si···F2 distance shortens to 1.78 Å and α is 5.6°. Finally, **TS (*mer*-15″ – 16)** links to **16** and $FSi(OMe)_3$.

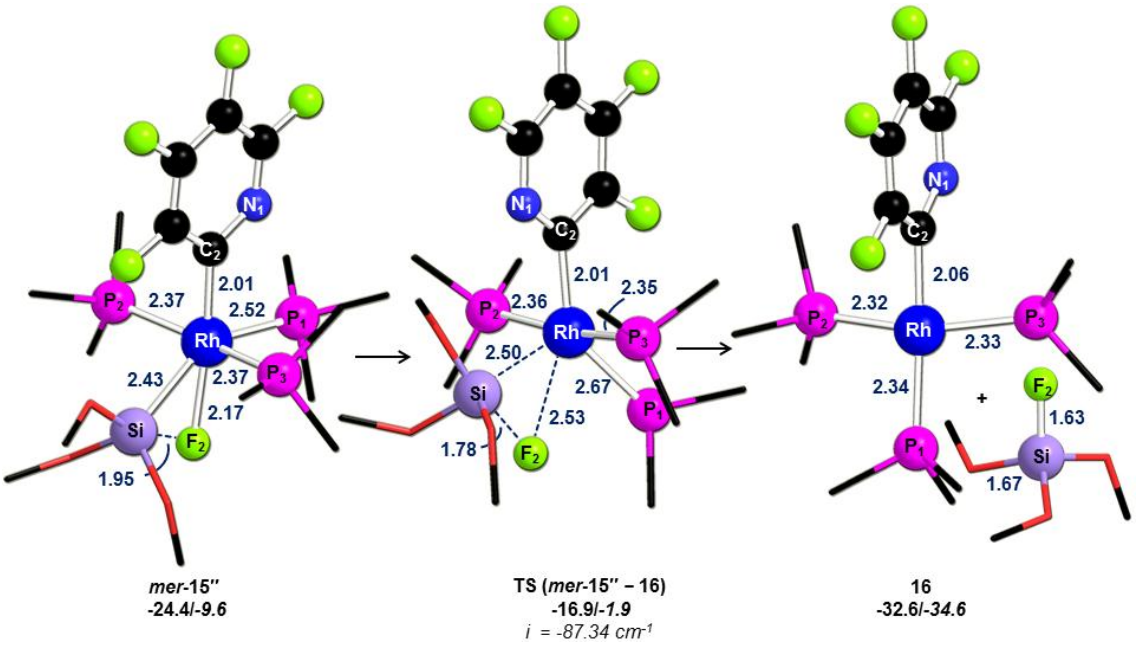

Figure 4.9: Computed geometries and energies for Si–F reductive elimination to give 16 and $FSi(OMe)_3$.

Overall, the lowest pathway for formation of $[Rh(2\text{-}C_5NF_4)(PMe_3)_3]$, **16**, and $FSi(OMe)_3$ is shown in Figure 4.10. The rate-limiting transition state, as seen in Chapter 3, is the C–F activation step which, in this case, has a computed barrier of +17.3 kcal/mol. After formation of ***mer*-15′**, the phosphine loss/isomerisation is facile and occurs via **TS (*mer*-15′ – *trans*-17′)** to yield the 5-coordinate intermediate ***trans*-17′**. The Si–F reductive elimination from ***trans*-17′** and ***mer*-15″** are relative close in energy, computed at -15.7 kcal/mol and -16.9 kcal/mol, respectively. Computed free

energies confirm the C–F oxidative addition step as rate-limiting transition state (G = +33.2 kcal/mol). In addition, the phosphine loss/isomerisation step remains facile, however, the lowest pathway for Si–F reductive elimination now proceeds via **TS (*trans*-17′ – *trans*-17″)** which is more favourable kinetically than **TS (*mer*-15″ – 16)** ($\Delta\Delta G^{\ddagger}$ = 13.2 kcal/mol). Overall the process is exothermic by 32.6 kcal/mol (ΔG = -34.6 kcal/mol).

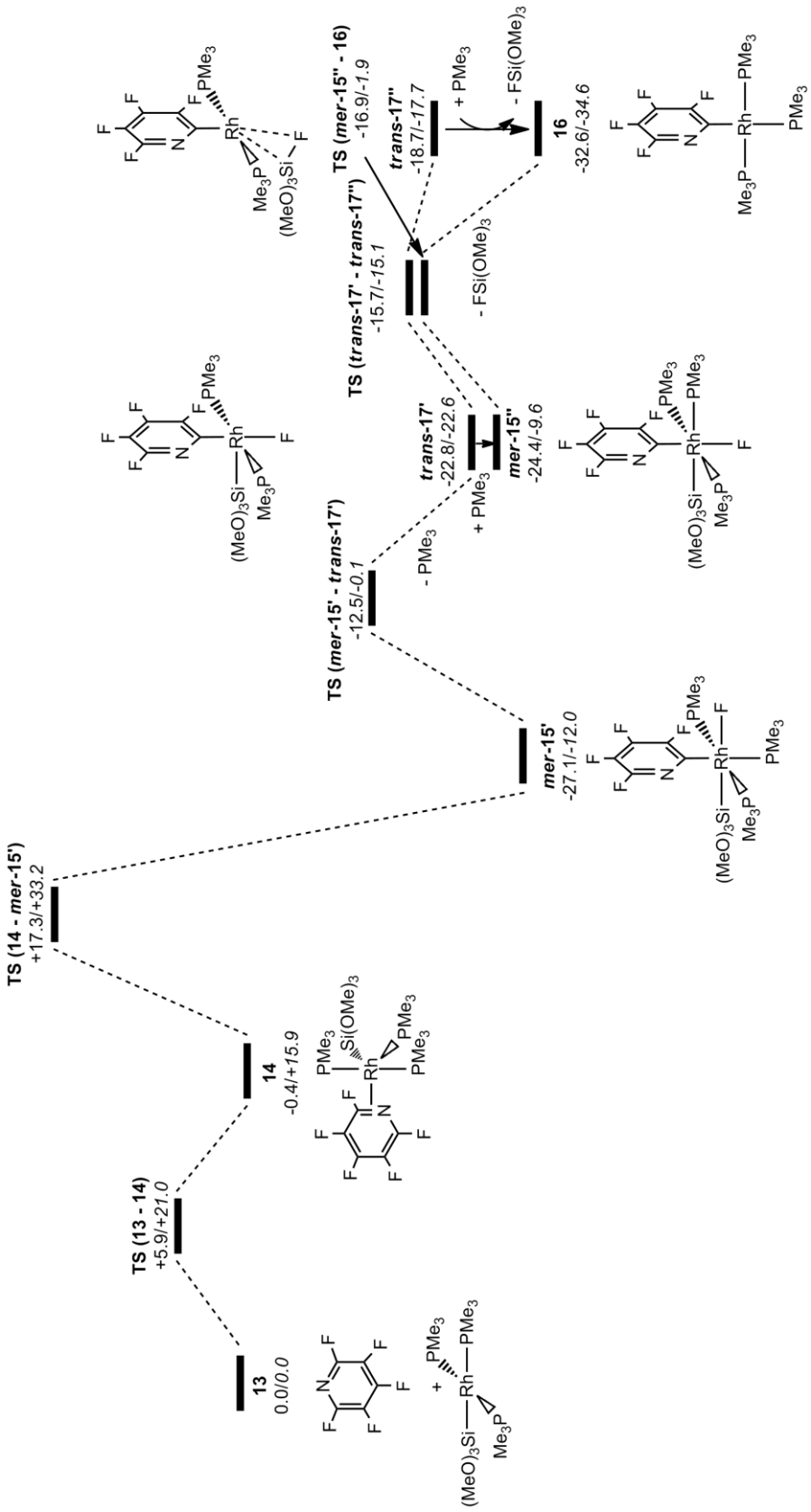

Figure 4.10: Formation of [Rh(2-C_5NF_4)(PMe_3)$_3$], 16, and $FSi(OMe)_3$ via C-F activation of C_5NF_5 at the 2-position, along Pathway 1.

4.2.3 Pathway 1: C–F Oxidative Addition of C_5NF_5 at the 4-Position

To understand the formation of [Rh(4-C_5NF_4)(PEt_3)$_3$] observed experimentally, the C–F oxidative addition of C_5NF_5 at the 4-position has been computed. The stationary points and relative energies involved in this process are shown in Figure 4.11.

The highest process is again the formation of the *mer*-isomer, ***mer*-18** (H = -33.4 kcal/mol). The computed transition state, **TS (13 – *mer*-18)** (H = +22.7 kcal/mol), shows an elongation of the C4···F4 bond to 1.64 Å and α is 44.0°. **TS (13 – *mer*-18)** shows a weak P2···F4 interaction (2.74 Å) which is, however, longer than the Rh···F4 distance (2.55 Å). These features are similar to the ones computed in **TS (13 – *mer*-15)** (P2···F2 = 2.83 Å, Rh···F2 = 2.48 Å). Finally, oxidative addition at the 4-position is slightly lower than at the 2-position ($\Delta\Delta H^{‡}$ = 1.2 kcal/mol, $\Delta\Delta H^{‡}$ = 1.0 kcal/mol) for formation of the *mer*-isomer.

The second computed transition state is **TS (13 – *fac*-18)** (H = +20.6 kcal/mol) and corresponds to the formation of ***fac*-18** (H = -31.8 kcal/mol). This transition state is quite different to **TS (13 – *fac*-15)**, which was the lowest lying C–F activation transition state to give ***fac*-15**. In **TS (13 – *fac*-18)**, F4 clearly interacts with P1 (2.66 Å) while no similar interaction between P1 and F2 was found in **TS (13 – *fac*-15)**. In addition, in **TS (13 – *fac*-18)**, α is 47.9° while a coplanar arrangement was seen in **TS (13 – *fac*-15)** (α = 7.2°). All these difference can suggest that N1 played a role in the conformation of **TS (13 – *fac*-15)** and affects the energies of the transition states, as **TS (13 – *fac*-18)** and **TS (13 – *fac*-15)** have similar energies being +20.6 kcal/mol (G = +35.9 kcal/mol) and +20.4 kcal/mol (G = +36.1 kcal/mol), respectively.

Formation of the final computed species ***mer*-18′** (H = -34.9 kcal/mol) involves the lowest energy process. The C–F activation proceeds via **TS (13 – *mer*-18′)** (H = +13.2 kcal/mol) in which the key C4···F4 bond is stretched to 1.62 Å. The angle α is 64.0° (P2–Rh–C4–F4 = +29.2°) and therefore smaller than in **TS (14 – *mer*-15′)** (α = 71.5°, P3–Rh–C2–F2 = +23.2°). This suggests that **TS (14 – *mer*-15′)** proceeds with a higher degree of phosphine-assistance in which F2 interacts more strongly with the phosphine ligand (P3···F2 = 2.46 Å; **TS (13 – *mer*-18′)**, P2···F4 = 2.63 Å). This last feature implies that the short Rh…N1 contact in **TS (14 – *mer*-15′)** does not help to stabilise

the energy of the transition state as C–F activation at the 2-position is higher than at the 4-position ($\Delta\Delta H^{\ddagger}$ = 4.1 kcal/mol, $\Delta\Delta G^{\ddagger}$ = 3.9 kcal/mol) but may affect the geometry of the stationary points.

In contrast to C–F activation at the 2-position, all the three transition states link, in the reverse direction, to the two separated species **13** and therefore no η^2-adduct, analogous to **14**, has been located.

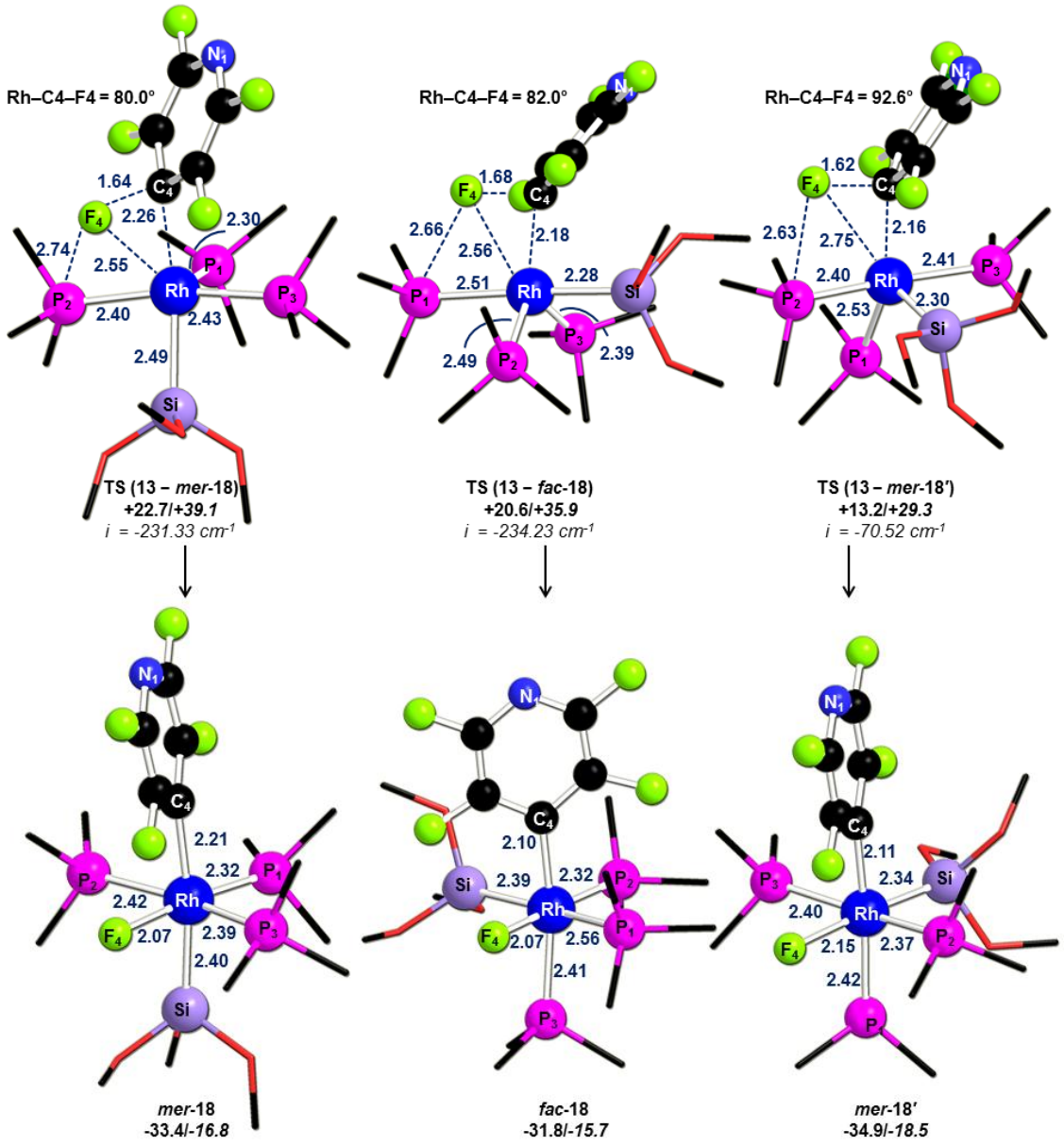

Figure 4.11: Computed geometries and energies for C–F oxidative addition at the 4-position of C_5NF_5.

The reaction profiles for C–F oxidative addition at the 4-position are shown in Figure 4.12. The most stable isomer again has silyl trans to F (e.g. ***mer*-18′**). In contrast with

the previous C–F activation processes, ***mer*-18** (H = -33.4 kcal/mol) where $Si(OMe)_3$ is trans to 4-C_5NF_4 is actually more stable than ***fac*-18** (H = -31.8 kcal/mol). This difference is partially explained by the weaker *trans*-influence of $Si(OMe)_3$ compared to $SiMe_3$. A second contribution can be the weaker *trans*-influence of 4-C_5NF_4 compared to 2-C_5NF_4. Indeed, in ***mer*-15**, the Rh–Si bond trans to 2-C_5NF_4 is elongated to 2.44 Å while in ***mer*-18**, the same Rh–Si distance is 2.40 Å. Therefore this second argument can stabilise slightly more ***mer*-18** than ***mer*-15** which now becomes more stable than ***fac*-18**.

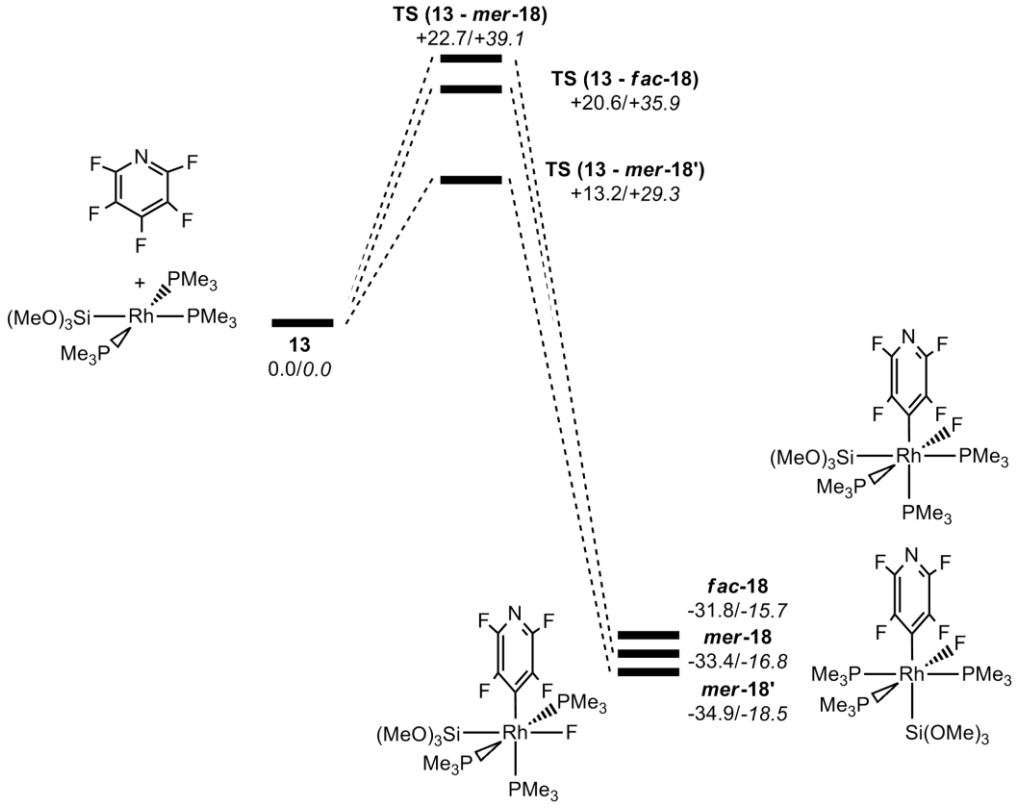

Figure 4.12: Formation of *mer*-18, *fac*-18 and *mer*-18′ via C–F oxidative addition at the 4-position, along Pathway 1.

The lowest lying transition state for C–F activation has again $Si(OMe)_3$ trans to the vacant site and corresponds to **TS (13 – *mer*-18′)** (H = +13.2 kcal/mol). Computed free energies increase the energy of **TS (13 – *mer*-18′)** to +29.3 kcal/mol.

Experimentally, the final product [Rh(4-C_5NF_4)(PMe_3)$_3$], **19**, is formed and so Si–F reductive elimination is required. This process again will be described for the lowest lying transition state for C–F activation and starts from ***mer*-18′**.

*4.2.4 Pathway 1: Phosphine Loss/Isomerisation and Subsequent Si–F Reductive Elimination from **mer-18′***

***Mer*-18′** requires a phosphine loss/isomerisation step prior to Si–F reductive elimination. The stationary points and energies involved in this process are shown in Figure 4.13.

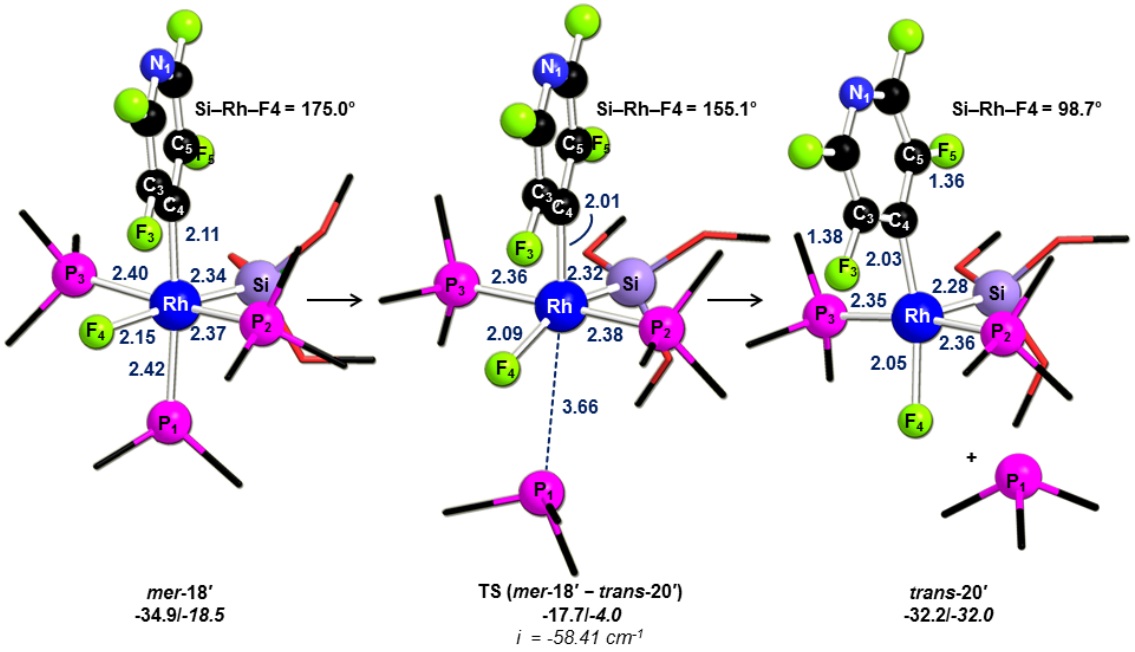

Figure 4.13: Computed geometries and energies for the phosphine loss/isomerisation to give *trans*-20′.

The computed transition state for this process, **TS (*mer*-18′ – *trans*-20′)**, is very similar to the ones described previously where the Rh···P1 distance lengthens by 1.24 Å to 3.66 Å and the Si–Rh–F4 angle bends back to 155.1°. **TS (*mer*-18′ – *trans*-20′)** links to ***trans*-20′** (H = -32.2 kcal/mol) which has a square pyramidal geometry. As seen for ***trans*-5′** (see Section 3.2.2 in Chapter 3) this distorted geometry is due to some interaction between the metal centre and the fluoroaryl moiety. In ***trans*-20′**, short Rh···C3 and Rh···F3 contacts of 2.90 Å and 2.95 Å are computed, respectively. Another consequence of these interactions is the elongation of the C3–F3 bond to 1.38 Å (*cf.* C5–F5 =1.36 Å). ***Trans*-20′** is slightly less stable than ***mer*-18′** (ΔΔH = 2.7 kcal/mol), as already seen for ***trans*-17′** which was higher in energy than ***mer*-15′** (ΔΔH = 4.3 kcal/mol). However, computed free energies show that ***trans*-17′** is more stable than ***mer*-18′** by 13.5 kcal/mol.

Si–F reductive elimination from ***trans*-20′**, occurs via **TS (*trans*-20′ – *trans*-20″)** (H = -25.7 kcal/mol, see Figure 4.14). In the transition state, the major change is the shortening of the Si···F4 contact to 2.36 Å. **TS (*trans*-20′ – *trans*-20″)** links to ***trans*-20″** (H = -28.6 kcal/mol) in which the $FSi(OMe)_3$ group is loosely bound to the rhodium metal centre. Formation of the highly exothermic product [Rh(4-C_5NF_4)(PMe_3)$_3$] (**16**, H = -45.6 kcal/mol, see Figure 4.15) is then obtained by substituting the $FSi(OMe)_3$ group by the dissociated phosphine.

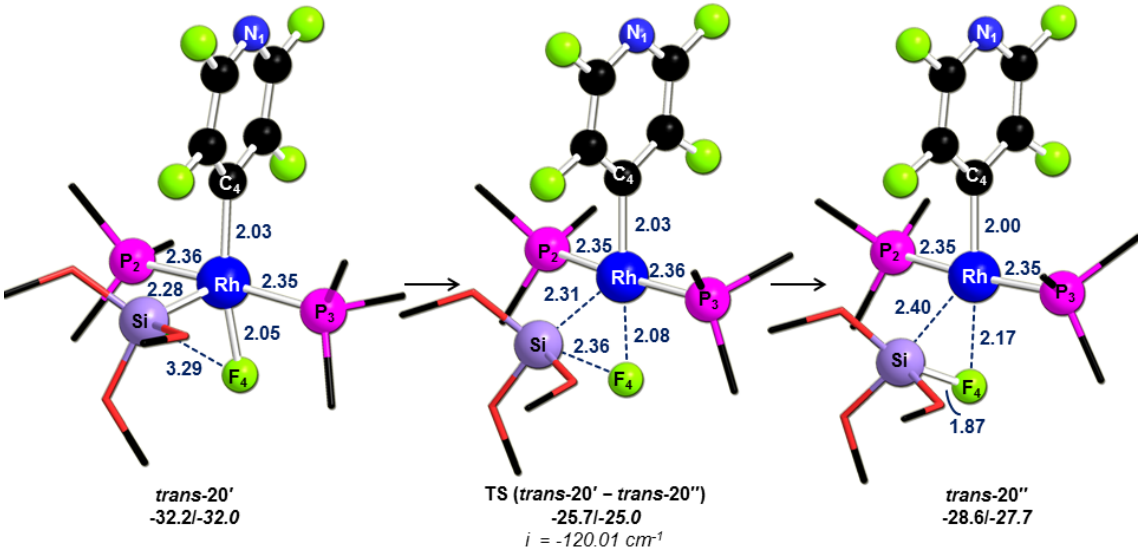

Figure 4.14: Computed geometries and energies for Si–F reductive elimination to give *trans*-20″.

The 6-coordinate intermediate ***mer*-18″** can be formed from ***trans*-20′** by binding PMe_3 trans to $Si(OMe)_3$, as shown in Figure 4.15. ***Mer*-18″** has again a distorted octahedral geometry (Si–Rh–P1 = 136.5°, Si–Rh–F4 = 50.0°). A short Si···F4 contact is also computed (1.95 Å) and reflects the Lewis acidic character of the $Si(OMe)_3$ ligand. The Si–F reductive elimination from ***mer*-18″** is accessed via **TS (*mer*-18″ – 19)** (H = -24.2 kcal/mol) by widening the P1–Rh–C4 angle to 133.4°. This transition state shows again a significant elongation of the Rh···F4 distance by 0.39 Å to 2.54 Å. In addition, the Si···F4 contact shortens to 1.76 Å and is found to be coplanar to the P1–Rh–C4 plane (α = 3.1°). Finally, the transition state **TS (*mer*-18″ – 19)** links to **19** and $FSi(OMe)_3$.

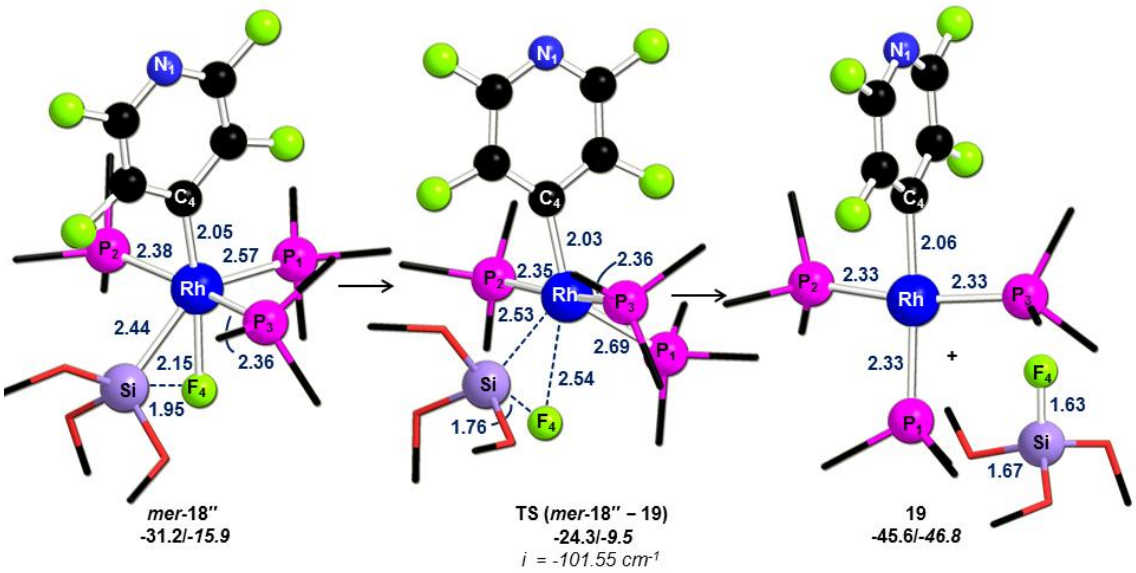

Figure 4.15: Computed geometries and energies for Si–F reductive elimination to give 19 and $FSi(OMe)_3$.

The key stationary points for the lowest pathway to yield **19** and $FSi(OMe)_3$ are shown in Figure 4.16. Computed enthalpies confirms that the rate-limiting transition state corresponds to **TS (13 – *mer*-18′)** (H = +13.2 kcal/mol) and involves the oxidative addition step. The subsequent phosphine loss/isomerisation process and Si–F reductive elimination from ***trans*-20′** are facile and involves transition states at -17.7 kcal/mol and -25.7 kcal/mol, respectively. In addition, computed free energies confirm the rate-limiting transition state as **TS (13 – *mer*-18′)** (G = +29.3 kcal/mol). Moreover, after the phosphine loss/isomerisation step, the lowest Si–F reductive elimination pathway remains via **TS (*trans*-20′ – *trans*-20″)**. This final point is similar to the formation of $[Rh(C_6F_5)(PMe_3)_3]$ and $FSiMe_3$, in which both computed enthalpies and free energies showed that the lowest pathway for Si–F reductive elimination occurred directly at the 5-coordinate ***trans*-5′** (see Section 3.2.2 in Chapter 3).

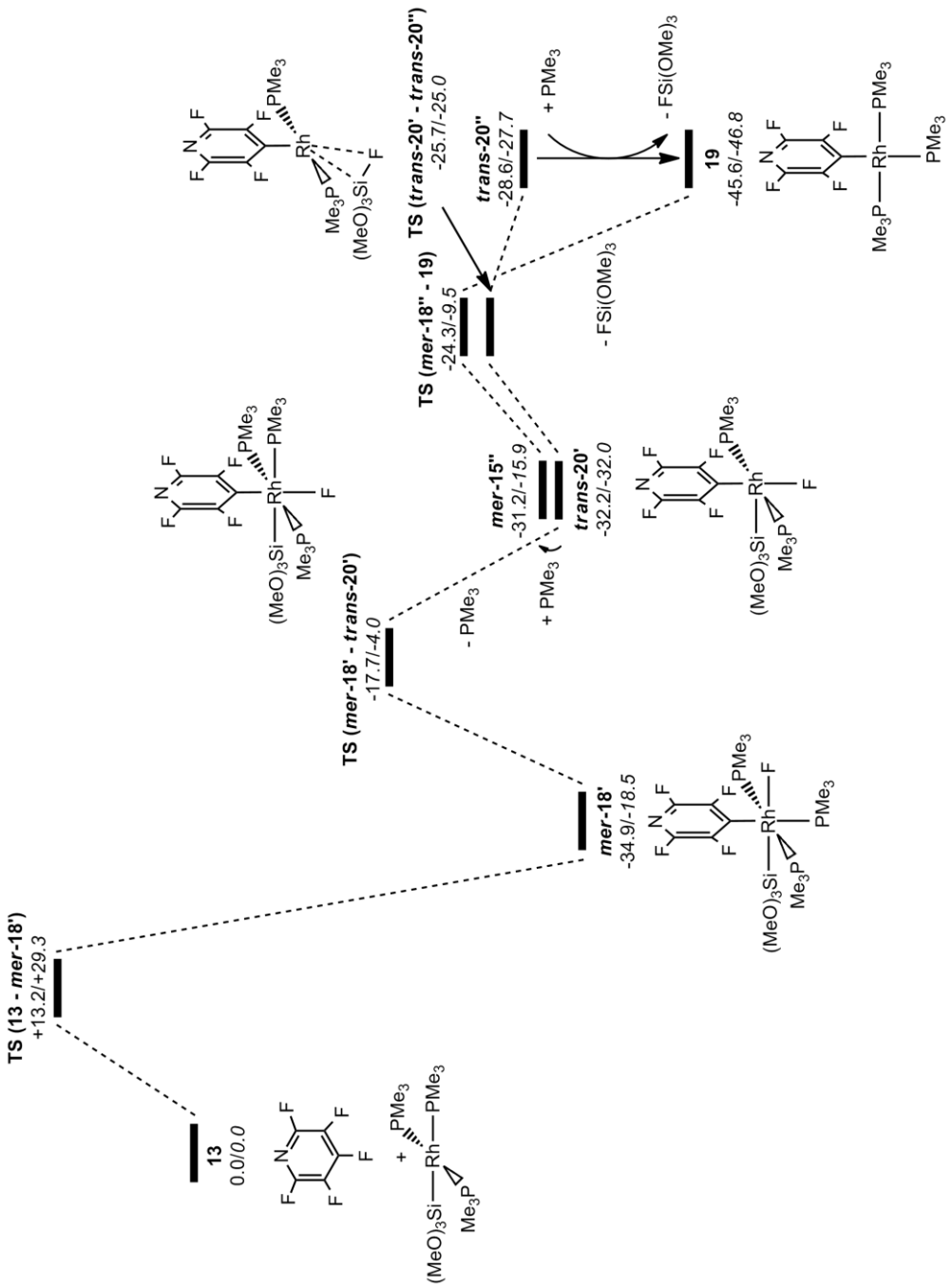

Figure 4.16: Formation of [Rh(4-C_5NF_4)(PMe_3)$_3$], 19, and $FSi(OMe)_3$ via C–F activation of C_5NF_5 at the 4-position, along Pathway 1.

In summary, calculations indicate a kinetic preference for reaction at the 4-position, via **TS (13 – *mer*-18′)**, rather than at the 2-position, through **TS (14 – *mer*-15′)** ($\Delta\Delta H^{\ddagger}$ = 4.1 kcal/mol, $\Delta\Delta G^{\ddagger}$ = 4.0 kcal/mol). This is odds with the experimental observations, therefore, another pathway must be considered in order to explain the experimental selectivity.

4.2.5 Pathway 2: Silyl-Assisted C–F Activation of C_5NF_5 at the 2-Position

This process shows the direct transfer of fluorine onto silicon with simultaneous Rh–C_{Aryl} bond formation (see Figure 4.2). The computed geometries and relative energies of the key stationary points for this process are shown in Figures 4.17-4.19. The first step is the formation of a η^2-arene intermediate **21** (H = +5.0 kcal/mol), an isomer of **14** but now the Si is axial. Species **21** shows an elongation of the C2=N1 and C2–F2 bonds to 1.39 Å and 1.43 Å, respectively. A computed transition state for formation of **21**, **TS (13 – 21)** (H = +9.6 kcal/mol) is accessed by widening the P2–Rh–P3 angle to 130.1°.

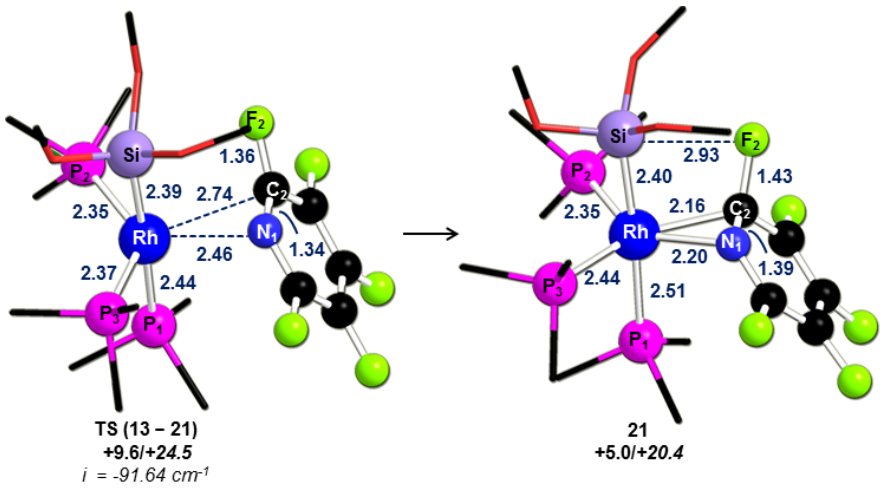

Figure 4.17: Computed geometries and energies for formation of 21.

From the η^2-arene intermediate **21**, a 4-centred transition state has been found, **TS (21 – 22)** (H = +10.2 kcal/mol), for silyl-assisted C–F activation (see Figure 4.18). In the transition state, significant elongation of the C2···F2 distance to 1.71 Å is computed while the Si···F2 contact shortens to 2.21 Å. Also, the Si–Rh–C2–F2 angle is -14.3, consistent with a silyl-assisted mechanism rather than a concerted oxidative addition. Moreover, **TS (21 – 22)** shows that the nitrogen of the pyridyl ring interacts with the metal centre (Rh–N1 = 2.17 Å) in which donation of electron density from the nitrogen atom lone pair serves to stabilise the rhodium metal centre. [60,68b] **TS (21 – 22)** links to a benzyne type complex **22** (H = -5.2 kcal/mol), similar to that previously reported by Perutz and co-workers at $[Ni(PMe_3)_2]$.[60] Complex **22** shows that $FSi(OMe)_3$ weakly interacts with the rhodium metal centre (Rh···Si = 2.57 Å).

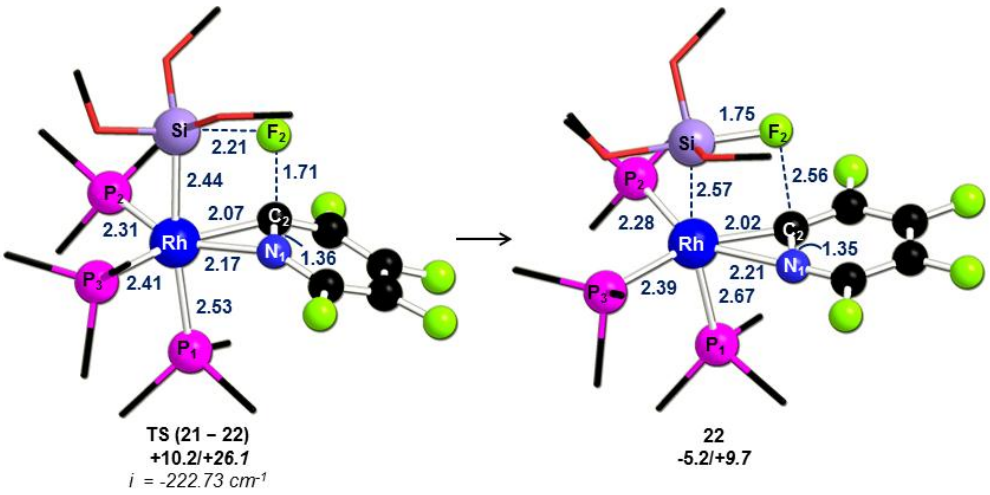

Figure 4.18: Computed geometries and energies for silyl-assisted C–F activation to give 22.

Formation of **16** and $FSi(OMe)_3$ happens from **22** via **TS (22 – 16)** (H = -4.1 kcal/mol). In the transition state, the Rh···N1 contact increases to 2.69 Å as the widening of the P1–Rh–P2 angle to 121.3° (*cf.* 97.9° in **22**) does not permit the π-back donation from the metal centre to stabilise the benzyne like species **22**. This process is relatively facile and has a computed barrier of 1.1 kcal/mol ($\Delta G^{\ddagger}$ = +1.7 kcal/mol).

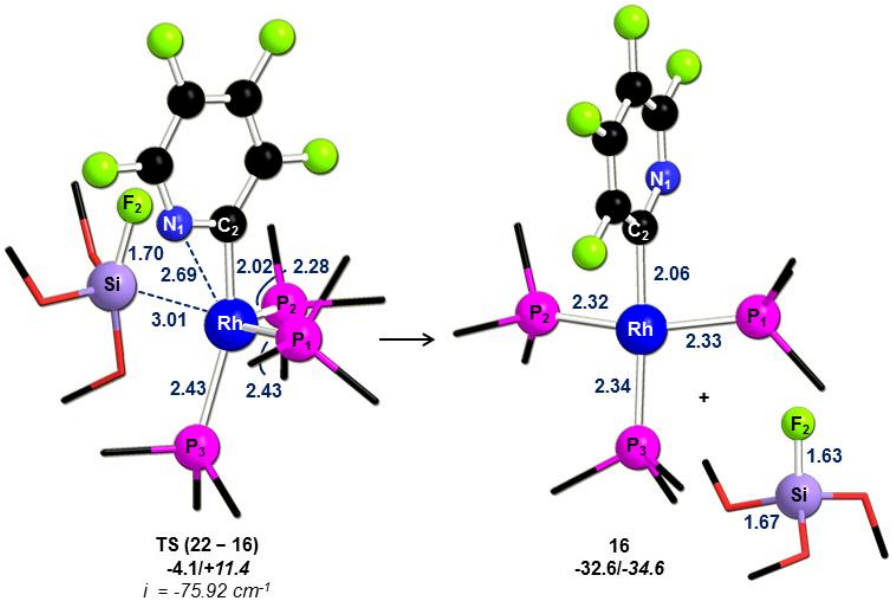

Figure 4.19: Computed geometries and energies for formation of 16 and $FSi(OMe)_3$ from the intermediate 22.

In addition to **TS (21 – 22)**, an alternative silyl-assisted transition state at the 2-position, **TS (13 – 23)** (H = +14.6 kcal/mol) has been located but found to be higher in energy (see Figure 4.20). In both of these transition states the silyl ligand is involved in the process, with Si–Rh–C2–F2 angles of -14.3° and -11.2° in **TS (21 – 22)** and **TS (13 –**

23), respectively. In addition, the Rh···N1 contact is rather long (2.85 Å) in **TS (13 – 23)** compared to **TS (21 – 22)** (2.17 Å). Knowing that **TS (13 – 23)** is higher in energy than **TS (21 – 22)** ($\Delta\Delta H^{‡}$ = 4.4 kcal/mol, $\Delta\Delta G^{‡}$ = 5.3 kcal/mol) confirms that the nitrogen atom is essential in stabilising the transition state through its lone pair. Finally, **TS (13 – 23)** links, in the reverse direction to the two separated reactants **13**, and in the forward direction to the intermediate **23** (H = -27.6 kcal/mol) in which one oxygen from the $Si(OMe)_3$ group interacts with the metal centre (Rh···O = 2.20 Å, Rh–Si = 2.43 Å).

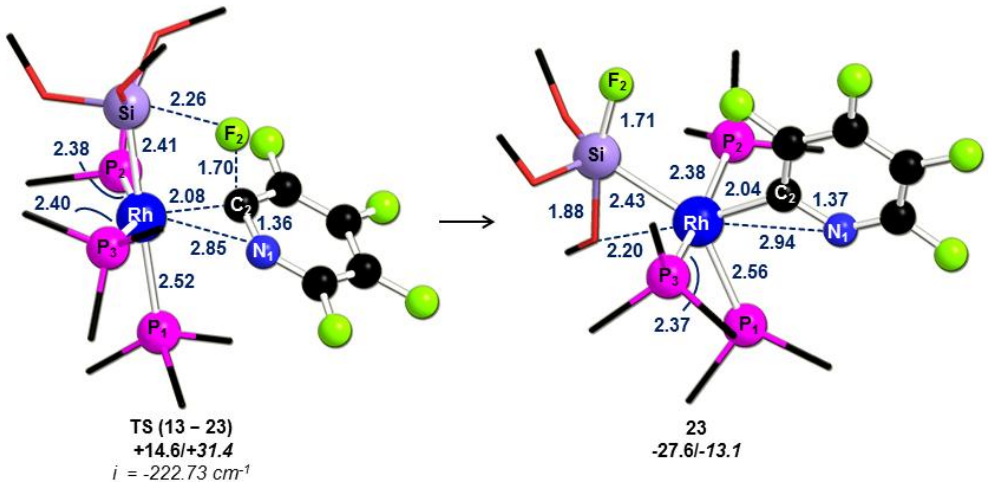

Figure 4.20: Computed geometries and energies for silyl-assisted C–F activation to give 23.

Formation **16** and $FSi(OMe)_3$ from **23** occurs by increasing the P1–Rh–C2 angle to 138.7° (*cf.* 96.9° in **23**), as shown in Figure 4.21. In the transition state **TS (23 – 16)** (H = -17.4 kcal/mol), both Rh···O and Rh···Si contacts increase to 2.61 Å and 2.49 Å, respectively.

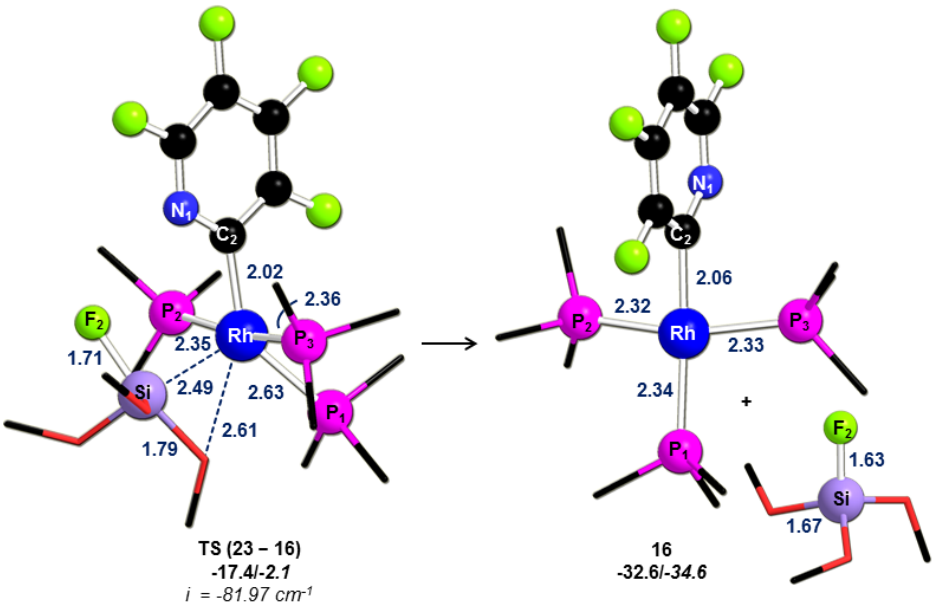

Figure 4.21: Computed geometries and energies for formation of 16 and $FSi(OMe)_3$ from 23.

The key stationary points for the lowest silyl-assisted C–F activation process are shown in Figure 4.22. Computed enthalpies show that the rate-limiting transition state corresponds to the C–F activation step through **TS (21 – 22)**, with a computed transition state located at +10.2 kcal/mol. From the benzyne-like complex **22**, formation of $[Rh(2\text{-}C_5NF_4)(PMe_3)_3]$ and $FSi(OMe)_3$ is facile ($\Delta H^{\ddagger}$ = 1.1 kcal/mol). Computed free energies do not change the rate-limiting process which is now located at +26.1 kcal/mol. Formation of the final products proceeds with a computed free energy of 11.4 kcal/mol. Overall the process is exothermic by 32.6 kcal/mol (ΔG = -34.6 kcal/mol).

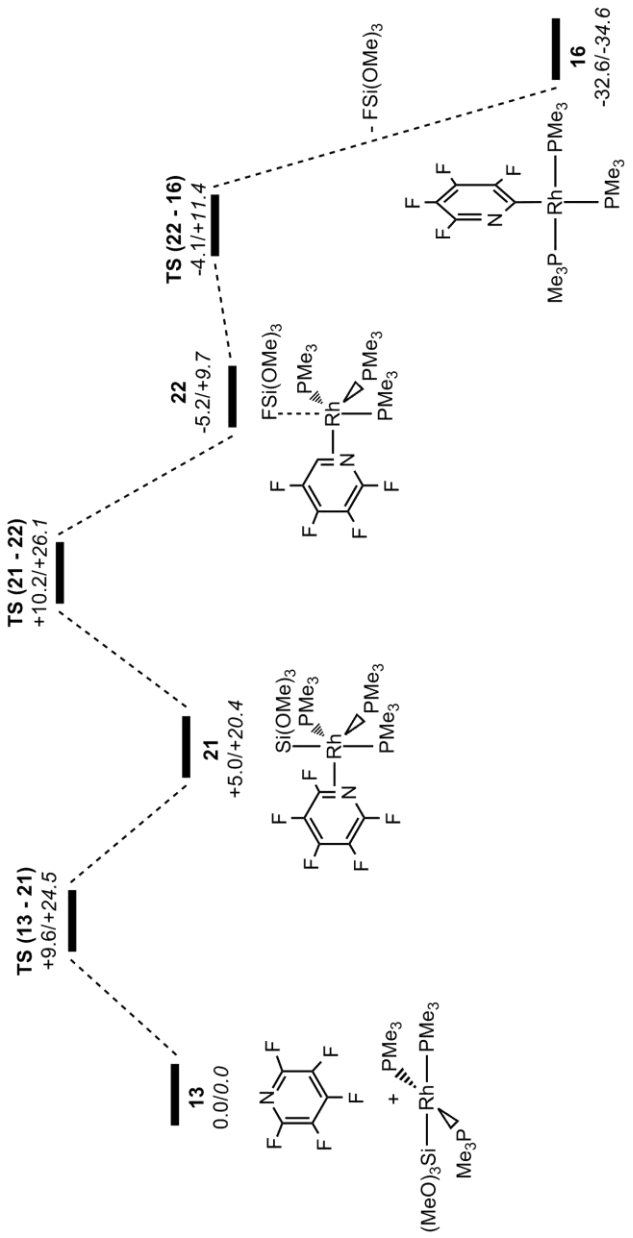

Figure 4.22: Formation of [Rh(2-C_5NF_4)(PMe_3)$_3$], 16, and $FSi(OMe)_3$ via silyl-assisted C-F activation of C_5NF_5 at the 2-position.

4.2.6 Pathway 2: Silyl-Assisted C–F Activation of C_5NF_5 at the 4-Position

In contrast with the silyl-assisted C–F activation at the 2-position, no η^2-arene species has been located for C–F activation at the 4-position. Instead the C–F cleavage occurs directly from the two separated species **13** via **TS (13 – 24)** (H = +11.9 kcal/mol, see Figure 4.23). In the transition state, the C4···F4 distance lengthens to 1.70 Å and the Si–Rh–C4–F4 angle is +14.6°. Also, both the Rh···C4 and Si···F4 distances shorten to 2.09 Å and 2.24 Å, respectively. **TS (13 – 24)**, links to the intermediate **24** (H = -33.2 kcal/mol) in which the $FSi(OMe)_3$ group interacts with the rhodium metal centre

(Rh···O = 2.19 Å, Rh–Si = 2.42 Å), as previously seen for formation of **23** via **TS (13 – 23)**.

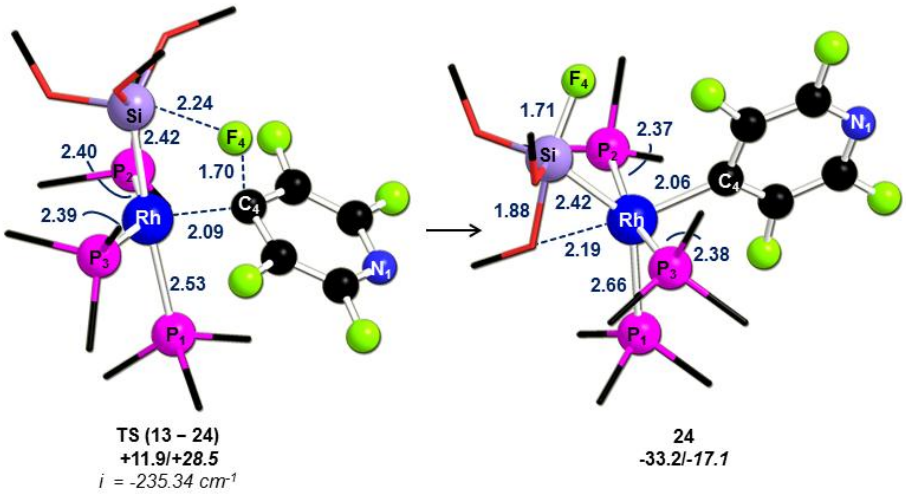

Figure 4.23: Computed geometries and energies for silyl-assisted C–F activation to form 24.

Formation of **19** and $FSi(OMe)_3$ from **24** proceeds via **TS (24 – 19)** (H = -24.4 kcal/mol, see Figure 4.24). This transition state shows the widening of the P1–Rh–C4 angle to 134.0° (*cf.* +105.3 in **24**) in order to break both Rh···O and Rh···Si interactions (Rh···O = 2.62 Å, Rh···Si = 2.52 Å).

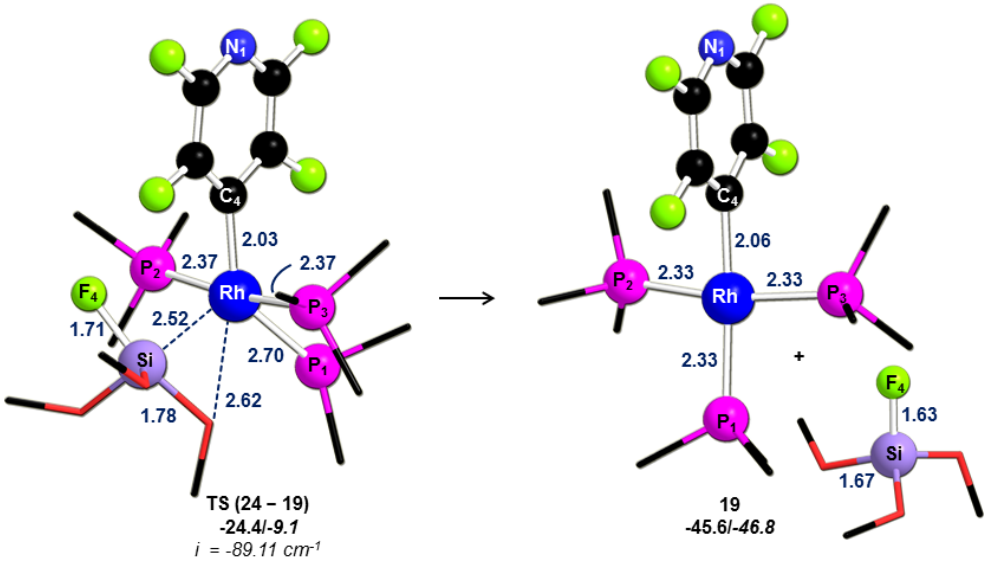

Figure 4.24: Computed geometries and energies for formation of 19 and $FSi(OMe)_3$ from 24.

The stationary points for silyl-assisted C–F activation at the 4-position are shown in Figure 4.25. As seen for the activation at the 2-position, the rate-limiting transition state

corresponds to the C–F activation via **TS (13 – 24)** with a computed enthalpy of +11.9 kcal/mol and free energy of +28.5 kcal/mol. Overall the process is exothermic by 45.6 kcal/mol (ΔG = -46.8 kcal/mol).

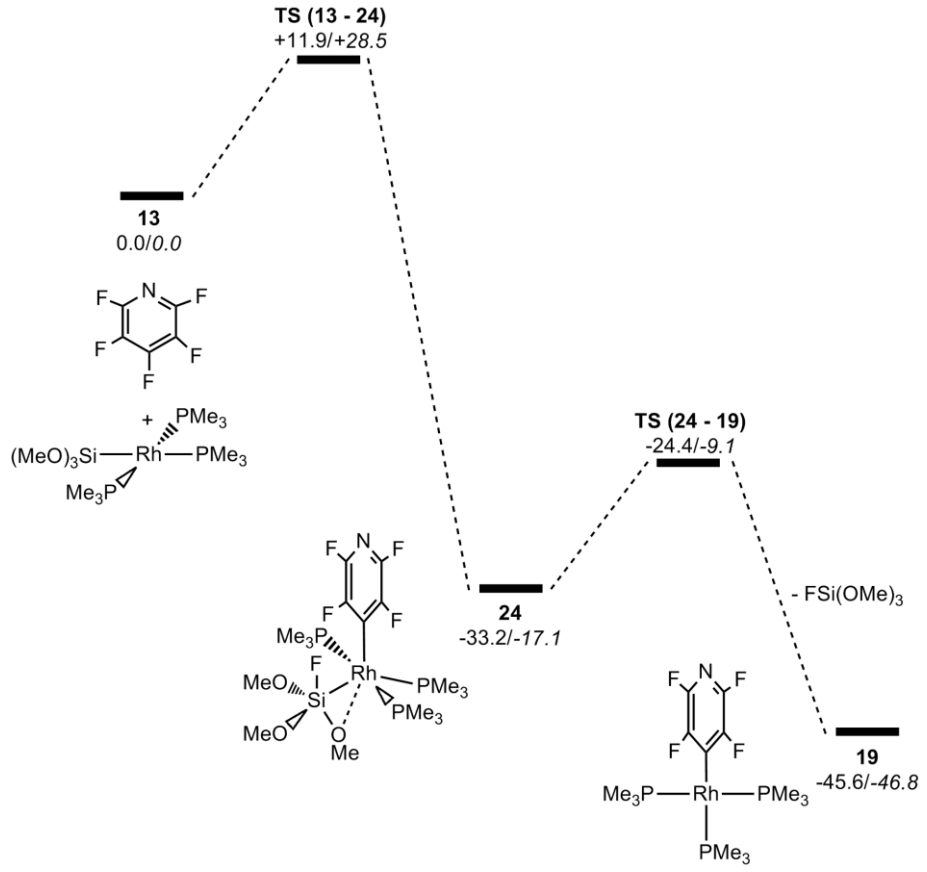

Figure 4.25: Formation of [Rh(4-C_5NF_4)(PMe_3)$_3$], 19, and $FSi(OMe)_3$ via silyl-assisted C-F activation of C_5NF_5 at the 4-position.

4.2.7 Summary for the C–F activation of C_5NF_5 at the 2- and 4-positions at ***1*$_{Si(OMe)3}$**

The rate-limiting transition states for C–F activation of C_5NF_5 at the 2- and 4-positions at **1**$_{Si(OMe)3}$ are summarised in Figure 4.26.

With oxidative addition the most accessible process corresponds to the activation at the 4-position ($\Delta H^{\ddagger}$ = +13.2 kcal/mol *cf.* $\Delta H^{\ddagger}$ = +17.3 kcal/mol at the 2-position) which is at odds with experimental observations. In contrast, silyl-assisted C–F activation favours the 2-position ($\Delta H^{\ddagger}$ = +10.2 kcal/mol *cf.* $\Delta H^{\ddagger}$ = +11.9 kcal/mol at the 4-position). Moreover, both silyl-assisted C–F activation at the 2- and 4-positions are more accessible than oxidative addition at the 4-position. This pathway accounts for the experimentally observed selectivity where both [Rh(2-C_5NF_4)(PEt_3)$_3$] and [Rh(4-

$C_5NF_4)(PEt_3)_3]$ are obtained in a 9:1 ratio in which phosphine dissociation is not required. In addition, computed free energies confirm that the lowest pathways for C–F activation at the 2- and 4-positions are via the silyl-assisted mechanism ($\Delta G^{\ddagger}$ = +26.1 kcal/mol at the 2-position, $\Delta G^{\ddagger}$ = +28.5 kcal/mol at the 4-position)

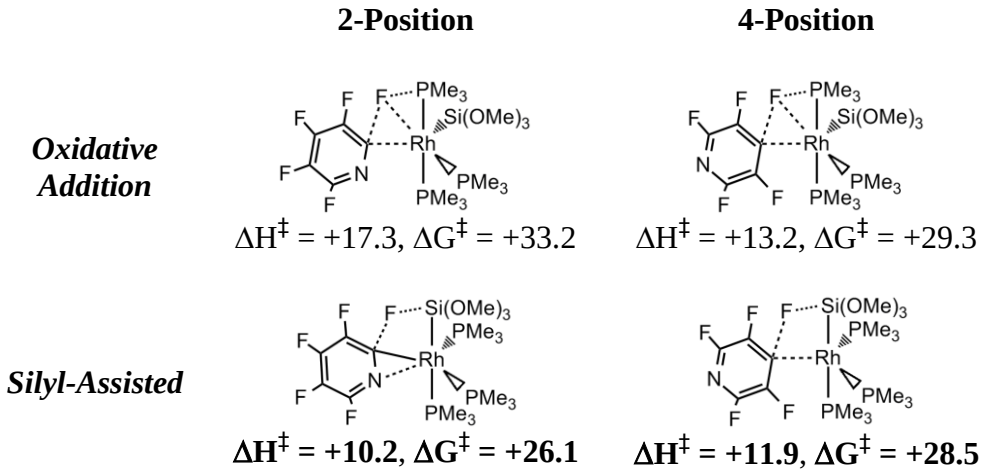

Figure 4.26: Rate-limiting transition states for C–F activation of C_5NF_5 at the 2- and 4-positions at $\mathbf{1}_{Si(OMe)3}$.

4.3 Computational Studies on the Reactions of [Rh(Bpin)(PMe_3)$_3$] with Pentafluoropyridine

4.3.1 Pathway 1: C–F Oxidative Addition of C_5NF_5 at the 2-Position

Experimentally, the reaction between [Rh(Bpin)(PEt_3)$_3$] and C_5NF_5 undergoes C–F activation at the 2-position to form [Rh(2-C_5NF_4)(PEt_3)$_3$] and FBpin (see Figure 4.1). Three distinct isomers can be formed upon oxidative addition at $\mathbf{1_{Bpin}}$: ***mer*-27**, ***fac*-27** or ***mer*-27′** (see Figure 4.2), and reaction via the last of these was found to be more accessible and so will be discussed here. In this section, all reported energies are relative to the two separated reactants, $\mathbf{1_{Bpin}}$ and C_5NF_5, denoted by **25**.

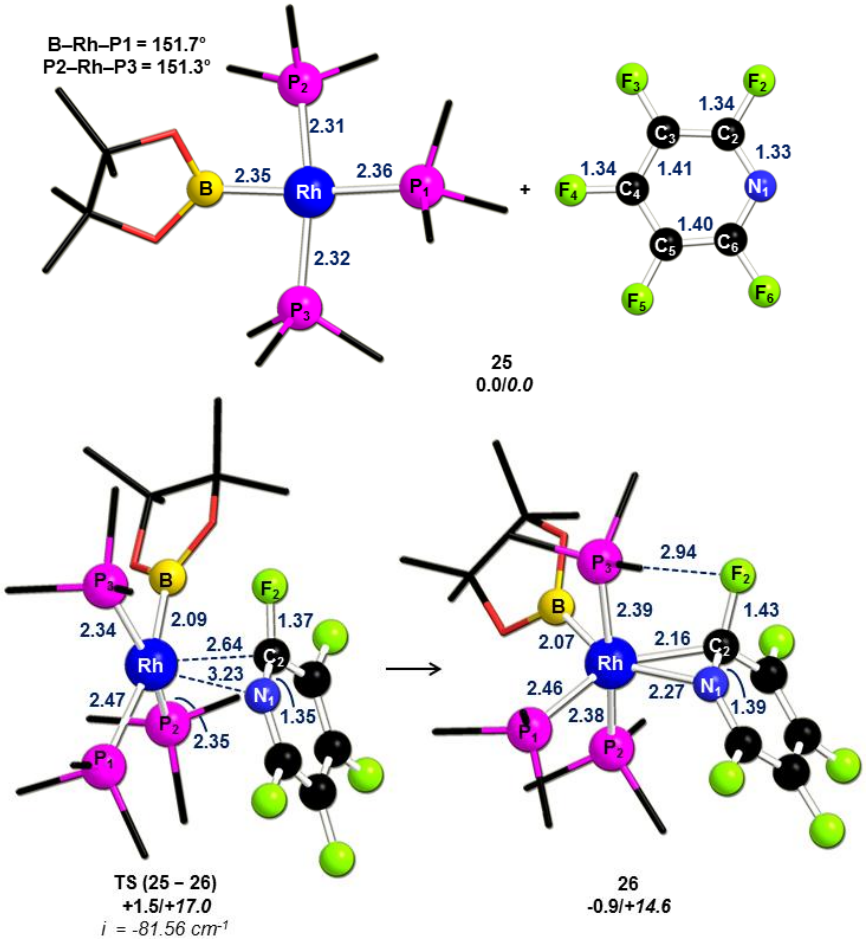

Figure 4.27: Computed geometries and energies for formation of 26.

Initially, an η^2-arene species **26** (H = -0.9 kcal/mol) is formed which is analogous to **14** in which the X ligand, in this case Bpin, is in an equatorial position. Complex **26** is formed via **TS (25 – 26)** (H = +1.5 kcal/mol) in which both B–Rh–P1 and P2–Rh–P3

angles widen to 166.0° (*cf.* 151.7° in $\mathbf{1}_{\mathbf{Bpin}}$) and 159.3° (*cf.* 151.3° in $\mathbf{1}_{\mathbf{Bpin}}$). The η^2-arene species **26** exhibits a trigonal bypiramidal geometry and shows an elongation of the C2=N1 bond due to the π-back donation from the metal centre to the π* antibonding orbital of the C_5NF_5 moiety.

C–F oxidative addition step from the η^2-adduct **26** occurs via **TS (26 – *mer*-27′)** (H = +11.2 kcal/mol, see Figure 4.28). In the transition state, the rhodium metal centre migrates away from the aromatic π system along the C2–F2 bond and therefore weakens the Rh···N1 interaction (2.73 Å). **TS (26 – *mer*-27′)** shows similar features to **TS (14 – *mer*-15′)** where the key C2···F2 distance increases to 1.70 Å and the C2···F2 vector is twisted away relative to the B–Rh–P1 angle (α = 66.4°, P3–Rh–C2–F2 = +27.2°). Also, F2 interacts with P3 (2.60 Å) and this interaction is shorter than the Rh···F2 distances (2.78 Å) which suggests a certain degree of phosphine-assistance in the process. **TS (26 – *mer*-27′)** links to the 6-coordinate species ***mer*-27′** (H = -31.8 kcal/mol).

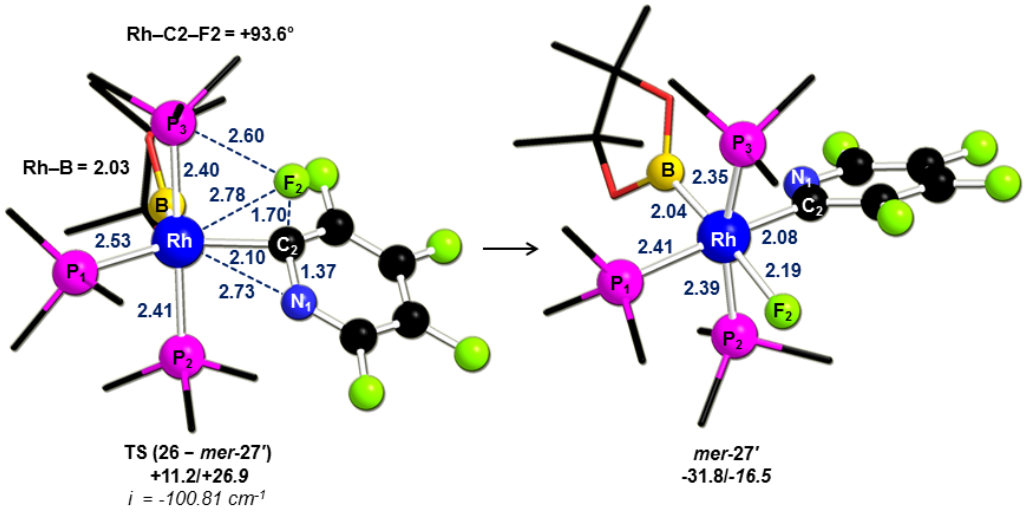

Figure 4.28: Computed geometries and energies for C–F oxidative addition to give *mer*-27′.

Species ***mer*-27′** shows that the Rh–F2 bond trans to Bpin is 2.19 Å, and therefore longer than in ***mer*-15′** (Rh–F2 = 2.15 Å, trans to $Si(OMe)_3$). This implies that Bpin has a stronger *trans*-influence than $SiOMe_3$. In ***mer*-27′**, however, the Rh–F2 distance is the same as the Rh–F1 bond (2.19 Å) in ***mer*-3′** which is trans to $SiMe_3$. This implies that Bpin and $SiMe_3$ have similar *trans*-influence and therefore the trend in terms of the *trans*-influence for the X-ligand is the following $SiMe_3 \approx$ Bpin > $Si(OMe)_3$.

4.3.2 Pathway 1: Phosphine Loss/ Isomerisation and Subsequent B–F Reductive Elimination from ***mer-27′***

Initial phosphine isomerisation step to a F/Bpin cis arrangement is achieved via **TS (*mer*-27′ – *trans*-29′)** (H = -20.1 kcal/mol) in which the phosphine ligand trans to the 2-C_5F_4N ligand dissociates (Rh···P1 = 3.45 Å, see Figure 4.29). The 5-coordinate structure undergoes spontaneous isomerisation to give ***trans*-29′** (-30.1 kcal/mol) in which the C3–F3 bond is slightly elongated to 1.37 Å.

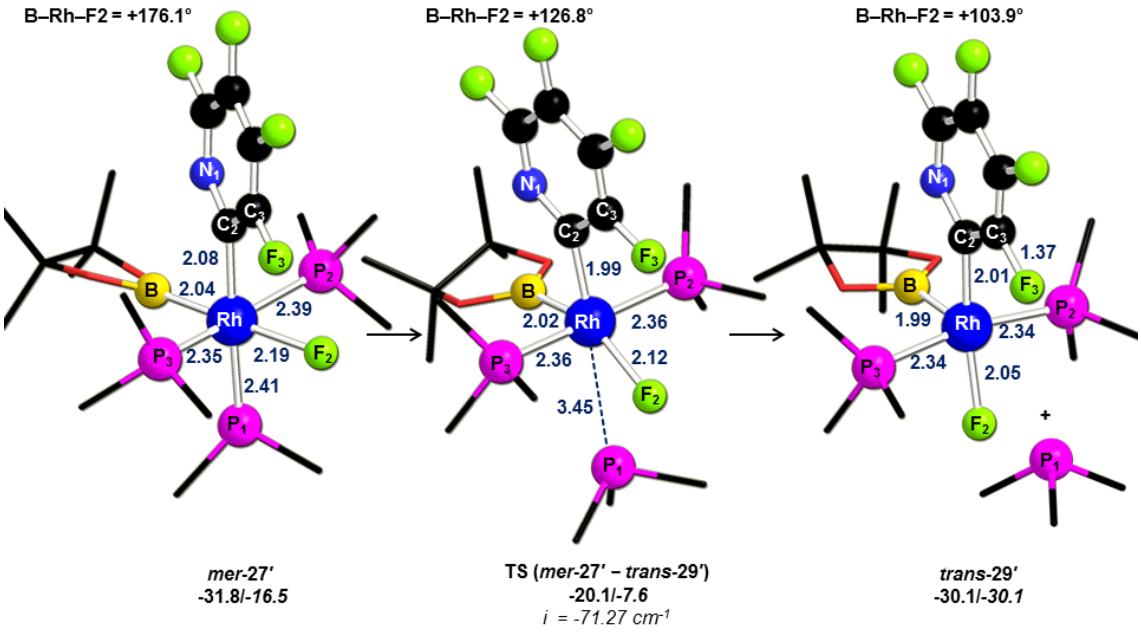

Figure 4.29: Computed geometries and energies for initial phosphine loss/isomerisation to give *trans*-29′.

B–F reductive elimination can then proceed via **TS (*trans*-29′ – *trans*-29″)** (H = -25.7 kcal/mol) in which the B···F2 contact shortens by 1.04 Å to 2.14 Å (see Figure 4.30). Finally, **TS (*trans*-29′ – *trans*-29″)** links to ***trans*-29″** (H = -34.6 kcal/mol) that can yield the final product **28** by displacing FBpin by the dissociated phosphine.

On the other hand, PMe_3 can bind ***trans*-29′** trans to Bpin to give ***mer*-27″**, from which B–F reductive elimination can occur via **TS (*mer*-27″ – 28)** (H = -32.5 kcal/mol) to yield **28** and FBpin. The *mer*″-isomer again shows a distorted octahedral geometry, however, ***mer*-27″** is less distorted (B–Rh–P1 = 151.7°, B–Rh–F2 = 76.1°) than ***mer*-15″** (Si–Rh–P1 = 141.5°, Si–Rh–F2 = 49.7°). In addition, the B···F2 contact is longer in ***mer*-27″** (2.57 Å) than the Si···F2 interaction in ***mer*-15″** (1.95 Å).

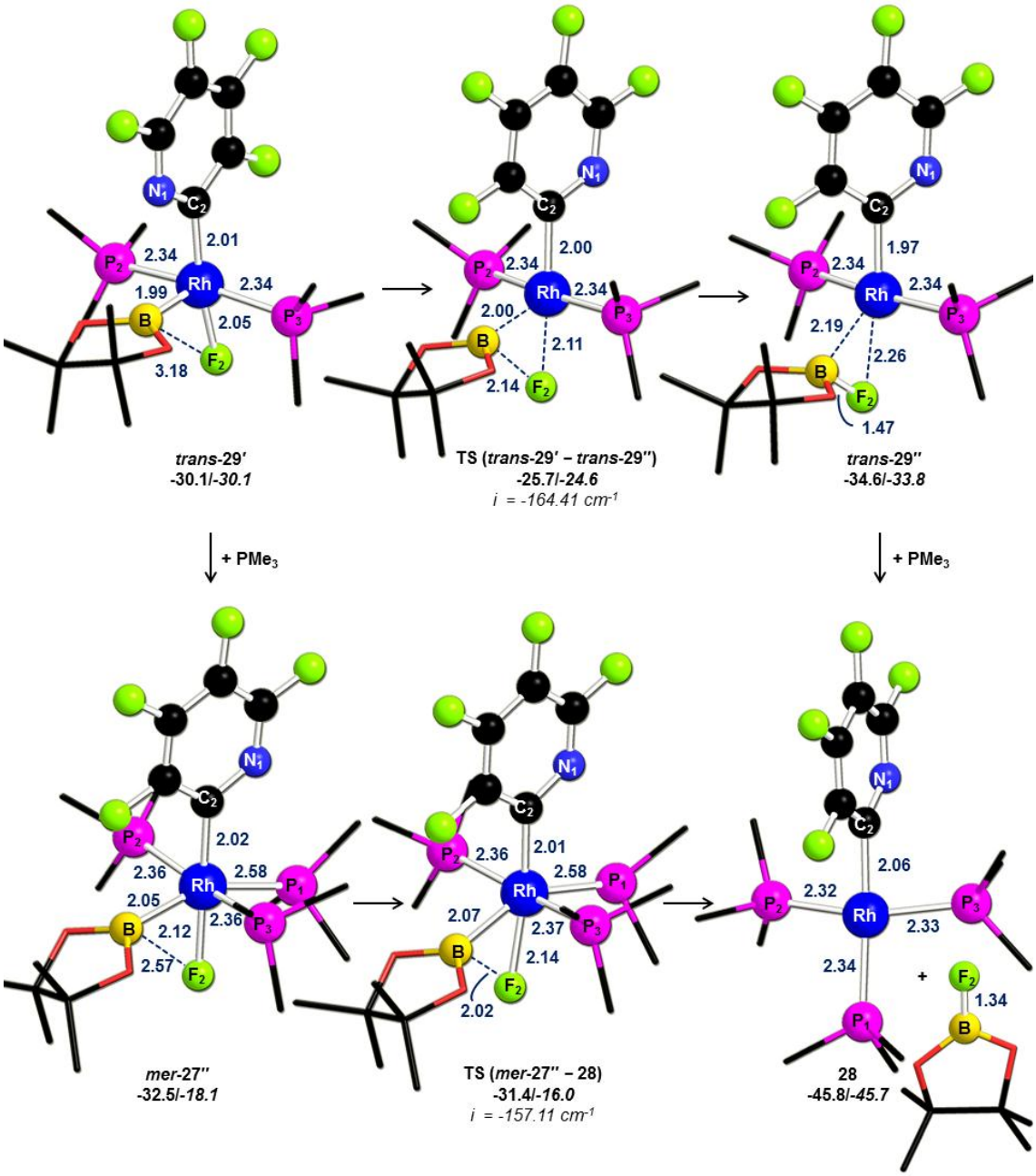

Figure 4.30: Computed geometries and energies for B–F reductive elimination from *trans*-29′ (top) and from *mer*-27″ (bottom).

B–F reductive elimination from ***mer*-27″** occurs via **TS (*mer*-27″ – 28)** by decreasing the B···F2 contact to 2.02 Å. In this case α is 1.0° and therefore consistent with a 3-centred transition state. In contrast to **TS (*mer*-15″ – 16)** which is the Si–F reductive elimination at the 2-position, **TS (*mer*-27″ – 28)** shows that the breaking Rh···F2 bond barely changes while in the former, the same bond was significantly elongated by 0.36 Å to 2.53 Å. Finally, **TS (*mer*-27″ – 28)** links to the final product **28** and FBpin.

The stationary points involved in the C–F activation of C_5NF_5 at the 2-position are shown in Figure 4.31. Overall, the rate-limiting transition state is the C–F oxidative addition step which occurs through **TS (26 – *mer*-27′)** and has a computed enthalpy of +11.2 kcal/mol. Once ***mer*-27′** is formed, subsequent phosphine loss/isomerisation and B–F reductive elimination from ***mer*-27″** are facile and involve transition states at -20.1 kcal/mol and -31.1 kcal/mol, respectively. Computed free energies confirm the C–F oxidative addition step as the rate-limiting transition state (G = +26.9 kcal/mol), however, the B–F reductive elimination now proceeds at the 5-coordinate ***trans*-29′** via **TS (*trans*-29′ – *trans*-29″)** (G = -24.6 kcal/mol). This last point is similar to formation of $[Rh(2\text{-}C_5NF_4)(PMe_3)_3]$ and $FSi(OMe)_3$ where computed enthalpies showed that this process was more accessible at the 6-coordinate species ***mer*-15″** while free energies suggested that Si–F reductive elimination at ***trans*-17′** was easier. Overall, the process for formation of **28** and FBpin is exothermic by 45.8 kcal/mol (ΔG = -45.7 kcal/mol).

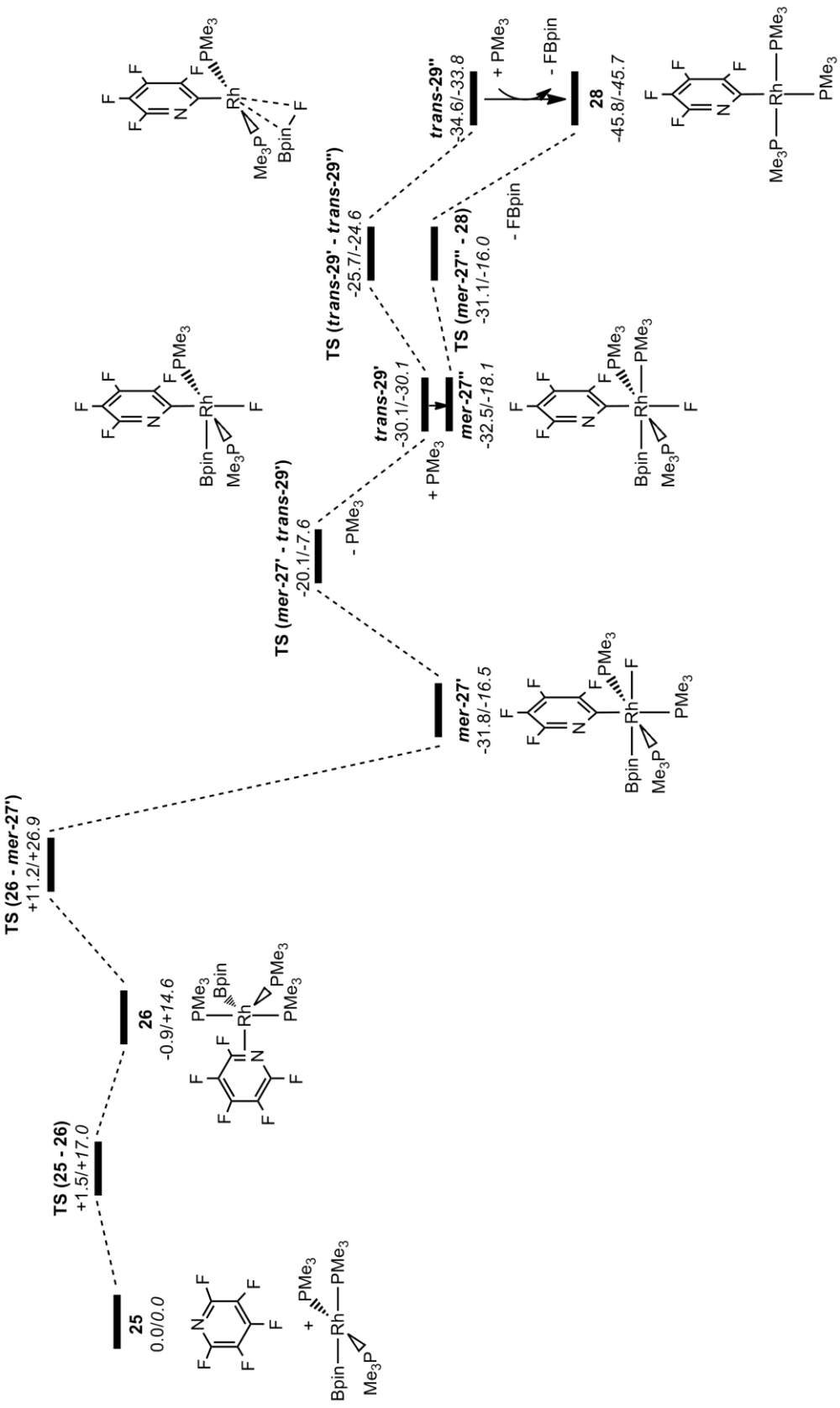

Figure 4.31: Formation of [Rh(2-C_5NF_4)(PMe_3)$_3$], 28, and FBpin via C-F activation of C_5NF_5 at the 2-position, along Pathway 1.

4.3.3 Pathway 1: C–F Oxidative Addition of C_5NF_5 at the 4-Position

The first step on the lowest energy pathway for C–F activation at the 4-position is the formation of the η^1-arene species **30** through **TS (25 – 30)** (H = -3.4 kcal/mol) in which the Bpin ligand is in an axial position (see Figure 4.32). In the transition state, the C_5NF_5 moiety approaches the rhodium metal centre forming a weak Rh···C4 contact (2.82 Å) while both the P2–Rh–P3 and B–Rh–P1 angles widen to 158.7° (*cf.* 151.7° in $\mathbf{1_{Bpin}}$) and 170.0° (*cf.* 159.3° in $\mathbf{1_{Bpin}}$), respectively. **TS (25 – 30)** links to the η^1-arene species **30** in which the fluoroaromatic moiety is loosely bound to the complex (Rh···C4 = 2.32 Å).

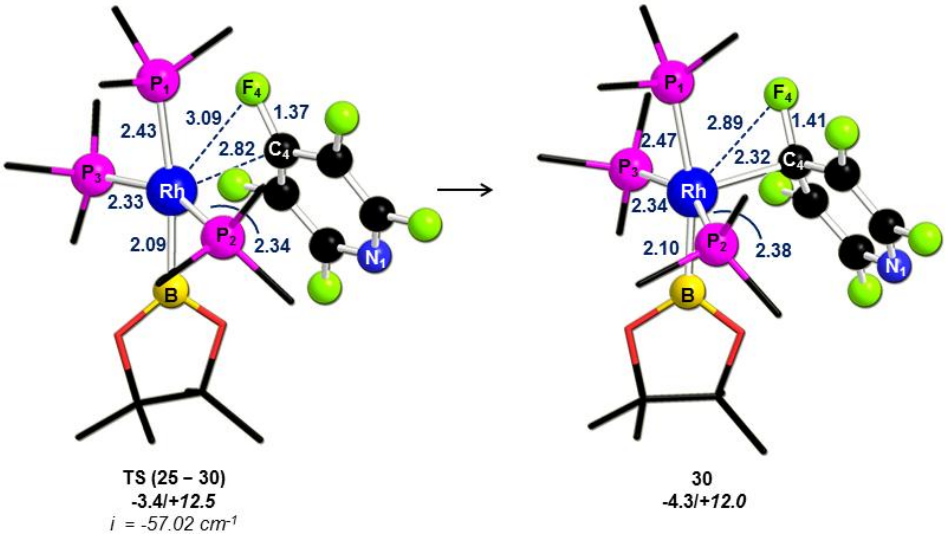

Figure 4.32: Computed geometries and energies for formation of 30.

Complex **30** shows an elongation of the C4–F4 bond to 1.41 Å and allows the location of **TS (30 – *mer*-31′)** (H = +5.8 kcal/mol, see Figure 4.32). In the transition state, the key C4···F4 distance increases to 1.61 Å while α and the P3–Rh–C4–F4 angles are 66.4° and +27.1°, respectively. In addition, the Rh···F4 contact remains rather long (2.77 Å) while a shorter P3···F4 interaction is computed (2.65 Å), which suggest a degree of phosphine-assistance during the C–F cleavage. **TS (30 – *mer*-31′)** links to the 6-coordinate species, ***mer*-31′** (H = -41.6 kcal/mol) in which F is trans to B.

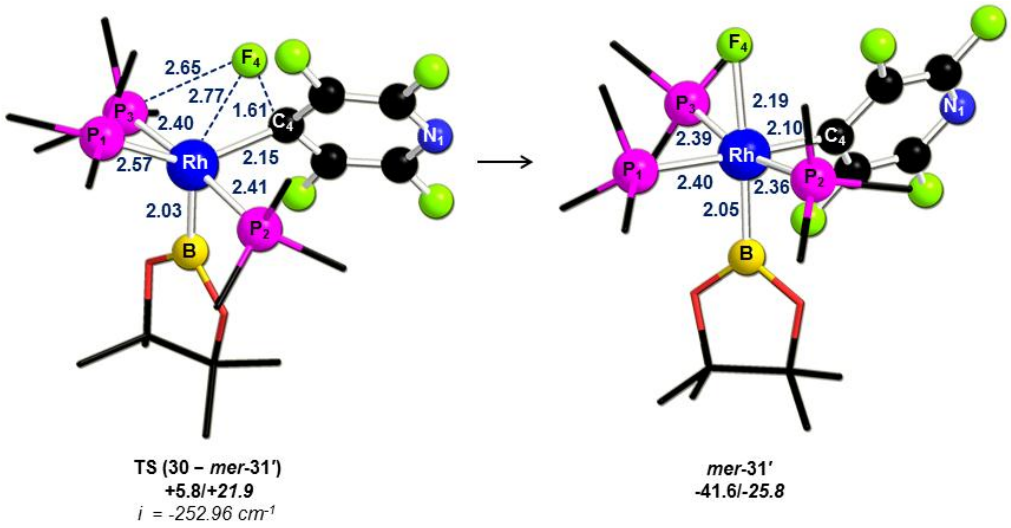

Figure 4.33: Computed geometries and energies for C–F oxidative addition to give *mer*-31′.

4.3.4 Pathway 1: Phosphine Loss/ Isomerisation and Subsequent B–F Reductive Elimination from ***mer-31′***

The stationary points involved in this process are shown in Figures 4.34 and 4.35.

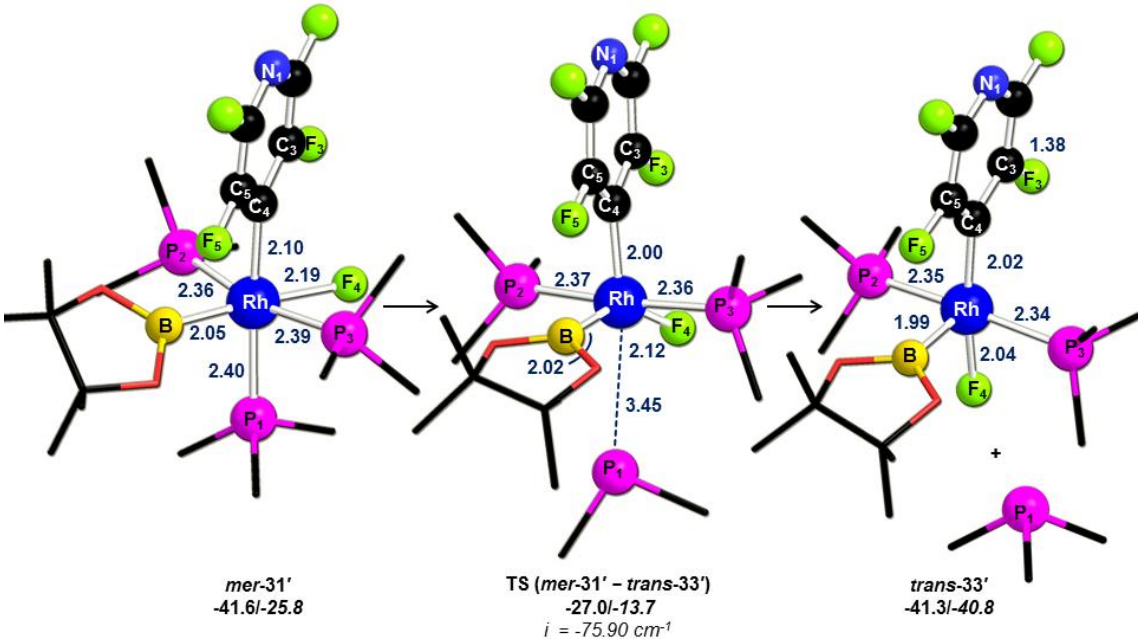

Figure 4.34: Computed geometries and energies for initial phosphine loss/isomerisation to give *trans*-35′.

The initial phosphine loss/isomerisation step prior to B–F reductive elimination proceeds via **TS (*mer*-31′ – *trans*-33′)** (H = -27.0 kcal/mol) in which the Rh···P1 distance increases to 3.45 Å trans to 2-C_5NF_4. **TS (*mer*-31′ – *trans*-33′)** links to the square pyramidal structure ***trans*-33′**. An elongation of the C3–F3 bond to 1.38 Å is

also computed due to weak Rh···C3 and Rh···F3 contacts of 2.93 Å and 3.02 Å, respectively.

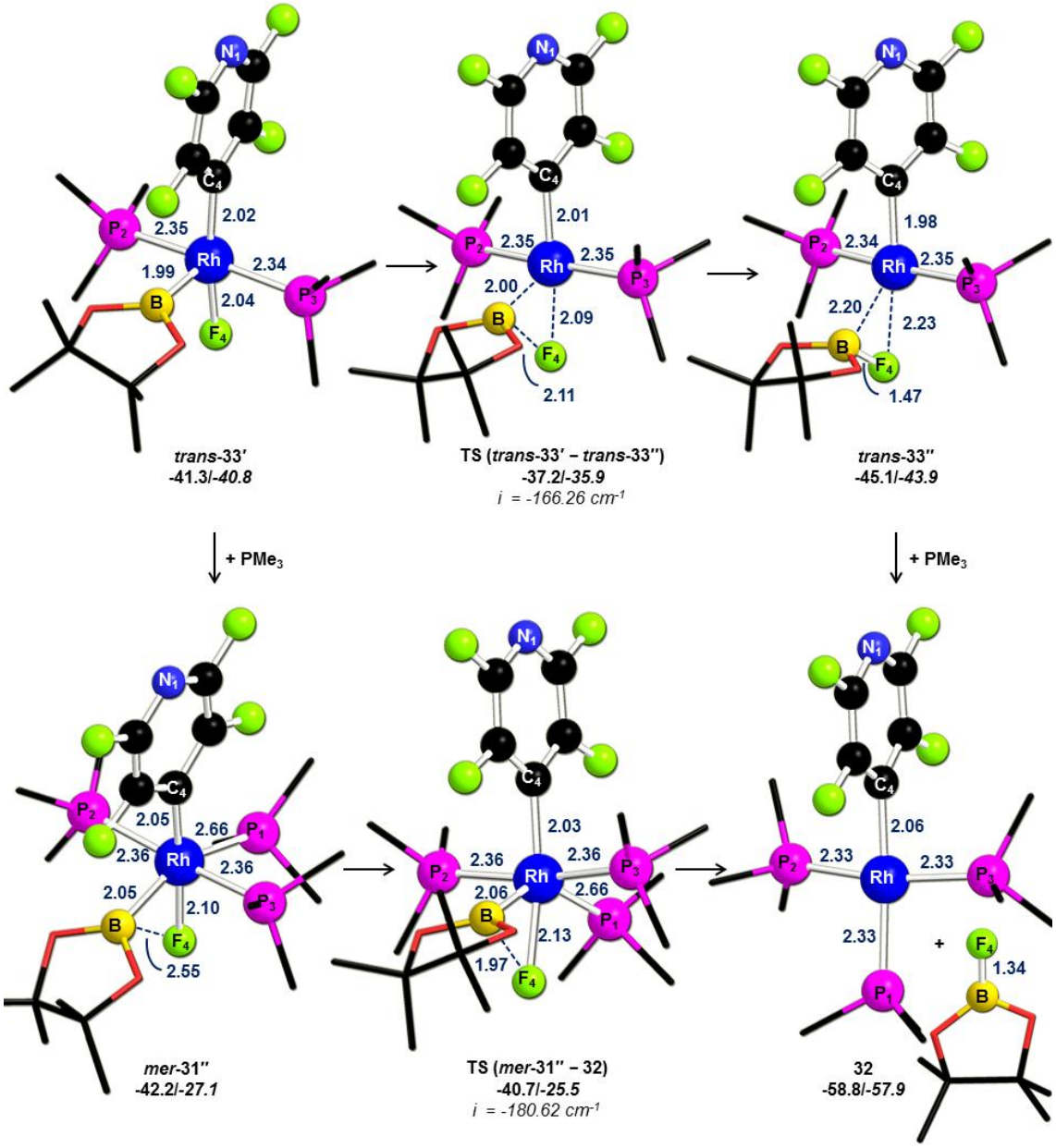

Figure 4.35: Computed geometries and energies for B–F reductive elimination from *trans*-33′ (top) and from *mer*-31″ (bottom).

From the 5-coordinate structure ***trans*-33′** (H = -41.3 kcal/mol) B–F reductive elimination happens through **TS (*trans*-33′ – *trans*-33″)** (H = -37.2 kcal/mol) with the shortening of the B···F4 contact to 2.11 Å (*cf.* 3.00 in ***trans*-33′**). IRC calculations showed that **TS (*trans*-33′ – *trans*-33″)** links to ***trans*-33″** (H = -45.1 kcal/mol) from which FBpin can be displaced by the dissociated phosphine to give **32**.

B–F reductive elimination via **TS (*mer*-31″ – 32)** (H = -40.7 kcal/mol) starts with the formation of ***mer*-31″**. In ***mer*-31″**, the B–Rh–P1 and B–Rh–F4 angles are 148.3° and 76.0°, respectively, while the B···F4 contact is 2.55 Å. In the transition state, as seen for the B–F reductive elimination at the 2-position, the main change is the shortening of the B···F contact by 0.58 Å to 1.97 Å. In addition, α is 0.3, coherent with a 3-centred transition state for reductive elimination.

The reaction profile for C–F activation at the 4-position is shown in Figure 4.36. Again, the rate-limiting transition state is the C–F oxidative addition step (H = +5.8, G = +21.9 kcal/mol) which involves **TS (30 – *mer*-31′)**. After formation of ***mer*-31′**, subsequent phosphine loss/isomerisation and B–F reductive elimination are facile. Computed enthalpies show that the lowest pathway for B–F reductive elimination occurs at the 6-coordinate species ***mer*-31″** (**TS (*mer*-31′ – 32)**, H = -40.7 kcal/mol) while computed free energies suggest that the process happens at ***trans*-33′** (**TS (*trans*-33′ – *trans*-33″)**, G = -35.9 kcal/mol). Overall, the process is exothermic by 58.8 kcal/mol (G = -57.9 kcal/mol).

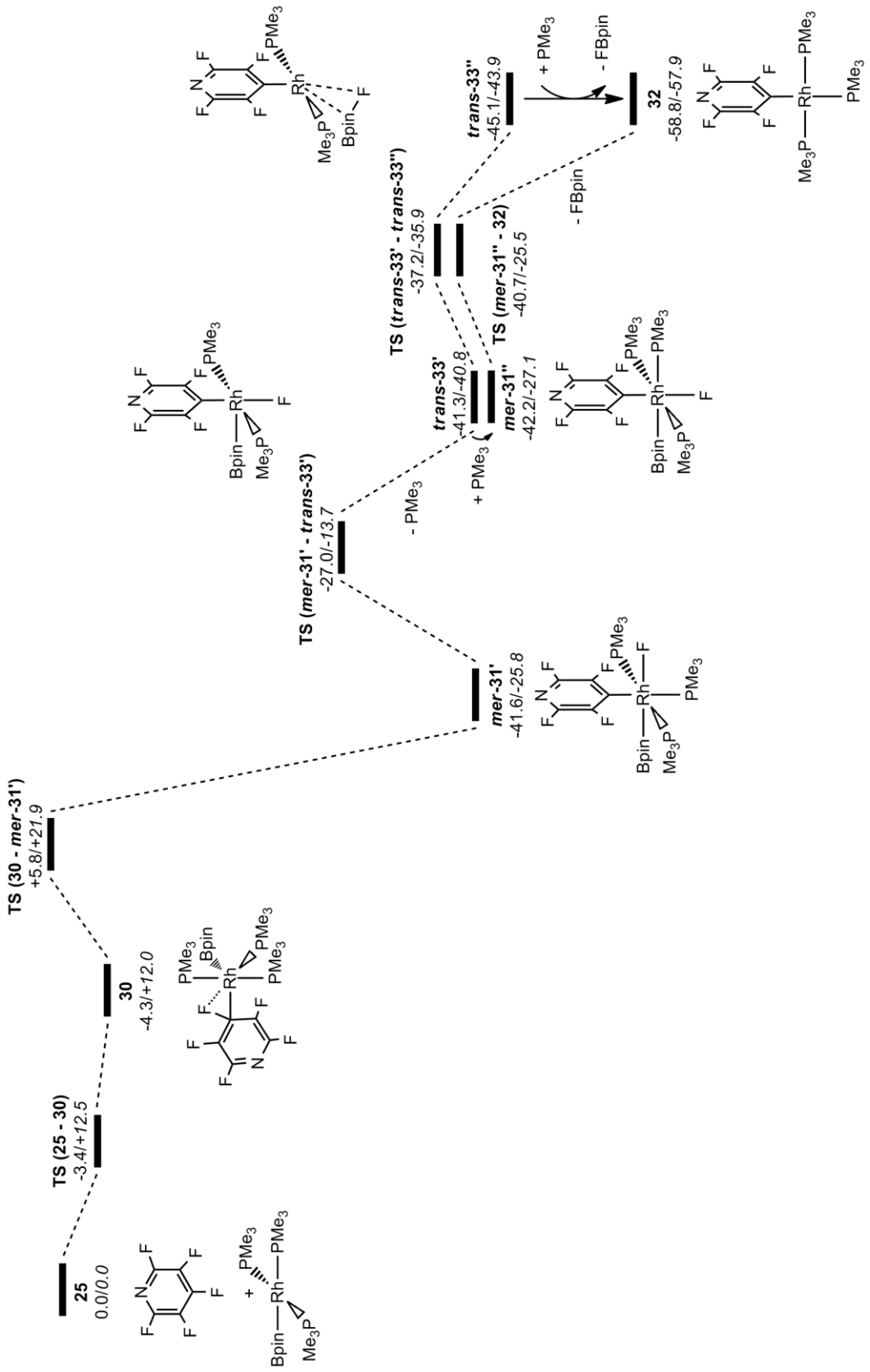

Figure 4.36: Formation of [Rh(2-C_5NF_4)(PMe_3)$_3$], 32, and FBpin via C-F activation of C_5NF_5 at the 4-position, along Pathway 1.

4.3.5 Pathway 2: Boryl-Assisted C–F Addition of C_5NF_5 at the 2- and 4-Positions

The computed and relative energies of the stationary points for boryl-assisted C–F activation at the 2- and 4-positions are compared in Figure 4.37. C–F activation at the 2-position starts with formation of a trigonal bipyramidal η^2-arene species **34** (H = -2.3 kcal/mol) in which both C2=N1 and C2–F2 bonds lengthen to 1.39 Å and 1.44 Å, respectively. In contrast, activation at the 4-position initially forms a square pyramidal η^1-intermediate **35** in which the C4–F4 increases to 1.40 Å due to a short Rh–C4 contact (2.27 Å). The η^2-arene intermediate is formed via **TS (25 – 34)** (H = +3.8 kcal/mol) in which the P2–Rh–P3 angle widens to 149.1° (*cf.* 111.6° in **34**) and the C2=N1 shorten to 1.35 Å. On the other hand, **TS (25 – 35)** (H = -0.8 kcal/mol) which gives **35** has been located by lengthening the Rh···C4 bond to 2.85 Å.

From **34** and **35**, two transition states, **TS (34 – 28)** and **TS (35 – 32)**, for boryl-assisted C–F activation at the 2- and 4-positions, respectively, have been located. The key feature of **TS (34 – 28)** is the short Rh–N1 interaction (2.22 Å) which stabilises the transition state as seen for the equivalent silyl-assisted process at the 2-position and previously reported.[60,68b] In addition, the B–Rh–C2–F2 angle is -13.1°, consistent with a boryl-assisted C–F activation mechanism. **TS (34 –28)** leads to a shallow intermediate in which FBpin is weakly bound through boron, as seen for formation of **22** in which $FSi(OMe)_3$ interacts with Rh. Formation of the products **28** and FBpin then occurs by extension of the Rh–B distance and the barrier to this step was found to cost less than 0.2 kcal/mol.

In contrast, C–F activation at the 4-position proceeds via **TS (35 – 32)** (H = +10.0 kcal/mol). In the transition state, the Rh–C4 bond is fully formed (2.07 Å) while the breaking C4···F4 bond increases to 1.76 Å and the B–Rh–4–F4 angle is +22.8°. In terms of the C···F and B···F contacts, **TS (35 – 32)** has a late geometry compared to **TS (34 –28)**, consistent with its higher energy. **TS (35 – 32)** links as well to a shallow intermediate as described previously for **TS (34 –28)** and the final product **32** and FBpin are formed by breaking the Rh–B interaction.

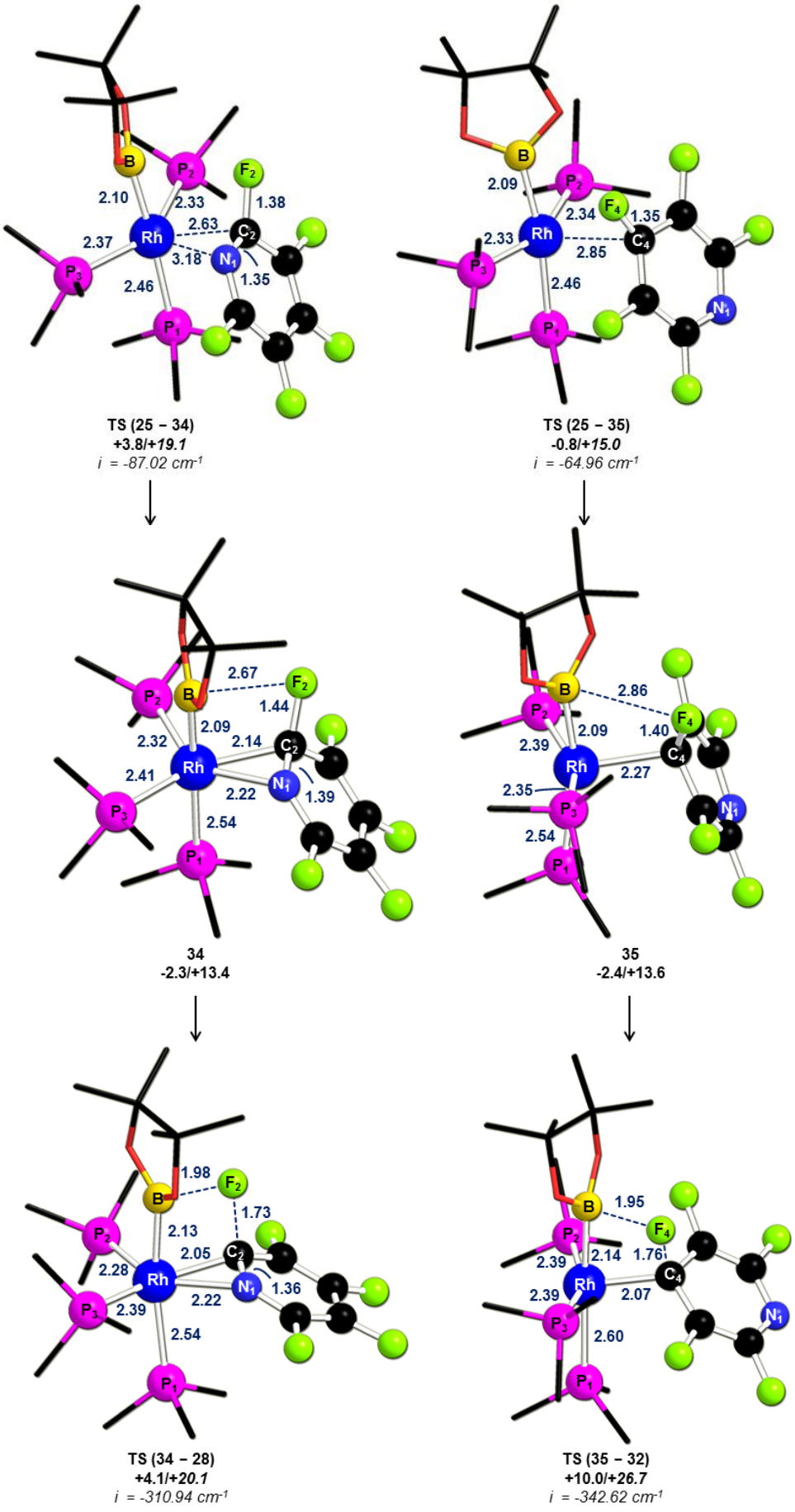

Figure 4.37: Computed geometries and energies for boryl-assisted C–F activation at the 2- (left) and 4-positions (right) to give 28 and 32, respectively, plus FBpin.

The reaction profiles for boryl-assisted C–F activation at the 2- and 4-positions are compared in Figure 4.38. In both cases the rate-limiting transition states correspond to the C–F activation. In addition, boron-assisted C–F activation favours the activation at the 2-position ($\Delta H^{\ddagger}$ = +4.1 kcal/mol *cf.* $\Delta H^{\ddagger}$ = +10.0 kcal/mol at the 4-position).

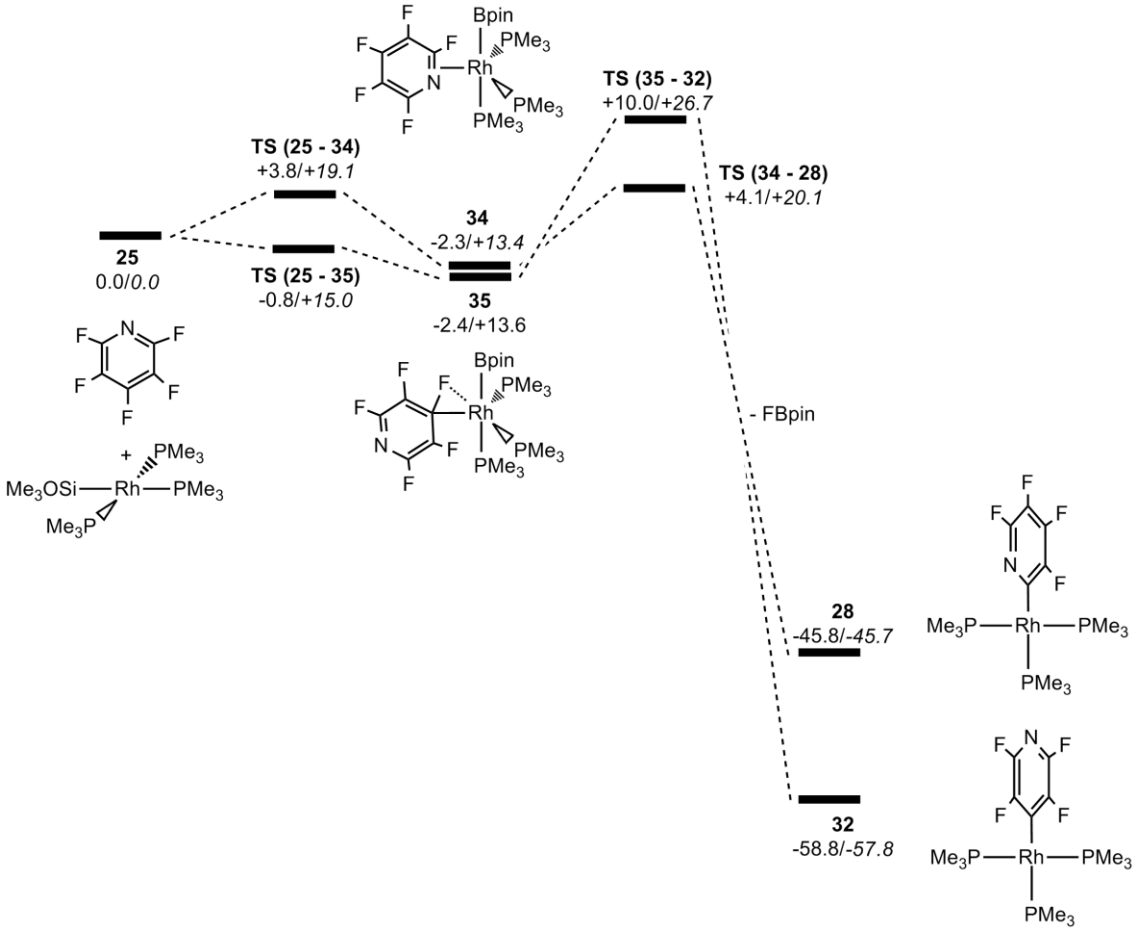

Figure 4.38: Computed geometries and energies (kcal/mol) for boryl-assisted C–F activation at the 2- and 4-positions via 34 and 35, respectively.

This contrasts with the C–F oxidative addition where activation at the 4-position was lower in energy ($\Delta H^{\ddagger}$ = +5.8 kcal/mol *cf.* $\Delta H^{\ddagger}$ = +11.2 kcal/mol at the 2-position), as shown in Figure 4.39. Moreover, boron-assisted C–F activation at the 2-position is now more accessible than oxidative addition at the 4-position and therefore accounts for the experimental selectivity. It should be, however, noted that the two transition states for boryl-assisted at the 2-position and oxidative addition at the 4-position are relatively close in energy. However, experimentally the [Rh(4-C_5NF_4)(PEt_3)$_3$] product is not observed.

	2-Position	4-Position
Oxidative Addition	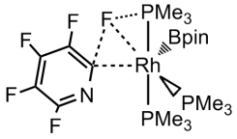	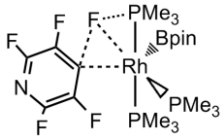
	$\Delta H^{‡}$ = +11.2, $\Delta G^{‡}$ = +26.9	**$\Delta H^{‡}$ = +5.8, $\Delta G^{‡}$ = +21.9**
Boryl-Assisted	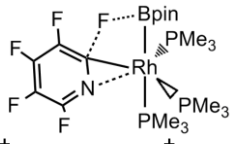	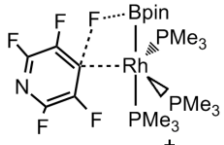
	$\Delta H^{‡}$ = +4.1, $\Delta G^{‡}$ = +20.1	$\Delta H^{‡}$ = +10.0, $\Delta G^{‡}$ = +26.7

Figure 4.39: Rate-limiting transition states for C–F activation of C_5NF_5 at the 2- and 4-positions.

4.4 Comparisons of Ligand-Assisted C–F Activation Processes at [Rh(X)(PMe$_3$)$_3$] (X = Si(OMe)$_3$, Bpin)

The lowest pathways for C–F activation of C_5NF_5 at the 2-position, which occurs in both cases via a ligand-assisted C–F activation, are shown in Figure 4.40. All energies (kcal/mol) are related to the two separated reactants, [Rh(X)(PMe$_3$)$_3$] and C_5NF_5. Also, free energies are in italics and selected distances are given in Å.

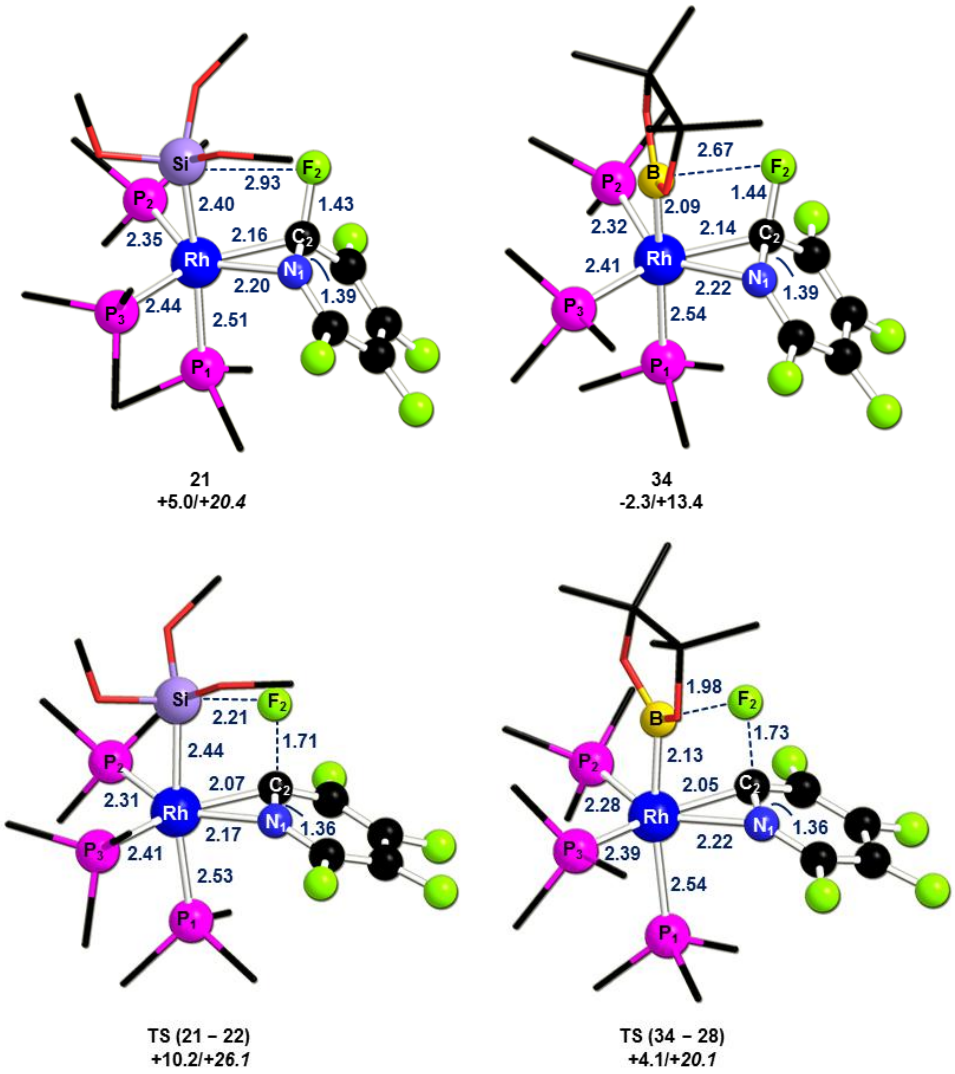

Figure 4.40: Computed geometries and energies for the trigonal bipyramidal η^2-intermediate and transition states for C–F activation of C_5NF_5 at the 2-position for ligand-assisted C–F activation.

Both silyl- and boryl-assisted C–F activation proceeds via initial formation of a trigonal bipyramidal η^2-precursor, **21** and **34**, respectively. In **21**, the Rh–C2 bond (2.16 Å) is slightly longer than in **34** (Rh···C2 = 2.14 Å) and the Rh···N1 interaction is shorter in the former (2.20 Å *cf.* 2.22 Å in **34**). More interestingly, the X···F2 contact is stronger

in **34** than **21**, being respectively 2.67 Å and 2.93 Å. This difference of 0.26 Å may be due to the better Lewis acidic character of the Bpin ligand. In addition, **34** is found to be 7.3 kcal/mol (ΔG = +7.0 kcal/mol) more stable than **21**.

In the transition states, **TS (21 – 22)** and **TS (34 – 28)**, the Si···F2 and B···F2 interactions decrease by 0.72 Å and 0.69 Å, respectively, while both Rh–C2 bonds shorten by 0.09 Å. The major difference between the two transition states is found in the Rh···N1 contact which shortens by 0.03 Å in **TS (21 – 22)** whereas this interaction remains constant at 2.22 Å in **TS (34 – 28)**. This last feature may suggest that the nitrogen lone pair in **TS (21 – 22)** needs to stabilise slightly more the transition state while for the boryl-assisted C–F activation this contact was already made in the trigonal bipyramidal η^2-precursor **34**. In addition, the computed barriers for silyl- and boryl-assisted C–F activation are +5.2 kcal/mol and +6.4 kcal/mol, respectively, relative to the η^2-precursor. Computed free energies show that the computed barriers are again very similar, being +5.7 kcal/mol and +6.7 kcal/mol, respectively. Therefore, the transition state for boryl-assisted C–F activation (H = +4.1 kcal/mol) is lower than **TS (21 – 22)** (H = +10.2 kcal/mol) only because the η^2-precursor **34** prior to C–F activation is more stable.

It should be mentioned that experimentally C–F activation of C_5NF_5 at [Rh(Bpin)(PEt_3)$_3$] occurs at -25 °C while the reaction with [Rh($SiOEt_3$)(PEt_3)$_3$] happens at room temperature. In addition, the lowest pathway for C–F activation proceeds via either silyl- or boryl-assisted C–F activation in which the activation barrier relative to the most stable precursor (see above) is similar. Therefore the temperature dependence of these catalysts is not well reproduced in the calculations. However, the important point in this chapter is to understand why C–F activation of C_5NF_5 is observed experimentally at the 2-position. In this case, DFT calculations reproduced properly this last feature.

4.5 Conclusions

Density functional theory calculations have been used to model the reaction between $[Rh(X)(PEt_3)_3]$ (X = $Si(OMe)_3$ or Bpin) and C_5NF_5. Calculations showed that the unusual experimental selectivity at the 2-position (i.e the C–F bond *ortho* to the pyridyl nitrogen) is obtained via novel ligand-assisted C–F activation mechanisms, silyl- or boron-assisted. Both of these processes involve direct transfer of fluorine onto either silicon or boron via a 4-centred transition state. In addition, these mechanisms show that the selective activation at the 2-position arises due to a stabilising Rh···N1 contact in the relevant transition state.

Chapter 5: Catalytic Hydrodefluorination of Pentafluorobenzene by $[Ru(H)_2(CO)(NHC)(PPh_3)_2]$: An Explanation for the Unusual *Ortho*-Regioselecivity

5.1 Introduction

The aim of this chapter is to model the hydrodefluorination (HDF) reaction reported by Whittlesey and co-workers (see Figure 5.1).[15f] Experimentally, the HDF of C_6F_5H at ruthenium N-heterocyclic carbene (NHC) complexes, $[Ru(H)_2(CO)(NHC)(PPh_3)_2]$ (**36**$_{NHC}$, NHC = SIMes, SIPr, IMes, IPr, see Figure 5.1) occurs at 70 °C in THF to give in high selectivity (> 90 %) 1,2,3,4-$C_6F_4H_2$ and $[Ru(F)(H)(CO)(NHC)(PPh_3)_2]$ (**45**$_{NHC}$, see Figure 5.1). Isolation of **45**$_{NHC}$ shows that it can react in the presence of trialkylsilanes to release $FSiR_3$ and restart the catalytic cycle.

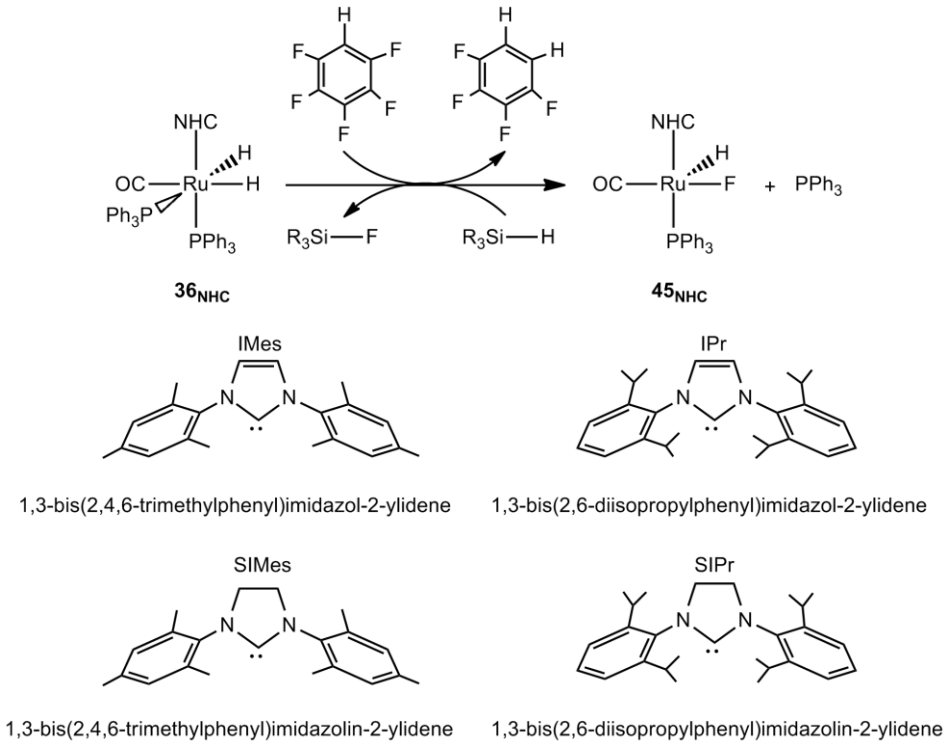

Figure 5.1: Catalytic HDF of C_6F_5H at 36_{NHC} in the presence of trialkylsilane.[15f]

Experimentally, the reaction is shut down when 3 equivalents of PPh_3 are added, which implies a phosphine dissociation step. In addition, kinetic studies showed a first-order dependence with respect to the concentration of both C_6F_5H and the ruthenium precursor, while a zero-order dependence is observed on the concentration of silane.[15f] These last observations suggest that the rate-limiting step is contained within the HDF

of C_6F_5H. This is in contrast with Holland's results which showed that the rate-determining is the reaction between the β-diketiminate iron(II) and silane.[15c]

5.1.1 Proposed Mechanism for Catalytic HDF of C_6F_5H

The most unusual feature of the Whittlesey system is that the HDF of C_6F_5H results in a high regioselectivity for the formation of 1,2,3,4-$C_6F_4H_2$ (see Figure 5.1) in complete contrast to the Milstein[15a,15b] and Holland[15c] systems in which 1,2,4,5-$C_6F_4H_2$ is formed experimentally. To account for this unusual *ortho*-regioselectivity, the involvement of a tetrafluorobenzyne intermediate (**42$_{NHC}$**) has been postulated that could be formed by successive C–H and *ortho*-C–F activation of C_6F_5H (see Figure 5.2). The first step of the catalytic cycle may result in phosphine dissociation to create a vacant site at the metal centre and give [Ru(H)$_2$(CO)(NHC)(PPh$_3$)] (**38$_{NHC}$**). C–H activation rather than C–F activation can occur from **38$_{NHC}$** via oxidative addition/metathesis reactions in which H_2 is released to form [Ru(C_6F_5)(H)(CO)(NHC)(PPh$_3$)] (**41$_{NHC}$**). Subsequent *ortho*-C–F activation can happen at **41$_{NHC}$** to form a tetrafluorobenzyne intermediate **42$_{NHC}$**. This type of structure has already been observed experimentally[82] and a computational[83] study by Hall and Wu showed this type of structure is accessible. Indeed, the authors studied the C–H and the C–Cl activation of C_6ClH_5 at {Ir(PNP}$^+$ (PNP = bis(Z-2-(dimethylphosphino)vinyl)amino) and showed that the lowest pathway for C–Cl activation proceeds via a benzyne intermediate ($\Delta G^{\ddagger}$ = +24.2 kcal/mol). Species **43$_{NHC}$** can be formed from **42$_{NHC}$** by subsequent hydrogen transfer from Ru to the ring. Then, H_2 can recoordinate the metal centre to give **44$_{NHC}$** and subsequent σ-bond metathesis leads to the hydrodefluorinated product, 1,2,3,4-$C_6F_4H_2$ and **45$_{NHC}$**. Finally, **45$_{NHC}$** reacts with silane to restart the catalytic cycle.

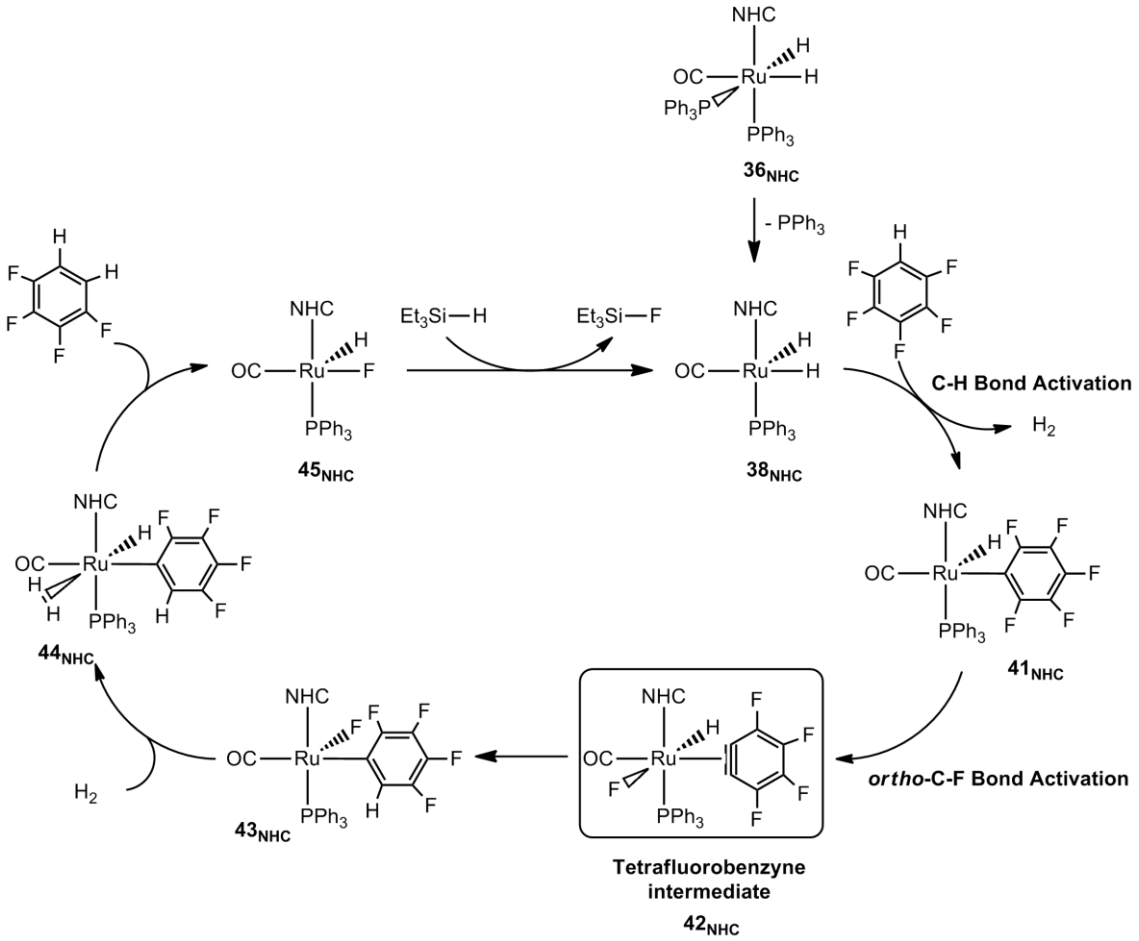

Figure 5.2: Postulated mechanism for the HDF of C_6F_5H to yield 1,2,3,4-$C_6F_4H_2$ via formation of 42_{NHC}.[15f]

5.1.2 Comparison between Experimental and Calculated Structures

The first step was to compute the model species $[Ru(H)_2(CO)(IMe)(PH_3)]$ (**36′** IMe = IMe = 1,3-dimethylimidazol-2-ylidene) and $[Ru(F)(H)(CO)(IMe)(PH_3)]$ (**45′**) used to study the HDF of C_6F_5H. In addition, the X–ray crystallographic structures of $[Ru(H)_2(CO)(IMes)(PPh_3)]$ (**36_{IMes}**) and $[Ru(F)(H)(CO)(IMes)(PPh_3)]$ (**45_{IMes}**) have also been optimised. From these different structures, bond lengths and bond angles were compared with the reported experimental data (see Table 5.1 and Figure 5.3).[15f] It should be also mentioned that complexes **36_{IMes}** and **45_{IMes}** have been computed as they will be studied computationally in the HDF of C_6F_5H (see Section 5.5). In addition, bond lengths and bond angles for **36_{IMes}** and **45_{IMes}** in Table 5.1 are the ones computed from the X–ray crystallographic structures, however, lower conformations (< 0.5 kcal/mol) have been obtained from the extensive conformation searching. In contrast, in the mechanistic study the lowest conformation is always used.

Table 5.1: Experimental (Exp.) and calculated (Calc.) bond lengths (Å) and bond angles (degrees) in $[Ru(H)_2(CO)(NHC)(PH_3)_2]$.[15f]

	36′	**36_{IMes}**		**45′**	**45_{IMes}**	
	Calc.	Calc.	Exp.	Calc.	Calc.	Exp.
Ru–C8	2.063	2.085	2.0956 (17)	2.064	2.062	2.077 (2)
Ru–P1	2.365	2.426	2.3628 (4)	–	–	–
Ru–P2	2.326	2.377	2.2985 (5)	2.367	2.396	2.3403 (6)
Ru–C7	1.903	1.907	1.9145 (17)	1.826	1.821	1.820 (3)
Ru–F5	–	–	–	2.018	2.048	2.0315 (13)
P1–Ru–C8	96.18	103.182	104.94 (5)	–	–	–
P2–Ru–C8	162.07	151.257	146.33 (5)	172.93	173.75	173.28 (6)
N1–C8–N2	102.87	101.59	101.55 (14)	103.45	103.59	103.61 (18)
C7–Ru–F5	–	–	–	165.30	169.00	174.13 (16)

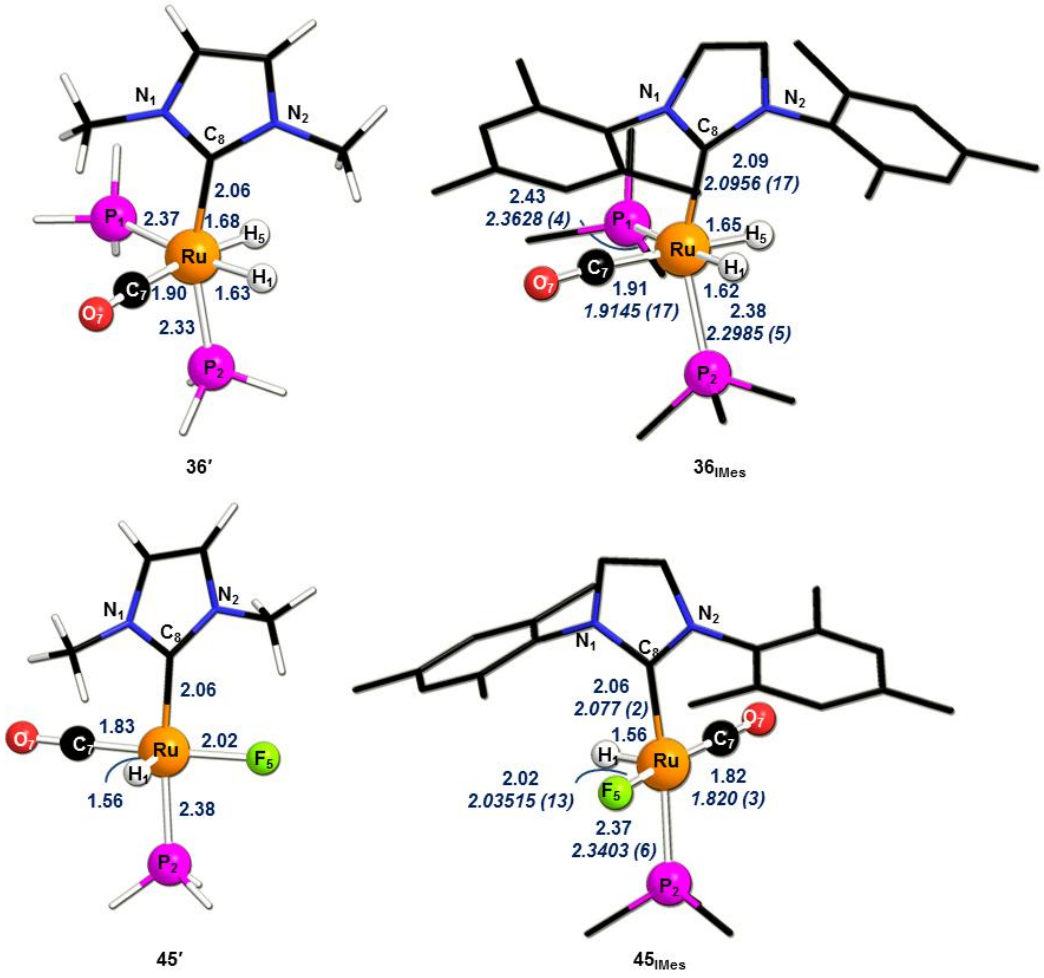

Figure 5.3: Computed geometries (with selected key distances in Å) in 36′, 36_{IMes}, 45′ and 45_{IMes}. Experimental bond lengths for 36_{IMes} and 45_{IMes} are shown in italics while phosphine Ph groups are truncated at the *ipso* carbon centre and non-participating hydrogen atoms are omitted.[15f]

Complex **36′** shows an elongation of the Rh–P1 bond by 0.04 Å, trans to H1, compared to the Ru–P2 bond, trans to NHC, which implies a higher *trans*-influence of the hydride ligand. This last feature is seen in **36$_{IMes}$** as well, in which calculated and experimental structures show an elongation of the Ru–P1 bond by 0.05 Å and 0.06 Å, respectively. In addition, the X-ray crystallographic structure **36$_{IMes}$** has a slightly distorted octahedral geometry with P1–Ru–C8 and P2–Ru–C8 angles of 104.94° and 146.33°, respectively. The calculated species also show a distortion in the geometry, however, this is less pronounced (P2–Ru–C8 = 151.26°). This small distortion was not seen in **36′**, probably due to the use of less bulky substituents on the NHC and phosphine ligands. The computed bond lengths and bond angles in **36$_{IMes}$** are in reasonable agreement with the reported experimental data. The major discrepancy results in the elongation of the Ru–P1 and Ru–P2 bond which are overestimated in the computed species **36$_{IMes}$** by 0.06 Å and 0.08 Å.

The calculated structure **45′** shows a small elongation of the Ru–P2 bond by 0.04 Å compared to the reactant **36′.** In addition, the Ru–C7 bond is shorter in **45′** (1.826 Å), trans to F5, than in **36′** (Ru–C7 = 1.903 Å), trans to H5. This may be explained by a weaker *trans*-influence of fluorine ligand compared to hydride ligand or by a "push-pull" effect.[84] Similar trends are observed in the calculated and experimental structures of **45$_{IMes}$**. In addition, the bond lengths and bond angles are relatively well represented in the calculated species **45$_{IMes}$** compared to the experimental data. Again, the major difference is the Ru–P2 bond which is slightly more elongated in the calculated structure with a bond length of 2.40 Å (*cf.* 2.34 Å in experimental species **45$_{IMes}$**).

5.2 Computational Studies on the Reaction of $[Ru(H)_2(CO)(IMe)(PH_3)]$ with C_6F_5H: Identification of a Tetrafluorobenzyne Intermediate

DFT studies have been performed on the reaction of C_6F_5H at the computational model $[Ru(H)_2(CO)(IMe)(PH_3)_2]$ (**36′**, IMe = 1,3,-dimethylimidazol-2-ylidene) in order to test the presence of a tetrafluorobenzene intermediate (**42′**) and therefore explain the unusual *ortho*-regioselectivity observed experimentally.

In this chapter, all selected key distances are in Å and all energies (kcal/mol) are self-consistent field (SCF) energies, in contrast to Chapters 3 and 4. This choice is useful as it highlights certain key intermediates essential to the discussion. Indeed, by considering enthalpy these intermediates were found to be higher than the preceding transition states. In addition, free energies will not be discussed as all reactions involve equivalent dissociative and associative processes. In Sections 5.2-5.4, all energies are quoted relative to the two separated reactants, **36′** and C_6F_5H, together denoted as **37′**.

The first step is therefore dissociation of PH_3 to yield the 5-coordinate species **38′** (E = +25.8 kcal/mol), as shown in Figure 5.4. The major change in **38′** is the shortening of the Ru–H1 bond to 1.56 Å, as a vacant site is created trans to H1.

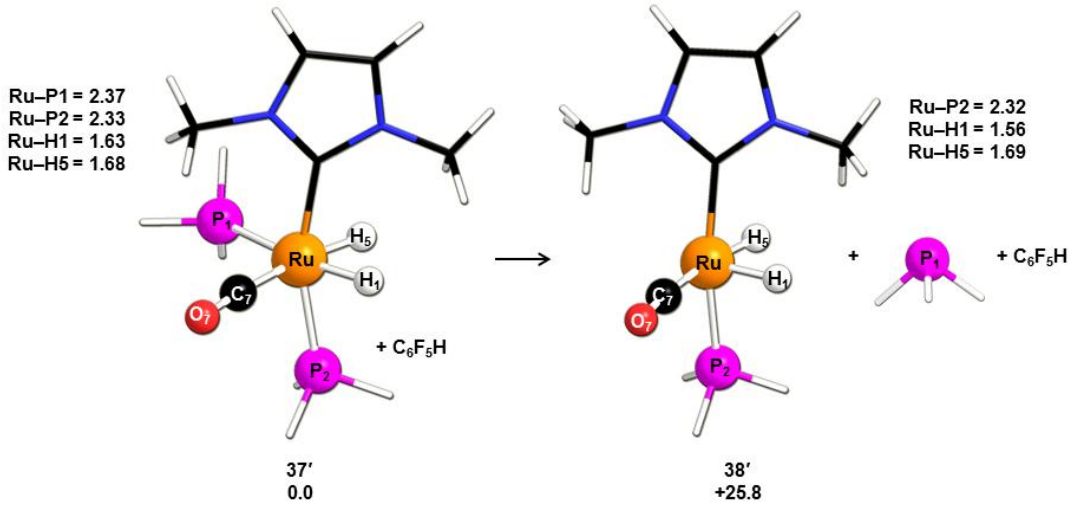

Figure 5.4: Computed geometries and energies for phosphine dissociation.

C–H activation occurs from **38′** via initial formation of a σ-complex (**39′**, E = +18.2 kcal/mol) where the C_6F_5H moiety interacts with the metal centre through the C6–H6 bond (Ru···H6 = 2.03 Å, Ru···C6 = 2.67 Å) which therefore lengthens to 1.13 Å (see

Figure 5.5). A transition state for C–H activation from **39′** has been located, **TS (39′ – 40′)** (E = +27.9 kcal/mol) by decreasing the Ru···C6 contact. In the transition state therefore the Ru···C6 contact shortens to 2.32 Å while the C6···H6 distance lengthens to 1.49 Å. In addition, the computed transition state shows that the H5···H6 distance shortens to 1.19 Å and surprisingly the Ru–H5 bond lengthens slightly to 1.72 Å (*cf.* 1.68 in **39′**). Moreover, ICR calculations showed that **TS (39′ – 40′)** leads to a η^2-H_2 complex **40′** (E = +15.6 kcal/mol), prior to H_2 elimination. This C–H activation, therefore, proceeds via a σ-complex-assisted mechanism (σ-CAM) in which an intermediate is involved, **40′**, before elimination of H_2 (see a) in Figure 5.6).[85] This is in contrast with a σ-bond metathesis mechanism which proceeds via a 4-centred transition state and where no intermediate is observed (see b) in Figure 5.6).

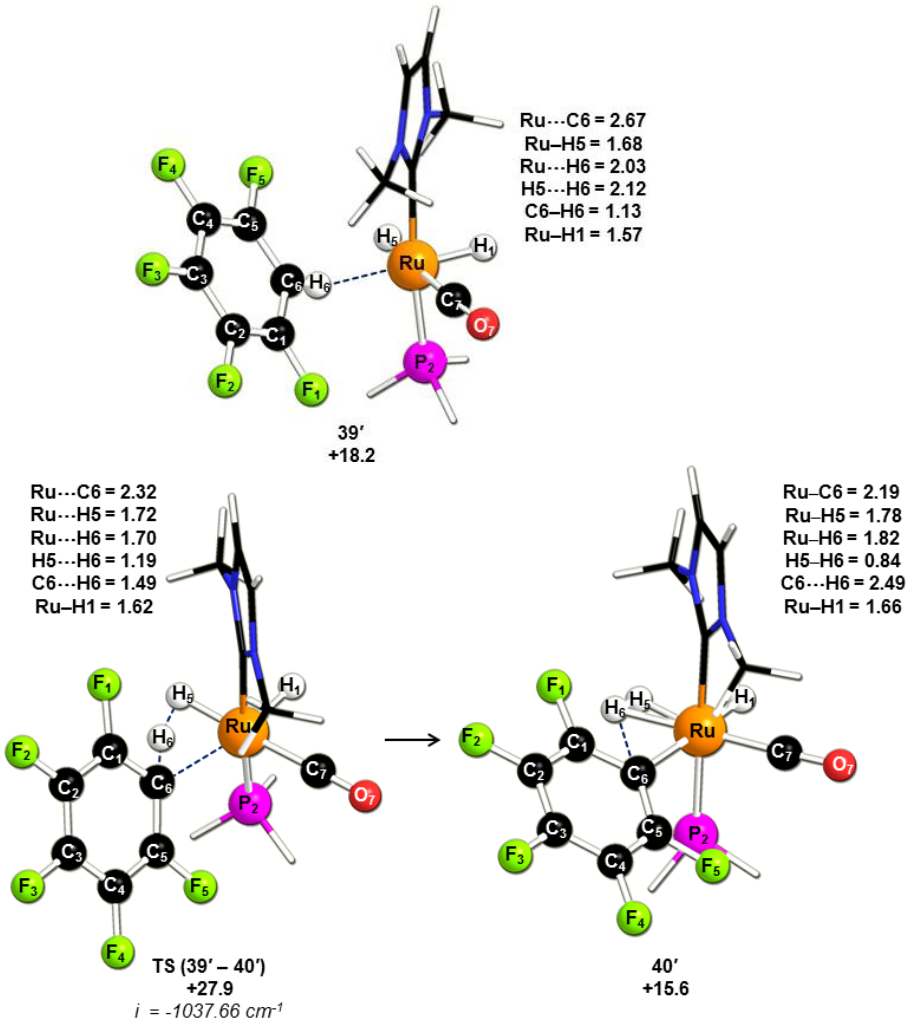

Figure 5.5: Computed geometries and energies for C–H activation of C_6F_5H to give the η^2-H_2 complex 40′.

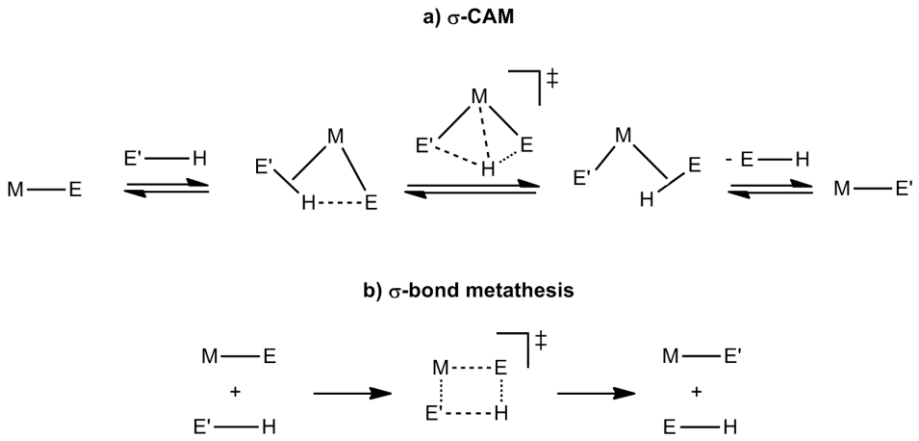

Figure 5.6: Schematic representation of a) σ-CAM and b) σ-bond metathesis.[85]

H_2 elimination at **40′** proceeds via **TS (40′ – 41′)** (E = +28.6 kcal/mol) which is competitive with the C–H activation **TS (39′ – 40′)** (E = +27.9 kcal/mol, see Figure 5.7). **TS (40′ – 41′)** has been located by widening of the C6–Ru–C7 angle in order to dissociate H_2. Therefore the C6–Ru–C7 angle increases to 119.81° (*cf.* 99.1 in **40′**) while the Ru···H5 and Ru···H6 distances increase to 2.82 Å and 3.44 Å as H_2 dissociates. Finally, complex **41′** (E = +20.6 kcal/mol) is formed in which H_2 is fully dissociated and where the CO ligand is trans to the C_6F_5 moiety (C6–Ru–C7 = 175.9°). Also, the Ru–H1 bond decreases to 1.55 Å as a vacant site is created trans to H1.

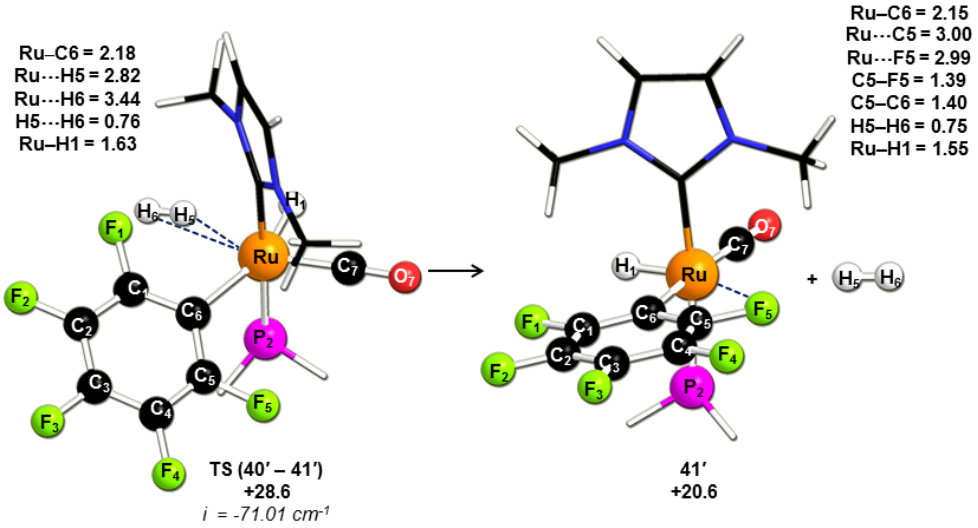

Figure 5.7: Computed geometries and energies for H_2 elimination/isomerisation process to give 41′.

The presence of this vacant site allows the *ortho*-C–F activation via **TS (41′ – 42′)** (E = +58.3 kcal/mol, see Figure 5.8). This transition state has been located by shortening the Ru···C5 distance. In the transition state, the breaking C5···F5 bond is stretched to 1.97 Å (*cf.* 1.39 Å in **38**) as the Ru···C5 and Ru···F5 distances shorten to 2.21 Å and 2.24 Å,

respectively. **TS (41′ – 42′)** links to the tetrafluorobenzyne intermediate **41′** which has an energy located at +43.0 kcal/mol.

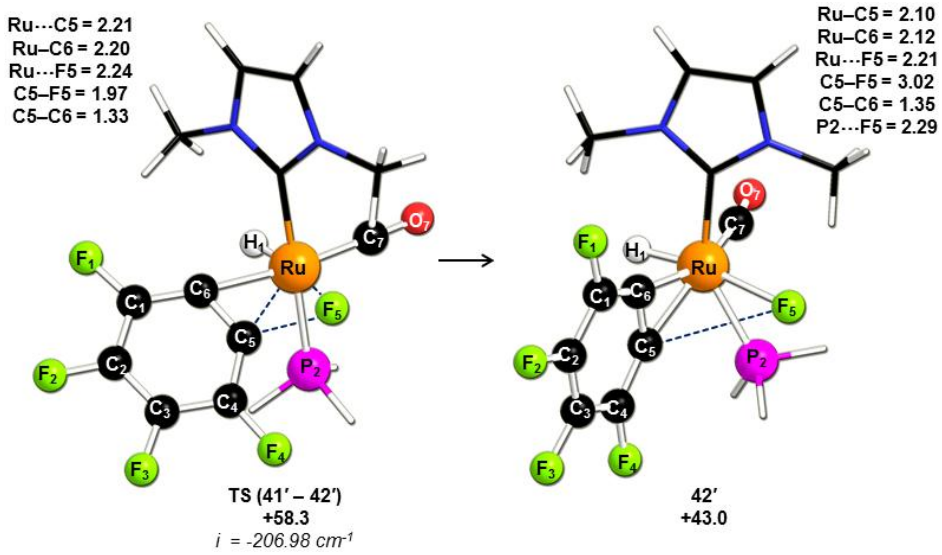

Figure 5.8: Computed geometries and energies for *ortho*-C–F activation to form tetrafluorobenzyne intermediate 42′.

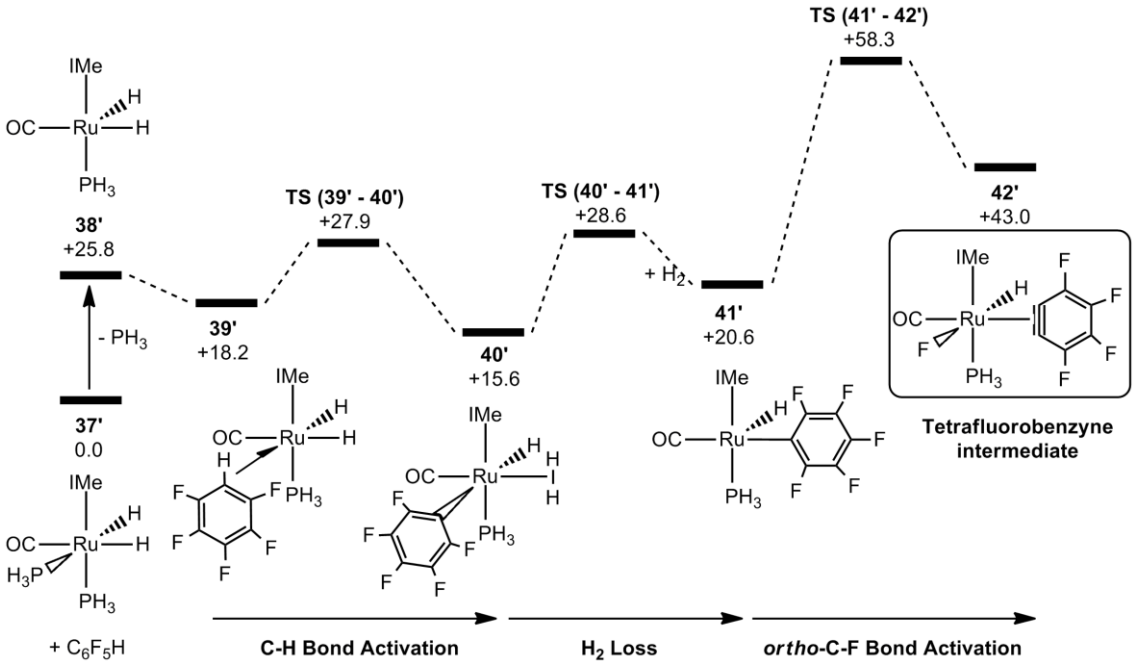

Figure 5.9: Reaction profile for phosphine dissociation followed by C–H activation, H_2 loss and *ortho*-C–F bond activation to give 42′.

The reaction profile for formation of **42′** is shown in Figure 5.9. The rate-limiting transition state corresponds to the *ortho*-C–F activation which has a computed energy of +58.3 kcal/mol. Therefore this step is kinetically unfeasible under the conditions used

experimentally. In addition, the tetrafluorobenzyne intermediate is found to be more than 40.0 kcal/mol above the reactants, and so ruled out as a viable intermediate.

5.3 HDF of C_6F_5H at $[Ru(H)_2(CO)(IMe)(PH_3)]$ via Initial Formation of an η^2-Arene Intermediate

At this stage, another mechanism needed to be considered in order to explain the unusual *ortho*-regioselectivity observed experimentally. Since phosphine dissociation happens experimentally, initial formation of η^2-arene intermediate was plausible. Therefore the η^2-adduct **46′** (E = +16.7 kcal/mol) has been optimised and the computed geometry and energy are shown in Figure 5.10. Complex **46′** shows an elongation of the C5–F5 bonds to 1.39 Å (*cf.* 1.35 Å in free C_6F_5H) as well as a lengthening of the C5–C6 distance to 1.44 Å (*cf.* 1.40 Å). This last elongation is caused by π-back donation from the metal centre to the π* antibonding orbitals of C_6F_5H. Interestingly, **46′** is found to be slightly more stable than the σ-complex **39′** (E = +18.2 kcal/mol) computed prior to C–H activation.

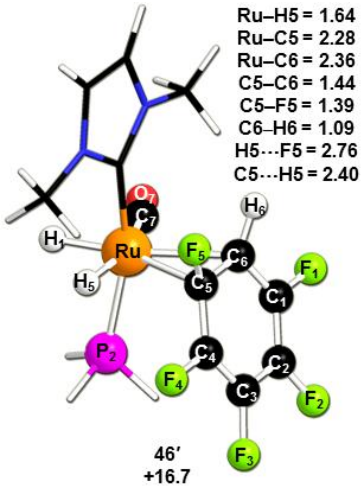

Figure 5.10: Computed geometry and energy for the η^2-arene intermediate.

The second step was to perform a scan from **46′** involving the shortening of the H5···F5 interaction as in principle HDF reaction results in the substitution of fluorine by hydrogen. In this case, HF could be eliminated to give a σ-aryl species $[Ru(C_6F_5)(H)(CO)(NHC)(PH_3)]$ (**48′**) which could lead to the final products $[Ru(F)(H)(CO)(NHC)(PH_3)]$ (**45′**) and 1,2,3,4-$C_6F_4H_2$ via a protonolysis step of HF (see Figure 5.11).

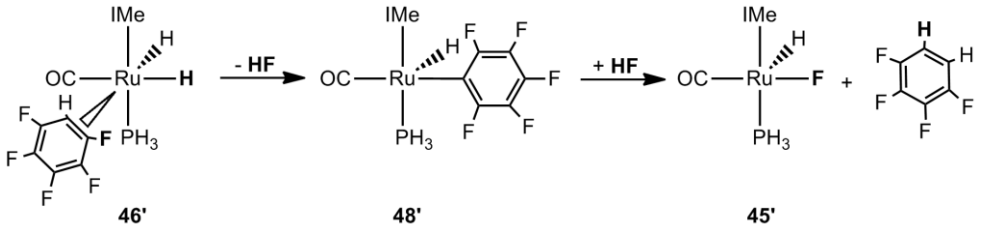

Figure 5.11: Alternative mechanism considered for the HDF of C_6F_5H via initial formation of 46′.

Therefore the shortening of the H5···F5 distance via a scan calculation has been performed and allowed the location of a transition state, **TS (46′ – 47′)** (E = +24.5 kcal/mol, see Figure 5.12). In the transition state, the H5···F5 contact shortens, as anticipated, to 2.07 Å, but more interestingly the C5···H5 distance decreases to 1.50 Å while the Ru···H5 and Ru···C5 bonds elongate to 1.72 Å and 2.34 Å, respectively. IRC calculations link to the species **47′** which showed, unexpectedly, the formation of a new C5–H5 bond (1.25 Å) and therefore contrast with the expected HF formation.

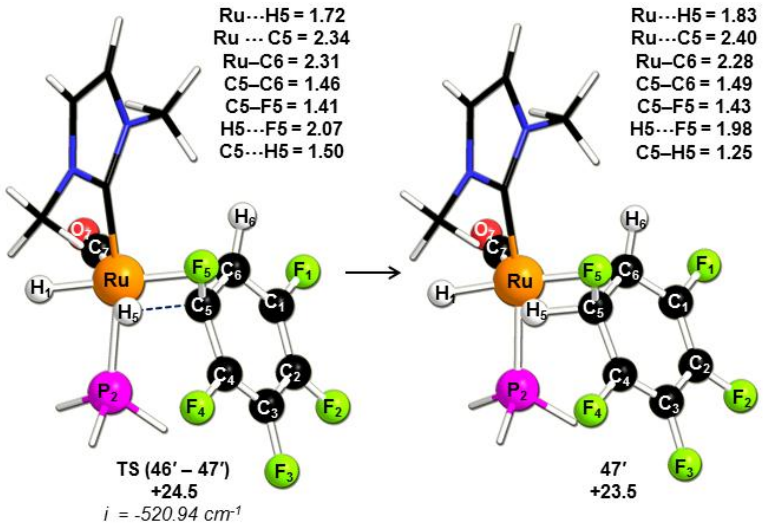

Figure 5.12: Computed geometries and energies for formation of 47′.

At this point further characterisation of the structures involved in this process has been undertaken by comparing the bond lengths and computing the natural atomic charges of the different species (see Figure 5.13). During the process the C5–C6 distances becomes longer, from 1.44 Å in **46′** to 1.49 Å in **47′**, suggesting a change in bond order. In addition, the C1–C6, C2–C3 and C4–C5 distances are slightly longer in **47′** while the C1–C2 and C3–C4 becomes shorter. Computed natural atomic charges show that H5 becomes more positive, from -0.074 in **46′** to +0.177 in **47′,** while C5 is less positive in **47′** (+0.117) than in **46′** (+0.261). Overall, the entire C_6F_5H moiety becomes more negative in **47′** (total charge = -0.524) than in the η^2-arene intermediate **46′** (total charge

= -0.208) while the metal centre is less negative in **47′** (-0.454 *cf.* -0.536 in **46′**). All these features suggests that the process occurs via a nucleophilic attack of H5 at C5 to lead the complex **47′** in which the $\{C_6F_5H_2\}^-$ moiety resembles a Meisenheimer intermediate. This last species is stabilised by interaction of the *ortho* position with the metal centre (Ru–C6 = 2.28 Å) as shown in Figure 5.12.

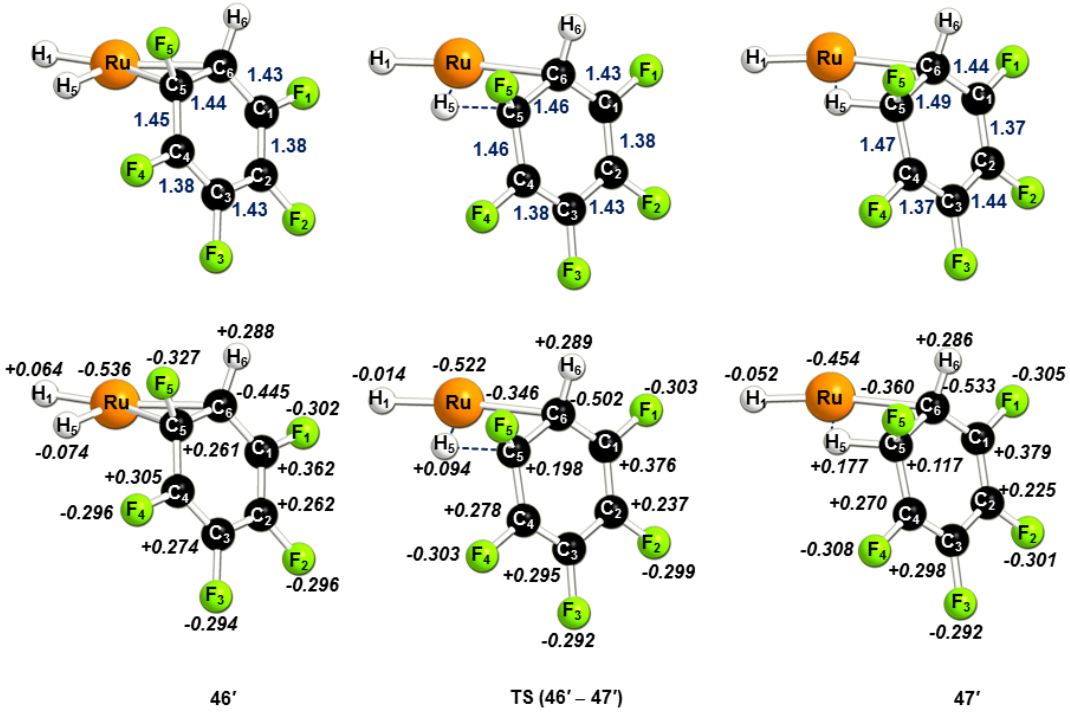

Figure 5.13: Selected computed bond lengths (top) and natural atomic charges (bottom) for 46′, TS (46′ – 47′) and 47′, respectively. Non-participating atoms are omitted for clarity.

Since HF formation did not occur as expected, another approach has been considered. Intermediate **47′** consists in the formation of a $\{C_6F_5H_2\}^-$ moiety and the final product [Ru(F)(H)(CO)(NHC)(PH_3)] (**45′**) and 1,2,3,4-$C_6F_4H_2$ can in principle be formed by transferring F5 onto the metal centre. A calculation involving the shortening of the Ru···F5 distance therefore was performed (see Figure 5.14). A transition state, **TS (47′ – 48′)** (E = +36.3 kcal/mol) was located in which the C5···F5 bond increases to 1.98 Å and the Ru···C5 contacts decreases to 2.29 Å (*cf.* 2.40 Å in **47′**). However, another unexpected feature happens with the shortening of the H5···F5 distance to 1.71 Å (*cf.* 1.98 Å in **47′**). In reality, IRC calculations showed that the highly fluoridic centre F5 (computed charge = -0.53) is able to abstract H5 to form HF and the σ-aryl species [Ru(C_6F_4H)(H)(CO)(NHC)(PH_3)] (**48′**). Also, calculations suggest that the HF

molecule weakly interacts within **48′** with a H1···H5 contact of 1.47 Å (Ru···H5 = 2.37 Å, C5···H5 = 2.73 Å).

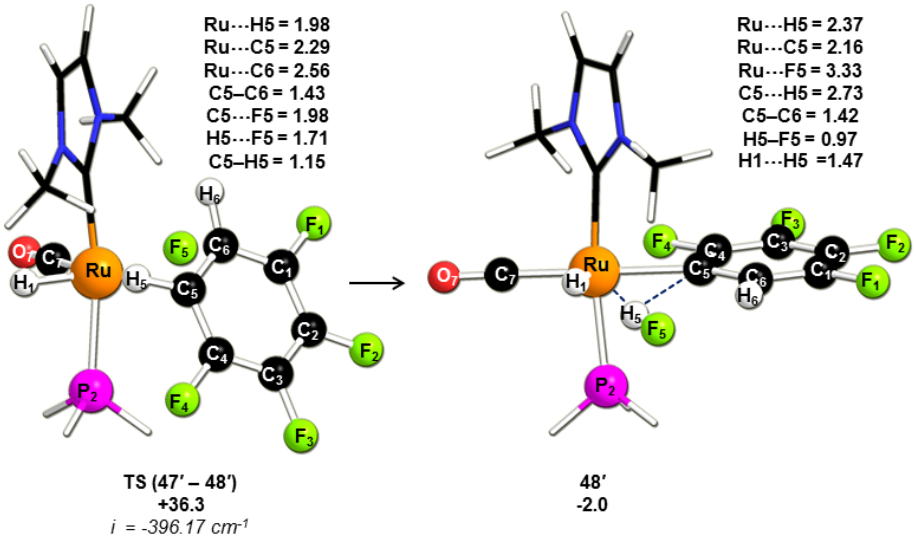

Figure 5.14: Computed geometries and energies for formation of HF and the σ-aryl species 48′.

The final products [Ru(F)(H)(CO)(NHC)(PH_3)] (**45′**) and 1,2,3,4-$C_6F_4H_2$ can then be formed from **48′** via a protonolysis step. This process occurs via **TS (48′ – 45′)** (E = +3.8 kcal/mol) in which the breaking Ru···C5 bond lengthens to 2.26 Å (*cf.* 2.16 Å in **48′**, see Figure 5.15).

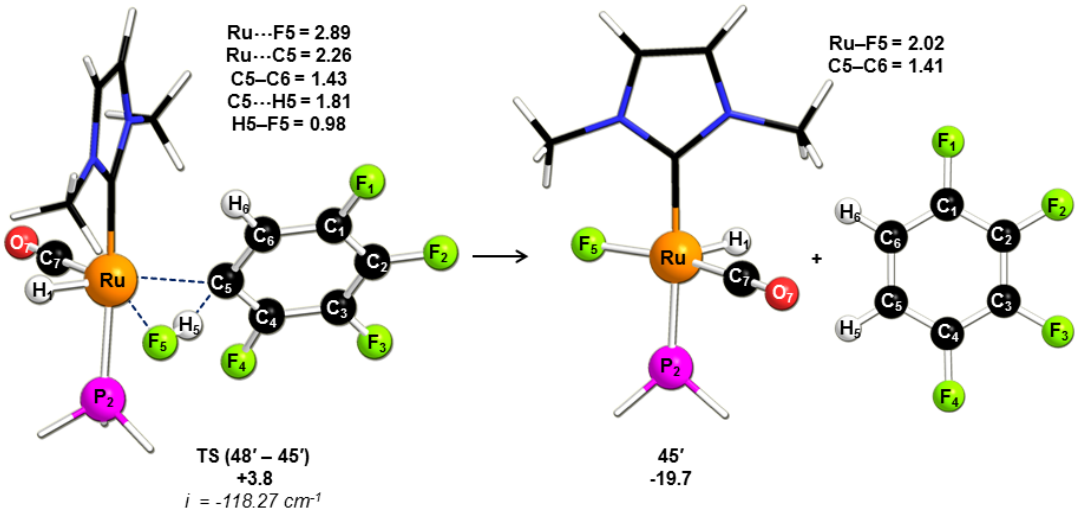

Figure 5.15: Computed geometries and energies for the protonolysis step to give [Ru(F)(H)(CO)(NHC)(PH_3)] (45′) and 1,2,3,4-$C_6F_4H_2$

In addition, the Ru···F5 and C5···H5 interactions shorten to 2.89 Å (*cf.* 3.33 Å in **48′**) and 1.81 Å (*cf.* 2.73 Å in **48′**), respectively. IRC calculations showed that **TS (48′ –**

45′) links to an adduct of **45′**, **45′.$C_6F_4H_2$** (E = -24.7 kcal/mol), which is found to be more stable than the two separated products, **45′** and 1,2,3,4-$C_6F_4H_2$ (E = -19.7 kcal/mol). This difference in energy may come from the H5···F5 contact of 1.95Å in **45′.$C_6F_4H_2$** and a basis set superposition error (BSSE).

The reaction profile for the HDF of C_6F_5H to give **45′** and 1,2,3,4-$C_6F_4H_2$ is summarised in Figure 5.16. This mechanism involves initial phosphine dissociation in which the C_6F_5H can bind the metal centre to form an η^2-arene intermediate **46′** (E = +16.7 kcal/mol). A nucleophilic attack process happens from **46′** to form a Meisenheimer intermediate **47′** (E = +23.5 kcal/mol) via **TS (46′ – 47′)** (E = +24.5 kcal/mol). In this case, instead of transferring the fluorine atom directly onto the metal centre, a σ-aryl complex (**48′**, E = -2.0 kcal/mol) is formed via HF loss. Finally, the protonolysis by HF with concomitant F transfer to the metal centre gives **45′** and 1,2,3,4-$C_6F_4H_2$. The overall process can be described as a stepwise mechanism with the rate-limiting transition state being the HF elimination corresponding to **TS (47′ – 48′)** (E = +36.3 kcal/mol). This transition state is much lower than **TS (41′ – 42′)** for the formation of tetrafluorobenzyne intermediate **42′** which had an energy of +58.3 kcal/mol.

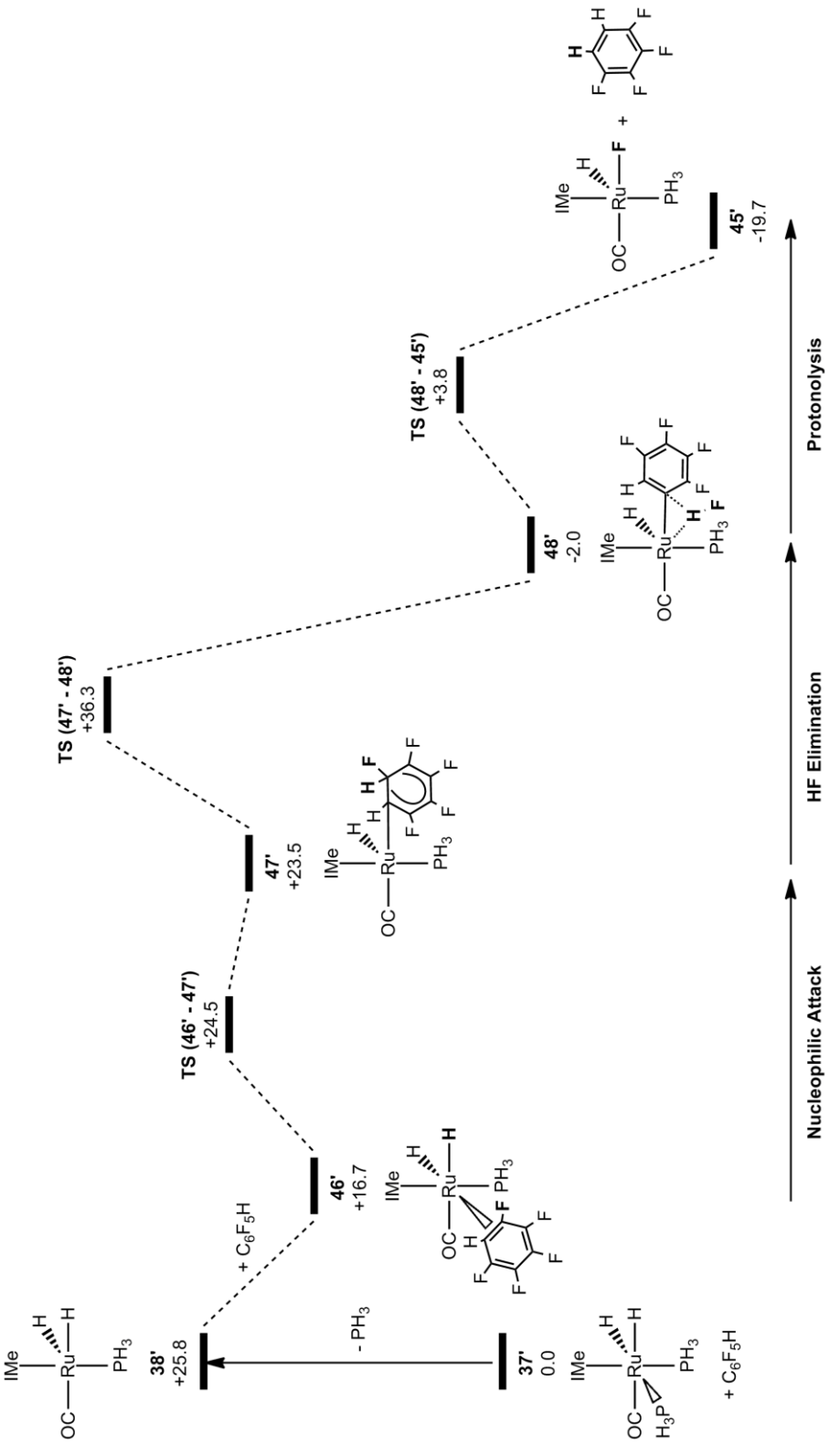

Figure 5.16: Reaction profile for the HDF of C_6F_5H to give 45′ and 1,2,3,4-$C_6F_4H_2$.

5.4 HDF of C_6F_5H at $[Ru(H)_2(CO)(IMe)(PH_3)]$ without Initial Formation of an η^2-Arene Intermediate

When investigating this novel nucleophilic attack mechanism via initial PH_3/C_6F_5H substitution a second pathway has been identified, involving a direct transfer of the hydride ligand on the fluoroaromatic without initial formation of a η^2-arene intermediate.

Initially, a loosely bound adduct is formed (**49′**, E = +21.0 kcal/mol) in which the C_6F_5H moiety interacts with the ruthenium metal centre (see Figure 5.17). The C5–F5 bond lengthens to 1.36 Å due to a short Ru···F5 contact (2.67 Å). This adduct is actually higher in energy than the η^2-arene species **46′** (E = +16.7 kcal/mol) and the σ-complex **39′** (E = +18.2 kcal/mol), formed prior C–H activation of C_6F_5H.

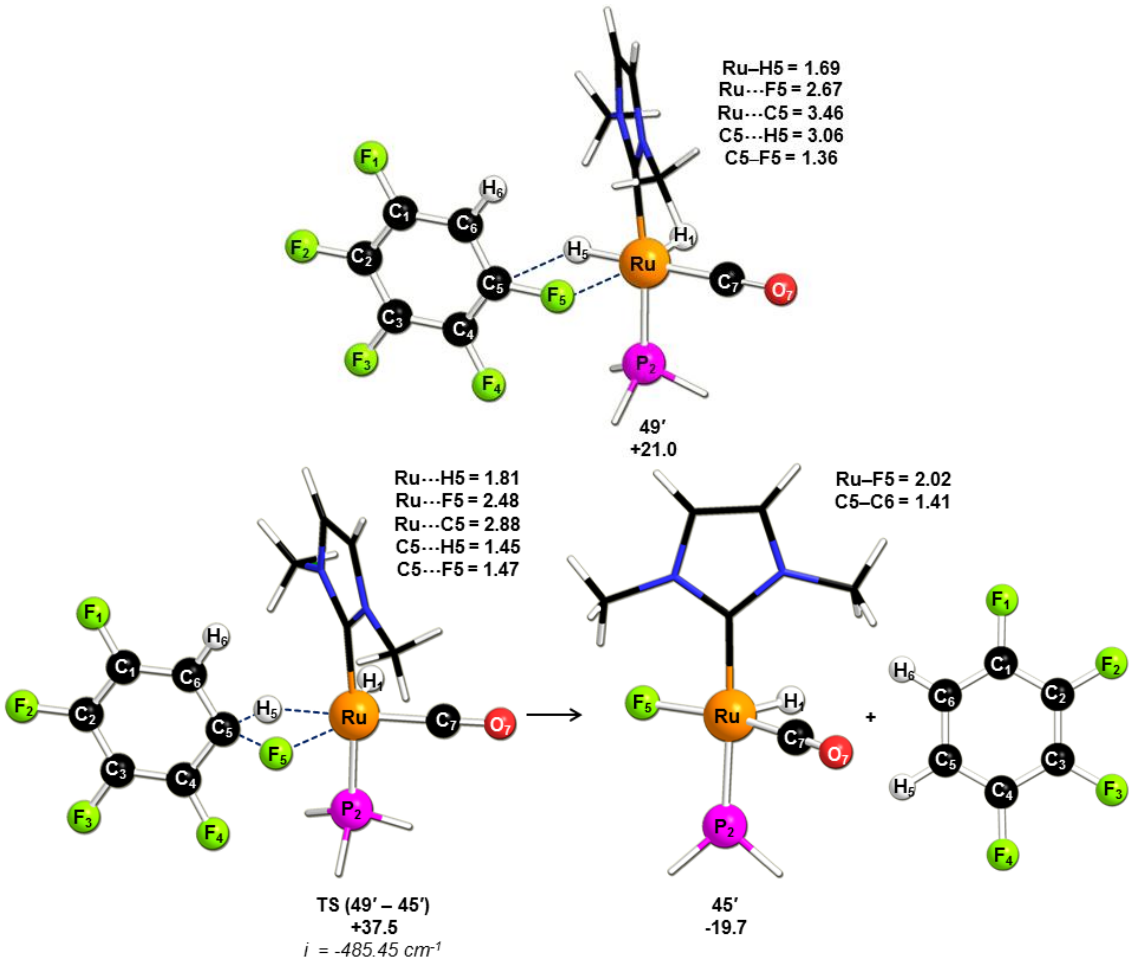

Figure 5.17: Computed geometries for HDF of C_6F_5H at $[Ru(H)_2(CO)(IMe)(PH_3)]$ to give 45′ and 1,2,3,4-$C_6F_4H_2$.

A transition state, **TS (49′ – 45′)** (E = +37.5 kcal/mol) has been located from **49′**, by shortening the C5···H5 contact to transfer the hydride onto the C_6F_5H moiety. Therefore, in **TS (49′ – 45′)**, the C5···H5 distance decreases to 1.45 Å but at the same time the C5···F5 bond lengthens to 1.47 Å. In addition, due to the different orientation of the C_6F_5H moiety compared to the η^2-arene species **46′**, the vacant site at the metal centre remains available. This implies that fluorine can be transferred to Ru, suggested by the shortening of the Ru···F5 distance to 2.48 Å. IRC calculations links to the separated products **45′** and 1,2,3,4-$C_6F_4H_2$.

Again to understand the nature of the transition state, the computed bond lengths and natural atomic charges have been compared between **49′** and the transition state **TS (49′ – 45′)** (see Figure 5.18). The major changes in terms of the bond lengths results in the increase of the C4–C5 and C5–C6 distances to 1.43 Å in the transition state **TS (49′ – 45′)** (*cf.* 1.40 in **49′**). In addition, computed natural atomic charges show that H5 becomes less negative in the transition state (-0.138 *cf.* -0.228 in **49′**) while the entire C_6F_5H moiety is more negative (total charge = -0.374 *cf.* +0.049 in **49′**). Therefore, as seen in **TS (46′ – 47′)**, this process involves a nucleophilic attack of H5 at C5.

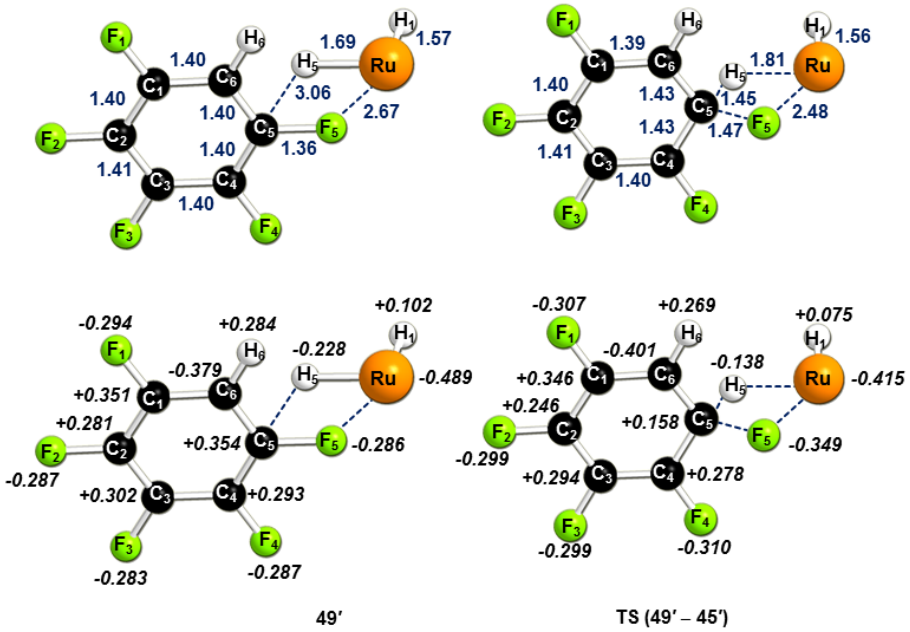

Figure 5.18: Selected computed bond lengths and natural atomic charges for 49′ and TS (49′ – 45′), respectively. Non-participating atoms are omitted for clarity.

In parallel, a similar example has been recently reported by Llusar and co-workers in the catalytic HDF of C_5NF_5 at $[M_3S_4H_3(dmpe)_3]^+$ (M = Mo, W) clusters in the presence

of $HSiMe_2Ph$ to yield exclusively 2,3,5,6-C_5NF_4 (see Figure 5.19).[86] DFT calculations have shown that initial phosphine dissociation is required to create a vacant site at the metal centre followed by a "σ-bond metathesis transition state". The transition state for M = Mo is located at +38.6 kcal while for M = W the energy of the transition state is at +41.4 kcal/mol. This trend is in agreement with the experimental observations where faster conversion at Mo is observed.

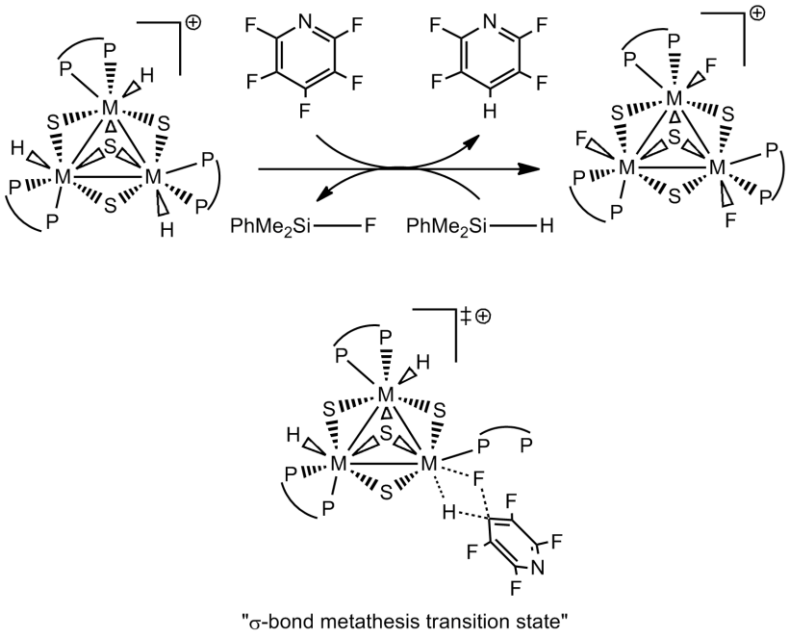

Figure 5.19: HDF of C_5NF_5 at $[M_3S_4H_3(dmpe)_3]^+$ (M = Mo, W) in the presence of $HSiMe_2Ph$ to give 2,3,5,6-C_5NF_4 with a schematic representation of the transition state proposed for this process.[86]

In summary, the concerted mechanism for the HDF of C_6F_5H proceeds via a nucleophilic attack of H5 at C5 with a computed transition state **TS (49′ – 45′)** located at +37.5 kcal/mol. This is lower than formation of tetrafluorobenzyne intermediate **42′** via **TS (41′ – 42′)** (E = +58.3 kcal/mol), but this slightly higher than the stepwise mechanism in which the rate-limiting transition state, HF loss, is located at +36.3 kcal/mol. Therefore, from this point forward the proposed mechanism via initial phosphine dissociation followed by C–H and *ortho*-C–F activation to form tetrafluorobenzyne intermediate **42′** will be discarded.

5.5 HDF of C_6F_5H at $[Ru(H)_2(CO)(IMes)(PPh_3)]$

5.5.1 Phosphine Dissociation

In addition to the small computational model **36′**, calculations have also been performed on the full experimental model by using IMes and PPh_3 ligands. In Section 5.5, all energies are quoted relative to the two separated reactants, $\mathbf{36}_{\mathbf{IMes}}$ and C_6F_5H, denoted by $\mathbf{37}_{\mathbf{IMes}}$. In the figures, energies in italics include a solvent correction (PCM Approach, THF) and the energies that are underlined are those for the reaction of the small model **36′** with C_6F_5H. Also, for clarity, phosphine Ph groups are truncated at the *ipso* carbon centre and non-participating hydrogen atoms are omitted.

Because of the use of the more sterically encumbered full system, the Ru–P1 bond (2.43 Å, see Figure 5.20) is weaker in the full model than in **36′** (Ru–P1 = 2.37 Å). One direct consequence is that phosphine dissociation becomes more accessible than at **36′** by 14.7 kcal/mol with a computed energy of +11.1 kcal/mol. In addition, this step now costs only +7.8 kcal/mol in THF.

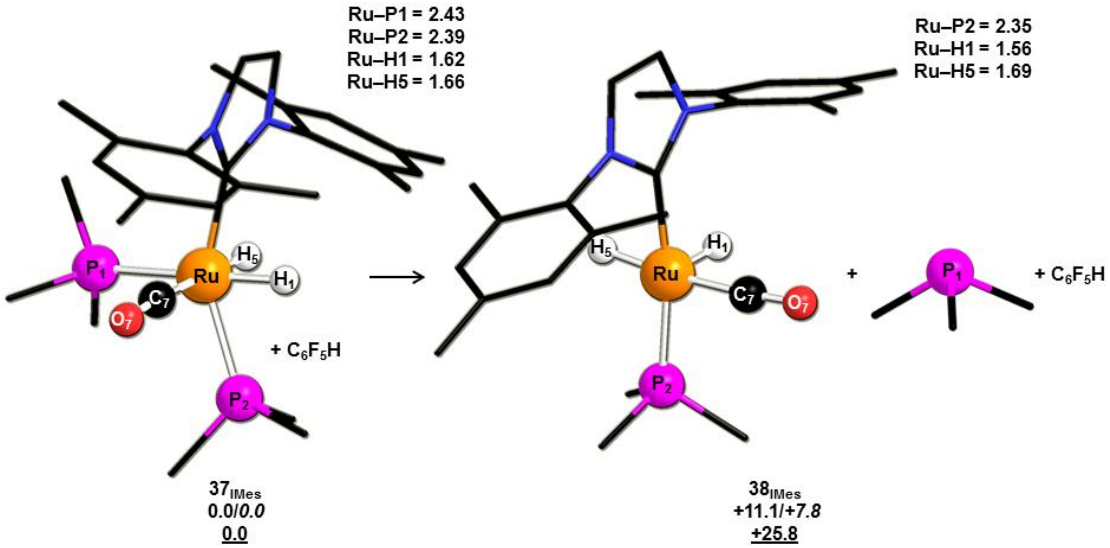

Figure 5.20: Computed geometries and energies for phosphine dissociation.

5.5.2 HDF via a Stepwise Mechanism

After phosphine dissociation, formation of the η^2-arene intermediate $\mathbf{46}_{\mathbf{IMes}}$ (E = +10.9 kcal/mol) is computed (see Figure 5.21). In $\mathbf{46}_{\mathbf{IMes}}$, the Ru···C5 and Ru···C6 bonds are slightly longer than in **46′**, being 2.30 Å (*cf.* 2.28 Å in **46′**) and 2.38 Å (*cf.* 2.36 Å in

46′), respectively. This reflects a more weakly bound arene in **46$_{IMes}$** and the PPh_3/C_6F_5H substitution step has now a computed energy of +10.9 kcal/mol (+9.0 kcal/mol in THF) and is found to be 5.8 kcal/mol more accessible compared to **46′.**

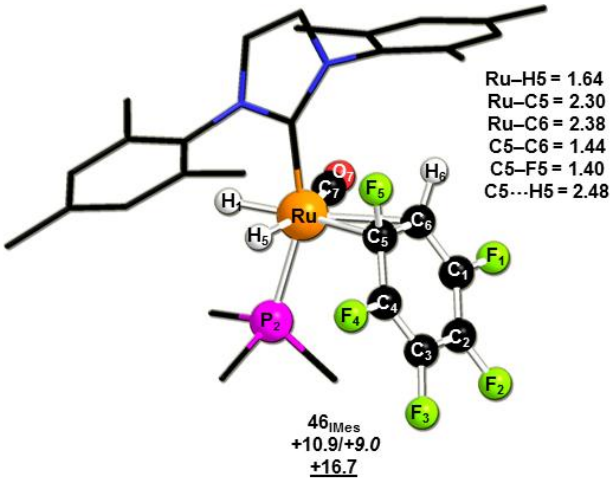

Figure 5.21: Computed geometry and energy for the η^2-arene intermediate.

A similar trend is observed for the nucleophilic attack (see Figure 5.22). In the transition state, **TS (46 – 47)$_{IMes}$** (E = +24.5), again the Ru···C5 and Ru···C6 distances are slightly longer than in **TS (46′ – 47′)** by 0.03 Å and 0.02 Å, respectively. With the full model, the nucleophilic attack is now more favourable kinetically by 4.0 kcal/mol than at **46′** with a computed energy located at +20.5 kcal/mol (+18.0 kcal/mol in THF).

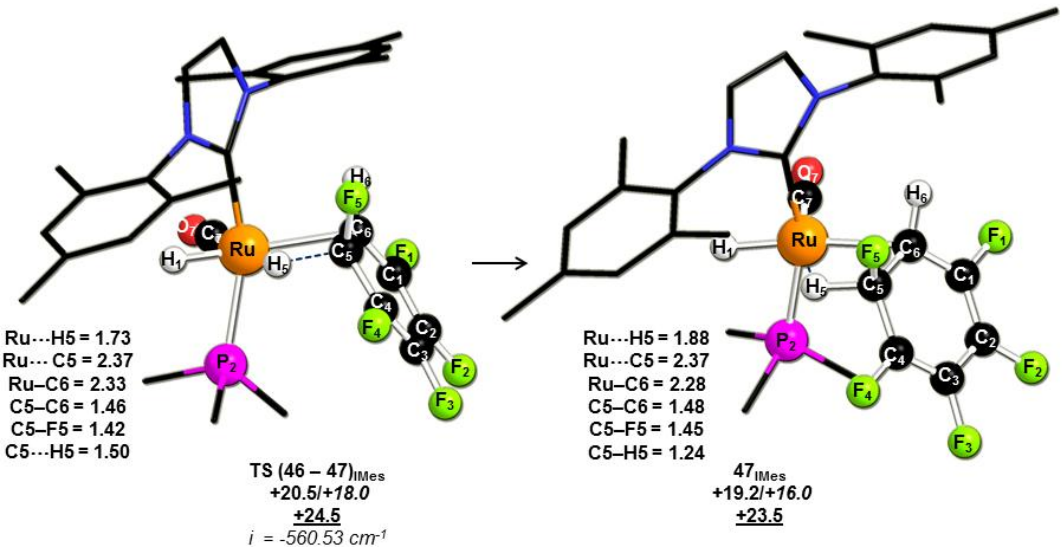

Figure 5.22: Computed geometries and relative energies for the nucleophilic attack of H5 at C5 to give 47$_{IMes}$.

The Meisenheimer intermediate **47$_{IMes}$** shows shorter Ru···C5 and Ru···H5 contacts than in **47′**, however, the Ru···C6 bond (2.28 Å) is similar in **47$_{IMes}$** and **47′**. Species

47$_{IMes}$ is computed to be more stable by 4.3 kcal/mol than **47′**, with a computed energy of +19.2 kcal/mol (+16.0 kcal/mol in THF).

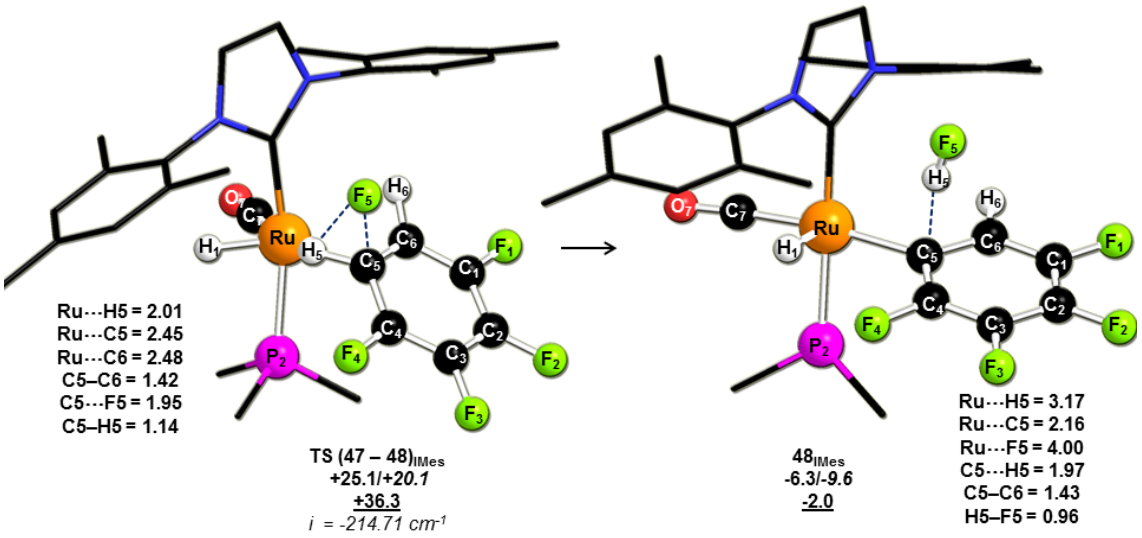

Figure 5.23: Computed geometries and relative energies for formation of 48$_{IMes}$.

The effect of bulky substituents is particularly large for the HF elimination. **TS (47 – 48)$_{IMes}$** (E = +25.1 kcal/mol) is computed to be 11.2 kcal/mol lower than with the small model (**TS (47′ – 48′)**, E = +36.3 kcal/mol). This difference in energy can be explained by short contacts between the fluoride (computed charge = -0.54) and the NHC ligands. This last feature will be discussed later (see Section 5.5.4 and Figure 5.27). In addition, the HF molecule strongly interacts with the {C_6F_4H} moiety (C5···H5 = 1.97 Å) and shows the importance of the HF hydrogen bonding due to the difference in electronegativity between H5 and F5. Finally THF stabilises the energy of **TS (47 – 48)$_{IMes}$** to +20.1 kcal/mol.

Intermediate **48$_{IMes}$** shows that the HF molecule strongly interacts with the C_6F_4H moiety (C5···H5 = 1.97 Å *cf.* 2.73 in **48′**) which may explain the stabilisation of the former by 4.3 kcal/mol.

Finally, the protonolysis step shows similar behaviour in which the transition state, **TS (47 – 48)$_{IMes}$**, is stabilised relative to the small model by 4.7 kcal/mol and the final products **45$_{IMes}$** and 1,2,3,4-$C_6F_4H_2$ by 15.7 kcal/mol (see Figure 5.24). It should also mentioned that **TS (47 – 48)$_{IMes}$** links to an adduct, as seen with the small model, that is slightly lower in energy than the separated product (E = -39.6 kcal/mol; E = -42.1 kcal/mol in THF).

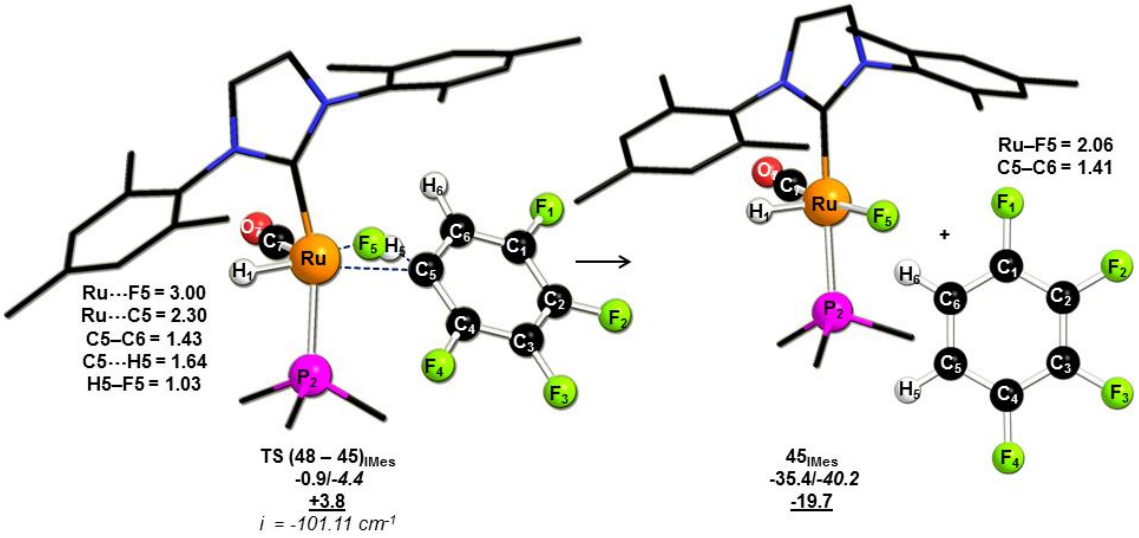

Figure 5.24: Computed geometries and relative energies for the protonolysis step to give 45_{IMes} and 1,2,3,4-$C_6F_4H_2$.

The reaction profiles for the HDF of C_6F_5H at $[Ru(H)_2(CO)(NHC)(PR_3)]$ are shown in Figure 5.25. Calculations with the full model stabilised all the different stationary points along the stepwise mechanism compared to the HDF of C_6F_5H at $[Ru(H)_2(CO)(IMe)(PH_3)]$. These differences in energies can be explained by the use of a more sterically encumbered full system which facilitates the initial phosphine dissociation. The rate-limiting transition state remains the HF elimination, **TS (47 – 48)$_{IMes}$**, with a computed barrier of +25.1 kcal/mol which drops to +20.1 kcal/mol in THF, qualitatively in agreement with the conditions used experimentally. Overall the reaction is exothermic by 35.4 kcal/mol (ΔE = -40.2 kcal/mol in THF).

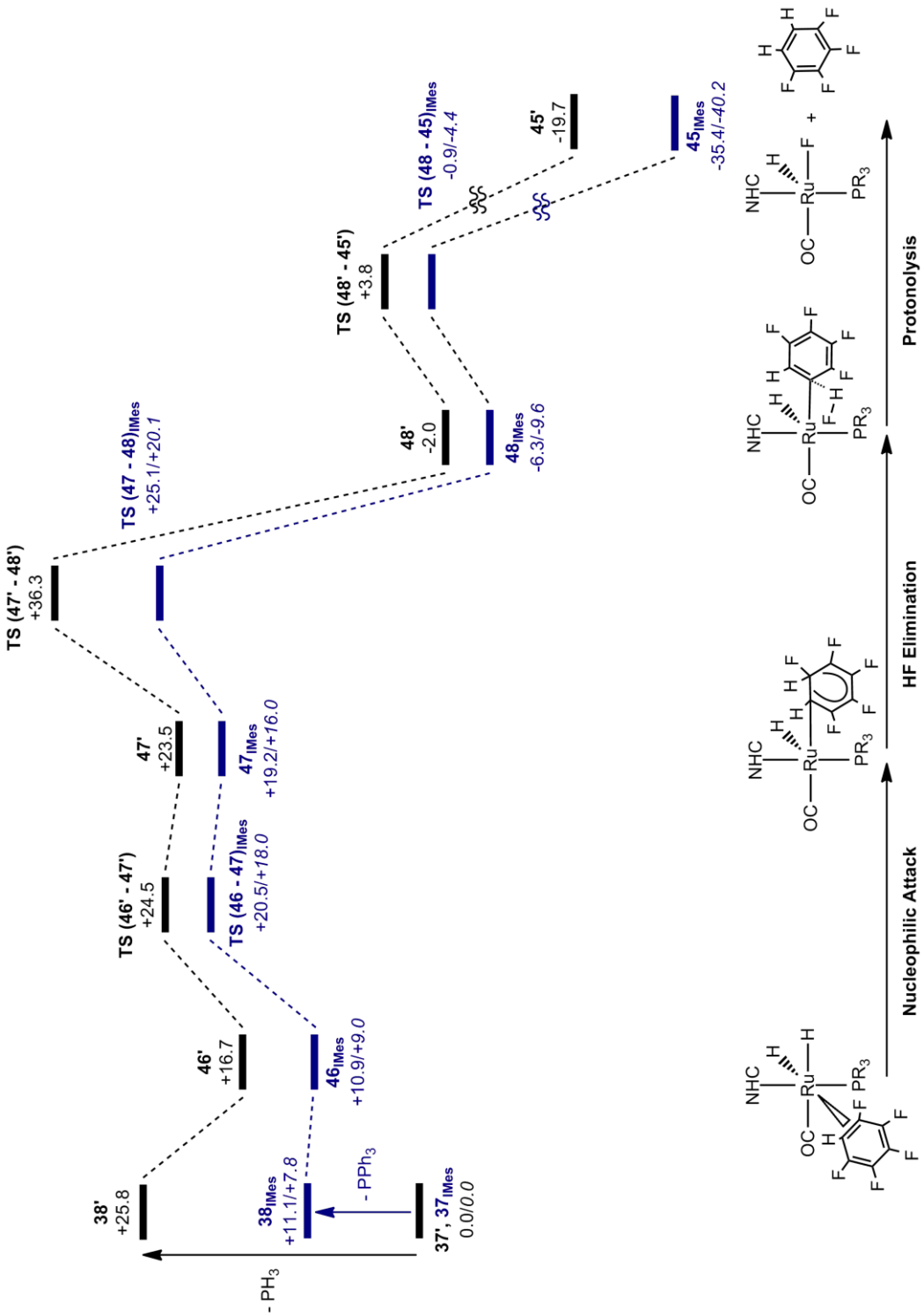

Figure 5.25: Reaction profiles for the HDF of C_6F_5H at $[Ru(H)_2(CO)(NHC)(PR_3)]$, to give $[Ru(F)(H)(CO)(NHC)(PR_3)]$ and 1,2,3,4-$C_6F_4H_2$. Energies in italics include a solvent correction (PCM method, THF).

5.5.3 HDF via a Concerted Mechanism

A similar trend has been obtained for HDF via a concerted mechanism. The transition state, **TS (49 – 45)$_{IMes}$** shows an elongation of the Ru···H5 distance to 1.84 Å, 0.03 Å longer than in **TS (49′ – 45′)**. The C_6F_5H moiety weakly interacts in the full model with computed Ru···C5 and Ru···F5 contacts of 2.96 Å and 2.57 Å, respectively (*cf.* **TS (49′ – 45′)**, 2.88 Å and 2.48 Å). **TS (49 – 45)$_{IMes}$** is more accessible than **TS (49′ – 45′)** by 7.7 kcal/mol. In addition, no adduct has been located prior to the nucleophilic attack probably due to the steric bulk in the full model.

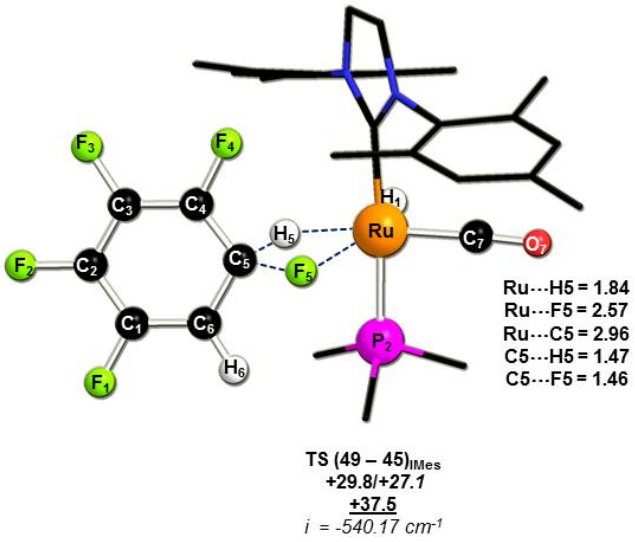

Figure 5.26: Computed geometry and relative energy for TS (49 – 45)$_{IMes}$ to give 45$_{IMes}$ and 1,2,3,4-$C_6F_4H_2$.

Finally, **TS (49 – 45)$_{IMes}$** has an energy of +29.8 kcal/mol (+27.1 kcal/mol in THF) and therefore remains higher in energy than the stepwise mechanism with a rate-limiting transition state energy located at +25.1 kcal/mol (+20.1 kcal/mol in THF), corresponding to **TS (47 – 48)$_{IMes}$**.

5.5.4 Regioselectivity of HDF of C_6F_5H

The formation of the three different isomers of $C_6F_4H_2$ after HDF has also been considered and in all cases both transition states for concerted and stepwise mechanisms have been characterised. The energies of the rate-limiting transition states for the computational and full models involved in these processes are tabulated in Table 5.2. In the case of the stepwise mechanism the rate-limiting transition state always corresponds to the HF elimination step.

Table 5.2: Energies for the rate-limiting transition states for the concerted and stepwise mechanisms for the small and full models. The most stable transition states for each model are shown in bold. Energies in italics include a solvent correction (PCM method, THF).

	$[Ru(H)_2(CO)(IMe)(PH_3)]$ (**38′**)		$[Ru(H)_2(CO)(IMes)(PPh_3)]$ (**38$_{IMes}$**)	
	Concerted	**Stepwise**	**Concerted**	**Stepwise**
ortho	+37.5	**+36.3**	+29.8/+*27.1*	**+25.1/+*20.1***
meta	+34.9	+37.3	+29.0/+*26.2*	+32.0/+*23.5*
para	**+33.4**	+38.3	**+27.2/+*24.7***	+31.9/+*23.8*

Interestingly, the concerted mechanism predicts that HDF of C_6F_5H at $[Ru(H)_2(CO)(IMe)(PH_3)]$, would result in formation of the *para*-isomer (i.e. 1,2,4,5-$C_6F_4H_2$). This is in fact the idea of a nucleophilic attack pathway which usually shows selectivity for the 4-position. In contrast, the stepwise mechanism predicts the formation of 1,2,3,4-$C_6F_4H_2$ with a computed barrier +36.3 kcal/mol and this is consistent with the *ortho*-regioselectivity that is observed experimentally. However, by comparing the concerted and stepwise mechanisms for the small model, formation of the *para*-isomer is slightly more favourable ($\Delta\Delta E^{\ddagger}$ = 2.9 kcal/mol).

Some similarities are seen for the HDF of C_6F_5H at $[Ru(H)_2(CO)(IMes)(PPh_3)]$. The concerted mechanism predicts again formation of 1,2,4,5-$C_6F_4H_2$, now with a barrier of +27.2 kcal/mol, while the stepwise pathway forms 1,2,3,4-$C_6F_4H_2$ ($\Delta E^{\ddagger}$ = +25.1 kcal/mol). However, the stepwise mechanism becomes more accessible kinetically than the concerted nucleophilic attack and is now consistent with the unusual *ortho*-regioselectivity observed experimentally ($\Delta\Delta E^{\ddagger}$ = 2.2 kcal/mol). In addition, by including the solvent effect the stepwise mechanism remains lower in energy with a transition state located at +20.1 kcal/mol ($\Delta\Delta E^{\ddagger}$ = 4.6 kcal/mol). The stepwise mechanism corresponds, in fact, to the lowest energy barriers for the formation of 1,2,3,5- and 1,2,4,5-$C_6F_4H_2$ in THF with transition states located at +23.5 kcal/mol and +23.8 kcal/mol, respectively. It should be noted that the solvent effect is really significant as by not taking it into account then formation of 1,2,3,5- and 1,2,4,5-$C_6F_4H_2$ would be predicted to proceed via the concerted pathway.

This can be explained by looking at the three different transition states corresponding to the HF elimination step (see Figure 5.27). All these transition states, as all computed species with the full model, have been obtained after extensive conformation searching.

The two transition states **TS (47a – 48a)$_{IMes}$** and **TS (47b – 48b)$_{IMes}$** correspond to the HDF of C_6F_5H to give 1,2,3,5-$C_6F_4H_2$ and 1,2,4,5-$C_6F_4H_2$, respectively. First of all, the stability of **TS (47 – 48)$_{IMes}$** compared to **TS (47a – 48a)$_{IMes}$** and **TS (47b – 48b)$_{IMes}$** can be explained by the interactions between the mesityl groups and the displaced fluoride. In **TS (47 – 48)$_{IMes}$**, two short H···F5 contacts of 1.91 Å and 1.92 Å are computed. In contrast, in **TS (47a – 48a)$_{IMes}$** and **TS (47b – 48b)$_{IMes}$**, the displaced fluorides, F4 and F3, respectively, interact only with one mesityl group (H···F4 = 1.80 Å, H···F3 =1.81 Å). This difference is due to the orientation of the C_6F_5H moiety in the transition state which is twisted away from the NHC ligand. Indeed, in **TS (47 – 48)$_{IMes}$**, the presence of H6 in the *ortho*-position permits an interaction between the hydrogen atom and the mesityl group. However, in the case of **TS (47a – 48a)$_{IMes}$** and **TS (47b – 48b)$_{IMes}$**, due to their high electronegativity, F2 and F1, respectively cannot interact with the mesityl group and the C_6F_5H twisted away from the NHC ligand. Therefore, the *ortho*-regioselectivity may be explained by the use of bulky NHC ligands.

Due to these different interactions between the displaced fluoride and the mesityl groups, the inclusion of the solvent effect is indispensable. Recomputation of **TS (47 – 48)$_{IMes}$** in THF shows that the transition state is stabilised by 5.0 kcal/mol while the energies of **TS (47a – 48a)$_{IMes}$** and **TS (47b – 48b)$_{IMes}$** decrease by around 8.0 kcal/mol. This difference of 3.0 kcal/mol can be explained by the higher total dipole moment **TS (47a – 48a)$_{IMes}$** and **TS (47b – 48b)$_{IMes}$** than in **TS (47 – 48)$_{IMes}$**, these being +12.14 Debye, +11.19 Debye and +6.86 Debye, respectively. Therefore the use of polar aprotic solvent such as THF will stabilise the first two transition states more than the last one. Another contribution may result from the computed H···F interactions between the displaced fluoride and the mesityl groups. Indeed, in **TS (47 – 48)$_{IMes}$**, as mentioned above, two short contacts are computed while in **TS (47a – 48a)$_{IMes}$** and **TS (47b – 48b)$_{IMes}$** only one is seen. This implies that in **TS (47 – 48)$_{IMes}$** the displaced fluoride is more stabilised and therefore the solvent effect affects less the energy of the transition state compared to **TS (47a – 48a)$_{IMes}$** and **TS (47b – 48b)$_{IMes}$**.

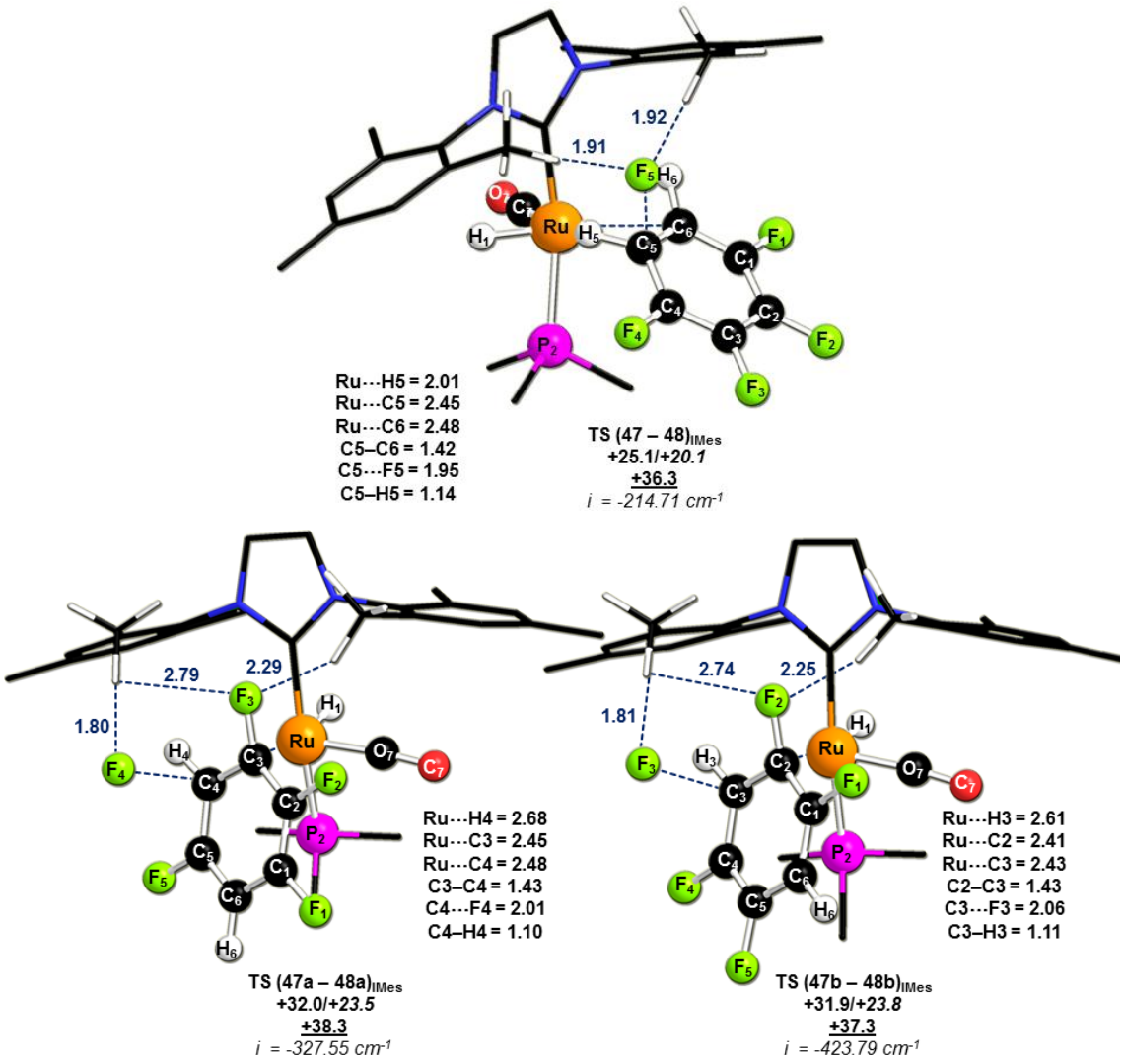

Figure 5.27: Computed transition states corresponding to the HF elimination via TS (47 – 48)$_{IMes}$, TS (47a – 48a)$_{IMes}$ and TS (47b – 48b)$_{IMes}$, respectively.

5.6 Conclusions

Density functional theory calculations have defined a novel class of reaction mechanism for the HDF of C_6F_5H catalysed by [Ru(H)$_2$(CO)(NHC)(PR$_3$)]. The key feature is the nucleophilic attack of one hydride ligand at the fluoroarene moiety. Two different pathways have been characterised, concerted or stepwise, in which the more accessible process for the full model is seen for the latter. In this case, formation of 1,2,3,4-$C_6F_4H_2$ involves 1) PPh_3/C_6F_5H substitution; 2) nucleophilic attack by the Ru hydride ligand at the *ortho* position on the ring; 3) HF loss and Ru fluoroaryl formation; and 4) protonolysis by HF with concomitant fluoride transfer to Ru to give the 1,2,3,4-$C_6F_4H_2$ and [Ru(F)(H)(CO)(IMes)(PPh_3)]. Overall, the rate-limiting transition state has a computed barrier of 20.1 kcal/mol in THF, which corresponds to the HF elimination, and is consistent with the unusual *ortho*-regioselectivity observed experimentally.

Chapter 6: Computational Background

6.1 Introduction

The following chapter deals with some fundamental aspects of density functional theory (DFT) which is the main computational method employed in this thesis.[55] The discussion will begin with background quantum mechanics (QM) and continue with an overview of the Hartree-Fock approximation. In addition, the key concepts in the development of DFT will be reviewed. Finally, the results of benchmark calculations to compare different basis sets and functionals will be presented.

6.2 Background QM

6.2.1 The Schrödinger Equation

The main purpose of quantum chemical approaches is to solve, as far as possible, the time-independent Schrödinger equation:

$$\hat{H}\Psi_i = E_i\Psi_i. \tag{6.1}$$

In Equation (6.1), $\hat{H}$ is the Hamiltonian operator for a system of M nuclei (with charges Z_I and mass m_I, $I = 1,\ldots, M$) and N electrons. The Hamiltonian operator is described as:

$$\hat{H} = \hat{T}_n + \hat{T}_e + \hat{V} \tag{6.2}$$

where $\hat{T}_n$ and $\hat{T}_e$ represent the kinetic energy operators for the nuclei and electrons, respectively:

$$\hat{T}_n = -\frac{1}{2}\sum_{I=1}^{M}\frac{1}{m_I}\nabla_I^2 \tag{6.3}$$

$$\hat{T}_e = -\frac{1}{2}\sum_{i=1}^{N}\nabla_i^2. \tag{6.4}$$

In Equations 6.3 and 6.4, the Laplacians are respectively

$$\nabla_I^2 = \frac{\partial^2}{\partial X_I^2} + \frac{\partial^2}{\partial Y_I^2} + \frac{\partial^2}{\partial Z_I^2},$$

$$\nabla_i^2 = \frac{\partial^2}{\partial x_i^2} + \frac{\partial^2}{\partial y_i^2} + \frac{\partial^2}{\partial z_i^2},$$

where x, y, z are the Cartesian coordinates of the nuclei and electrons and correspond to $\boldsymbol{R}_I = (X_I, Y_I, Z_I)$ and $\boldsymbol{r}_i = (x_i, y_i, z_i)$, respectively.

$\hat{V}$ represents the attractive electrostatic interaction between the nuclei and the electrons, and the repulsive potential due to the nucleus-nucleus and electron-electron interactions, respectively:

$$\hat{V} = -\sum_{I=1}^{M}\sum_{i=1}^{N}\frac{Z_I}{r_{iI}} + \sum_{I=1}^{M}\sum_{J>1}^{M}\frac{Z_I Z_J}{R_{IJ}} + \sum_{i=1}^{N}\sum_{j>1}^{N}\frac{1}{r_{ij}} \tag{6.5}$$

or in a simplified form:

$$\hat{V} = \hat{V}_{Ne} + \hat{V}_{NN} + \hat{V}_{ee}. \tag{6.6}$$

In Equation (6.1), E is the energy of a specific system and Ψ is the wave function of this system. In addition, the square of the wave function:

$$|\Psi(\vec{x}_1, \vec{x}_2, \dots, \vec{x}_N)|^2 d\vec{x}_1 d\vec{x}_2 \dots d\vec{x}_N \tag{6.7}$$

corresponds to the probability that electrons $1,2,\dots,N$ are present in volume elements, $d\vec{x}_1 d\vec{x}_2 \dots d\vec{x}_N$. Also, as electrons are indistinguishable, the probability must remain the same, even if two electrons are interchanged:

$$\left|\Psi(\vec{x}_1, \vec{x}_2, \dots, \vec{x}_i, \vec{x}_j, \dots, \vec{x}_N)\right|^2 = \left|\Psi(\vec{x}_1, \vec{x}_2, \dots, \vec{x}_j, \vec{x}_i, \dots, \vec{x}_N)\right|^2. \tag{6.8}$$

Moreover, as electrons are fermions, the wave function must be antisymmetric which means that Ψ changes sign when two electrons are interchanged. This is described as:

$$\left|\Psi(\vec{x}_1, \vec{x}_2, \ldots, \vec{x}_i, \vec{x}_j, \ldots, \vec{x}_N)\right| = -\left|\Psi(\vec{x}_1, \vec{x}_2, \ldots, \vec{x}_j, \vec{x}_i, \ldots, \vec{x}_N)\right|. \qquad (6.9)$$

This last point is very important as it is a direct consequence of Pauli's exclusion principle where two electrons cannot occupy the same state.

Finally, knowing that the square of the wave function is the probability of finding N electrons in all space, the wave function must be normalised:

$$\int \ldots \int \ |\Psi(\vec{x}_1, \vec{x}_2, \ldots, \vec{x}_N)|^2 d\vec{x}_1 d\vec{x}_2 \ldots d\vec{x}_N = 1. \qquad (6.10)$$

6.2.2 The Born-Oppenheimer Approximation

The Born-Oppenheimer approximation is essential to simplify the Schrödinger equation. This approximation deals with the significant differences between the masses of nuclei and electrons. Indeed, the smallest nucleus, a proton, is approximately 1800 times heavier than an electron and therefore moves much more slowly. One direct consequence is that the nuclei can be considered as fixed and therefore their kinetic energy in Equation (6.3) is zero. Another key point is that the potential energy for the nucleus-nucleus repulsion in Equation (6.6), $\hat{V}_{NN}$, is a constant. Thus, the complete Hamiltonian is reduced to the so-called electronic Hamiltonian, read as:

$$\hat{H}_{elec} = -\frac{1}{2}\sum_{i=1}^{N} \nabla_i^2 - \sum_{I=1}^{M}\sum_{i=1}^{N} \frac{Z_I}{r_{iI}} + \sum_{i=1}^{N}\sum_{j>1}^{N} \frac{1}{r_{ij}} = \hat{T}_e + \hat{V}_{Ne} + \hat{V}_{ee}. \qquad (6.11)$$

This implies that the electronic Schrödinger equation is therefore

$$\hat{H}_{elec}\Psi_{elec} = E_{elec}\Psi_{elec} \qquad (6.12)$$

where Ψ_{elec} and E_{elec} are the electronic wave function and energy, respectively.

6.2.3 The Variational Principle

The variational principle is important to many quantum mechanical applications as it provides a way for approaching the wave function of the ground state, Ψ_0, which is the state that delivers the lowest energy E_0. The variational principle states that all energies calculated from a trial wave function Ψ_{trial} will be always equal or higher to the actual ground state energy, E_0, described as:

$$E_0 \leq \min_{\Psi \to N} E[\Psi] \leq \min_{\Psi \to N} \langle \Psi | \hat{T}_e + \hat{V}_{Ne} + \hat{V}_{ee} | \Psi \rangle \tag{6.13}$$

It is therefore possible to assess the quality of trial wave functions, as the lower the energy, the better the trial wave function.

6.2.4 The Hartree-Fock Approximation

It is impossible to solve the Equation (6.13) by searching through all possible acceptable N-electron wave functions. Therefore a suitable subset has to be defined which incorporates a physically reasonable approximation to the exact wave function. A solution to this problem is the Hartree-Fock approximation where the N-electron wave function is considered through an antisymmetrized product of N one-electron wave functions called the Slater determinant, Φ_{SD},

$$\Psi_0 \approx \Phi_{SD} = \frac{1}{\sqrt{N!}} \begin{vmatrix} \chi_1(\vec{x}_1) & \chi_2(\vec{x}_1) & \dots & \chi_N(\vec{x}_1) \\ \chi_1(\vec{x}_2) & \chi_2(\vec{x}_2) & \dots & \chi_N(\vec{x}_2) \\ \vdots & \vdots & & \vdots \\ \chi_1(\vec{x}_N) & \chi_2(\vec{x}_N) & \dots & \chi_N(\vec{x}_N) \end{vmatrix} \tag{6.14}$$

where $\chi_i(\vec{x}_i)$ are the spin orbitals and are composed of a spatial orbital $\phi_i(\vec{r})$ and one of the two spin functions, $\alpha(s)$or $\beta(s)$, spin up or down, respectively.

A Slater determinant is antisymmetric with respect to the interchange of any two electrons. This means that swapping two rows will result in a change in the sign of Φ_{SD}. In addition, if two columns are the same, Φ_{SD} goes to zero, thus obeying the Pauli's exclusion principle.

Hartree-Fock theory adopts a self-consistent field (SCF) approach. In this method, molecular orbitals are guessed before being introduced to the Fock operator, $\hat{f}_i$, as shown in Equation (6.15), where ε_i corresponds to the *orbital energies*:

$$\hat{f}_i \chi_i = \varepsilon_i \chi_i, i = 1,2, \dots, N. \tag{6.15}$$

This eigenvalue problem is then solved and a new set of molecular orbitals is obtained. This process is repeated until the set of orbitals no longer change (i.e. the Fock equation is solved).

The Fock operator, $\hat{f}_i$, is described as:

$$\hat{f}_i = -\frac{1}{2}\nabla_i^2 - \sum_{I=1}^{M} \frac{Z_I}{r_{iI}} + V_{HF}(i) \tag{6.16}$$

where the first two terms are the kinetic energy of the electrons and the potential energy due to the electron-nucleus attraction, respectively. $V_{HF}(i)$ is the Hartree-Fock potential and is another key approximation that represents the average repulsive potential by an electron due to the remaining N-1 electrons. This simple electron operator $V_{HF}(i)$ has two components, the Coulomb operator, $\hat{J}$, and the exchange operator, $\hat{K}$.

$$V_{HF}(i) = \sum_{j=1}^{N} \left(\hat{J}_j(\vec{x}_1) - \hat{K}_j(\vec{x}_1) \right) \tag{6.17}$$

The Coulomb operator represents the potential experienced by an electron at position $\vec{x}_1$ due to the charge distribution of another electron described by a spin orbital χ_J:

$$\hat{J}_j(\vec{x}_1) = \int \left|\chi_j(\vec{x}_2)\right|^2 \frac{1}{r_{12}} \mathrm{d}\vec{x}_2 \tag{6.18}$$

where the integration is over all space and spin coordinates, weighted by the probability that the other electron is at position $\vec{x}_2$.

The second term in Equation (6.17), $\widehat{K}_j(\vec{x}_1)$, corresponds to the exchange contribution. This operator does not have a classical interpretation and is defined by operating on a spin orbital, read as:

$$\widehat{K}_j(\vec{x}_1)\chi_i(\vec{x}_1) = \int \chi_j{}^*(\vec{x}_2)\frac{1}{r_{12}}\chi_i(\vec{x}_2)\mathrm{d}\vec{x}_2\ \chi_j(\vec{x}_1). \tag{6.19}$$

$\widehat{K}_j(\vec{x}_1)$ leads to an exchange of the two electrons in the two spin orbitals χ_i and χ_j. This implies that the integration depends of the value of χ_i on all points in space, as χ_i is related to $\vec{x}_2$, and for these reasons this operator is *non-local*. In addition, the exchange term resolves the artefact of *self-interaction*, generated by the Coulomb operator in equation (6.18), in which the result is non-zero for $i = j$. In reality, there can be no electron-electron repulsion in a one electron system such as a hydrogen atom. $\widehat{K}_j(\vec{x}_1)$ removes this problem by producing an identical value to $\hat{J}_j(\vec{x}_1)$ when $i = j$, as shown in Equation 6.20, therefore the *self-interaction* is exactly cancelled and in this case the result is zero.

$$\widehat{K}_j(\vec{x}_1) = \hat{J}_j(\vec{x}_1) \text{ for } i = j \tag{6.20}$$

6.2.5 The Electron Correlation

The Hartree-Fock method considers the electron-electron repulsion term as an average interaction. In reality, however, the motion of electrons is correlated, meaning that they do not move independently. One direct consequence is that the Hartree-Fock energy, E_{HF}, is overestimated and lies above that of the ground state energy, E_0. This error between E_{HF} and E_0 is defined as the electron-correlation energy, E_C^{HF}:

$$E_C^{HF} = E_{HF} - E_0 \tag{6.21}$$

The correlation energy connected to the movement of the individual electrons is called the *dynamical* electron correlation. This is a short range effect. A second contribution to E_C^{HF} is the *static* correlation, where a single ground state Slater determinant is not enough to describe a specific system. This implies that other Slater determinants have comparable energies.

For example, the Hartree-Fock approximation fails to model correctly infinitively separated particles, as more than one Slater determinant must be used. For example in the H_2 molecule, the Slater determinant will describe the wave function as being made up by the following contributions:

$$\left(\mathrm{H}^{\uparrow}\cdots\mathrm{H}^{\downarrow}\right)+\left(\mathrm{H}^{\downarrow}\cdots\mathrm{H}^{\uparrow}\right)+\left(\mathrm{H}^{-\uparrow\downarrow}\cdots\mathrm{H}^{+}\right)+\left(\mathrm{H}^{+}\cdots\mathrm{H}^{-\uparrow\downarrow}\right).$$

The first two terms corresponds to the probability of each electron being distributed evenly over both nuclei. In contrast, the third and fourth terms represent the formation of a hydride and a proton. This description provides a reasonable approximation when the system is at its equilibrium geometry, however, when $r \to \infty$ the ionic contribution should tend to zero which is not the case in the Hartree-Fock approximation. This results in an overestimation of the interaction energy as in reality H_2 dissociates to give two neutral atoms.

6.3 Density Functional Theory

6.3.1 The Electron Density

The electron density, $\rho(\vec{r})$, is defined in quantum mechanics as the probability of finding any of the N electrons in a particular volume element. $\rho(\vec{r})$ is derived from Equation 6.10 and is read as:

$$\rho(\vec{r}) = N \int \dots \int \ |\Psi(\vec{x}_1, \vec{x}_2, \dots, \vec{x}_N)|^2 ds_1 d\vec{x}_2 \dots d\vec{x}_N. \qquad (6.22)$$

The main advantage is that the electron density only has 3 spatial variables regardless of the size of the system. This is in contrast with wave function theory (WFT) methods in which 3N variables are taken into account for an N-electron system, which therefore increases considerably the size of the calculations.

6.3.2 The Hohenberg-Kohn Theorems

The history of DFT started in 1927 with the Thomas-Fermi model in which the electron density was considered explicitly instead of a wave function. However, modern DFT

has seen its foundation in 1964 with the publication of two theorems of Hohenberg and Kohn that consider a non-degenerate ground state.

The first Hohenberg-Kohn theorem states that the ground state electron density, ρ_0, determines a unique external potential, $\hat{V}_{ext}$, and thus all properties of the system. Therefore, the ground state electron density defines the ground state energy of a system:

$$E_0[\rho_0] = E_{Ne}[\rho_0] + T[\rho_0] + E_{ee}[\rho_0]. \tag{6.23}$$

Equation 6.23 can be separated into two parts and rewritten as:

$$E_0[\rho_0] = \int \rho_0(\vec{r}) V_{Ne} d\vec{r} + F_{HK}[\rho_0]. \tag{6.24}$$

The first part involves the nuclei and the electron density. This term is therefore system dependent as it depends on the properties of the molecule or system studied. In contrast, the Hohenberg-Kohn functional, $F_{HK}[\rho_0]$, is system independent and is described as:

$$F_{HK}[\rho_0] = T[\rho_0] + E_{ee}[\rho_0]. \tag{6.25}$$

$F_{HK}[\rho_0]$ contains the functional for the kinetic energy, $T[\rho_0]$, and the electron-electron interaction, $E_{ee}[\rho_0]$. In addition, the latter is composed of a classical Coulomb part, $J[\rho_0]$, and a *non-classical* contribution to the electron-electron interactions, $E_{ncl}[\rho_0]$:

$$E_{ee}[\rho_0] = \frac{1}{2}\int\int \frac{\rho(\vec{r}_1)\rho(\vec{r}_2)}{r_{12}} \mathrm{d}\vec{r}_1 \mathrm{d}\vec{r}_2 + E_{ncl}[\rho_0] = J[\rho_0] + E_{ncl}[\rho_0]. \tag{6.26}$$

The second Hohenberg-Kohn theorem is related to the variational principle (see Section 6.2.3). This theorem stipulates that the energy calculated from a trial density, $\tilde{\rho}(\vec{r})$, will give always an upper bound to the exact ground state energy, E_0:

$$E_0 \leq E[\tilde{\rho}] = T[\tilde{\rho}] + E_{Ne}[\tilde{\rho}] + E_{ee}[\tilde{\rho}]. \tag{6.27}$$

In addition, according to Equation 6.27, the minimum is bound to be the exact ground state energy, E_0, when ρ_0 is the exact ground-state density distribution.

6.3.3 The Kohn-Sham Approach

The practical breakthrough of DFT was made by Kohn and Sham in 1965. They realised that a large part of the kinetic energy of electrons could be calculated accurately. This is achieved by using a system of non-interacting electrons built from one-electron functions, in which electrons are uncharged fermions and therefore do not interact with each other via Coulomb repulsion.

The non-interacting reference is constructed from a Slater determinant:

$$\Phi_S = \frac{1}{\sqrt{N!}} \begin{vmatrix} \varphi_1(\vec{x}_1) & \varphi_2(\vec{x}_1) & \dots & \varphi_N(\vec{x}_1) \\ \varphi_1(\vec{x}_2) & \varphi_2(\vec{x}_2) & \dots & \varphi_N(\vec{x}_2) \\ \vdots & \vdots & & \vdots \\ \varphi_1(\vec{x}_N) & \varphi_2(\vec{x}_N) & \dots & \varphi_N(\vec{x}_N) \end{vmatrix} \tag{6.28}$$

where φ_i are the Kohn-Sham orbitals.

The large part of the kinetic energy is calculated by using the kinetic operator in Hartree-Fock theory and substituting the spin orbitals, χ_i, by the Kohn-Sham orbitals, φ_i, to give:

$$T_s = -\frac{1}{2}\sum_{i=1}^{N} \langle \varphi_i | \nabla^2 | \varphi_i \rangle. \tag{6.29}$$

The rest of the kinetic energy can be included in the Hohenberg-Kohn functional $F[p]$:

$$F[\rho(\vec{r})] = T_s[\rho(\vec{r})] + J[\rho(\vec{r})] + E_{XC}[\rho(\vec{r})] \tag{6.30}$$

where the *exchange-correlation energy*, E_{XC}, is defined by

$$E_{XC}[\rho] \equiv (T[\rho] - T_s[\rho]) + (E_{ee}[\rho] - J[\rho]) = T_c[\rho] + E_{ncl} \tag{6.31}$$

in which $T_c[\rho]$ is the residual part of the true kinetic energy.

At this stage, the best Kohn-Sham orbitals correspond to the lowest energy, expressed as:

$$\hat{f}^{KS}\varphi_i = \varepsilon_i\varphi_i \tag{6.32}$$

where $\hat{f}^{KS}$ represents the one-electron Kohn-Sham operator, described as:

$$\hat{f}^{KS} = -\frac{1}{2}\nabla^2 + V_{\text{eff}}(\vec{r}). \tag{6.33}$$

$V_{\text{eff}}(\vec{r})$ is the Kohn-Sham effective potential:

$$V_{\text{eff}}(\vec{r}) = \int \frac{\rho(\vec{r}_2)}{r_{12}} d\vec{r}_2 + V_{XC}(\vec{r}_1) - \sum_{I=1}^{M} \frac{Z_A}{r_{1A}} \tag{6.34}$$

where V_{XC} is the potential due to the exchange-correlation E_{XC} and described as:

$$V_{XC} \equiv \frac{\delta E_{XC}}{\delta \rho}. \tag{6.35}$$

Unfortunately, the exact function for E_{XC} is unknown and has to be approximated.

6.3.4 Jacob's Ladder

The concept of the Jacob's ladder has been introduced by Perdew in order to classify different density functionals.[87] Jacob's ladder leads from earth (Hartree-Fock Theory) to heaven (chemical accuracy), in which users are described as angels in order to climb or descend on it. Jacob's ladder contains five rungs which represent the hierarchy of density approximations: the local density approximation (LDA), the generalized gradient approximations (GGA), the meta generalized gradient approximation (M-GGA), the hybrid and hybrid meta generalized approximations (H-GGA and MH-GGA, respectively) and finally the fully non-local description.

(i) The Local Density Approximation

The local density approximation (LDA) provides a way of modelling the exchange-correlation energy, E_{XC}. LDA is based on the uniform electron gas (UEG) of density:

$$\rho = \frac{N}{V} \tag{6.36}$$

obtained when N and V approach infinity, where N represents a set of uniformly distributed electrons and V is the volume of the system. In addition, the UEG is set against a uniformly positively charged background potential, to neutralise the system and this is similar to an idealised metal, often called *jellium*.

This model is useful as both the exact exchange and correlation energies can be known accurately. In the local density approximation, E_{XC} is expressed as:

$$E_{XC}^{LDA}[\rho] = \int \rho(\vec{r})\varepsilon_{XC}\big(\rho(\vec{r})\big)d\vec{r} \tag{6.37}$$

where $\varepsilon_{XC}\big(\rho(\vec{r})\big)$ represents the exchange-correlation energy per particle of a UEG of density $\rho(\vec{r})$. In addition, $\varepsilon_{XC}\big(\rho(\vec{r})\big)$ can be separated in two terms for the exchange and correlation contributions:

$$\varepsilon_{XC}\big(\rho(\vec{r})\big) = \varepsilon_X\big(\rho(\vec{r})\big) + \varepsilon_C\big(\rho(\vec{r})\big). \tag{6.38}$$

In addition, the exchange part, $\varepsilon_X\big(\rho(\vec{r})\big)$, is described exactly as:

$$\varepsilon_X\big(\rho(\vec{r})\big) = -\frac{3}{4}\left(\frac{3\rho(\vec{r})}{\pi}\right)^{\frac{1}{3}}. \tag{6.39}$$

In contrast, there is no known exact equation for the correlation energy, $\varepsilon_X\big(\rho(\vec{r})\big)$, however, values can be obtained based on fitting data from Monte-Carlo simulations for a UEG.

One major discrepancy with LDA is that it overestimates atomisation energies, resulting in overbinding.

(ii) The Generalized Gradient Approximation

Generalized gradient approximation (GGA) is one way to improve LDA by using not only the density $\rho(\vec{r})$ at a particular point $\vec{r}$, but by supplementing the density with the gradient of the charge density $\nabla\rho(\vec{r})$:

$$E_{XC}^{GGA}[\rho_\alpha, \rho_\beta] = \int f(\rho_\alpha, \rho_\beta, \nabla\rho_\alpha, \nabla\rho_\beta) d\vec{r}. \tag{6.40}$$

The exchange and correlation contributions of E_{XC}^{GGA} can be, as well, separated:

$$E_{XC}^{GGA} = E_X^{GGA} + E_C^{GGA} \tag{6.41}$$

where the exchange part, E_X^{GGA}, is equal to:

$$E_X^{GGA} = E_X^{LDA} - \sum \int F(s_\sigma)\rho_\sigma^{4/3}(\vec{r})\ d\vec{r}. \tag{6.42}$$

The term s_σ corresponds to the local inhomogeneity parameter and described as:

$$s_\sigma(\vec{r}) = \frac{|\nabla\rho_\sigma(\vec{r})|}{\rho_\sigma^{4/3}(\vec{r})}. \tag{6.43}$$

There are several types of GGA exchange functionals. The first such functional has been published by Becke[71] in 1988 and is commonly abbreviated as B:

$$F^B = \frac{\beta s_\sigma^2}{1 + 6\beta s_\sigma \sinh^{-1} s_\sigma}. \tag{6.44}$$

where β is an empirical parameter (0.0042) which has been fitted to the exactly known exchange energies of the six nobles gases, He to Rn.

A second class of GGA exchange functionals have been developed with no empirical parameters. Instead, a rational function of the reduced density gradient is used. Examples of this approach include Becke, 1986 (B86),[88] Perdew, 1986 (P86),[89] Lacks and Gordon, 1993 (LG)[90] and Perdew, Burke and Ernzerhof, 1996 (PBE).[91]

There are as well several correlation functionals, such as the 1986 Perdew exchange functional (P86)[72] which contains an empirical parameter fitted to the correlation energy of the neon atom. This correlation functional was then developed by Perdew and Wang in 1991 (PW91)[92] which is free of any empirical parameters. In contrast, Lee, Yang and Parr created in 1988 a correlation functional (LYP)[93] which is not based on the uniform electron gas but derived from a correlated wave function that reproduces the correlation energy for the helium atom. Therefore, this correlation functional contains one empirical parameter.

The exchange and correlation functionals can be paired together; for example BP86 includes the gradient corrected exchange functional of Becke[71] and the correlation functional of Perdew.[72]

(iii) Meta-GGA Functionals

The *meta*-GGA functionals are another improvement of the GGA functionals. They employ the kinetic energy density, τ_σ, and the second derivative of the electron density (i.e. the Laplacian), in addition to the reduced gradient density. The kinetic energy density is described as:

$$\tau_\sigma = \sum_i^{occ.} \frac{1}{2} |\nabla \psi_i|^2 . \qquad (6.45)$$

One example of a *meta*-GGA is TPSS which employs the exchange and the τ-dependent gradient-corrected functional of Tao, Perdew, Staroveroz and Scuseria.[94]

(iv) Hybrid-GGA and Meta-Hybrid-GGA Functionals

The first idea of hybrid functionals was to compute an exact value of the Hartree-Fock exchange term, E_X^{HF} and use the Kohn-Sham orbitals rather than Hartree-Fock orbitals:

$$E_{XC} = E_X^{HF} + E_C^{KS} \tag{6.46}$$

However, this did not give the expected improvement and so instead, a part of the exchange and correlation contributions calculated using LDA was added. The first to use this approach was Becke[95] in 1993 with the B3PW91[92,95] functional:

$$E_{XC}^{B3PW91} = E_{XC}^{LSD} + a\left(E_{XC}^{\lambda=0} - E_X^{LSD}\right) + bE_X^B + cE_C^{PW91} \tag{6.47}$$

where a, b and c are semi-empirical parameters, used to determine the weight of each contribution and fitted to reproduce atomization and ionization energies, proton affinities and some total energies.

The most popular hybrid functional is B3LYP[88,93] which was suggested by Stephen et *al.*[96] and described as:

$$E_{XC}^{B3LYP} = (1-a)E_X^{LSD} + aE_{XC}^{\lambda=0} + bE_X^{B88} + cE_C^{LYP} + (1-c)E_c^{LSD} \tag{6.48}$$

The *meta*-hybrid-GGA functionals are based on *meta*-GGA functionals and contain a percentage of exact exchange. TPSSh[94] is one example as well as the highly parameterized Truhlar M06 suite of functionals (M06, M06-L, M06-2X and M06-HF).[97] M06 has 27% exact exchange while in M06-2X this doubles to 54% and M06-HF has 100 % exact exchange. M06-L is actually a pure functional in which no exact exchange is computed, therefore this functional can be considered as a *meta*-GGA rather than a *meta*-hybrid-GGA.

(v) Double Hybrid Functionals

A final type of functionals has recently emerged called the double hybrid functionals. One of them has been introduced by Grimme (B2-PLYP)[98] which includes a part of

Becke exchange (B) and the correlation reported by Lee, Yang and Parr (LYP) with a percentage of exact exchange and a contribution from MP2:

$$E_{XC}^{B2-PLYP} = (1 - a_x)E_X^B + a_x E_X^{HF} + bE_c^{LYP} + cE_c^{MP2} \tag{6.49}$$

The double hybrid functionals are, in a way, considered as the fifth rung of Jacob's Ladder.

6.3.5 Dispersion-Corrected Functional

One of the biggest challenges in density functional theory is to account for weak non-covalent interactions or dispersion forces. The M06 functional has been parameterized (36 parameters) to consider non-covalent interactions, however, a new type of dispersion-corrected functional has also been recently developed. These are known as Grimme's DFT-D functionals and use a semi-empirical dispersion correction.[99] DFT-D functionals compute energies as:

$$E_{DFT-D} = E_{DFT} + E_{disp} \tag{6.50}$$

where E_{DFT} is the DFT energy for a specific functional (e.g. BP86), and E_{disp} is semi-empirical dispersion correction given by:

$$E_{disp} = -s_6 \sum_{i=1}^{N_{at}-1} \sum_{j=i+1}^{N_{at}} \frac{C_6^{ij}}{R_{ij}^6} f_{dmp}(R_{ij}) \tag{6.51}$$

where, N_{at} is the number of atoms in the system, s_6 is the global scaling factor, C_6^{ij} corresponds to the dispersion coefficient for atom pairs ij and R_{ij} is the interatomic distance. Also, f_{dmp} represents the damping function, used to avoid near-singularities for small R_{ij}.

6.4 Basis Sets

Basis sets are employed to provide a number of predefined basis functions which are then used to describe the orbitals of an atom or molecule mathematically. The accuracy

of wave function calculations is maximised for an infinite number of basis functions, however, the calculation time increases rapidly and therefore becomes unpractical. On the other hand, in the Kohn-Sham scheme, the orbitals are used to construct the density:

$$\rho(\vec{r}) = \sum_{i=1}^{N} |\varphi_i(\vec{r})|^2 \qquad (6.52)$$

and therefore the basis set requirements in Kohn-Sham calculations are less strong.

There are two types of basis functions commonly used for molecular calculations: Slater-type orbitals (STOs) and Gaussian-type orbitals (GTOs):

$$\text{STO:} \qquad \chi_{\zeta,n,l,m}(r,\theta,\varphi) = NY_{l,m}(\Theta,\varphi)\, r^{n-1}\, exp[-\zeta r] \qquad (6.53)$$

$$\text{GTO:} \qquad \chi_{\zeta,n,l,m}(r,\theta,\varphi) = NY_{l,m}(\Theta,\varphi)\, r^{(2n-2-l)}\, exp[-\zeta r^2] \qquad (6.54)$$

where N is a normalisation constant, while r, θ, and φ are spherical coordinates. In addition, $Y_{l,m}$ corresponds to the angular momentum and n, l, and m are quantum numbers. The GTOs depend on r^2 which makes them less accurate than the STOs. Indeed, at the nucleus ($r = 0$), the GTO has a slope that goes to zero and they also fail to model the wave function well as $r \to \infty$. However, this model can be improved by using linear combination of several primitive GTOs to model each STO.

The choice of the basis set is key as it needs to strike a balance between accuracy and the time of calculation. The minimal basis set only contains the number of basis functions which is required to accommodate all the electrons of the atom in the ground state. The most common minimal basis set is STO-3G in which 3 primitive GTOs are contracted to produce one STO.

These small basis sets can be improved by increasing the number of basis functions. For example, double-zeta basis sets can be used in which the number of basis functions will be double to describe each atomic orbital. These include the 3-21G and 6-31G basis sets developed by Pople and co-workers.[76a] In 3-21G, the core electrons are represented by a contraction of 3 GTOs, while the valence electrons are described by 2

basis functions made up of 2 GTOs and 1 GTO, respectively. In 6-31G, the difference is that the core electrons are contracted by 6 GTOs, while the valence orbitals are contracted as 3 GTOs and 1 GTO.

The accuracy of the calculations can be further improved by addition of polarisation and diffuse functions. For example, 6-31G** adds d-orbital polarisation functions to the heavy atoms (e.g. carbon atoms) and p-orbital polarisation functions for light atoms (i.e. hydrogen and helium atoms). The use of diffuse basis sets (e.g. 6-31+G) will add a set of orbital functions with small exponents which decay slowly as the distance from the nucleus increases.

Finally, when the system contains atoms from the third row onwards, effective core potentials (ECPs) are generally employed to represent the electron core shells rather than modelling the core electrons explicitly. A set of associated basis sets is also used to model the valence electrons. In addition, ECPs can be designed to treat implicitly the scalar-relativistic effects for heavy atoms.

6.5 Benchmarking of Different Basis Sets and Exchange-Correlation Methods

Basis sets and DFT functionals were benchmarked for the rate-limiting transition states and key species involved in the reaction of C_6F_5H at $[Rh(SiMe_3)(PMe_3)_3]$ (**1**$_{\mathbf{SiMe3}}$, see Chapter 3). All reported energies are relative to **1**$_{\mathbf{SiMe3}}$ plus C_6F_5H.

The basis sets were tested by using the geometries optimised with the BP86 functional and 6-31G** basis sets for all atoms, except Rh, Si and P in which SDD pseudo-potentials and basis sets were employed. From these optimised structures, single point calculations were performed by using triple-zeta polarised (6-311G**), diffuse double-zeta polarised (6-31++G**) and diffuse triple-zeta polarised (6-311++G**) basis sets. The results are summarised in Table 6.1. As seen in Chapter 3, direct C–H activation is preferred over C–F activation at **1**$_{\mathbf{SiMe3}}$. Using 6-31G** basis sets, calculations showed indeed that C–H activation is more accessible by 3.5 kcal/mol, with 6-311G** by 3.2 kcal/mol, with 6-31++G** by 5.1 kcal/mol and finally with 6-311++G** basis sets by 4.4 kcal/mol. This implies that there is a relatively small energy difference by using richer basis sets for this pathway and therefore the use of 6-31G** is sufficient. In contrast, C–F activation was found to be kinetically and thermodynamically more

accessible at the 3-coordinate *trans*-[Rh($SiMe_3$)(PMe_3)$_2$] (***trans*-1$_{SiMe3}$**). C–F activation is lower than C–H activation by 4.0 kcal/mol (6-31G**), 3.4 kcal/mol (6-311G**), 1.4 kcal/mol (6-31++G**) and 1.6 kcal/mol (6-311G**), respectively. In this case, the same behaviour is seen and the key point is that C–F activation remains kinetically more accessible. In addition, phosphine dissociation to form ***trans*-1$_{SiMe3}$** is computed to similar with all basis sets. Finally, the C–F activation product is much more favourable thermodynamically with relative energies of -53.1 kcal/mol, -51.5 kcal/mol, -52.5 kcal/mol and -50.9 kcal/mol, respectively. This is consistent with the experimental selectivity and again the use of 6-31G** basis sets represents properly this feature.

Table 6.1: Single point energies (kcal/mol) using BP86 functional with double-zeta polarised (6-31G), triple-zeta polarised (6-311G**), diffuse double-zeta polarised (6-31++G**) and diffuse triple-zeta polarised (6-311++G**) basis sets.**

	6-31G**	**6-311G****	**6-31++G****	**6-311++G****
		C–F and C–H activation at ***1$_{SiMe3}$***		
C–F Activation	+16.3	+18.1	+23.6	+22.3
C–H Activation	+12.8	+14.9	+18.5	+17.9
		Phosphine dissociation at ***1$_{SiMe3}$***		
TS	+17.9	+18.0	+17.9	+18.0
***trans*-[Rh(SiMe$_3$)(PMe$_3$)$_2$]**	+17.9	+17.4	+17.3	+17.2
		C–F and C–H activation at ***trans-1$_{SiMe3}$***		
C–F Activation	+12.1	+14.4	+19.5	+18.7
C–H Activation	+16.1	+17.8	+20.9	+20.3
		Final products		
[Rh(4-C$_6$F$_4$H)(PMe$_3$)$_3$]	-60.6	-58.4	-56.3	-55.6
[Rh(C$_6$F$_5$)(PMe$_3$)$_3$]	-7.5	-6.9	-3.8	-4.7

DFT functionals were as well benchmarked on the same species and the results are summarised in Tables 6.2 and 6.3. Before comparing the different functionals, it should be mentioned that no transition state for C–F activation of C_6F_5H at $\mathbf{1_{SiMe3}}$ to form the *mer′*-isomer has been located using the BLYP functional. In all the cases, one phosphine ligand was fully dissociated (< 3.5 Å).

In general, the idea that C–F activation of C_6F_5H occurs at the three-coordinate ***trans*-$\mathbf{1_{SiMe3}}$** is confirmed. In the case of BLYP and B3LYP, phosphine dissociation is facile with computed enthalpies of +10.3 kcal/mol and +12.1 kcal/mol. For the remaining functionals this step can vary between +16.8 kcal/mol (B3PW91) to +18.1 kcal/mol (B3P86). TPSS and TPSSh show that phosphine dissociation is barrierless as the 3-coordinate ***trans*-$\mathbf{1_{SiMe3}}$** is slightly less stable. This may come from a basis set superposition error (BSSE) as in the transition state, the two fragments, $[Rh(SiMe_3)(PMe_3)_2]$ and PMe_3 are computed together. From ***trans*-$\mathbf{1_{SiMe3}}$**, most of the functionals confirm that C–F activation is kinetically more accessible. Only B3P86 shows that C–F and C–H activation are competitive, with computed energies located at +17.9 kcal/mol and +17.0 kcal/mol, respectively, while B3PW91 shows that C–H activation is more accessible by 1.9 kcal/mol. On the other hand, as described in Chapter 3, C–H activation at $\mathbf{1_{SiMe3}}$ is preferred over both C–F activation and C–H activation at ***trans*-$\mathbf{1_{SiMe3}}$** as the initial phosphine dissociation is higher in energy. This hierarchy is respected with all the functionals except BLYP and B3LYP, which show that phosphine dissociation and subsequent C–F activation are more favourable than C–H activation at $\mathbf{1_{SiMe3}}$.

Table 6.2: Enthalpies energies (kcal/mol) using a range of GGA (BP86, BLYP), hybrid GGA (B3P86, B3LYP, B3PW91), meta GGA (TPSS) and hybrid meta GGA (TPSSh) functionals with double-zeta polarised (6-31G) basis sets.**

	BP86	**BLYP**	**B3P86**	**B3LYP**	**B3PW91**	**TPSS**	**TPSSh**
				C–F and C–H activation at ***1$_{SiMe3}$***			
C–F Activation	+17.8	–	+20.0	+20.9	+25.3	+13.0	+15.9
C–H Activation	+12.1	+15.6	+12.1	+16.7	+16.0	+9.8	+11.1
				Phosphine dissociation at ***1$_{SiMe3}$***			
TS	+17.0	+10.3	+18.1	+12.1	+16.8	+17.2	+17.5
***trans*-[Rh(SiMe$_3$)(PMe$_3$)$_2$]**	+16.6	+9.0	+18.5	+11.4	+15.7	+17.8	+18.1
				C–F and C–H activation at ***trans-1$_{SiMe3}$***			
C–F Activation	+10.9	+3.6	+17.9	+12.0	+18.8	+8.5	+12.4
C–H Activation	+13.9	+10.0	+17.0	+14.5	+16.9	+13.2	+15.2
				Final products			
[Rh(4-C$_6$F$_4$H)(PMe$_3$)$_3$]	-59.4	-65.7	-64.4	-69.2	-63.5	-63.7	-64.3
[Rh(C$_6$F$_5$)(PMe$_3$)$_3$]	-8.2	-12.2	-10.3	-13.2	-9.8	-12.1	-12.4

Computed free energies are consistent with the experimental selectivity (see Table 6.3). First of all, the phosphine dissociation pathway becomes more favourable and in most cases subsequent C–F activation is kinetically more accessible than C–H activation. This is true with BP86, BLYP, B3LYP, TPSS and TPSSh functionals. B3P86 and B3PW91 functionals show the C–H activation is competitive. However, as mentioned in Chapter 3, C–H activation can be reversible and therefore the more favourable product, in this case through C–F activation, will be observed.

In conclusion, the use of different functionals does not change the outcome of the reaction in which the C–F activation product is observed experimentally. Indeed, all functionals confirm that this is the most stable thermodynamic product. Functionals such as BP86, BLYP, B3LYP, TPSS and TPSSh show that computed free energies for C–F activation are kinetically and thermodynamically more accessible while B3P86 and B3PW91 imply that C–F activation and C–H activation of C_6F_5H are competitive and thus the most stable product will be formed, [Rh(4-C_6F_4H)(PMe_3)$_3$], in agreement with the experiment.

Table 6.3: Free energies (kcal/mol) using a range of GGA (BP86, BLYP), hybrid GGA (B3P86, B3LYP, B3PW91), meta GGA (TPSS) and hybrid meta GGA (TPSSh) functionals with double-zeta polarised (6-31G) basis sets.**

	BP86	**BLYP**	**B3P86**	**B3LYP**	**B3PW91**	**TPSS**	**TPSSh**
				C–F and C–H activation at ***1$_{SiMe3}$***			
C–F Activation	+33.9	–	+36.2	+36.1	+41.4	+28.6	+31.7
C–H Activation	+27.3	+30.1	+26.9	+31.4	+31.0	+24.5	+25.9
				Phosphine dissociation at ***1$_{SiMe3}$***			
TS	+13.2	+7.1	+13.8	+9.1	+13.2	+13.2	+13.8
***trans*-[Rh(SiMe$_3$)(PMe$_3$)$_2$]**	+2.3	-5.0	+4.8	-2.5	+2.0	+4.3	+4.6
				C–F and C–H activation at ***trans-1$_{SiMe3}$***			
C–F Activation	+12.4	+4.9	+19.0	+13.3	+20.2	+9.8	+13.7
C–H Activation	+15.3	+10.1	+16.9	+14.6	+17.0	+13.3	+15.2
				Final products			
[Rh(4-C$_6$F$_4$H)(PMe$_3$)$_3$]	-59.0	-66.0	-65.4	-69.7	-64.3	-64.0	-64.9
[Rh(C$_6$F$_5$)(PMe$_3$)$_3$]	-7.7	-12.1	-10.9	-13.4	-10.1	-12.3	-13.2

Overall Conclusion

Density functional theory calculations have been carried out in order to understand the selective C–F activation of fluoroaromatics at rhodium and ruthenium. Novel mechanisms such as silyl- and boryl-assisted C–F activation have been defined. This last idea could be a further step in the synthesis of catalysts containing atoms that may become hypervalent (e.g. silicon) or Lewis acidic ligands (e.g. BR_2) to activate inert C–F bonds of fluoroorganic molecules.

In addition, a novel nucleophilic attack of one hydride ligand at the fluoroarene moiety has been calculated. This type of mechanism could be taken into account to explain the selectivity for C–F activation of other systems previously described in the literature.[15b,15c,40,49-50]

References

(1) (a) Moissan, H. *C. R. Acad. Sci.* **1886**, *102*, 1534; (b) Moissan, H. *C. R. Acad. Sci.* **1886**, *103*, 202; (c) Moissan, H. *C. R. Acad. Sci.* **1886**, *103*, 256.

(2) Kirsch, P. *Modern Fluoroorganic Chemistry: Synthesis, Reactivity, Applications*; Wiley-VCH: Weinheim, 2004.

(3) Balz, G.; Schiemann, G. *Chem. Ber.* **1927**, *60*, 1186.

(4) Banks, R. E.; Smart, B. E.; Tatlow, J. C. *Organofluorine Chemistry: Principles and Commercial Applications*; Plenum Press: New York, 1994.

(5) Powell, R. L. Applications: Polymers In *Houben–Weyl: Organo-Fluorine Compounds*; Baasner, B.; Hagemann, H.; Tatlow, J. C.; Georg Thieme Verlag: Stuttgart, 2000; Vol. E 10a, p 76.

(6) (a) Simons, J. H. *J. Electrochem. Soc.* **1949**, *95*, 47; (b) Simons, J. H.; Francis, H. T.; Hogg, J. A. *J. Electrochem. Soc.* **1949**, *95*, 53; (c) Simons, J. H.; J., H. W. *J. Electrochem. Soc.* **1949**, *95*, 55; (d) Simons, J. H.; Pearlson, W. H.; Brice, T. J.; Wilson, W. A.; Dresdner, R. D. *J. Electrochem. Soc.* **1949**, *95*, 59; (e) Simons, J. H.; Dresdner, R. D. *J. Electrochem. Soc.* **1949**, *95*, 64.

(7) Rhodes, R. *The Making of the Atomic Bomb*; Simon and Schuster: New York, 1986.

(8) Molina, M. J.; Rowland, F. S. *Nature* **1974**, *249*, 819.

(9) Thayer, A. M. *Chem. Eng. News* **2006**, *84*, 15.

(10) (a) Ainsworth, S. J. *Chem. Eng. News* **2008**, *86*, 15; (b) Grushin, V. V. *Acc. Chem. Res.* **2010**, *43*, 160.

(11) Yoneda, N.; Fukuhara, T. *Tetrahedron* **1996**, *52*, 23.

(12) Subramanian, M. A.; Manzer, L. E. *Science* **2002**, *297*, 1665.

(13) (a) Kiplinger, J. L.; Richmond, T. G.; Osterberg, C. E. *Chem. Rev.* **1994**, *94*, 373; (b) Burdeniuc, J.; Jedlicka, B.; Crabtree, R. H. *Chem. Ber./Recueil* **1997**, *130*, 145; (c) Murphy, E. F.; Murugavel, R.; Roesky, H. W. *Chem. Rev.* **1997**, *97*, 3425; (d) Braun, T.; Perutz, R. N. *Chem. Commun.* **2002**, 2749; (e) Sun, A. D.; Love, J. A. *Dalton Trans.* **2010**, *39*, 10362; (f) Jones, W. D. *Dalton Trans.* **2003**, 3991; (g) Torrens, H. *Coord. Chem. Rev.* **2005**, *249*, 1957; (h) Perutz, R. N. *Science* **2008**, *321*, 1168; (i) Amii, H.; Uneyama, K. *Chem. Rev.* **2009**, *109*, 2119; (j) Clot, E.; Eisenstein, O.; Jasim, N.; Macgregor, S. A.; McGrady, J. E.; Perutz, R. N. *Acc. Chem. Res.* **2011**, *44*, 333; (k) Braun, T.; Perutz, R. N. Transition Metal-Mediated C-F Bond Activation. In

Comprehensive Organometallic Chemistry III; Crabtree, R. H.; Mingos, D. M. P.; Elsevier: Oxford, 2006; Vol. 1, Chap. 26.

(14) (a) Braun, T.; Parsons, S.; Perutz, R. N.; Voith, M. *Organometallics* **1999**, *18*, 1710; (b) Braun, T.; Perutz, R. N.; Sladek, M. I. *Chem. Commun.* **2001**, 2254; (c) Noveski, D.; Braun, T.; Neumann, B.; Stammler, A.; Stammler, H.-G. *Dalton Trans.* **2004**, 4106; (d) Steffen, A.; Sladek, M. I.; Braun, T.; Neumann, B.; Stammler, H.-G. *Organometallics* **2005**, *24*, 4057.

(15) (a) Aizenberg, M.; Milstein, D. *Science* **1994**, *265*, 359; (b) Aizenberg, M.; Milstein, D. *J. Am. Chem. Soc.* **1995**, *117*, 8674; (c) Vela, J.; Smith, J. M.; Yu, Y.; Ketterer, N. A.; Flaschenriem, C. J.; Lachicotte, R. J.; Holland, P. L. *J. Am. Chem. Soc.* **2005**, *127*, 7857; (d) Braun, T.; Noveski, D.; Ahijado, M.; Wehmeier, F. *Dalton Trans.* **2007**, 3820; (e) Meier, G.; Braun, T. *Angew. Chem., Int. Ed.* **2009**, *48*, 1546; (f) Reade, S. P.; Mahon, M. F.; Whittlesey, M. K. *J. Am. Chem. Soc.* **2009**, *131*, 1847.

(16) O'Hagan, D. *Chem. Soc. Rev.* **2008**, *37*, 308.

(17) Fahey, D. R.; Mahan, J. E. *J. Am. Chem. Soc.* **1977**, *99*, 2501.

(18) Yamamoto, T.; Abla, M. *J. Organomet. Chem.* **1997**, *535*, 209.

(19) Cronin, L.; Higgitt, C. L.; Karch, R.; Perutz, R. N. *Organometallics* **1997**, *16*, 4920.

(20) Burling, S.; Elliott, P. I. P.; Jasim, N. A.; Lindup, R. J.; McKenna, J.; Perutz, R. N.; Archibald, S. J.; Whitwood, A. C. *Dalton Trans.* **2005**, 3686.

(21) Archibald, S. J.; Braun, T.; Gaunt, J. A.; Hobson, J. E.; Perutz, R. N. *J. Chem. Soc., Dalton Trans* **2000**, 2013.

(22) Braun, T.; Foxon, S. P.; Perutz, R. N.; Walton, P. H. *Angew. Chem., Int. Ed.* **1999**, *38*, 3326.

(23) Bach, I.; Pörschke, K.-R.; Goddard, R.; Kopiske, C.; Krüger, C.; Rufińska, A.; Seevogel, K. *Organometallics* **1996**, *15*, 4959.

(24) Braun, T.; Cronin, L.; Higgitt, C. L.; McGrady, J. E.; Perutz, R. N.; Reinhold, M. *New J. Chem.* **2001**, *25*, 19.

(25) Johnson, S. A.; Taylor, E. T.; Cruise, S. J. *Organometallics* **2009**, *28*, 3842.

(26) (a) Johnson, S. A.; Huff, C. W.; Mustafa, F.; Saliba, M. *J. Am. Chem. Soc.* **2008**, *130*, 17278; (b) Johnson, S. A.; Mroz, N. M.; Valdizon, R.; Murray, S. *Organometallics* **2011**, *30*, 441.

(27) Hatnean, J. A.; Beck, R.; Borrelli, J. D.; Johnson, S. A. *Organometallics* **2010**, *29*, 6077.

(28) Sladek, M. I.; Braun, T.; Neumann, B.; Stammler, H.-G. *J. Chem. Soc., Dalton Trans* **2002**, 297.

(29) Doster, M. E.; Johnson, S. A. *Angew. Chem., Int. Ed.* **2009**, *48*, 2185.

(30) Arduengo, A. J.; Harlow, R. L.; Kline, M. *J. Am. Chem. Soc.* **1991**, *113*, 361.

(31) (a) Crabtree, R. H. *Coord. Chem. Rev.* **2007**, *251*, 595; (b) Díez-González, S.; Marion, N.; Nolan, S. P. *Chem. Rev.* **2009**, *109*, 3612; (c) Hermann, H.; Lohrenz, J. C. W.; Kuhn, A.; Boche, G. *Tetrahedron* **2000**, *56*, 4109; (d) Herrmann, W. A. *Angew. Chem., Int. Ed.* **2002**, *41*, 1290; (e) Herrmann, W. A.; Köcher, C. *Angew. Chem., Int. Ed.* **1997**, *36*, 2162; (f) Peris, E.; Crabtree, R. H. *Coord. Chem. Rev.* **2004**, *248*, 2239; (g) Sommer, W. J.; Weck, M. *Coord. Chem. Rev.* **2007**, *251*, 860.

(32) (a) Schaub, T.; Radius, U. *Chem. Eur. J.* **2005**, *11*, 5024; (b) Schaub, T.; Backes, M.; Radius, U. *J. Am. Chem. Soc.* **2006**, *128*, 15964; (c) Schaub, T.; Backes, M.; Radius, U. *Eur. J. Inorg. Chem.* **2008**, *2008*, 2680; (d) Schaub, T.; Fischer, P.; Steffen, A.; Braun, T.; Radius, U.; Mix, A. *J. Am. Chem. Soc.* **2008**, *130*, 9304; (e) Schaub, T.; Fischer, P.; Meins, T.; Radius, U. *Eur. J. Inorg. Chem.* **2011**, *2011*, 3122.

(33) Jasim, N. A.; Perutz, R. N.; Whitwood, A. C.; Braun, T.; Izundu, J.; Neumann, B.; Rothfeld, S.; Stammler, H. G. *Organometallics* **2004**, *23*, 6140.

(34) Macgregor, S. A.; Roe, D. C.; Marshall, W. J.; Bloch, K. M.; Bakhmutov, V. I.; Grushin, V. V. *J. Am. Chem. Soc.* **2005**, *127*, 15304.

(35) Hofmann, P.; Unfried, G. *Chem. Ber.* **1992**, *125*, 659.

(36) Jasim, N. A.; Perutz, R. N. *J. Am. Chem. Soc.* **2000**, *122*, 8685.

(37) Nova, A.; Erhardt, S.; Jasim, N. A.; Perutz, R. N.; Macgregor, S. A.; McGrady, J. E.; Whitwood, A. C. *J. Am. Chem. Soc.* **2008**, *130*, 15499.

(38) Kiplinger, J. L.; Richmond, T. G. *Chem. Commun.* **1996**, 1115.

(39) Kiplinger, J. L.; Richmond, T. G. *J. Am. Chem. Soc.* **1996**, *118*, 1805.

(40) (a) Edelbach, B. L.; Fazlur Rahman, A. K.; Lachicotte, R. J.; Jones, W. D. *Organometallics* **1999**, *18*, 3170; (b) Kraft, B. M.; Jones, W. D. *J. Organomet. Chem.* **2002**, *658*, 132; (c) Kraft, B. M.; Lachicotte, R. J.; Jones, W. D. *J. Am. Chem. Soc.* **2001**, *123*, 10973.

(41) Jäger-Fiedler, U.; Klahn, M.; Arndt, P.; Baumann, W.; Spannenberg, A.; Burlakov, V. V.; Rosenthal, U. *J. Mol. Catal. A: Chem.* **2007**, *261*, 184.

(42) Maron, L.; Werkema, E. L.; Perrin, L.; Eisenstein, O.; Andersen, R. A. *J. Am. Chem. Soc.* **2005**, *127*, 279.

(43) Lindup, R. J.; Marder, T. B.; Perutz, R. N.; Whitwood, A. C. *Chem. Commun.* **2007**, 3664.

(44) Young, R. J.; Grushin, V. V. *Organometallics* **1999**, *18*, 294.

(45) Yang, H.; Gao, H.; Angelici, R. J. *Organometallics* **1999**, *18*, 2285.

(46) (a) Desmarets, C.; Kuhl, S.; Schneider, R.; Fort, Y. *Organometallics* **2002**, *21*, 1554; (b) Kuhl, S.; Schneider, R.; Fort, Y. *Adv. Synth. Catal.* **2003**, *345*, 341.

(47) Braun, T.; Izundu, J.; Steffen, A.; Neumann, B.; Stammler, H.-G. *Dalton Trans.* **2006**, 5118.

(48) Breyer, D.; Braun, T.; Penner, A. *Dalton Trans.* **2010**, *39*, 7513.

(49) Hintermann, S.; Pregosin, P. S.; Rüegger, H.; Clark, H. C. *J. Organomet. Chem.* **1992**, *435*, 225.

(50) Whittlesey, M. K.; Perutz, R. N.; Moore, M. H. *Chem. Commun.* **1996**, 787.

(51) King, R. B.; Bisnette, M. B. *J. Organomet. Chem.* **1964**, *2*, 38.

(52) Edelbach, B. L.; Jones, W. D. *J. Am. Chem. Soc.* **1997**, *119*, 7734.

(53) Blum, O.; Frolow, F.; Milstein, D. *J. Chem. Soc., Chem. Commun.* **1991**, 258.

(54) Erhardt, S.; Macgregor, S. A. *J. Am. Chem. Soc.* **2008**, *130*, 15490.

(55) (a) Ziegler, T.; Autschbach, J. *Chem. Rev.* **2005**, *105*, 2695; (b) Geerlings, P.; De Proft, F.; Langenaeker, W. *Chem. Rev.* **2003**, *103*, 1793; (c) Dedieu, A. *Chem. Rev.* **2000**, *100*, 543; (d) Niu, S.; Hall, M. B. *Chem. Rev.* **2000**, *100*, 353; (e) Torrent, M.; Solà, M.; Frenking, G. *Chem. Rev.* **2000**, *100*, 439; (f) Ziegler, T. *Chem. Rev.* **1991**, *91*, 651; (g) Sousa, S. F.; Fernandes, P. A.; Ramos, M. J. *J. Phys. Chem. A* **2007**, *111*, 10439; (h) Koch, W.; Holthausen, M. C. *A Chemist's Guide to Density Functional Theory*; Wiley-VCH, 2001.

(56) Cohen, A. J.; Mori-Sánchez, P.; Yang, W. *Chem. Rev.* **2011**, *112*, 289.

(57) Bosque, R.; Clot, E.; Fantacci, S.; Maseras, F.; Eisenstein, O.; Perutz, R. N.; Renkema, K. B.; Caulton, K. G. *J. Am. Chem. Soc.* **1998**, *120*, 12634.

(58) Reinhold, M.; McGrady, J. E.; Perutz, R. N. *J. Am. Chem. Soc.* **2004**, *126*, 5268.

(59) Su, M.-D.; Chu, S.-Y. *Inorg. Chem.* **1998**, *37*, 3400.

(60) Nova, A.; Reinhold, M.; Perutz, R. N.; Macgregor, S. A.; McGrady, J. E. *Organometallics* **2010**, *29*, 1824.

(61) Liu, W. J.; Welch, K.; Trindle, C. O.; Sabat, M.; Myers, W. H.; Harman, W. D. *Organometallics* **2007**, *26*, 2589.

(62) Jakt, M.; Johannissen, L.; Rzepa, H. S.; Widdowson, D. A.; Wilhelm, R. *J. Chem. Soc., Perkin Trans. 2* **2002**, 576.

(63) Bahmanyar, S.; Borer, B. C.; Kim, Y. M.; Kurtz, D. M.; Yu, S. *Org. Lett.* **2005**, *7*, 1011.

(64) Goodman, J.; Macgregor, S. A. *Coord. Chem. Rev.* **2010**, *254*, 1295.

(65) Jiao, E.; Xia, F.; Zhu, H. *Comput. Theor. Chem.* **2011**, *965*, 92.

(66) Yoshikai, N.; Matsuda, H.; Nakamura, E. *J. Am. Chem. Soc.* **2009**, *131*, 9590.

(67) Nova, A.; Mas-Ballesté, R.; Ujaque, G.; González-Duarte, P.; Lledós, A. *Dalton Trans.* **2009**, 5980.

(68) (a) Reza, A. L.; Braun, T. *Unpublished results*; (b) Teltewskoi, M.; Panetier, J. A.; Macgregor, S. A.; Braun, T. *Angew. Chem., Int. Ed.* **2010**, *49*, 3947.

(69) Frisch, M. J.; Trucks, G. W.; Schlegel, H. B.; Scuseria, G. E.; Robb, M. A.; Cheeseman, J. R.; Montgomery, J., J. A. ; Vreven, T.; Kudin, K. N.; Burant, J. C.; Millam, J. M.; Iyengar, S. S.; Tomasi, J.; Barone, V.; Mennucci, B.; Cossi, M.; Scalmani, G.; Rega, N.; Petersson, G. A.; Nakatsuji, H.; Hada, M.; Ehara, M.; Toyota, K.; Fukuda, R.; Hasegawa, J.; Ishida, M.; Nakajima, T.; Honda, Y.; Kitao, O.; Nakai, H.; Klene, M.; Li, X. H.; Knox, J. E.; Hratchian, H. P.; Cross, J. B.; Bakken, V.; Adamo, C.; Jaramillo, J.; Gomperts, R.; Stratmann, R. E.; Yazyev, O.; Austin, A. J.; Cammi, R.; Pomelli, C.; Ochterski, J. W.; Ayala, P. Y.; Morokuma, K.; Voth, G. A.; Salvador, P.; Dannenberg, J. J.; Zakrzewski, V. G.; Dapprich, S.; Daniels, A. D.; Strain, M. C.; Farkas, O.; Malick, D. K.; Rabuck, A. D.; Raghavachari, K.; Foresman, J. B.; Ortiz, J. V.; Cui, Q.; Baboul, A. G.; Clifford, S.; Cioslowski, J.; Stefanov, B. B.; Liu, G.; Liashenko, A.; Piskorz, P.; Komaromi, I.; Martin, R. L.; Fox, D. J.; Keith, T.; Al-Laham, M. A.; Peng, C. Y.; Nanayakkara, A.; Challacombe, M.; Gill, P. M. W.; Johnson, B.; Chen, W.; Wong, M. W.; Gonzalez, C.; Pople, J. A. *Gaussian 03*, revision D.01; Gaussian, Inc.: Wallingford, CT, 2003.

(70) Frisch, M. J.; Trucks, G. W.; Schlegel, H. B.; Scuseria, G. E.; Robb, M. A.; Cheeseman, J. R.; Scalmani, G.; Barone, V.; Mennucci, B.; Petersson, G. A.; Nakatsuji, H.; Caricato, M.; Li, X.; Hratchian, H. P.; Izmaylov, A. F.; Bloino, J.; Zheng, G.; Sonnenberg, J. L.; Hada, M.; Ehara, M.; Toyota, K.; Fukuda, R.; Hasegawa, J.; Ishida, M.; Nakajima, T.; Honda, Y.; Kitao, O.; Nakai, H.; Vreven, T.; Montgomery, J., J. A. ; Peralta, J. E.; Ogliaro, F.; Bearpark, M.; Heyd, J. J.; Brothers, E.; Kudin, K. N.; Staroverov, V. N.; Kobayashi, R.; Normand, J.; Raghavachari, K.; Rendell, A.; Burant, J. C.; Iyengar, S. S.; Tomasi, J.; Cossi, M.; Rega, N.; Millam, N. J.; Klene, M.; Knox, J. E.; Cross, J. B.; Bakken, V.; Adamo, C.; Jaramillo, J.; Gomperts, R.; Stratmann, R. E.; Yazyev, O.; Austin, A. J.; Cammi, R.; Pomelli, C.; Ochterski, J. W.; Martin, R. L.; Morokuma, K.; Zakrzewski, V. G.; Voth, G. A.; Salvador, P.; Dannenberg, J. J.; Dapprich, S.; Daniels, A. D.; Farkas, Ö.; Foresman, J. B.; Ortiz, J. V.; Cioslowski, J.; Fox, D. J. *Gaussian 09*, revision A.01; Gaussian, Inc.: Wallingford, CT, 2009.

(71) Becke, A. D. *Phys. Rev. A* **1988**, *38*, 3098.

(72) Perdew, J. P. *Phys. Rev. B* **1986**, *33*, 8822.

(73) Andrae, D.; Häußermann, U.; Dolg, M.; Stoll, H.; Preuß, H. *Theor. Chim. Acta* **1990**, *77*, 123.

(74) Höllwarth, A.; Böhme, M.; Dapprich, S.; Ehlers, A. W.; Gobbi, A.; Jonas, V.; Köhler, K. F.; Stegmann, R.; Veldkamp, A.; Frenking, G. *Chem. Phys. Lett.* **1993**, *208*, 237.

(75) (a) Hariharan, P. C.; Pople, J. A. *Theor. Chim. Acta* **1973**, *28*, 213; (b) Hehre, W. *J. Chem. Phys.* **1972**, *56*, 2257.

(76) (a) Krishnan, R.; Binkley, J. S.; Seeger, R.; Pople, J. A. *J. Chem. Phys.* **1980**, *72*, 650; (b) Clark, T.; Chandrasekhar, J.; Spitznagel, G. W.; Schleyer, P. V. *J. Comput. Chem.* **1983**, *4*, 294.

(77) Häller, L. J. L.; Page, M. J.; Erhardt, S.; Macgregor, S. A.; Mahon, M. F.; Naser, M. A.; Vélez, A.; Whittlesey, M. K. *J. Am. Chem. Soc.* **2010**, *132*, 18408.

(78) McQuarrie, D. A.; Simon, J. S. *Molecular Thermodynamics*; University Science Books: Sausalito, 1999.

(79) Aizenberg, M.; Ott, J.; Elsevier, C. J.; Milstein, D. *J. Organomet. Chem.* **1998**, *551*, 81.

(80) Thorn, D. L.; Harlow, R. L. *Inorg. Chem.* **1990**, *29*, 2017.

(81) (a) Goodman, J.; Grushin, V. V.; Larichev, R. B.; Macgregor, S. A.; Marshall, W. J.; Roe, D. C. *J. Am. Chem. Soc.* **2009**, *131*, 4236; (b) Goodman, J.; Grushin, V. V.; Larichev, R. B.; Macgregor, S. A.; Marshall, W. J.; Roe, D. C. *J. Am. Chem. Soc.* **2010**, *132*, 12013.

(82) (a) Hughes, R. P.; Williamson, A.; Sommer, R. D.; Rheingold, A. L. *J. Am. Chem. Soc.* **2001**, *123*, 7443; (b) Hughes, R. P.; Laritchev, R. B.; Williamson, A.; Incarvito, C. D.; Zakharov, L. N.; Rheingold, A. L. *Organometallics* **2002**, *21*, 4873.

(83) Wu, H.; Hall, M. B. *Dalton Trans.* **2009**, 5933.

(84) Caulton, K. G. *New J. Chem.* **1994**, *18*, 25.

(85) Perutz, R. N.; Sabo-Etienne, S. *Angew. Chem., Int. Ed.* **2007**, *46*, 2578.

(86) Beltrán, T. s. F.; Feliz, M.; Llusar, R.; Mata, J. A.; Safont, V. S. *Organometallics* **2010**, *30*, 290.

(87) Perdew, J. P.; Schmidt, K. Jacob's Ladder of Density Functional Approximations for the Exchange-Correlation Energy. In *Density Functional Theory and Its Applications to Materials*; Van Doren, V. E.; Van Alseoy, K.; Geerlings, P.; AID Press: New York, 2001.

(88) Becke, A. D. *J. Chem. Phys.* **1986**, *84*, 4524.

(89) Perdew, J. P.; Yue, W. *Phys. Rev. B* **1986**, *33*, 8800.

(90) Lacks, D. J.; Gordon, R. G. *Phys. Rev. A* **1993**, *47*, 4681.

(91) Perdew, J. P.; Burke, K.; Ernzerhof, M. *Phys. Rev. Lett.* **1996**, *77*, 3865.

(92) (a) Perdew, J. P. Unified Theory of Exchange and Correlation Beyond the Local Density Approximation In *Electronic Structure of Solids*; Ziesche, P.; Eschrig, H.; Akademie Verlag: Berlin, 1991, p 11. ; (b) Perdew, J. P.; Wang, Y. *Phys. Rev. B* **1992**, *45*, 13244.

(93) Lee, C. T.; Yang, W. T.; Parr, R. G. *Phys. Rev. B* **1988**, *37*, 785.

(94) Tao, J. M.; Perdew, J. P.; Staroverov, V. N.; Scuseria, G. E. *Phys. Rev. Lett.* **2003**, *91*.

(95) Becke, A. *J. Chem. Phys.* **1993**, *98*, 5648.

(96) Stephens, P. J.; Devlin, F. J.; Chabalowski, C. F.; Frisch, M. J. *J. Phys. Chem.* **1994**, *98*, 11623.

(97) (a) Zhao, Y.; Truhlar, D. G. *J. Chem. Phys.* **2006**, *125*; (b) Zhao, Y.; Truhlar, D. G. *Theo. Chem. Acc.* **2008**, *120*, 215.

(98) Grimme, S. *J. Chem. Phys.* **2006**, *124*, 034108.

(99) (a) Grimme, S. *J. Comput. Chem.* **2004**, *25*, 1463; (b) Grimme, S. *J. Comput. Chem.* **2006**, *27*, 1787.

Aspects of the work in this thesis have been published and are reproduced here on the following pages.

Boryl Complexes

DOI: 10.1002/anie.201001070

A Highly Reactive Rhodium(I)–Boryl Complex as a Useful Tool for C–H Bond Activation and Catalytic C–F Bond Borylation**

Michael Teltewskoi, Julien A. Panetier, Stuart A. Macgregor, and Thomas Braun**

Transition-metal–boryl complexes are key intermediates in catalytic hydroboration and borylation reactions and find applications in boron-based materials.[1] Rhodium complexes can be applied in the rhodium-mediated hydroboration or dehydrogenative borylation reactions of olefins or even in the borylation of alkanes.[2,3] Rhodium and iridium boronates also play a crucial role in the borylation of arenes to give, for instance, Bpin derivatives.[4,5] Thus, it has been reported that rhodium complexes with boryl and phosphine ligands are intermediates in the catalytic borylation reactions of benzene, toluene, *para*-xylene, and mesitylene with HBpin (HBpin = 4,4,5,5-tetramethyl-1,3,2-dioxaborolane, pinacolborane).[4] Although it is conceivable that the C–H activation step occurs at the 14-electron species $\{Rh(Bpin)(P\mathit{i}Pr_3)_2\}$, density functional theory (DFT) calculations indicate that benzylic activation takes place at $\{Rh(H)(P\mathit{i}Pr_3)_2\}$.[4b] In this case, Rh^I–Rh^{III} cycles have been suggested, whereas iridium-based catalysts may operate through Ir^{III}–Ir^V cycles.[4,5]

Examples of C–F bond functionalization, i.e. where fluorine is replaced by a new group to access higher-value fluorinated compounds, are very limited,[6,7] and most examples involve hydrodefluorination.[6] C–F bond activation is generally thermodynamically favorable, because of the strength of the H–F and Si–F bonds, or even of the M–F bonds that are formed.[6] We have developed a catalytic process for the conversion of hexafluoropropene and HBpin into Bpin derivatives of trifluoropropane using $[Rh(H)(PEt_3)_3]$ as a catalyst.[8] Mechanistic considerations suggest the involvement of a rhodium(I)–boryl species in some of the C–F activation steps, but such a compound could not be detected. The thermodynamic driving force in this case is apparently the generation of B–F bonds.[8] Rhodium(I)–boryl complexes are almost without any precedent in the literature,[1,9] although $[Rh(Bcat)(PMe_3)_4]$ has been synthesized by Marder and co-workers from the treatment of $[Rh(Me)(PMe_3)_4]$ with B_2cat_2 (Bcat = B{1,2-$O_2C_6H_4$}).[10]

Herein, we report the identification of a unique 16-electron rhodium(I) species, $[Rh(Bpin)(PEt_3)_3]$ (**3**). This complex is highly reactive and can effect the C–H activation of benzene, as well as the stoichiometric C–F activation and catalytic C–F borylation of fluorinated substrates.

We reasoned that a phenoxo complex might be an ideal starting compound for the formation of a rhodium(I)–boryl complex, partly because of the high stability of a boron–oxygen bond.[11,12] Treatment of the chloro complex $[Rh(Cl)(PEt_3)_3]$ (**1**) with NaOPh gave the rhodium phenoxide $[Rh(OPh)(PEt_3)_3]$ (**2**; Scheme 1). The ^1H and ^{31}P NMR spectra of

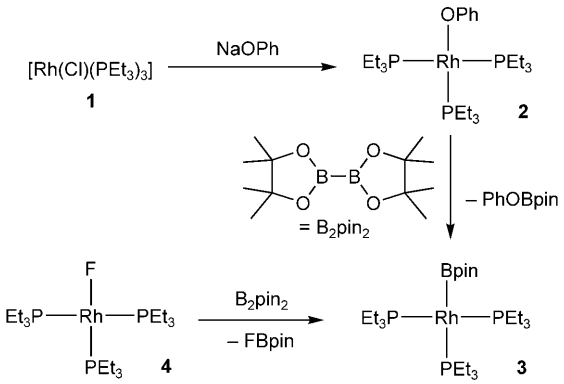

Scheme 1. Synthesis of a rhodium(I)–boryl complex.

complex **2** showed the expected splitting patterns; the phosphorus–rhodium coupling constants in the ^{31}P NMR spectrum of 169 and 142 Hz are characteristic of a rhodium(I) compound.[13] Reaction of **2** in benzene with excess B_2pin_2 (3 equiv) gave $[Rh(Bpin)(PEt_3)_3]$ (**3**) after 16 hours, along with PhOBpin (Scheme 1). Moreover, we found that **3** can be generated in a comparable reaction, starting from the fluoro compound $[Rh(F)(PEt_3)_3]$ (**4**).[14] The fluoroborane FBpin that was also formed can be removed in vacuo. Note that boryl complex **3** does not react with another equivalent of B_2pin_2 to give a Rh^{III} complex that would be comparable to *fac*-$[Rh(Bcat)_3(PMe_3)_3]$.[10]

Complex **3** was only characterized in solution; the ^{31}P NMR spectrum at room temperature revealed only one broad signal at $\delta = 15.1$ ppm. This indicates a dynamic behavior, which involves the exchange of the phosphine

[*] Dipl.-Chem. M. Teltewskoi, Prof. Dr. T. Braun
Institut für Chemie, Humboldt-Universität zu Berlin
Brook-Taylor-Strasse 2, 12489 Berlin (Germany)
E-mail: thomas.braun@chemie.hu-berlin.de
J. A. Panetier, Prof. S. A. Macgregor
School of EPS – Chemistry, Heriot-Watt University
Edinburgh EH14 4AS (UK)
E-mail: s.a.macgregor@hw.ac.uk

[**] We would like to acknowledge the Humboldt-Universität as well as Heriot-Watt University and the EPSRC for financial support. We also thank Dr. Marcel Ahijado Salomon, Ann-Katrin Jungton (Berlin), Kai Altenhöner (University of Bielefeld), and Prof. D. Lentz (FU Berlin) for help with NMR spectroscopic analysis, preliminary experiments, and helpful discussions. The Cluster of Excellence "Unifying Concepts in Catalysis" funded by the DFG is gratefully acknowledged. We thank the Solvay Fluor GmbH for a gift of hexafluoropropene. M.T. is a fellow of the graduate school "Fluorine as a Key Element" financed by the DFG.

Supporting information for this article is available on the WWW under http://dx.doi.org/10.1002/anie.201001070.

ligands, similar to the fluxionality which has been observed for $[Rh(H)(PEt_3)_3]$ (**5**).[15] Variable-temperature ^{31}P NMR analysis shows that the free phosphine has no influence on the dynamic behavior, which suggests that the process is intramolecular. The ^{31}P NMR spectrum at 203 K exhibits a signal at $\delta = 20.5$ ppm for the phosphine atoms that are in a mutually *trans* position. The resonance features characteristic couplings for a rhodium(I) compound, with doublet couplings to rhodium and to phosphorus of 166 Hz and 30 Hz, respectively.[12,13] A second resonance at $\delta = 9.1$ ppm, with a coupling to rhodium of 110 Hz, can be assigned to the phosphorus ligand that is in the position *trans* to the Bpin group. We could not resolve any couplings to the ^{11}B nucleus. The ^{11}B NMR spectrum of **3** shows one broad signal at $\delta =$ 46.5 ppm ($\Delta\nu_{1/2} = 338$ Hz); this chemical shift is typical for a rhodium derivative of a 1,3,2-dioxaborolane.[16]

NMR spectroscopic investigations revealed that **3** is not very stable in benzene and converts slowly into the hydride $[Rh(H)(PEt_3)_3]$ (**5**) at room temperature, with concomitant formation of PhBpin (Scheme 2). In the presence of B_2pin_2, complex **5** reacts further to give the Rh^{III} complex *cis-fac*-$[Rh(H)(Bpin)_2(PEt_3)_3]$ (**6**).

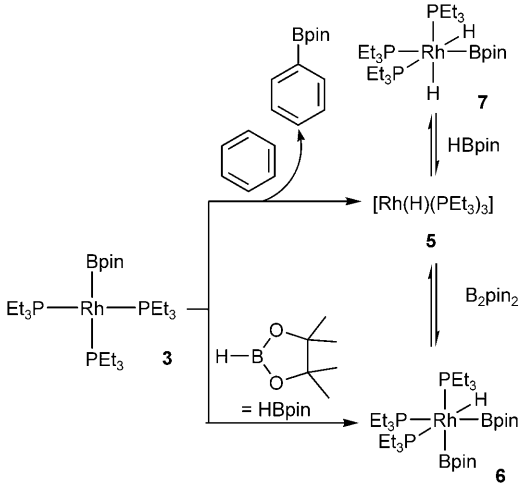

Scheme 2. Formation and reactivity of rhodium–boryl complexes.

These observations indicate that C–H activation of benzene may occur at $[Rh(Bpin)(PEt_3)_3]$ (**3**), possibly via a Rh^{III} intermediate, $[Rh(H)(Ph)(Bpin)(PEt_3)_3]$, although this could not be detected.[4] Reaction of **3** in C_6D_6 furnished (D_5C_6)Bpin and $[Rh(H)(PEt_3)_3]$ (**5**). ^1H NMR EXSY spectra (400 MHz; EXSY = exchange spectroscopy) of **5** confirmed exchange between the hydrogen atom that is bound to the metal and the CH_2 and CH_3 hydrogen atoms of the *cis* phosphine ligands. It appears that intramolecular cyclometalation processes are occurring, which result in the transfer of deuterium atoms from being bound to the metal onto the phosphine alkyl groups.[17]

We have no indication for the generation of HBpin. It seems that reductive elimination from **6** to afford rhodium(I)–boryl complex **3** does not occur under the reaction conditions. This observation might explain why it was not possible to develop a catalytic process for the generation of PhBpin from benzene and B_2pin_2. Complex **6** can also be synthesized independently, starting from $[Rh(Bpin)(PEt_3)_3]$ (**3**; Scheme 2). A solution of **3** was treated with HBpin to give **6** plus considerable amounts of *cis-fac*-$[Rh(H)_2(Bpin)(PEt_3)_3]$ (**7**). The formation of **7** can be explained by the reductive elimination of B_2pin_2 from **6** to furnish the hydrido complex $[Rh(H)(PEt_3)_3]$ (**5**). It has been previously reported that treatment of **5** with HBpin affords **7**.[8]

A signal at $\delta = -10.18$ ppm in the ^1H NMR spectrum of **6** confirms the presence of the hydrido ligand. The ^{31}P NMR spectrum shows rhodium–phosphorus coupling constants of 98 Hz and 75 Hz for the doublet of triplets at $\delta = 8.1$ ppm and the doublet of doublets at $\delta = 2.3$ ppm, respectively, reveal the presence of a Rh^{III} compound.[12] The relatively small coupling constant of 75 Hz suggests that the two equivalent phosphine ligands are located *trans* to the boryl ligands. This arrangement is compatible with a *fac* configuration for **6**; for complex **7**, $^1J(Rh,P) = 78$ Hz for the phosphorus atom in the position *trans* to the boryl ligand has been observed.[8] The ^{11}B NMR spectrum of **6** shows one broad signal at $\delta =$ 47.1 ppm ($\Delta\nu_{1/2} = 633$ Hz), which confirms the presence of the boryl ligands.[8]

To avoid activation of the aromatic C–H bonds on **3**, the phenoxo complex $[Rh(OPh)(PEt_3)_3]$ (**2**) and the fluoro compound $[Rh(F)(PEt_3)_3]$ (**4**) were treated stoichiometrically with B_2pin_2 in $Me_3SiSiMe_3$ as a solvent. Under these reaction conditions, boryl complex **3** was observed as the sole product (Scheme 1). The stability of **3** in $Me_3SiSiMe_3$ enabled us to perform further studies on the reactivity of **3** towards the activation of carbon–fluorine bonds.[6]

Treatment of **3** with perfluoropropene in $Me_3SiSiMe_3$ gave the propenyl compound $[Rh\{(Z)CF{=}CF(CF_3)\}(PEt_3)_3]$ (**8a**) and the isomeric complex $[Rh\{C(CF_3){=}CF_2\}(PEt_3)_3]$ (**8b**) in a ratio of 2:7 (Scheme 3). Therefore, compound **3** might indeed be an intermediate in the conversion of hexafluoropropene and HBpin into Bpin derivatives of trifluoropropane, as has been previously proposed.[8] The formation of complex **8a** has been previously reported from the treatment of $[Rh(H)(PEt_3)_3]$ (**5**) with perfluoropropene.[14c] The NMR spectra of **8b** show the expected splitting pattern with a geminal fluorine–fluorine coupling constant of 61 Hz in the ^{19}F NMR spectrum.[18]

Fluorinated pyridines are also interesting substrates for investigating C–F activation reactions with boryl complex **3**.[19–21] For instance, the reaction of C_5NF_5 with $[Rh(H)(PEt_3)_3]$ (**5**) gives $[Rh(4\text{-}C_5NF_4)(PEt_3)_3]$ (**9a**) and HF,[20] whilst reaction with $[Rh(SiPh_3)(PMe_3)_3]$ revealed the isomeric compounds $[Rh(2\text{-}C_5NF_4)(PMe_3)_3]$ and $[Rh(4\text{-}C_5NF_4)(PMe_3)_3]$ in a 3:1 ratio, along with $FSiPh_3$.[19,22] When 2,3,5,6-tetrafluoropyridine was used as the substrate, a delicate balance between C–H and C–F activation was observed.[6,21e,23] Thus, reaction with $[Rh(H)(PEt_3)_3]$ (**5**) furnished **9a** by C–H activation,[7] whereas reaction with $[Rh(SiPh_3)(PMe_3)_3]$ gave a mixture of products that were derived from activation at the 2-(C–F) and 4-(C–H) positions.[19]

Reaction of **3** with 2,3,5,6-tetrafluoropyridine gave the C–H activation product $[Rh(4\text{-}C_5NF_4)(PEt_3)_3]$ (**9a**) and HBpin, with no observed C–F bond cleavage (Scheme 3).

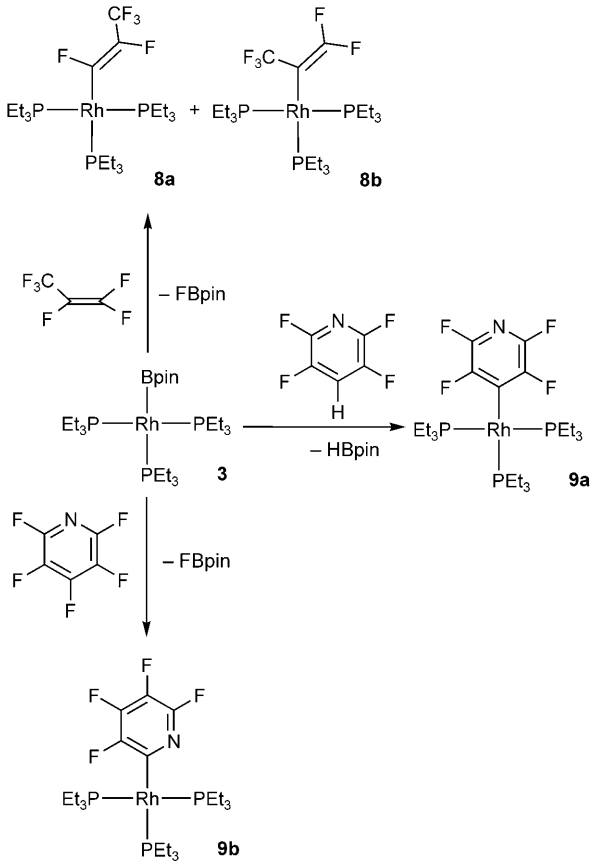

Scheme 3. C–F Activation at the rhodium–boryl complex **3**.

However, treatment of in situ generated **3** with pentafluoropyridine selectively gave the C–F activation product [Rh(2-C_5NF_4)(PEt_3)$_3$] (**9b**), with FBpin by-product at room temperature. Thus, C–F activation at the boryl species **3** occurs exclusively at the 2-position of the fluorinated substrate. The ^{31}P NMR spectrum of **9b** showed a doublet of doublets at $\delta =$ 16.0 ppm and a resonance at $\delta = 19.7$ ppm, with a complex splitting pattern arising from coupling with phosphorus, rhodium, and fluorine atoms. The four signals at $\delta = -87.7$, -125.0, -155.4, and -175.9 ppm in the ^{19}F NMR spectrum indicate the presence of the pyridyl ligand, with the metal at the 2-position.[19,21]

C–F bond activation of pentafluoropyridine most frequently involves reaction at the 4-position, *para* to the nitrogen, and such selectivity is often associated with radical pathways or those involving initial nucleophilic attack. Activation at the 2-position is less common, although it has been suggested that it may occur by a concerted oxidative addition process.[6,21,24] Therefore, we wanted to investigate this unusual selectivity in the reaction of **3** with pentafluoropyridine.

Recently, a novel mechanism for aromatic C–F bond activation has been characterized at electron-rich iridium and platinum metal centers.[25] This process involves the addition of a C–F bond across a {M–PR_3} moiety via a four-centered transition state, which can account for the selective activation at the 2-position of pentafluoropyridine and {Ni(PEt_3)$_2$} fragments.[25,26] Key to such phosphine-assisted processes is the Lewis acidity of the accepting phosphine ligand. By analogy, we reasoned that an equivalent boryl-assisted process may be possible for complex **3**, wherein the formally sp^2-hybridized boron atom may be a particularly effective Lewis acid.

The mechanism and selectivity of the reaction of pentafluoropyridine with **3** were investigated using DFT calculations on model complex [Rh(Bpin)(PMe_3)$_3$] (**3′**).[27] Both concerted oxidative addition and boryl-assisted processes were considered, and the lowest energy C–F activation transition states for reaction at the 2- and 4-positions are shown schematically in Figure 1.

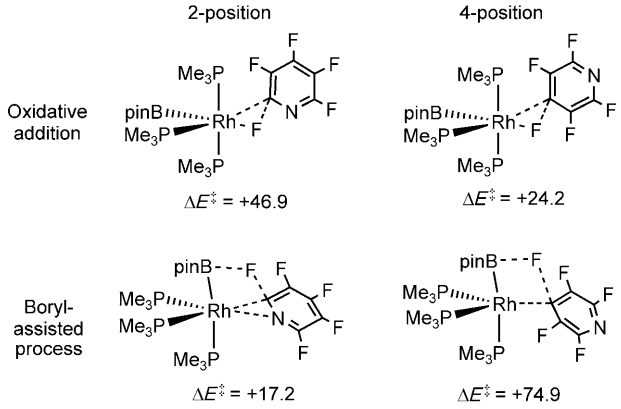

Figure 1. Computed transition states and energies [kJ mol^{-1}] for C–F activation of pentafluoropyridine at [Rh(Bpin)(PMe_3)$_3$] (**3′**).

The most accessible oxidative addition process corresponds to activation at the 4-position ($\Delta E^{\ddagger} = +24.2$ kJ mol^{-1} cf. $+46.9$ kJ mol^{-1} at the 2-position). These processes give stable *mer*-[Rh(Bpin)(F)(4-C_5NF_4)(PMe_3)$_3$] and *mer*-[Rh(Bpin)(F)(2-C_5NF_4)(PMe_3)$_3$] complexes, in which the fluoride ligand is *trans* to the Bpin group. However, subsequent isomerization and reductive elimination of FBpin to give [Rh(4- or 2-C_5NF_4)(PMe_3)$_3$] (**9′a** or **9′b**) is facile (see the Supporting Information). Therefore, oxidative addition of the C–F bond is the overall rate-determining step and, most importantly, indicates a kinetic preference for reaction at the 4-position, which is at odds with experimental observations.

In contrast, boryl-assisted C–F activation clearly favors the 2-position ($\Delta E^{\ddagger} = +17.2$ kJ mol^{-1} cf. $+74.9$ kJ mol^{-1} at the 4-position). Both processes lead directly to **9′a/b** and FBpin. Moreover, boryl-assisted C–F activation at the 2-position is now more accessible than oxidative addition at the 4-position, and so this pathway accounts for the experimentally observed selectivity. One factor that might contribute to the greater accessibility of the boryl-assisted process at the 2-position is the short Rh···N contact in the transition state (2.22 Å); donation of electron density from the nitrogen atom lone pair serves to stabilize the rhodium center (Figure 2).[25c]

We also experimentally investigated the reactivity of **3** in catalytic borylation reactions of pentafluoropyridine. In $Me_3SiSiMe_3$ solvent, we anticipated a selective borylation reaction at the 2-position of pentafluoropyridine, because the formation of [Rh(H)(PEt_3)$_3$] (**5**) would not occur. As

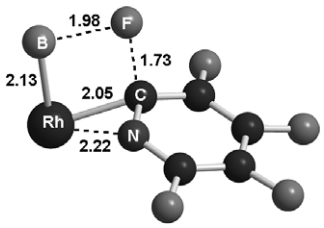

Figure 2. Key computed distances [Å] in the boryl-assisted transition state for activation at the 2-position of pentafluoropyridine at **3′**.

mentioned above, the latter led to C–F bond cleavage at the 4-position.[20] Indeed, pentafluorpyridine was catalytically converted into its 2-boryl derivative **10** (45% yield) in the presence of 2.5 mol% **3** as the catalyst (based on equimolar amounts of C_5NF_5 and B_2pin_2; Scheme 4). Borylation of the

Scheme 4. Catalytic formation of a pyridyl boronate ester.

C–F bond has also been reported by Marder, Perutz, and co-workers[19] The treatment of C–F activation products, such as $[Rh(2\text{-}C_5NF_4)(PMe_3)_3]$ or $[Rh(4\text{-}C_5NF_4)(PMe_3)_3]$, with B_2cat_2 gave the pyridyl boronate esters and the Rh^{III} complex *fac*-$[Rh(Bcat)_3(PMe_3)_3]$. However, in these examples the reactions were not catalytic.

In conclusion, a 16-electron rhodium(I)–boryl complex (**3**) has been synthesized which undergoes C–H activation at room temperature with benzene to give PhBpin. Reaction with fluorinated substrates, such as pentafluoropyridine and perfluoropropene, results in C–F activation products. DFT calculations suggest that C–F activation proceeds along a boryl-assisted pathway that involves direct transfer of fluorine onto the boron center via a four-membered transition state. This mechanism also shows that the selective activation at the 2-position arises because of a stabilizing Rh···N interaction in the transition state. Investigation of the catalytic borylation reaction led to the formation of tetrafluoropyridyl boronate esters, which can provide new fluorinated building blocks.[28] Note that it is extremely difficult to access tetrafluoropyridines that are further functionalized at the 2-position.[6,21]

Received: February 22, 2010
Published online: April 23, 2010

Keywords: boryl ligands · borylation · C–F activation · C–H activation · rhodium

[1] For reviews on boryl complexes, see: a) G. J. Irvine, M. J. G. Lesley, T. B. Marder, N. C. Norman, C. R. Rice, E. G. Robins, W. R. Roper, G. R. Whittell, L. J. Wright, *Chem. Rev.* **1998**, *98*, 2685–2722; b) S. Aldridge, D. L. Coombs, *Coord. Chem. Rev.* **2004**, *248*, 535–559; c) H. Braunschweig, *Angew. Chem.* **1998**, *110*, 1882–1898; *Angew. Chem. Int. Ed.* **1998**, *37*, 1786–1801; d) H. Braunschweig, M. Colling, *Coord. Chem. Rev.* **2001**, *223*, 1–51; e) H. Braunschweig, C. Kollann, D. Rais, *Angew. Chem.* **2006**, *118*, 5380–5400; *Angew. Chem. Int. Ed.* **2006**, *45*, 5254–5274; f) L. Dang, Z. Lin, T. B. Marder, *Chem. Commun.* **2009**, 3987–3995.

[2] a) K. Burgess, W. A. van der Donk, S. A. Westcott, T. B. Marder, R. T. Baker, J. C. Calabrese, *J. Am. Chem. Soc.* **1992**, *114*, 9350–9359; b) R. B. Coapes, F. E. S. Souza, R. L. Thomas, J. J. Hall, T. B. Marder, *Chem. Commun.* **2003**, 613–615; c) V. J Olsson, K. J. Szabó, *Angew. Chem.* **2007**, *119*, 7015–7017; *Angew. Chem. Int. Ed.* **2007**, *46*, 6891–6893; d) D. I. McIsaac, S. J. Geier, C. M. Vogels, A. Decken, S. A. Westcott, *Inorg. Chim. Acta* **2006**, *359*, 2771–2779; e) I. A. I. Mkhalid, R. B. Coapes, S. N. Edes, D. N. Coventry, F. E. S. Souza, R. L. Thomas, J. J. Hall, S.-W. Bi, Z. Lin, T. B. Marder, *Dalton Trans.* **2008**, 1055–1064; f) C. B. Fritschi, S. M. Wernitz, C. M. Vogels, M. P. Shaver, A. Decken, A. Bell, S. A. Westcott, *Eur. J. Inorg. Chem.* **2008**, 779–785; g) C. N. Garon, D. I. McIsaac, C. M. Vogels, A. Decken, I. D. Williams, C. Kleeberg, T. B. Marder, S. A. Westcott, *Dalton Trans.* **2009**, 1624–1631.

[3] a) J. F. Hartwig, K. S. Cook, M. Hapke, C. D. Incarvito, Y. Fan, C. E. Webster, M. B. Hall, *J. Am. Chem. Soc.* **2005**, *127*, 2538–2552; b) H. Chen, S. Schlecht, T. C. Semple, J. F. Hartwig, *Science* **2000**, *287*, 1995–1997.

[4] a) S. Shimada, A. S. Batsanov, J. A. K. Howard, T. B. Marder, *Angew. Chem.* **2001**, *113*, 2226–2229; *Angew. Chem. Int. Ed.* **2001**, *40*, 2168–2171; b) W. H. Lam, K. C. Lam, Z. Lin, S. Shimada, R. N. Perutz, T. B. Marder, *Dalton Trans.* **2004**, 1556–1562.

[5] a) T. M. Boller, J. M. Murphy, M. Hapke, T. Ishiyama, N. Miyaura, J. F. Hartwig, *J. Am. Chem. Soc.* **2005**, *127*, 14263–14278; J.-Y. Cho, M. K. Tse, D. Holmes, R. E. Maleczka, Jr., M. R. Smith III, *Science* **2002**, *295*, 305–308.

[6] For reviews on C–F bond activation at transition metals, see: a) T. Braun, R. N. Perutz, *Chem. Commun.* **2002**, 2749–2757; b) J. Burdeniuc, B. Jedlicka, R. H. Crabtree, *Chem. Ber.* **1997**, *130*, 145–154; c) W. D. Jones, *Dalton Trans.* **2003**, 3991–3995; d) J. L. Kiplinger, T. G. Richmond, C. E. Osterberg, *Chem. Rev.* **1994**, *94*, 373–431; e) U. Mazurek, H. Schwarz, *Chem. Commun.* **2003**, 1321–1326; f) H. Torrens, *Coord. Chem. Rev.* **2005**, *249*, 1957–1985; g) R. N. Perutz, T. Braun in *Comprehensive Organometallic Chemistry III*, *Vol. 1* (Eds.: R. H. Crabtree, D. M. P. Mingos), Elsevier, Oxford, **2007**, pp. 725–758; h) H. Amii, K. Uneyama, *Chem. Rev.* **2009**, *109*, 2119–2183; i) G. Meier, T. Braun, *Angew. Chem.* **2009**, *121*, 1575–1577; *Angew. Chem. Int. Ed.* **2009**, *48*, 1546–1548; j) R. P. Hughes, *Eur. J. Inorg. Chem.* **2009**, 4591–4606; k) T. G. Driver, *Angew. Chem.* **2009**, *121*, 8116–8119; *Angew. Chem. Int. Ed.* **2009**, *48*, 7974–7976.

[7] a) A. Steffen, M. I. Sladek, T. Braun, B. Neumann, H.-G. Stammler, *Organometallics* **2005**, *24*, 4057–4064; b) T. Braun, M. I. Sladek, R. N. Perutz, *Chem. Commun.* **2001**, 2254–2255; c) H. Guo, F. Kong, K. Kanno, J. He, K. Nakajima, T. Takahashi, *Organometallics* **2006**, *25*, 2045–2048; d) T. Schaub, M. Backes, U. Radius, *J. Am. Chem. Soc.* **2006**, *128*, 15964–15965; e) T. Braun, J. Izundu, A. Steffen, B. Neumann, H.-G. Stammler, *Dalton Trans.* **2006**, 5118–5123; f) Y. Ishii, N. Chatani, S. Yorimitsu, S. Murai, *Chem. Lett.* **1998**, 157–158; g) T. J. Korn, M. A. Schade, S. Wirth, P. Knochel, *Org. Lett.* **2006**, *8*, 725–728; h) T. Wang, J. A. Love, *Organometallics* **2008**, *27*, 3290–3296; i) M. Arisawa, T. Suzuki, T. Ishikawa, M. Yamaguchi, *J. Am. Chem. Soc.* **2008**, *130*, 12214–12215; j) K. Fuchibe, T. Kaneko, K. Mori, T. Akiyama, *Angew. Chem.* **2009**, *121*, 8214–8217; *Angew. Chem. Int. Ed.* **2009**, *48*, 8070–8073; k) R. P. Hughes, R. B. Laritchev, L. N. Zakharov, A. L. Rheingold, *J. Am. Chem. Soc.* **2005**, *127*, 6325–6334.

[8] T. Braun, M. Ahijado Salomon, K. Altenhöner, M. Teltewskoi, S. Hinze, *Angew. Chem.* **2009**, *121*, 1850 – 1854; *Angew. Chem. Int. Ed.* **2009**, *48*, 1818 – 1822.

[9] G. Schmid, *Chem. Ber.* **1969**, *102*, 191 – 195.

[10] C. Dai, G. Stringer, T. B. Marder, A. J. Scott, W. Clegg, N. C. Norman, *Inorg. Chem.* **1997**, *36*, 272 – 273.

[11] a) L. Dang, Z. Lin, T. B. Marder, *Organometallics* **2008**, *27*, 4443 – 4454; b) H. Zhao, L. Dang, T. B. Marder, Z. Lin, *J. Am. Chem. Soc.* **2008**, *130*, 5586 – 5594; c) T. Ohishi, M. Nishiura, Z. Hou, *Angew. Chem.* **2008**, *120*, 5876 – 5879; *Angew. Chem. Int. Ed.* **2008**, *47*, 5792 – 5795; d) D. S. Laitar, P. Müller, J. P. Sadighi, *J. Am. Chem. Soc.* **2005**, *127*, 17196 – 17197; e) C. Kleeberg, L. Dang, Z. Lin, T. B. Marder, *Angew. Chem.* **2009**, *121*, 5454 – 5458; *Angew. Chem. Int. Ed.* **2009**, *48*, 5350 – 5354; B. L. Tran, D. Adhikari, H. Fan, M. Pink, D. J. Mindiola, *Dalton Trans.* **2010**, *39*, 358 – 360.

[12] a) M. Ahijado, T. Braun, *Angew. Chem.* **2008**, *120*, 2996 – 3000; *Angew. Chem. Int. Ed.* **2008**, *47*, 2954 – 2958; b) M. Ahijado Salomon, T. Braun, A. Penner, *Angew. Chem.* **2008**, *120*, 8999 – 9003; *Angew. Chem. Int. Ed.* **2008**, *47*, 8867 – 8871.

[13] S. K. Hanson, D. M. Heinekey, K. I. Goldberg, *Organometallics* **2008**, *27*, 1454 – 1463.

[14] a) D. Noveski, T. Braun, M. Schulte, B. Neumann, H.-G. Stammler, *Dalton Trans.* **2003**, 4075 – 4083; b) D. Noveski, T. Braun, S. Krückemeier, *J. Fluorine Chem.* **2004**, *125*, 959 – 966; c) T. Braun, D. Noveski, B. Neumann, H.-G. Stammler, *Angew. Chem.* **2002**, *114*, 2870 – 2873; *Angew. Chem. Int. Ed.* **2002**, *41*, 2745 – 2748.

[15] a) T. Yoshida, D. L. Thorn, T. Okano, S. Otsuka, J. A. Ibers, *J. Am. Chem. Soc.* **1980**, *102*, 6451 – 6457; b) T. Braun, D. Noveski, M. Ahijado, F. Wehmeier, *Dalton Trans.* **2007**, 3820 – 3825.

[16] a) M. V. Câmpian, J. L. Harris, N. Jasim, R. N. Perutz, T. B. Marder, A. C. Whitwood, *Organometallics* **2006**, *25*, 5093 – 5104; b) K. S. Cook, C. D. Incarvito, C. E. Webster, Y. Fan, M. B. Hall, J. F. Hartwig, *Angew. Chem.* **2004**, *116*, 5590 – 5593; *Angew. Chem. Int. Ed.* **2004**, *43*, 5474 – 5477; c) P. L. Callaghan, R. Fernández-Pacheco, N. Jasim, S. Lachaize, T. B. Marder, R. N. Perutz, E. Rivalta, S. Sabo-Etienne, *Chem. Commun.* **2004**, 242 – 243.

[17] a) A. Y. Verat, M. Pink, H. Fan, J. Tomaszewski, K. G. Caulton, *Organometallics* **2008**, *27*, 166 – 168; b) V. V. Mainz, R. A. Andersen, *Organometallics* **1984**, *3*, 675 – 678; c) M. Ahijado Salomon, A. Jungton, T. Braun, *Dalton Trans.* **2009**, 7669 – 7677.

[18] a) M. F. Kühnel, D. Lentz, *Dalton Trans.* **2009**, 4747 – 4755; b) D. Lentz, N. Nickelt, S. Willemsen, *Chem. Eur. J.* **2002**, *8*, 1205 – 1216; c) R. P. Hughes, R. B. Laritchev, L. N. Zakharov, A. L. Rheingold, *J. Am. Chem. Soc.* **2004**, *126*, 2308 – 2309.

[19] R. J. Lindup, T. B. Marder, R. N. Perutz, A. C. Whitwood, *Chem. Commun.* **2007**, 3664 – 3666.

[20] D. Noveski, T. Braun, B. Neumann, A. Stammler, H.-G. Stammler, *Dalton Trans.* **2004**, 4106 – 4119.

[21] a) S. Burling, P. I. P. Elliott, N. A. Jasim, R. J. Lindup, J. McKenna, R. N. Perutz, S. J. Archibald, A. C. Whitwood, *Dalton Trans.* **2005**, 3686 – 3695; b) T. Braun, M. I. Sladek, B. Neumann, H.-G. Stammler, *New J. Chem.* **2003**, *27*, 313 – 318; c) N. A. Jasim, R. N. Perutz, A. C. Whitwood, T. Braun, J. Izundu, B. Neumann, S. Rothfeld, H.-G. Stammler, *Organometallics* **2004**, *23*, 6140 – 6149; d) I. M. Piglosiewicz, S. Kraft, R. Beckhaus, D. Haase, W. Saak, *Eur. J. Inorg. Chem.* **2005**, 938 – 945; e) U. Jäger-Fiedler, P. Arndt, W. Baumann, A. Spannenberg, V. V. Burlakov, U. Rosenthal, *Eur. J. Inorg. Chem.* **2005**, 2842 – 2849; f) T. Schaub, P. Fischer, A. Steffen, T. Braun, U. Radius, A. Mix, *J. Am. Chem. Soc.* **2008**, *130*, 9304 – 9317.

[22] see also: a) M. Aizenberg, D. Milstein, *Science* **1994**, *265*, 359 – 361; b) T. Braun, F. Wehmeier, K. Altenhöner, *Angew. Chem.* **2007**, *119*, 5415 – 5418; *Angew. Chem. Int. Ed.* **2007**, *46*, 5321 – 5324.

[23] a) M. Ahijado Salomon, T. Braun, I. Krossing, *Dalton Trans.* **2008**, 5197 – 5206; b) see also: S. A. Johnson, E. T. Taylor, S. J. Cruise, *Organometallics* **2009**, *28*, 3842 – 3855.

[24] J. E. McGrady, R. N. Perutz, M. Reinhold, *J. Am. Chem. Soc.* **2004**, *126*, 5268 – 5276.

[25] a) S. Erhardt, S. A. Macgregor, *J. Am. Chem. Soc.* **2008**, *130*, 15490 – 15498; b) A. Nova, S. Erhardt, N. A. Jasim, R. N. Perutz, S. A. Macgregor, J. E. McGrady, A. C. Whitwood, *J. Am. Chem. Soc.* **2008**, *130*, 15499 – 15511; c) A. Nova, M. Reinhold, R. N. Perutz, S. A. Macgregor, J. E. McGrady, *Organometallics* **2010**, in press.

[26] a) S. A. Macgregor, D. C. Roe, W. J. Marshall, K. M. Bloch, V. I. Bakhmutov, V. V. Grushin, *J. Am. Chem. Soc.* **2005**, *127*, 15304 – 15321; b) S. A. Macgregor, *Chem. Soc. Rev.* **2007**, *36*, 67 – 76; c) O. Blum, F. Frolow, D. Milstein, *J. Chem. Soc. Chem. Commun.* **1991**, 258 – 259; d) S. A. Macgregor, T. Wondimagegn, *Organometallics* **2007**, *26*, 1143 – 1149; e) J. Goodman, S. A. Macgregor, *Coord. Chem. Rev.* **2010**, *254*, 1295 – 1306.

[27] Gaussian 03, Revision D.01, M. J. Frisch et al. Gaussian, Inc. Pittsburgh PA, **2001**. The BP86 functional was employed with SDD RECPs and associated basis sets on rhodium and phosphorus (with d-orbital polarization on the latter) and 6-31G** basis sets on all other atoms. Energies include a correction for zero-point energies. See the Supporting Information for full details.

[28] For examples of fluorinated building blocks and their applications, see: a) "Organofluorine Chemistry: Fluorinated Alkenes and Reactive Intermediates": *Topics in Current Chemistry, Vol. 192* (Ed.: R. D. Chambers), Springer, Berlin, **1997**; b) T. Hiyama, *Organofluorine Compounds*, Springer, Berlin, **2000**; c) P. Kirsch, *Modern Fluoroorganic Chemistry*, Wiley-VCH, Weinheim, **2004**; L. A. Paquette, *Handbook of Reagents for Organic Syntheis: Fluorine-Containing Reagents*, Wiley, New York, **2007**.

C–F Activation

DOI: 10.1002/anie.201006789

Catalytic Hydrodefluorination of Pentafluorobenzene by [Ru(NHC)-$(PPh_3)_2(CO)H_2$]: A Nucleophilic Attack by a Metal-Bound Hydride Ligand Explains an Unusual *ortho*-Regioselectivity**

Julien A. Panetier, Stuart A. Macgregor, and Michael K. Whittlesey**

The selective synthesis of fluoroarene compounds is a subject of intense current interest, driven by the prominent role such species play in many pharmaceuticals, agrochemicals, and other industrially important products.[1] One attractive route to selectively substituted fluoroarenes involves the activation and functionalization of aromatic C–F bonds derived from readily available perfluoroarenes.[2] The simplest example of such a process is the hydrodefluorination reaction (HDF), in which fluorine is substituted for hydrogen. Catalytic HDF of C_6F_6 and C_6F_5H has been reported by Milstein et al.[3] and Holland et al.[4] using Rh and Fe catalysts.[5] However, both these systems exhibit practical problems that limit the mechanistic understanding of the HDF cycle. For example the Rh system requires high pressures of H_2 as well as a sacrificial amine to remove HF, while with Fe no C–F activation is observed in the absence of a reductant. As a consequence, the development of more active Rh or Fe catalysts has not been forthcoming.

We recently reported[6] the HDF of C_6F_6 and C_6F_5H using the ruthenium N-heterocyclic carbene (NHC) dihydride complex **1** (NHC = IMes, SIMes, IPr, SIPr;[7] see Scheme 1 a) in the presence of trialkylsilanes at 70 °C in THF. Isolation and characterization of **1** allowed detailed kinetic studies to be undertaken, and these supported a mechanism involving initial phosphine dissociation to form **2** followed by HDF of the substrate to give the Ru–F species, **3**. Isolation of this 16e complex allowed us to demonstrate its reaction with trialkylsilane in the presence of PPh_3 to regenerate catalyst **1**. The most unusual feature of this system was the high regioselectivity for the formation of 1,2,3,4-$C_6F_4H_2$ upon HDF of C_6F_5H, in complete contrast to the Milstein and Holland systems[3,4] where the 1,2,4,5-isomer dominated.

To account for the unusual *ortho*-regioselectivity we postulated the involvement of a tetrafluorobenzyne intermediate (Scheme 1 b). Such species have been reported previously[8] and could be formed here from **2** by successive C–H and *ortho*-C–F activation of C_6F_5H. However, density functional theory (DFT) calculations[9] (with NHC = IMes) have now shown that this species lies more than 200 kJ mol^{-1} above the reactants, effectively ruling it out as a viable intermediate under the conditions used experimentally.

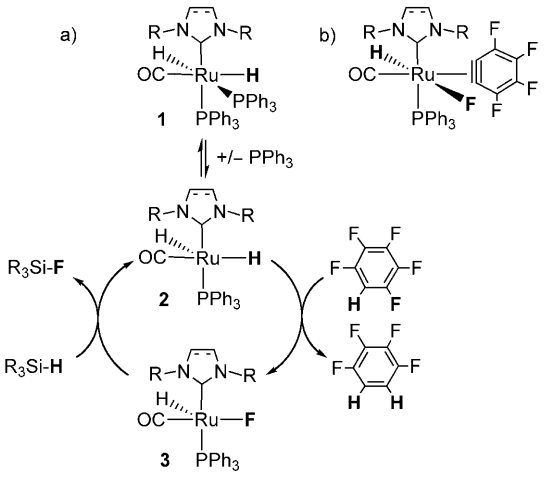

Scheme 1. a) Catalytic hydrodefluorination (HDF) of C_6F_5H to 1,2,3,4-$C_6F_4H_2$ by **1**; b) postulated tetrafluorobenzyne intermediate.

Further calculations, however, have now allowed us to define a series of alternative pathways which are based on a novel nucleophilic attack mechanism whereby a hydride ligand reacts directly with C_6F_5H.[10] These processes produced significantly lower barriers and, moreover, the lowest-energy pathway was found to be consistent with the unusual *ortho*-regioselectivity observed experimentally. Our calculations have shown that, after initial phosphine loss from **1**, nucleophilic attack of hydride at C_6F_5H can occur through two different pathways (Scheme 2). In the concerted pathway I, the hydride is transfered from the metal onto the arene ring and the displaced fluorine migrates directly onto the metal center. In the alternative stepwise pathway II, an η^2-arene adduct, **4**, is formed prior to the hydride attack. In this case the different orientation of the arene precludes direct transfer of fluorine onto the metal. Instead an intermediate is formed, **5**, from which HF can be lost to form a σ-aryl species, **6**. Protonolysis by HF with concomitant F transfer to metal then yields 1,2,3,4-$C_6F_4H_2$ and the M–F species **3**.

The lowest-energy reaction profile for the HDF of C_6F_5H by **1** to give 1,2,3,4-$C_6F_4H_2$ is computed to proceed through pathway II, and full details are shown in Figure 1.[11] Initial

[*] J. A. Panetier, Prof. S. A. Macgregor
School of EPS, Chemistry, Heriot-Watt University
Edinburgh EH14 4AS (UK)
E-mail: s.a.macgregor@hw.ac.uk
Dr. M. K. Whittlesey
Department of Chemistry, University of Bath
Claverton Down, Bath BA2 7AY (UK)
E-mail: m.k.whittlesey@bath.ac.uk

[**] We thank Heriot-Watt University and the EPSRC for funding J.A.P. through a DTA award. NHC = N-heterocyclic carbene.

Supporting information for this article is available on the WWW under http://dx.doi.org/10.1002/anie.201006789.

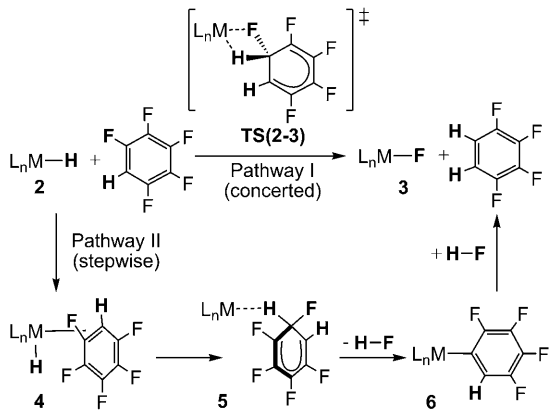

Scheme 2. Mechanisms of nucleophilic attack by a metal hydride ligand at C_6F_5H to give 1,2,3,4-$C_6F_4H_2$; L_nM = [Ru(NHC)(PPh_3)(CO)H].

PPh_3/C_6F_5H substitution gives **4** ($E = +37.7$ kJ mol^{-1} in THF[9]), in which the η^2-arene binds through the C5–C6 bond. Attack of H5 at C5 occurs through **TS(4–5)** ($E = +75.3$ kJ mol^{-1}) and gives **5** ($E = +69.5$ kJ mol^{-1}), in which the $\{C_6F_5H_2\}^-$ moiety resembles a Meisenheimer intermediate (C5–H5 1.24 Å, C5–F5 1.45 Å). This structure is also stabilized by interaction of the *ortho* position with the metal center (Ru–C6 2.28 Å). The subsequent step through **TS(5–6)** ($E = +84.1$ kJ mol^{-1}) involves elongation of the C5–F5 bond to 1.95 Å. To this point the reaction parallels nucleophilic aromatic substitution, however, rather than acting as a simple leaving group the highly fluoridic center F5 (computed charge −0.54) is able to abstract H5 to form HF. As this occurs, the remaining $\{C_6F_4H\}^-$ moiety is trapped by Ru to give **6** ($E = -40.2$ kJ mol^{-1}). The calculations suggest that HF remains loosely associated with the aryl ligand in **6** (H5···C5 1.97 Å), and so it is ideally placed to effect protonolysis of the Ru–C5 bond with concomitant F transfer to Ru. This step occurs through **TS(6–3)** ($E = -18.4$ kJ mol^{-1}) and gives [Ru(IMes)-(PPh_3)(CO)HF] (**3**) and 1,2,3,4-$C_6F_4H_2$. Overall, HDF of C_6F_5H is a highly favorable process ($\Delta E = -168.1$ kJ mol^{-1}) and proceeds with a barrier of 84.1 kJ mol^{-1} corresponding to **TS(5–6)**.

A transition state for the concerted HDF process through pathway I was also located (Figure 2). This process involves the direct reaction of C_6F_5H with five-coordinate [Ru(IMes)-(PPh_3)(CO)H_2] (**2**) to give 1,2,3,4-$C_6F_4H_2$ and **3** and proceeds through **TS(2–3)** ($E = +113.4$ kJ mol^{-1}). The structure of **TS(2–3)** features a side-on orientation of C_6F_5H, and this means that the vacant site at Ru is now readily available to accept the displaced F5 substituent directly. In contrast, in **TS(5–6)** this site is blocked by interaction with the *ortho* C6 position. Overall, the barrier computed in THF for the concerted reaction through **TS(2–3)** is 29.3 kJ mol^{-1} above that for the stepwise process through **TS(5–6)**.

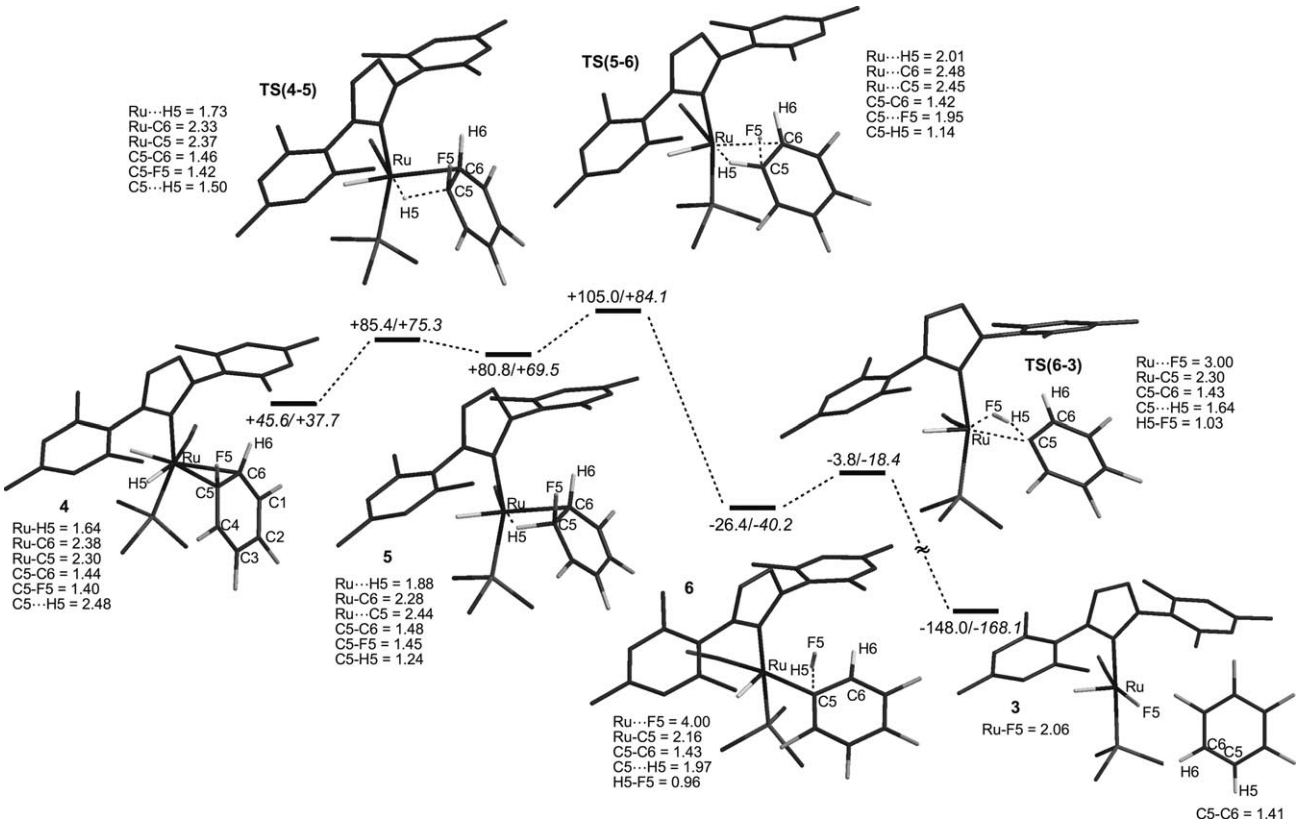

Figure 1. Computed reaction profile for HDF of C_6F_5H at [Ru(IMes)(PPh_3)(CO)H_2] to give 1,2,3,4-$C_6F_4H_2$ through pathway II. Energies (kJ mol^{-1}) are quoted relative to **1** and C_6F_5H computed separately; values in italics include a solvent correction (PCM method, THF). Selected distances are in Å. Phosphine Ph groups are truncated at the *ipso* carbon center and non-participating H atoms are omitted for clarity.

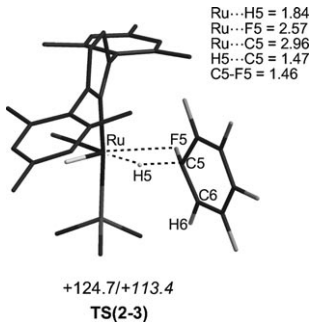

Figure 2. Computed transition state for HDF of C_6F_5H at [Ru(IMes)-$(PPh_3)(CO)H_2$] (**2**) to give 1,2,3,4-$C_6F_4H_2$ through pathway I. Energies are in kJ mol^{-1} and the solvent-corrected values are in italics (PCM method, THF). Selected distances are in Å. Phosphine Ph groups are truncated at the *ipso* carbon center and non-participating H atoms are omitted for clarity.

We have also considered the formation of different isomers of $C_6F_4H_2$, and in all cases were able to characterize both the stepwise and concerted pathways. The lowest energy barriers computed for the formation of 1,2,3,5- and 1,2,4,5-$C_6F_4H_2$ in THF were 98.3 kJ mol^{-1} and 99.5 kJ mol^{-1}, respectively, and in both cases corresponded to the stepwise mechanism, pathway II. The formation of 1,2,3,4-$C_6F_4H_2$ with a barrier of 84.1 kJ mol^{-1} therefore remains the most accessible reaction, and this kinetic preference is consistent with the *ortho*-selectivity that is observed experimentally.[12,13]

The factors promoting these unusual hydride ligand nucleophilic attack reactions have been probed by calculations with a small model system featuring an N-methyl substituted carbene and PH_3 ligands. Thus, [Ru(IMe)-$(PH_3)_2(CO)H_2$] (**1′**)[7] yields barriers that are between 20 and 45 kJ mol^{-1} higher than those computed with the full model. One reason for this difference is that the initial phosphine/C_6F_5H substitution step is more accessible for the more sterically encumbered full system. Reduced barriers for the nucleophilic attack/C–F bond cleavage steps are also seen in the full model system, and these may again reflect a more weakly bound arene. These steric effects are particularly large for the formation of the 1,2,3,4-$C_6F_4H_2$ isomer, where calculations with **1′** give a barrier 45 kJ mol^{-1} higher than that computed for the full system.

In summary, DFT calculations have defined a novel class of reaction mechanism for the HDF of C_6F_5H catalyzed by [Ru(IMes)$(PPh_3)_2(CO)H_2$]. The key feature is the direct nucleophilic attack of a Ru hydride ligand at the fluoroarene substrate. The overall HDF process may occur either through a stepwise or a concerted pathway. The most accessible process is seen for the formation of 1,2,3,4-$C_6F_4H_2$ and involves 1) PPh_3/C_6F_5H substitution; 2) nucleophilic attack by the Ru hydride ligand at the *ortho* position on the ring; 3) HF loss and Ru fluoroaryl formation; and 4) protonolysis by HF with concomitant fluoride transfer to Ru to give 1,2,3,4-$C_6F_4H_2$ and [Ru(IMes)(PPh_3)(CO)HF]. This pathway has a modest computed barrier of 84.1 kJ mol^{-1} in THF and is entirely consistent with the unusual *ortho*-regioselectivity that is observed experimentally. We believe that these results will provide a starting point for further experimental studies on transition metal hydride induced HDF and may allow the development of systems that display higher activity and additional control of regioselectivity.

Received: October 28, 2010
Revised: December 7, 2010
Published online: February 18, 2011

Keywords: C–F activation · density functional calculations · fluoroarenes · hydrodefluorination · ruthenium

[1] a) A. M. Thayer, *Chem. Eng. News* **2006**, *84*, 15–24; b) S. Purser, P. R. Moore, S. Swallow, V. Gouverneur, *Chem. Soc. Rev.* **2008**, *37*, 320; c) S. M. Ametamey, M. Honer, P. A. Schubiger, *Chem. Rev.* **2008**, *108*, 1501–1516; d) V. V. Grushin, *Acc. Chem. Res.* **2010**, *43*, 160–171; e) D. O'Hagan, *J. Fluorine Chem.* **2010**, *131*, 1071–1081.

[2] For reviews see: a) J. L. Kiplinger, T. G. Richmond, C. E. Osterberg, *Chem. Rev.* **1994**, *94*, 373–431; b) J. Burdeniuc, B. Jedlicka, R. H. Crabtree, *Chem. Ber. Rec.* **1997**, *130*, 145–154; c) T. Braun, R. N. Perutz, *Chem. Commun.* **2002**, 2749–2757; d) W. D. Jones, *Dalton Trans.* **2003**, 3991–3995; e) H. Torrens, *Coord. Chem. Rev.* **2005**, *249*, 1957–1985; f) R. N. Perutz, T. Braun in *Comprehensive Organometallic Chemistry III*, *Vol. 1* (Eds.: R. H. Crabtree, D. M. P. Mingos), Elsevier, Oxford, **2007**, p. 725–758; g) H. Amii, K. Uneyama, *Chem. Rev.* **2009**, *109*, 2119–2183; h) G. Meier, T. Braun, *Angew. Chem.* **2009**, *121*, 1575–1577; *Angew. Chem. Int. Ed.* **2009**, *48*, 1546–1548; i) A. D. Sun, J. A. Love, *Dalton Trans.* **2010**, *39*, 10362–10374.

[3] a) M. Aizenberg, D. Milstein, *Science* **1994**, *265*, 359–361; b) M. Aizenberg, D. Milstein, *J. Am. Chem. Soc.* **1995**, *117*, 8674–8675.

[4] J. Vela, J. M. Smith, Y. Yu, N. A. Ketterer, C. J. Flaschenriem, R. J. Lachicotte, P. L. Holland, *J. Am. Chem. Soc.* **2005**, *127*, 7857–7870.

[5] For other recent examples of catalytic HDF, see a) U. Jäger-Fiedler, M. Klahn, P. Arndt, W. Baumanna, A. Spannenberg, V. V. Burlakov, U. Rosenthal, *J. Mol. Catal. A* **2007**, *261*, 184–189; b) K. Fuchibe, Y. Ohshima, K. Mitomi, T. Akiyama, *J. Fluorine Chem.* **2007**, *128*, 1158–1167; c) T. Braun, D. Noveski M. Ahijado, F. Wehmeier, *Dalton Trans.* **2010**, *39*, 7513; d) C. Douvris, O. V. Ozerov, *Science* **2008**, *321*, 1188–1190; e) M. F. Kühnel, D. Lentz, *Angew. Chem.* **2010**, *122*, 2995–2998; *Angew. Chem. Int. Ed.* **2010**, *49*, 2933–2936; f) C. Douvris, C. M. Nagaraja, C.-H. Chen, B. M. Foxman, O. V. Ozerov, *J. Am. Chem. Soc.* **2010**, *132*, 4946–4953; g) D. Breyer, T. Braun, A. Penner, *Dalton Trans.* **2010**, *39*, 7513.

[6] S. P. Reade, M. F. Mahon, M. K. Whittlesey, *J. Am. Chem. Soc.* **2009**, *131*, 1847–1861.

[7] IMes = 1,3-bis(2,4,6-trimethylphenyl)imidazol-2-ylidene; SIMes = 1,3-bis(2,4,6-trimethylphenyl)imidazolin-2-ylidene; IPr = 1,3-bis(2,6-diiso-propylphenyl)imidazol-2-ylidene; SIPr = 1,3-bis(2,6-diisopropylphenyl)-imidazolin-2-ylidene; IMe = 1,3-dimethylimidazol-2-ylidene.

[8] a) R. P. Hughes, A. Williamson, R. D. Sommer, A. L. Rheingold, *J. Am. Chem. Soc.* **2001**, *123*, 7443–7444; b) R. P. Hughes, R. B. Larichev, A. Williamson, C. D. Incarvito, L. N. Zakharov, A. L. Rheingold, *Organometallics* **2002**, *21*, 4873–4885.

[9] Gaussian 03, Revision D.01, M. Frisch, et al. Gaussian, Inc. Pittsburgh PA, **2001**. The BP86 functional was employed with SDD RECPs and basis sets on Ru and P (with d-orbital polarization on the latter) and 6-31G** basis sets on all other atoms. See Supporting Information for full details and for all computed structures and energies. All energies in the text include a correction for the effects of THF solvent (PCM method).

[10] Related mechanisms have been postulated for H/F exchange in C_6F_6 and C_6F_5H at $[Cp^*_2ZrH_2]$[10a] and [{1,3,4-$(Me_3C)_3C_5H_2$}$_2$CeH].[10b] a) B. M. Kraft, W. D. Jones, *J. Organomet. Chem.* **2002**, *658*, 132–140; b) L. Maron, E. L. Werkema, L. Perrin, O. Eisenstein, R. A. Andersen, *J. Am. Chem. Soc.* **2005**, *127*, 279–292.

[11] All key stationary points were the subject of extensive conformational searching according to the protocol described in the Supporting Information.

[12] 1,2,3,4-$C_6F_4H_2$ can also be formed from an isomer of **4** in which the arene binds through the C1–C2 bond and H5 attacks C1. This process entailed a barrier of $+125.5\ kJ\,mol^{-1}$ in THF, significantly higher than the reaction shown in Figure 1.

[13] The lowest-energy pathway computed for HDF of C_6F_6 was also found to involve nucleophilic attack of the hydride ligand and had a barrier of $91.2\ kJ\,mol^{-1}$ corresponding to the stepwise pathway. This therefore supersedes the σ-bond metathesis mechanism proposed previously.[6]

